Synaptic Transmission in the Inner Ear between Basic Research and Gene Therapy

Dissertation

der Mathematisch-Naturwissenschaftlichen Fakultät
der Eberhard Karls Universität Tübingen
zur Erlangung des Grades eines
Doktors der Naturwissenschaften
(Dr. rer. nat.)

vorgelegt von
Xanthoula Smyrnakou-Biedenbänder
aus Thessaloniki/Griechenland

Tübingen
2025

Gedruckt mit Genehmigung der Mathematisch-Naturwissenschaftlichen Fakultät der Eberhard Karls Universität Tübingen.

Tag der mündlichen Qualifikation:	16.07.2025
Dekan:	Prof. Dr. Thilo Stehle
1. Berichterstatter/-in:	Prof. Dr. Andrea Burgalossi
2. Berichterstatter/-in:	Prof. Dr. Ellen Reisinger

Independence Declaration

Ich erkläre, dass ich die zur Promotion eingereichte Arbeit mit dem Titel:

„Synaptic Transmission in the Inner Ear between Basic Research and Gene Therapy“

selbständig verfasst, nur die angegebenen Quellen und Hilfsmittel benutzt und wörtlich oder inhaltlich übernommene Stellen (alternativ: Zitate) als solche gekennzeichnet habe. Ich erkläre, dass die Richtlinien zur Sicherung guter wissenschaftlicher Praxis der Universität Tübingen (Beschluss des Senats vom 25.5.2000) beachtet wurden. Ich Amtliche Bekanntmachungen der Universität Tübingen 2015, Nr.5, S. 154 versichere an Eides statt, dass diese Angaben wahr sind und dass ich nichts verschwiegen habe. Mir ist bekannt, dass die falsche Abgabe einer Versicherung an Eides statt mit Freiheitsstrafe bis zu drei Jahren oder mit Geldstrafe bestraft wird.“

I declare that I have completed the thesis submitted for my doctorate entitled:

‘Synaptic Transmission in the Inner Ear between Basic Research and Gene Therapy’

independently, have only used the sources and aids indicated and have labelled passages taken verbatim or in terms of content (alternatively: quotations) as such. I declare that the guidelines for safeguarding good scientific practice at the University of Tübingen (resolution of the Senate of 25 May 2000) have been observed. I declare on oath that this information is true and that I have not concealed anything. I am aware that making a false declaration in lieu of an oath is punishable by imprisonment of up to three years or a fine.’

Tübingen, den ....

Unterschrift /Signature

Acknowledgements

Zu Beginn möchte ich mich herzlich bei meinen Prüfer:innen Prof. Dr. Ellen Reisinger, Prof. Dr. Burgalossi, Prof. Dr. Wissinger und Prof. Dr. Stafforst für die Begleitung und Unterstützung während meiner Promotionszeit bedanken.

Mein besonderer Dank gilt jedoch meiner Doktormutter Prof. Dr. Ellen Reisinger. Liebe Ellen, ich danke dir von Herzen dafür, dass ich Teil deines großartigen Teams sein durfte. Ich habe jeden einzelnen Tag sehr genossen. Vielen Dank für deine kontinuierliche Unterstützung, sei es bei wissenschaftlichen Fragen oder persönlichen Angelegenheiten. Ich wusste immer, dass ich mich auf dich verlassen kann. Besonders dankbar bin ich dir dafür, dass du es als selbstverständlich angesehen hast, dass sich Karriere und Familie als Frau vereinbaren lassen. Ohne dein Vertrauen und deine Unterstützung wäre ich heute sicherlich keine (fast) Zweifachmama. Die Wissenschaft braucht definitiv mehr Power-Frauen wie dich! Ich wünsche dir für die Zukunft nur das Beste, viele tolle Publikationen und Preise. Das hast du wirklich verdient.

Ein herzliches Dankeschön auch an meine wunderbaren Kolleg:innen André, Franzi, Ramil, Johanna, Lucie, Karina und Andrea! Die Zeit mit euch war unvergesslich. Ich werde unsere Challenges, Blindverkostungen, gemeinsamen Brunches und unzähligen Kuchenrunden nie vergessen. Dank euch bin ich jeden Tag gerne ins Labor gekommen.

Vor allem möchte ich mich bei meinen liebsten Kolleg:innen Franzi und André für die außergewöhnlich schöne gemeinsame Zeit bedanken.
Liebe Franzi, wir zwei waren von Tag eins an unzertrennlich. Ich war von Anfang an

so froh, dass wir diese Reise gemeinsam gehen konnten. Zum Glück hattest du die Idee, während meiner Elternzeit nach Japan zu gehen. Es ist nämlich nur fair, dass wir gemeinsam anfangen und gemeinsam abschließen.
Lieber André, du bist vermutlich der netteste Mensch, den ich kenne. Ich habe es dir nie gesagt, aber du warst im Labor mein Vorbild. Du hast jede Herausforderung so cool gemeistert.
Ihr zwei habt mich durch einige der schönsten Zeiten meines Lebens begleitet – meine Hochzeit, meine Schwangerschaften etc. und ich wusste immer, dass ich zwei echte Freunde an meiner Seite habe, die mich unterstützen. Ich habe die Zeit mit euch sehr genossen und werde jede einzelne Sekunde vermissen.

Mein tiefster Dank gilt auch meiner Familie, meinen Eltern und Geschwistern, für ihre bedingungslose Unterstützung. Ich wusste immer, dass ich auf euch zählen kann, ganz gleich was passiert.
Danke, liebe Mami, dass du dich so liebevoll um meinen Jonas gekümmert hast, damit ich das hier durchziehen kann. Das werde ich nie vergessen.

Zum Schluss möchte ich mich bei meinem besten Freund und Ehemann bedanken, der seit über zehn Jahren an meiner Seite ist.
Ob Bachelorarbeit, Masterarbeit oder nun die Promotion, du warst immer da, hast mich unterstützt, mir Kraft gegeben, an mich geglaubt und mich motiviert, weiterzumachen und nicht aufzugeben.
Danke, dass du meine bessere Hälfte bist. Danke für unsere wundervolle Familie und vor allem: Danke für unsere (bald) zwei wunderbaren Kinder.

Meine Doktorarbeit möchte ich gerne euch dreien widmen!

Abstract

Hearing loss can result from a variety of factors, including chronic diseases, ear infections, and genetic mutations. One genetic contributor is the *OTOF* gene, which encodes the protein otoferlin, essential for synaptic transmission from auditory inner hair cells (IHCs) to spiral ganglion neurons (SGNs), the first neurons in the auditory pathway. Mutations in *OTOF* cause autosomal recessive prelingual hearing impairment, classified as DFNB9, which is typically severe to profound in degree.

Otoferlin contains multiple C2 domains and a C2-FerA domain which forms a flexible superhelix composed of four α-helices and has been shown to bind calcium ions (Ca^{2+}) and phospholipids. However, its specific role in auditory function remains unclear.

In this thesis, a novel mouse line, designated Otof-p. KL>M, was characterized. This line carries a three-base pair deletion resulting in the substitution of lysine 824 and leucine 825 with a methionine, predicted to shorten one α-helical structure within the C2-FerA domain. Auditory brainstem response (ABR) measurements revealed that homozygous Otof-p. KL>M mice exhibit reduced ABR wave amplitudes at a young age and develop significant age-related hearing loss. By twelve months of age, these mice displayed elevated hearing thresholds reaching 90 dB sound pressure level (SPL) at the most sensitive frequency (4 kHz).

As anticipated, the Otof-p. KL>M mutation did not affect distortion product otoacoustic emissions (DPOAEs), indicating preserved outer hair cell (OHC) function. Consistently, the number of OHCs remained unchanged across all ages. In contrast, an age-dependent loss of IHCs was observed throughout all cochlear turns in Otof-p. KL>M mice. Moreover, IHCs in mutant mice demonstrated reduced otoferlin

expression with increasing age compared to wild-type controls. Collectively, these findings highlight a critical role for the otoferlin C2-FerA domain in maintaining IHC integrity and function.

Several gene therapy strategies targeting the otoferlin coding gene have been investigated in otoferlin-deficient mouse models and early-stage clinical trials. These studies have shown that dual-adeno-associated virus (AAV) gene therapy can effectively deliver a functional *OTOF* sequence to the inner ear. Nonetheless, optimization of these approaches remains necessary. One avenue of improvement involves engineering novel AAV capsids with enhanced tropism and transduction efficiency for both IHCs and OHCs. In this thesis, a novel in vitro AAV transduction method was developed using explanted organs of Corti to facilitate pre-screening of AAV serotypes. Initial testing of various GFP-expressing AAV serotypes identified PHP.eB (produced in-house) and AAV2 PT (provided by AG Michalakis, LMU Munich) as having the highest transduction efficiencies and specificity in hair cells. Furthermore, three AAV capsids were evaluated for dual-AAV transduction in in vitro experiments using otoferlin knockout organ of Corti cultures. Among these, the PHP.B serotype yielded the most promising results, demonstrating successful transduction of both IHCs and OHCs. These findings validate the utility of the newly developed in vitro method for assessing dual-AAV strategies. Importantly, this approach offers a time-efficient method to pre-screen AAV serotypes in vitro and thereby reducing the number of animals required.

In addition to *OTOF*, other genes also play vital roles in auditory function. In five patients from Tübingen and Heidelberg presenting with progressive hearing loss, a dominantly inherited point mutation in the *RAB4B* gene, encoding the Ras-related protein RAB4B, was identified. These individuals exhibit increasing difficulty with

speech comprehension, despite only moderately elevated hearing thresholds. To date, *RAB4B* has not been associated with auditory disorders. To investigate Rab4b expression in the auditory system, immunohistochemistry and RNA Scope in situ hybridization were performed on wild-type mouse inner ears. Both Rab4b protein and mRNA were detected, with expression localized to IHCs, OHCs, and strongly in SGNs. Subsequently, genetically engineered mice carrying the same point mutation as the human patients were generated to assess the functional consequences of the variant. The results presented in this thesis offer initial insights into the potential role of Rab4b in auditory physiology and pathophysiology.

Zusammenfassung

Hörverlust kann durch eine Vielzahl von Faktoren verursacht werden, darunter chronische Erkrankungen, Ohreninfektionen und genetische Ursachen.

Das Protein Otoferlin ist essenziell für die synaptische Signalübertragung von den auditorischen Haarzellen zu den Spiralganglienzellen, den ersten Neuronen der Hörbahn. Mutationen im *OTOF*-Gen, welches für Otoferlin kodiert, führen zu einer autosomal-rezessiv vererbten prälingualen Hörstörung (DFNB9), die meist schwer bis hochgradig ausgeprägt ist. Das Protein besteht aus mehreren C2-Domänen sowie einer C2-FerA-Domäne, die eine flexible Superhelix aus vier α-Helices bildet und Ca^{2+} und Phospholipide binden kann. Ihre genaue Funktion im Hörvorgang ist jedoch bislang ungeklärt.

Im Rahmen dieser Arbeit wurde eine Mauslinie mit der Bezeichnung Otof-p. KL>M charakterisiert, die eine Deletion von drei Basenpaaren trägt, welche zum Austausch der Aminosäuren Lysin 824 und Leucin 825 durch Methionin führt. Diese Mutation verkürzt, Strukturvorhersagen zufolge, eine α-Helix der C2-FerA-Domäne. Mittels Messungen der auditorisch evozierten Hirnstammpotenziale (ABR) konnte festgestellt werden, dass homozygote Otof-p. KL>M-Mäuse im jungen Alter reduzierte ABR-Wellenamplituden aufweisen und mit zunehmendem Alter einen signifikanten Hörverlust entwickeln. Zwölf Monate alte Otof-p. KL>M-Mäuse zeigten bei der besten Frequenz von 4 kHz Hörschwellen von 90 dB Schalldruckpegel (SPL). Wie erwartet hatte die Mutation keinen Einfluss auf die otoakustischen Emissionen (OAE). Entsprechend wurde in keiner Altersgruppe ein Unterschied in der Anzahl äußerer Haarzellen festgestellt. Im Gegensatz dazu wiesen Otof-p. KL>M-Mäuse einen altersabhängigen Verlust innerer Haarzellen in allen Windungen des Corti-Organs auf.

Darüber hinaus zeigten innere Haarzellen dieser Mäuse mit zunehmendem Alter eine geringere Proteinexpression im Vergleich zu Wildtyp-Mäusen. Insgesamt verdeutlicht dieser Teil der Arbeit die entscheidende Rolle der C2-FerA-Domäne von Otoferlin für die Funktion und das Überleben innerer Haarzellen.

Verschiedene Gentherapieansätze an Otoferlin-Mausmodellen sowie erste klinische Studien mit Betroffenen, die *OTOF*-Mutationen tragen, haben gezeigt, dass die duale AAV-Gentherapie erfolgreich zur Einführung einer korrekten *OTOF*-Sequenz im Innenohr eingesetzt werden kann. Dennoch besteht weiterhin Optimierungspotenzial. So werden beispielsweise AAV-Kapside mit verbesserter Effizienz und höherer Spezifität für innere und äußere Haarzellen entwickelt. In dieser Arbeit wird eine neuartige in vitro-AAV-Transduktionsmethode am Corti-Organ vorgestellt, die als Vorscreening für verschiedene AAV-Serotypen dient. Zunächst wurden verschiedene GFP-exprimierende AAV-Serotypen getestet, wobei PHP.eB (aus selbst produzierten AAVs) und AAV2 PT (aus der AG Michalakis, LMU München) die höchsten Transduktionsraten und die beste Spezifität für innere und äußere Haarzellen zeigten. Darüber hinaus wurden drei verschiedene Kapside hinsichtlich ihrer Eignung für die duale AAV-Transduktion an Otof-Knockout-Corti-Organen untersucht. Dabei zeigte der Serotyp PHP.B die vielversprechendsten Ergebnisse, da beide AAVs erfolgreich in IHCs und OHCs eindrangen, was die Machbarkeit der dualen Transduktion mit der neuen in vitro-Methode bestätigt. Insgesamt stellt die entwickelte Methode ein effektives Vorscreening-Tool für die AAV-Gentherapie des Innenohrs dar, das gegenüber in vivo-Experimenten erhebliche Zeit spart und den Bedarf an Versuchstieren reduziert.

Neben *OTOF* spielen auch andere Gene eine wesentliche Rolle im Hörvorgang. Bei fünf Patient:innen aus Tübingen und Heidelberg mit progredientem Hörverlust wurde

eine dominant vererbte Punktmutation im *RAB4B*-Gen identifiziert, das für das Ras-verwandte Protein RAB4B kodiert. Die Betroffenen zeigten zunehmende Schwierigkeiten beim Sprachverstehen, obwohl ihre Hörschwellen nur moderat erhöht waren. Bisher wurde *RAB4B* nicht mit Hörstörungen in Verbindung gebracht. Zur weiteren Charakterisierung der Funktion von Rab4b wurden Immunfärbungen und RNA Scope-Analysen am Innenohr von Wildtyp-Mäusen durchgeführt. Dabei konnte nachgewiesen werden, dass sowohl *Rab4b*-RNA als auch das entsprechende Protein im Innenohr exprimiert werden, insbesondere in innere und äußere Haarzellen und sehr ausgeprägt in den Spiralganglienneuronen. Zudem wurden genetisch veränderte Mäuse erzeugt, die dieselbe Punktmutation wie die betroffenen Patient:innen tragen, um zu prüfen, ob diese Mutation auch bei Mäusen zu Hörverlust führt. Zusammenfassend liefert diese Arbeit erste Hinweise auf die potenzielle Bedeutung von Rab4b für das Innenohr.

Table of Content

1. List of Abbreviations

ABR	Auditory Brainstem Response
AAV	Adeno-Associated Virus
AAVR	AAV Receptor
AdV	Adenovirus
AK	F1 Phage Recombination Region
AP	Alkaline Phosphatase
BFP	Blue Fluorescent Protein
bGH	Bovine Growth Hormone
BSA	Bovine Serum Albumin
bp	Base pair
Ca^{2+}	Calcium ions
CDS	Coding Sequence
CNS	Central Nervous System
dB	Decibel
DMEM	Dulbecco's Modified Eagle's Medium
DNA	Deoxyribonucleic Acid
DPOAE	Distortion Product Otoacoustic Emissions
EDTA	Ethylenediaminetetraacetic Acid
FBS	Fetal Bovine Serum
GEFs	Guanine Nucleotide Exchange Factors
GDP	Guanosine Diphosphate
GFP	Green Fluorescent Protein
GLUT4	Glucose Transporter Type 4

List of Abbreviations

GTP	Guanosine Triphosphate
GTPase	Guanosine Triphosphatase
gRNA	Guide RNA
HEPES	4-(2-Hydroxyethyl)-1-piperazineethanesulfonic Acid
IHC	Inner Hair Cell
ITR	Inverted Terminal Repeat
kb	Kilobase (1,000 base pairs)
NHPs	Non-Human Primates
OAE	Otoacoustic Emissions
OHC	Outer Hair Cell
PBS	Phosphate-Buffered Saline
PFA	Paraformaldehyde
PLA	Proximity Ligation Assay
PCR	Polymerase Chain Reaction
rAAV	Recombinant Adeno Associated Virus
RAB	Ras-related protein in brain
Ras	Reticular Activation System (likely referring to the protein family)
REPs	Rab Escort Proteins
RRP	Readily Releasable Pool
RT-PCR	Real Time Polymerase Chain Reaction
SA	Splice Acceptor
SC	Supporting Cells
SD	Splice Donor

SGN	Spiral Ganglion Neuron
sgRNA	Single guide RNA
SNHL	Sensorineural Hearing Loss
SPL	Sound Pressure Level
SV	Synaptic Vesicle
Taq	Thermus aquaticus (polymerase)
TMD	Transmembrane Domain
vg	Vector Genomes
WPRE	Woodchuck Hepatitis virus Posttranscriptional Regulatory Element

2. List of Figures

3. List of Tables

4. Introduction

4.1 The hearing process

The auditory process comprises a series of distinct steps that convert sound waves into electrical signals that can be interpreted by the brain. Initially, sound waves are collected by the outer ear and travel through the ear canal to reach the tympanic membrane, or eardrum. The vibration of the eardrum causes motion in the ossicles, comprising the malleus, incus, and stapes, within the middle ear, which ensures that the vibration force from the air is effectively transferred to the liquid (Fig. 1). These vibrations are transmitted to the cochlea in the inner ear, where they induce fluid movement, generating a traveling wave along the basilar membrane. This wave motion causes the stereocilia of cochlear sensory cells, known as hair cells, to deflect (Fig. 2). The deflection of the stereocilia stretches the tip links connecting them, resulting in the opening of mechanically gated ion channels. The opening of these channels allows potassium and calcium ions to enter the hair cells, leading to depolarization and the subsequent release of neurotransmitters at the base of the hair cells. This entire process, by which mechanical energy is converted into electrical signals, is referred to as mechanoelectrical transduction. The electrical signals are then transmitted via the auditory nerve to the brain, where they are interpreted as sound.

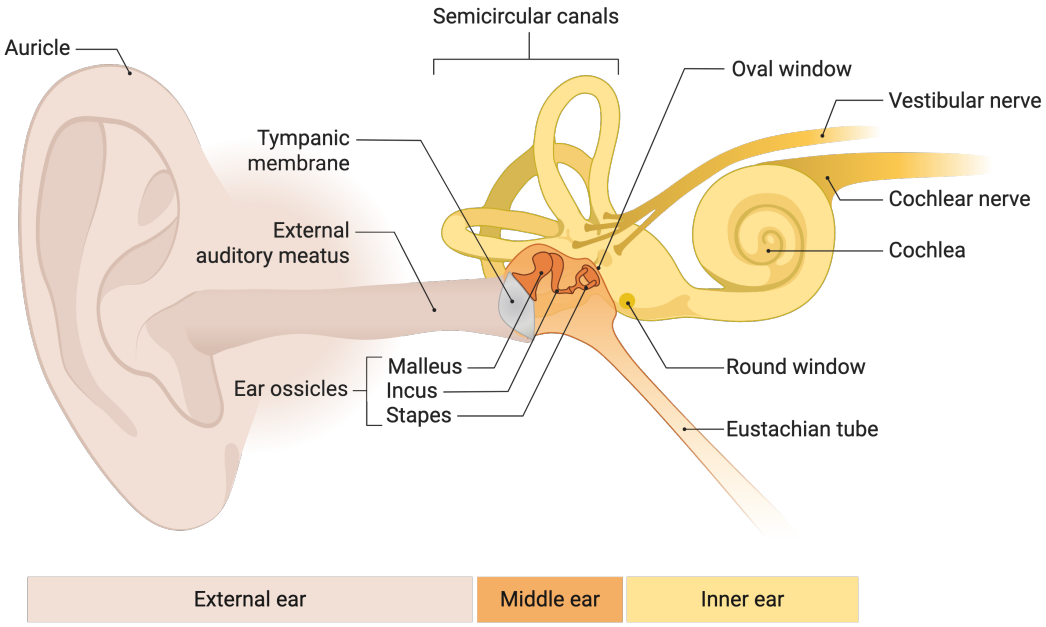

Figure 1 - Anatomical overview of the human ear, illustrating the external, middle, and inner ear compartments.

The external ear comprises the auricle and the external auditory meatus, which direct sound waves toward the tympanic membrane (eardrum). The middle ear contains the ossicular chain (malleus, incus, and stapes) which transmits mechanical vibrations from the tympanic membrane to the oval window. The inner ear includes the cochlea, responsible for auditory transduction, and the semicircular canals, which contribute to balance. Adapted from biorender.com.

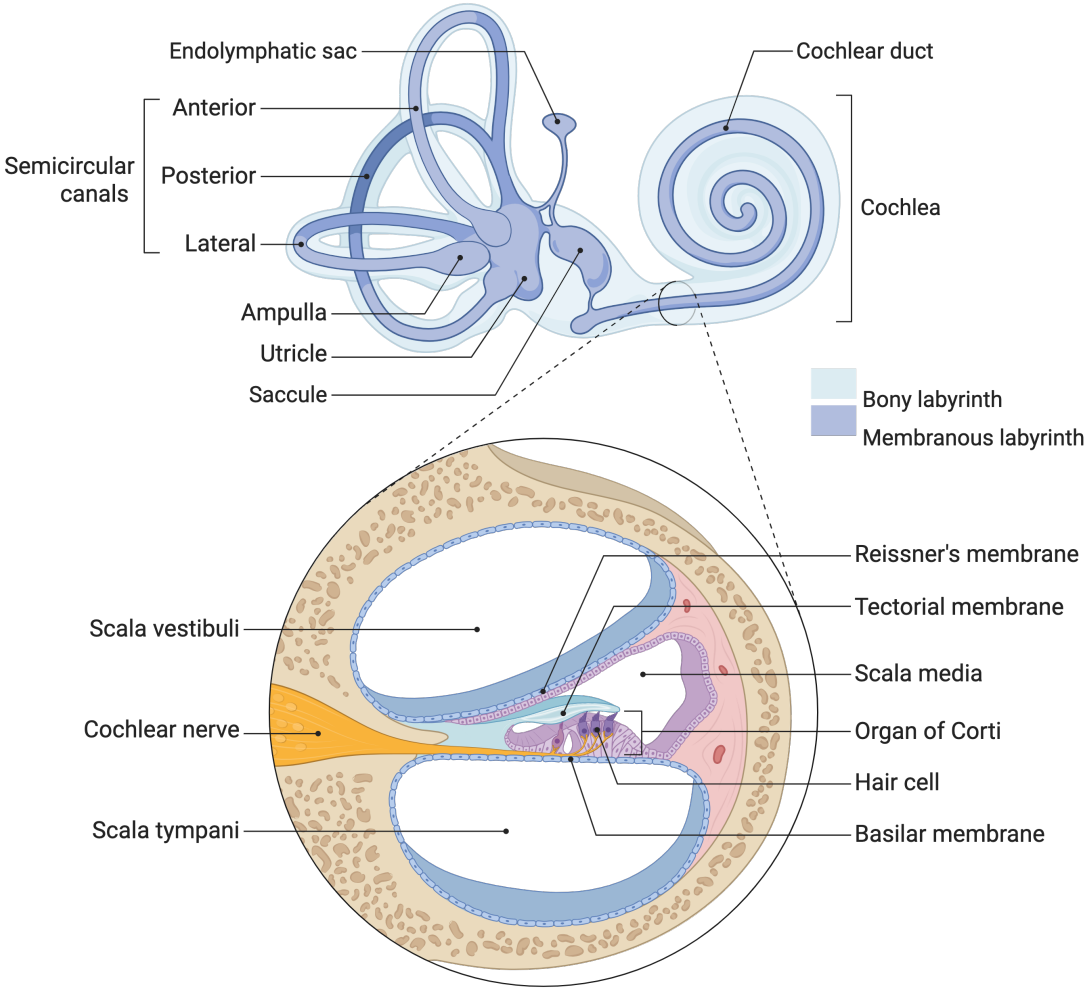

Figure 2 - Structural organization of the inner ear, highlighting the cochlear anatomy and a cross-section of the cochlear duct.
The upper part of the image displays the membranous and bony labyrinth of the inner ear, including the semicircular canals (anterior, posterior, and lateral), the vestibular organs (utricle and saccule) and the cochlea. The cochlear duct (scala media) is shown within the coiled cochlear structure. The lower part of the image presents a detailed cross-sectional view of the cochlea, illustrating the three fluid-filled chambers: the scala vestibuli, scala media, and scala tympani. The organ of Corti contains mechanosensory hair cells which are essential for auditory transduction. Key anatomical features include Reissner's membrane, the basilar membrane, the tectorial membrane, and the cochlear nerve, which transmits auditory signals to the brain. Adapted from biorender.com.

4.2 Hearing disorders

Over 5% of the global population, approximately 430 million individuals, including 34 million children, require rehabilitation for the management of disabling hearing loss. Projections indicate that by 2050, this number will exceed 700 million, representing approximately one in every ten individuals worldwide (WHO, 2025).

A person is considered to have hearing loss if their auditory thresholds are at least 20 dB (decibel) higher than on average (i.e. 20 dB hearing level (HL)) in one or both ears, compared to an individual with normal hearing. Hearing loss can be classified into several degrees of severity: mild (difficulty hearing soft sounds; 20 to <35 dB HL (Hearing Level)), moderate (difficulty understanding normal speech; 35 to <50 dB HL), moderately severe (difficulty with loud speech; 50 to <65 dB HL), severe (limited perception of sounds, only hearing very loud noises; 65 to <80 dB HL), or profound (near-total deafness, relying on visual communication or implants; 80 to <95 dB HL) (Olusanya *et al*, 2019; WHO, 2021). The condition may affect one or both ears and can significantly hinder the ability to hear conversational speech or even loud sounds. The term "hard of hearing" is used to describe individuals with hearing loss ranging from mild to severe. These individuals often communicate using spoken language and may benefit from hearing aids, cochlear implants, assistive devices, or captioning services (WHO, 2025). On the other hand, individuals classified as "deaf" generally experience profound hearing loss, characterized by little or no ability to hear. Although some may benefit from cochlear implants, many rely on sign language as their primary mode of communication (WHO, 2025).

Hearing loss and deafness can arise from a variety of causes across the lifespan. Prenatal causes include genetic disorders and intrauterine infections. In childhood,

common contributing factors include chronic ear infections and meningitis. In adulthood and older age, prolonged noise exposure, age-related degeneration (presbycusis), Meniere's disease, and otosclerosis are frequent causes of hearing impairment. Furthermore, lifelong risk factors such as head trauma, exposure to ototoxic medications, smoking, and chronic conditions like diabetes can also lead to hearing loss (WHO, 2025). Untreated hearing loss is associated with an increased risk of social isolation, cognitive decline, and dementia. Preventive strategies include the use of hearing protection in noisy environments, appropriate vaccination (e.g., against rubella), and the avoidance of ototoxic medications when alternatives are available (WHO, 2025; Healthline, 2025).

4.3 Genetic hearing disorders

Genetic hearing loss can be broadly categorized into syndromic and non-syndromic forms, depending on the presence or absence of additional clinical features. Approximately 70% of hereditary hearing loss cases are non-syndromic, whereas the remaining 30% are syndromic (Shearer *et al*, 1999).

4.3.1. Syndromic hearing loss

Syndromic hearing loss is characterized by additional clinical features affecting other organs or systems. These conditions are genetically heterogeneous and often involve mutations in genes expressed in multiple tissues. For instance, mutations in the *USH2A* gene are associated with Usher syndrome, which presents with both sensorineural hearing loss and progressive vision loss due to retinitis pigmentosa (Kimberling *et al*, 1990, 1995). Similarly, mutations in *PAX3* cause Waardenburg syndrome, which is characterized by pigmentary abnormalities and sensorineural

deafness (Read & Newton, 1997). Another example is Treacher Collins syndrome, which results from mutations affecting craniofacial development, leading to conductive hearing loss due to malformations in the external and middle ear (Trainor *et al*, 2009).

4.3.2. Non-Syndromic hearing loss

Non-syndromic hearing loss occurs without associated abnormalities in other organ systems. A significant portion of these cases is linked to mutations in the *GJB2* gene, which encodes connexin 26, a protein crucial for potassium ion recycling within the cochlea. Recessive mutations in *GJB2* disrupt this process, leading to sensorineural hearing loss (Kelsell *et al*, 1997). Non-syndromic hearing loss can vary in severity and is typically inherited in either an autosomal recessive or dominant manner. Some genes, like MYO7A can be inherited in recessive (DFNB2) and in dominant (DFNA11) manner (Chen *et al*, 2021; Kabahuma *et al*, 2021). Another rather common gene implicated in non-syndromic hearing loss is *STRC*, which encodes stereocilin, a protein essential for the structural integrity of the hair bundles in cochlear outer hair cells. Deletions in *STRC* are often associated with high-frequency hearing loss, but it can also affect all frequencies equally (Sloan-Heggen *et al*, 2016). Nevertheless, most other forms of genetic deafness apart from GJB2 and STRC are relatively rare.

4.3.3. Inheritance patterns in non-syndromic hearing loss

Non-syndromic hearing loss, which occurs without additional associated clinical features, can follow various genetic inheritance patterns, including autosomal recessive, autosomal dominant, X-linked, and mitochondrial inheritance. Approximately 75-80% of non-syndromic hearing loss cases are inherited in an

autosomal recessive manner (Smith *et al*, 2005). This pattern requires two copies of the mutated gene, one inherited from each parent, for the condition to manifest. Typically, both parents are asymptomatic carriers of the mutation. A well-known example of this is mutations in the *GJB2* gene. When both parents are carriers of *GJB2* mutations, there is a 25% chance that their child will be affected (Denoyelle *et al*, 1997).

Approximately 15-20% of non-syndromic hearing loss cases are inherited in an autosomal dominant manner (Shearer & Smith, 2012). In this inheritance pattern, a single copy of the mutated gene is sufficient to cause hearing impairment. Affected individuals often have a family history of hearing loss. An example and one of the first identified types of dominantly inherited hearing loss is DFNA2A (caused by mutations in the *KCNQ4* gene). These mutations lead to progressive sensorineural hearing loss, typically starting with high-frequency sounds and worsening over time to affect all frequencies (Kubisch *et al*, 1999; Smith & Hildebrand, 2015).

X-linked hearing loss primarily affects males, who possess only one X chromosome. Females typically act as carriers and can pass the mutation to their sons. DFNX1 for example is caused by mutations in the *PRPS1* gene, which encodes phosphoribosyl pyrophosphate synthetase 1 (essential for nucleotide biosynthesis). DFNX1 is characterized by progressive hearing loss, often starting in childhood (Corvino *et al*; Song *et al*, 2012).

Mitochondrial forms of hearing loss are rare and are inherited exclusively through the maternal line, as mitochondria are transmitted from mothers to their offspring. These cases are often associated with heightened sensitivity to aminoglycoside antibiotics,

which can trigger or exacerbate hearing impairment in genetically predisposed individuals (Fischel-Ghodsian, 2003).

4.4 Otoferlin

Otoferlin, a member of the ferlin protein family, is a large, tail-anchored protein characterized by multiple C2 domains and encoded by 48 exons of the *OTOF* gene (Yasunaga *et al*, 1999, 2000; Roux *et al*, 2006; Lek *et al*, 2012; Pangršič *et al*, 2012). Long otoferlin transcripts (~7 kb) in both human and mouse brain and inner ear tissues were identified (Yasunaga *et al*, 2000). Furthermore, shorter transcripts (~5 kb) were identified in various human tissues, including the heart, placenta, liver, pancreas, skeletal muscle, kidney, inner ear, and brain, although these were not detected in mouse tissues (Yasunaga *et al*, 1999, 2000). Mutations in the *OTOF* gene cause DFNB9, a recessive and non-syndromic form of prelingual deafness in humans which is characterized by impaired synaptic transmission from IHCs (Yasunaga *et al*, 1999, 2000; Roux *et al*, 2006; Vona *et al*, 2020).

Otoferlin consists of a transmembrane domain (TMD), the C2-FerA domain and several C2 domains (previously named C2A–F, more recently C2A-G), which are involved in calcium sensing and membrane interactions (Dominguez *et al*, 2022; Lek *et al*, 2012; Harsini *et al*, 2018)(Fig. 3). These C2 domains enable otoferlin to bind calcium ions, a critical step in its role in synaptic vesicle exocytosis. However, the C2A domain is unique in that it lacks the typical calcium-binding capacity due to a shortened loop, distinguishing it from homologous ferlins such as dysferlin (Helfmann *et al*, 2011).

The isolated FerA domain of ferlins has been shown to interact with phospholipids in a Ca^{2+}-depended manner (Harsini *et al*, 2018). Lastly, the C-terminal TMD anchors otoferlin to active zones of the synaptic membrane (Varga *et al*, 2003).

Figure 3 - A schematic representation of the otoferlin protein, illustrating its distinct structural domains. Depicted are the different C2 domains, labelled according to Dominguez (2022), the C2-FerA domain as well as the transmembrane domain. Created with biorender.com

Otoferlin functions as a calcium sensor at IHC ribbon synapses, where it facilitates synaptic vesicle (SV) fusion and neurotransmitter release, processes that are critical for transducing mechanical sound vibrations into electrical signals within the auditory nerve (Roux *et al*, 2006; Leclère & Dulon, 2023; Pangršič *et al*, 2012; Michalski *et al*, 2017). Beyond its role in exocytosis, otoferlin also regulates vesicle replenishment and endocytosis both of which are essential for sustaining high-frequency synaptic transmission and ensuring continuous auditory signalling (Pangrsic *et al*, 2010; Pangršič *et al*, 2012; Tertrais *et al*, 2019; Kroll *et al*, 2019; Strenzke *et al*, 2016). Specifically, otoferlin is indispensable for the late phases of readily releasable pool (RRP) exocytosis, including synaptic vesicle priming and membrane fusion. This is demonstrated by the near-complete absence of exocytotic activity in *Otof*$^{-/-}$ IHCs, despite the presence of normal calcium currents (Roux *et al*, 2006; Pangrsic *et al*, 2010; Reisinger *et al*, 2011) and unaltered SV counts (Roux *et al*, 2006; Vogl *et al*, 2016). In addition to mediating late-stage exocytosis, otoferlin is critical for the efficient replenishment of the RRP (Pangrsic *et al*, 2010; Jung *et al*, 2015; Strenzke *et al*, 2016; Michalski *et al*, 2017; Chakrabarti *et al*, 2018).

The C-terminal TMD of otoferlin is essential for proper membrane docking and vesicle recycling. Its absence seems to result in reduced otoferlin expression and impaired synaptic transmission (Leclère & Dulon, 2023; Manchanda *et al*, 2021).

A hallmark feature of *OTOF*-related hearing loss is the presence of normal otoacoustic emissions, indicating preserved outer hair cell function, alongside abnormal auditory brainstem responses. Biallelic variants in the *OTOF* gene are most commonly associated with congenital or early-onset hearing loss (reported in 114 cases). A small number of variants (3 cases) have been linked to progressive forms of hearing loss. Additionally, seven variants are associated with temperature-sensitive hearing loss, with one (p.Gly614Glu) located in the C2-FerA domain (Vona *et al*, 2020).

Premature stop codons and frameshift mutations usually lead to profound deafness before speech development (prelingual). In contrast, non-truncating variants, those that do not shorten the protein, can result in a wide range of clinical outcomes. The severity of these effects depends on the location of the mutation and the chemical nature of the altered or missing amino acids (Vona *et al*, 2020). Some variants significantly reduce otoferlin stability, promoting its degradation. However, in other cases, protein folding is only mildly affected, allowing a portion of the naturally produced otoferlin to reach the plasma membrane. The amount of functional otoferlin present in these instances can vary with the individual's age and body temperature (Vona *et al*, 2020). Temperature-sensitive auditory synaptopathy has been reported by parents who noticed that their children experienced profound hearing loss whenever they had a fever. In some cases, fluctuations in the child's ability to understand speech were observed throughout the day, reflecting natural changes in body temperature (Zhang *et al*, 2016; Vona *et al*, 2020). An example for temperature-sensitive auditory synaptopathy is the p.Ile515Thr variant (Varga *et al*, 2006).

To date, over 200 pathogenic and likely pathogenic variants in *OTOF* have been identified (Vona *et al*, 2020). Although most variants cause profound hearing impairment, a subset is linked to milder or progressive forms of deafness e.g. p.Ile1573Thr, p.Glu1700Gln and p.Ter1998Argext30Ter (Chiu *et al*, 2010; Yildirim-Baylan *et al*, 2014; Matsunaga *et al*, 2012). However, progressive hearing loss due to *OTOF* mutations has not yet been replicated in mouse models (Vona *et al*, 2020).

One notable mutation, referred to as the “Spanish” mutation (p.Gln829Ter), is a recurrent premature stop codon within the C2-FerA domain. This variant is responsible for non-syndromic prelingual hearing loss and is estimated to affect approximately 10 000 individuals globally. It is the third most prevalent cause of prelingual deafness in the Spanish population (Migliosi *et al*, 2002).

4.4 *Otof* mouse models

4.4.1 Otoferlin knockout mouse model

The absence of otoferlin in mice causes a defect in synaptic transmission (from the IHCs to the SGNs) leading to auditory neuropathy-like phenotypes (Roux *et al*, 2006; Pangrsic *et al*, 2010; Strenzke *et al*, 2016; Michalski *et al*, 2017). These phenotypes include preserved cochlear amplification, evidenced by intact otoacoustic emissions, alongside severely impaired neural encoding of sound, as indicated by the absence or elevated thresholds of auditory brainstem responses (Roux *et al*, 2006; Pangršič *et al*, 2012).

Otoferlin deficiency impairs exocytosis of synaptic vesicles at IHC ribbon synapses, thereby hindering efficient glutamate release onto SGNs (Roux *et al*, 2006). Although OHC function is maintained initially, as shown by preserved otoacoustic emissions,

synaptic transmission is fundamentally compromised, resulting in profound sensorineural deafness (Roux *et al*, 2006).

Developmental synaptic abnormalities are evident in otoferlin-deficient mice. Otoferlin is necessary for synaptic maturation already before onset of hearing (Stalmann *et al*, 2021). *Otof* $^{-/-}$ mice were found to have a higher number of synapses at young age (P6 and P8), however a faster decay of ribbon synapses compared to wild-type IHCs (Stalmann *et al*, 2021). Furthermore, the ribbon synapse numbers in *Otof* $^{-/-}$ IHCs decrease to 60% of the numbers in wild-type IHCs in the third and fourth postnatal week (Reisinger *et al*, 2011; Al-Moyed *et al*, 2019).

Over time, progressive degeneration affects both hair cells and SGNs. By six months of age, IHC counts decline to approximately 50% of wild-type levels across the cochlea (Stalmann *et al*, 2021). OHC loss progresses from base to apex, indicated by a decay in otoacoustic emissions observed by 24 weeks. This leads to the assumption that otoferlin could play a role in preserving OHCs and cochlear amplification (Stalmann *et al*, 2021).

While SGN degeneration is not observable in an age of eight weeks old *Otof* $^{-/-}$ mice, the afferent boutons from the SGNs are already reduced to approximately 50% of the wild type numbers (Stalmann *et al*, 2021). Nevertheless, at an age pf 48 weeks the numbers of SGNs are trend to decrease in *Otof* $^{-/-}$ mice (Stalmann *et al*, 2021).

4.4.2 Ile515Thr mutation mouse model

As already described before, the Ile515Thr missense mutation is an example for temperature-sensitive auditory synaptopathy. The mutation was identified in one *OTOF* allele in siblings which are suffering from severe to profound hearing loss when their body temperature raises to >38.1°C (Varga *et al*, 2006). Mice carrying the same mutation revealed substantial reduction (~65%) of otoferlin protein levels in IHCs,

presumably due to increased degradation of the mutated protein (Strenzke *et al*, 2016). The remaining otoferlin in *Otof* $^{I515T/I515T}$ IHCs localization was comparable to wild-type IHCs (Strenzke *et al*, 2016).

Electron microscopy revealed significantly enlarged otoferlin labelled vesicles, while synaptic vesicles were enlarged at 39°C in mutant IHCs compared to wild-type controls. Despite the accumulation of these vesicles, exocytosis during prolonged stimulation is impaired, indicating defective vesicle replenishment. Functionally, these defects result in synaptic fatigue and reduced auditory processing capacity, particularly under conditions of sustained stimulation (Strenzke *et al*, 2016).

Importantly, auditory deficits in *Otof* $^{I515T/I515T}$ mutant mice are exacerbated by elevated body temperature, a phenotype that closely mirrors temperature-sensitive auditory synaptopathy in human patients carrying the same mutation, although the heat induced phenotype seems to be weaker in mice compared to the human patients (Strenzke *et al*, 2016; Varga *et al*, 2006). This establishes a clear link between temperature sensitivity and synaptic dysfunction in *OTOF*-related hearing loss (Strenzke *et al*, 2016). Collectively, these findings underscore the critical role of otoferlin in maintaining synaptic vesicle dynamics and auditory reliability under physiological and stress conditions.

4.4.3 *Pachanga* (Pga) mouse model

The *Otof* $^{Pga/Pga}$ mouse line represents a recessive model of genetic deafness. *Otof* $^{Pga/Pga}$ mutants exhibit profound hearing loss, with absent ABRs at intensities exceeding 90 dB SPL confirming severe auditory dysfunction (Schwander *et al*, 2007; Pangrsic *et al*, 2010).

Different to otoferlin knockout mice, *Otof* $^{Pga/Pga}$ mice have a normal readily releasable pool (RRP) of vesicles upon depolarizations up to 10 ms (Pangrsic *et al*, 2010). The

RRP replenishment rates and the sustained IHC exocytosis levels upon longer IHC depolarizations are reduced in *Otof* $^{Pga/Pga}$ mice IHCs (Pangrsic *et al*, 2010). Furthermore, multiple-tethered and docked synaptic vesicles seem to accumulate at the active zone membrane in *Otof* $^{Pga/Pga}$ IHCs which indicates a defect in the active zone clearance (Chakrabarti *et al*, 2018). Similar to the Ile515Thr mice, otoferlin levels are reduced in *Otof* $^{Pga/Pga}$ mice IHCs. Interestingly, while in *Otof* $^{I515T/I515T}$ mice IHCs the remaining otoferlin localized comparable to wild-type, it was found more apically in *Otof* $^{Pga/Pga}$ mice IHCs (Strenzke *et al*, 2016). *Otof* $^{Pga/Pga}$ mice IHC hair bundles appeared normally structured with some IHCs occasionally observed to have slightly distorted hair bundles (Schwander *et al*, 2007).

4.5 Otoferlin's FerA domain

Structurally, the C2-FerA domain constitutes a novel C2-like fold that is interrupted between β-strands 4 and 5 by the insertion of a FerA-type four-helix bundle (Fig.4) (Dominguez *et al*, 2022).

This configuration preserves key structural features of both domains: the β-sandwich core typical of C2 domains and the characteristic helical bundle of FerA regions. Importantly, in type-2 ferlins such as otoferlin, the domain includes a negatively charged subdomain between β-strands 2 and 3, a feature absent in other ferlin family members, indicating a specialized adaptation for auditory function (Dominguez *et al*, 2022).

Despite its hybrid nature, the C2-FerA domain exhibits thermodynamic stability comparable to canonical C2 domains, with a reported free energy change of approximately 1.47 kcal/mol (Harsini *et al*, 2018). This stability supports its dynamic

interactions with cellular membranes, which are essential for the tightly regulated process of synaptic vesicle exocytosis.

C2-FerA adopts a fold characteristic of C2 domains, however, its functional activity appears to be primarily mediated by its distinctive β4–5 subdomain. Notably, the C2 region of C2-FerA lacks canonical lipid-binding residues in loops 1 and 3, as well as recognizable calcium-binding motifs (Dominguez *et al*, 2022). Consequently, the integration of the four-helix bundle into the C2-FerA structure is thought to facilitate membrane association specifically through this subdomain (Harsini *et al*, 2019). While the β4–5 subdomain alone has been associated with calcium-dependent membrane binding, the underlying mechanism remains undefined (Harsini *et al*, 2018). Structural modelling suggests that C2-FerA interacts with phospholipid membranes via hydrophobic interactions between the 'opened' FerA subdomain and a compatible membrane surface (Harsini *et al*, 2018).

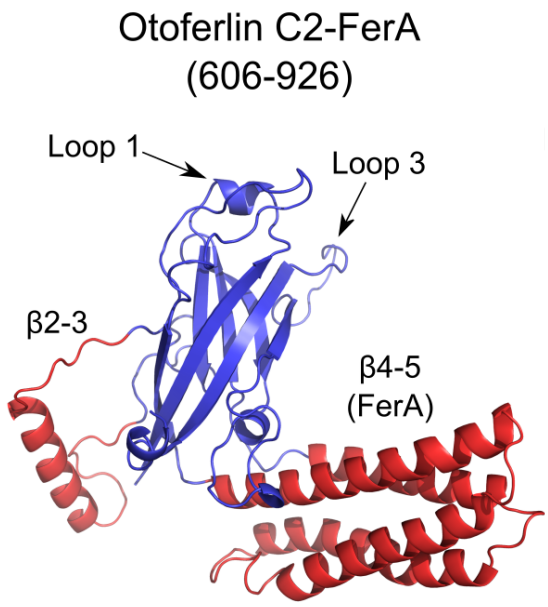

Figure 4 - C2-FerA otoferlin model. C2-FerA domain constitutes a novel C2-like fold that is interrupted between β-strands 4 and 5 by the insertion of a FerA-type four-helix bundle. Adapted and modified from (Dominguez *et al*, 2022)

4.6 Gene therapy

4.6.1 Adeno-associated viruses (AAVs) as vectors for gene therapy

AAVs are small, non-enveloped viral vectors that have become central to the development of gene therapy due to their safety profile and efficient gene delivery capabilities. They are members of the genus *Dependoparvovirus* within the family *Parvoviridae*. Their replication cycle requires the presence of a helper virus, such as adenovirus (AdV), which underlies both their nomenclature and taxonomic classification (Wang *et al*, 2019). AAVs have been identified in a variety of vertebrate species, including humans and non-human primates (NHPs). These, vectors are widely utilized for delivering therapeutic genes to a variety of cell types and tissues. AAVs have a ~25 nm icosahedral capsid composed of three viral proteins, VP1, VP2, and VP3 (Fields *et al*, 1996). Their single-stranded DNA genome spans approximately 4.7 to 4.8 kilobases and contains inverted terminal repeats (ITRs), which are essential for replication and packaging. The genome also encodes two primary genes: *rep*, involved in replication, and *cap*, which codes for the capsid proteins. These structural features enable AAVs to package and deliver transgenes efficiently to target cells (Fig. 5) (Bartel *et al*, 2012; Naso *et al*, 2017).

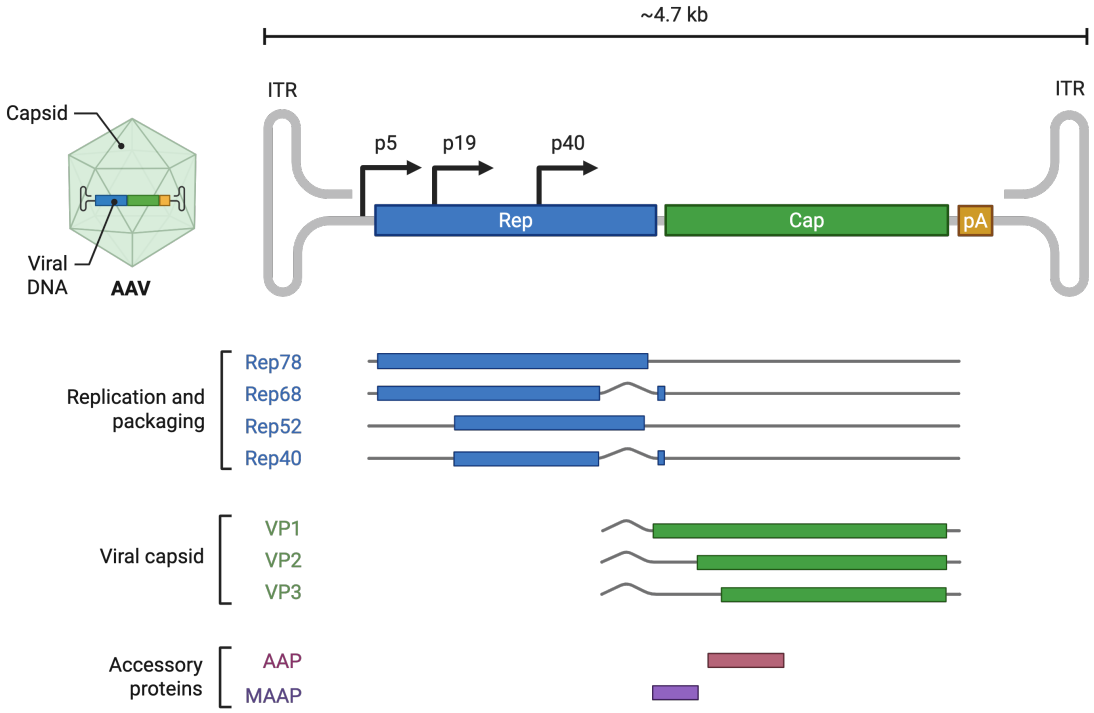

Figure 5 - Schematic representation of the AAV genome organization and encoded proteins. The AAV genome is approximately 4.7 kilobases in length and is flanked by ITRs, which are essential for viral genome replication and packaging. The genome contains two major open reading frames: *rep* and *cap*, transcribed from promoters p5, p19, and p40. The *rep* gene encodes four proteins (Rep78, Rep68, Rep52, and Rep40) involved in viral genome replication and packaging. The *cap* gene encodes three viral capsid proteins (VP1, VP2, and VP3) that form the AAV capsid. In addition to structural and replication proteins, the genome encodes accessory proteins, including the assembly-activating protein (AAP) and the membrane-associated accessory protein (MAAP), which support capsid assembly and function (Fields *et al*, 1996; Sonntag *et al*, 2010, 2011; Wang *et al*, 2019). A simplified illustration of the AAV capsid is shown on the left, highlighting the encapsidated viral DNA. Created with biorender.com.

Host-related factors that affect gene delivery start working as soon as recombinant adeno-associated virus (rAAV) vectors are introduced. For example, studies have shown that different AAV serotypes interact in different ways with serum proteins (Denard *et al*, 2018). However, the main factor determining how well rAAV transduction works is how the viral capsid interacts with specific receptors on the surface of target cells, followed by a series of steps inside the cell after the virus is taken in (Fig. 6)

(Huang *et al*, 2014; Agbandje-McKenna & Kleinschmidt, 2011; Nonnenmacher & Weber, 2012).

Different AAV serotypes recognize different cell surface receptors, often glycoproteins, which helps explain their ability to target specific tissues and cell types. In some cases, multiple receptors are involved in helping the virus bind to and enter the cell (Nonnenmacher & Weber, 2012).

One key receptor, called AAVR (AAV receptor), has been identified as important for the entry of several AAV serotypes (Pillay *et al*, 2016, 2017). Once the virus binds to its receptor, it is mostly taken up by the cell through endocytosis (Nonnenmacher & Weber, 2011; Duan *et al*, 1999). Inside endosomes, the virus undergoes pH-dependent changes in shape that are needed for successful transduction. The intact virus particles are then moved through the cytoplasm along the cell's cytoskeleton (Xiao & Samulski, 2012; Sonntag *et al*, 2006). After escaping the endosome, the virus enters the nucleus through the nuclear pore complex, where the capsid is uncoated to release the viral genome. Each step of this intracellular journey can be a potential barrier to efficient gene delivery. Therefore, understanding the cellular and molecular mechanisms that control these steps is essential for improving rAAV transduction (Xiao *et al*, 2002; Kelich *et al*, 2015).

Once inside the nucleus, the single-stranded rAAV genome needs to be converted into a double-stranded form before it can be transcribed, this is a key limiting step in the process (Fisher *et al*, 1996; Ferrari *et al*, 1996). This conversion usually begins at the ITR at the 3′ end of the genome (Zhong *et al*, 2008; Zhou *et al*, 2008). Another way a double-stranded genome can form is through strand annealing, where complementary strands from separate virus particles pair up inside the nucleus (Nakai *et al*, 2000).

To speed up this process, researchers have developed a genome design that includes a mutated ITR to produce a self-complementary genome. This version leads to faster

and stronger gene expression than the standard single-stranded genome but cuts the packaging capacity in half (McCarty *et al*, 2003; Wang *et al*, 2003). After forming a double-stranded genome, the DNA circularizes through recombination at the ITRs, creating stable episomal concatemers. These structures support long-term gene expression, especially in non-dividing cells (Fig. 6) (Duan *et al*, 1998, 1999).

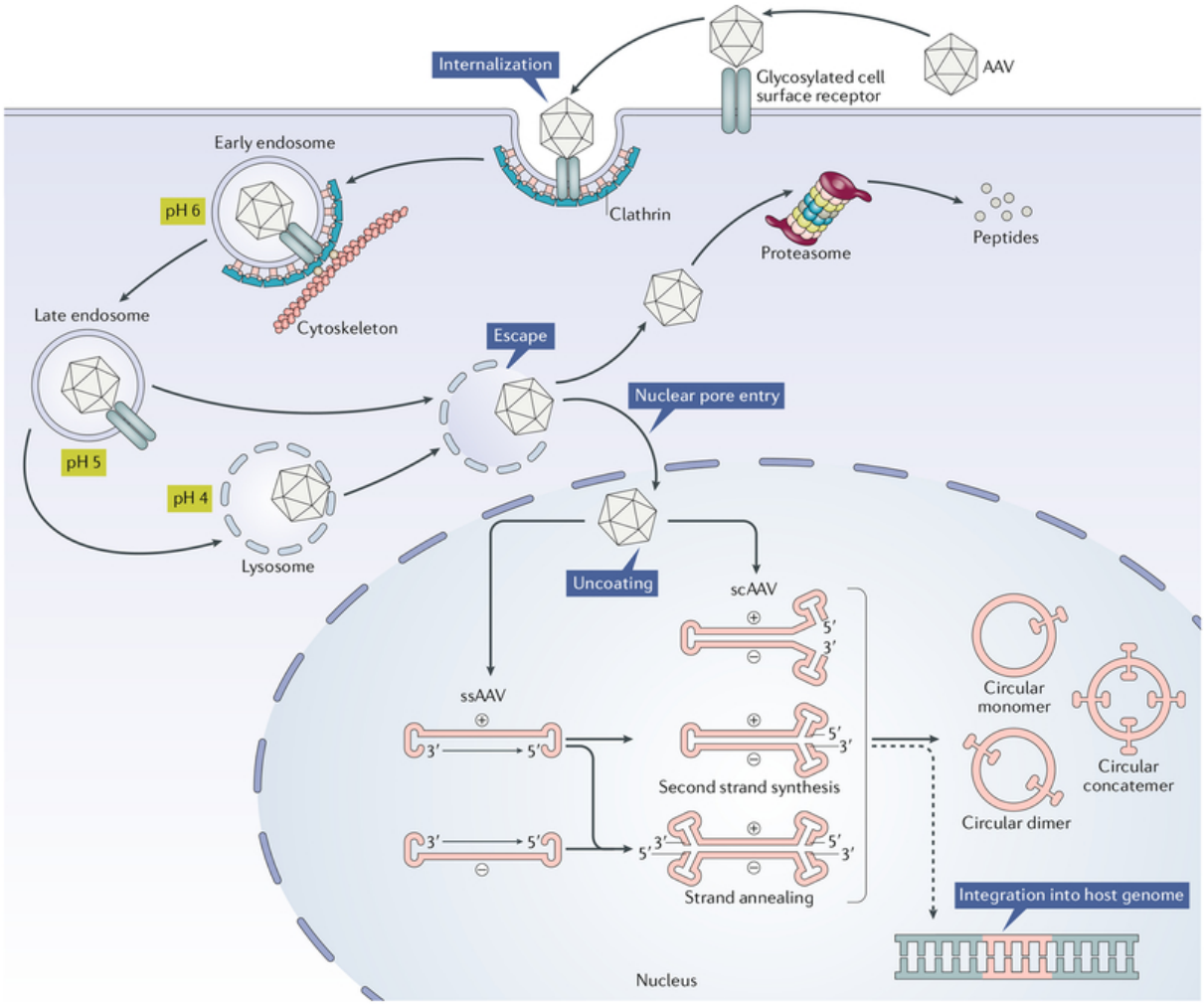

Figure 6 - Schematic overview of intracellular trafficking and uncoating of AAV particles. Following cellular entry, AAV particles are trafficked through the cytoplasm via the cytoskeletal network toward the perinuclear region. During this process, the virus undergoes endosomal escape, allowing the capsid to enter the cytosol. Subsequently, the capsid is transported to the nucleus, where uncoating occurs to release the viral genome. Adapted from Wang *et al*, 2019.

One of the key advantages of AAVs is their non-pathogenic nature and their predominantly episomal persistence in host cells, which minimizes the risk of insertional mutagenesis, a significant concern with integrating viral vectors (Wang *et al*, 2024b; Bulcha *et al*, 2021). Since AAVs lack autonomous replication capabilities, they require co-infection with a helper virus (e.g., adenovirus or herpesvirus) for productive replication. For gene therapy purposes, AAV vectors are engineered to replace all viral genes with therapeutic transgenes, ensuring that no viral proteins are expressed in transduced cells (Wang *et al*, 2019; Dong *et al*, 1996).

AAVs are capable of transducing both dividing and non-dividing cells, supporting long-term transgene expression, a crucial feature for treating chronic and genetic diseases (Wang *et al*, 2024b). As of 2022, more than 350 clinical trials have employed AAV vectors in various therapeutic contexts. Notable successes include the FDA-approved *Luxturna*® for inherited retinal dystrophy and *Zolgensma*® for spinal muscular atrophy. Additionally, AAV-based gene therapies are being developed for hemophilia, metabolic disorders, and other monogenic conditions (Wang *et al*, 2024b).

AAV vectors offer several practical and therapeutic advantages. Through the use of different serotypes or engineered capsids, AAVs can be tailored for specific tissue tropism (Denard *et al*, 2018). Moreover, incorporating cell-type-specific promoters further enhances targeting precision (Gessler *et al*, 2017; Gray *et al*, 2011). AAV capsids also exhibit considerable physicochemical stability, showing resistance to detergents and temperature fluctuations, which is beneficial for storage, handling, and global distribution (Howard & Harvey, 2017). Despite these advantages, AAV-based therapies face several limitations. Pre-existing neutralizing antibodies against natural AAV serotypes in the human population can hinder vector delivery and reduce therapeutic efficacy. Furthermore, large-scale vector production remains technically

challenging due to limitations in yield, scalability, and purification, all of which are critical for clinical-grade manufacturing (Wang *et al*, 2019).

Until April 2025, seven AAV-based gene therapies had received FDA approval, including treatments for visual impairment and systemic genetic disorders. Continued innovation is expanding the utility of AAVs in gene therapy. The development of next-generation capsids, directed evolution strategies, and the integration of genome editing tools such as CRISPR-Cas systems are poised to overcome current limitations and enhance therapeutic outcomes (Wang *et al*, 2024b).

4.6.2 AAV tropism

AAV tropism is primarily determined by the capsid serotype, which defines its natural preference for specific cell and tissue types. This specificity makes AAVs a valuable tool for gene therapy, as it allows for targeted gene delivery to precise locations within the body.

AAV2 for example is particularly effective at transducing skeletal muscles (Manno *et al*, 2003), neurons (Bartlett *et al*, 1998), vascular smooth muscle cells (Richter *et al*, 2000), and hepatocytes (Koeberl *et al*, 1997) while AAV1 is known for its ability to efficiently transduce vascular endothelial cells and the retina, making it ideal for ocular gene therapy (Kaludov *et al*, 2001; Chen *et al*, 2021).

Furthermore, AAV9 is capable of crossing the blood-brain barrier, allowing it to target cells in the central nervous system (CNS), liver, and smooth muscle (Issa *et al*, 2023) and AAV8 has strong tropism for the CNS, including the brain, as well as for the liver and smooth muscle (Issa *et al*, 2023; Wu *et al*, 2006).

The tropism of these serotypes arises from interactions between the AAV capsid and specific cell-surface receptors. The variation in capsid proteins across different AAV serotypes enables serotype-specific binding to these receptors (Huang *et al*, 2014; Agbandje-McKenna & Kleinschmidt, 2011). In addition, synthetic variants such as AAV-PHP.eB and AAV-DJ have been engineered to enhance the targeting efficiency of AAV vectors for particular tissues (Hu *et al*, 2019).

4.6.3 AAV tropism in the inner ear

Gene therapy for the inner ear relies on accurately targeting different cochlear cell types, including hair cells, supporting cells (SCs), and the stria vascularis.

AAV-DJ for example is effective at transducing non-sensory cells, such as Reissner's membrane and interdental cells, as well as SCs. However, its ability to transduce hair cells is limited compared to other serotypes (Kim *et al*, 2019; Hu *et al*, 2019).

AAV9 transduces IHCs in the cochlear basal and second turns, as well as vestibular hair cells, which is crucial for both cochlear and vestibular applications in gene therapy (Wang *et al*, 2022). Furthermore, the AAV9 derived AAV-PHP.B and AAV-PHP.eB: have shown exceptional efficiency in transducing both IHCs and OHCs, with AAV-PHP.eB achieving near-complete OHC transduction at low doses, making it a promising option for inner ear gene therapy (Shu *et al*, 2016; Hu *et al*, 2019).

Another serotype called Anc80L65 has demonstrated the ability to deliver genes to 80-95% of IHCs and 67-91% of OHCs when administered via the trans-round window or trans-stapes routes. Importantly, this approach results in minimal hearing loss, making it a highly effective candidate for clinical applications (Wang *et al*, 2022).

4.7 Inner ear gene therapy

Cochlear implants remain an effective clinical intervention for many patients with *OTOF* mutations, enabling auditory perception by directly stimulating the auditory nerve. In parallel, gene therapy trials are currently underway to restore synaptic function by targeting the *OTOF* gene, highlighting the potential of precision molecular therapies for genetic hearing loss.

4.7.1 Mouse studies

Because the *OTOF* cDNA (~6 kb) exceeds the packaging capacity of conventional AAV vectors (~4.7 kb), a dual-AAV strategy has been developed. In this approach, the full-length *Otof* cDNA is split into two fragments, each delivered via separate AAV vectors. Upon co-injection into the cochlea, the fragments recombine in IHCs to express full-length otoferlin (Akil *et al*, 2019; Al-Moyed *et al*, 2019). This strategy has achieved otoferlin expression in 50–85% of IHCs and led to the restoration of fast synaptic exocytosis to wild-type levels, along with partial recovery of synaptic vesicle replenishment (Al-Moyed *et al*, 2019).

Early postnatal administration at day 10 prevented deafness and restored hearing thresholds to within 10 dB of wild-type levels for over six months. Later treatments (e.g., at P17 or P30) also resulted in hearing restoration (Akil *et al*, 2019). ABR thresholds improved significantly, with restored responses to both clicks and tone bursts, whereas knockout mice exhibited no detectable responses (Akil *et al*, 2019; Al-Moyed *et al*, 2019). Ribbon synapse counts remained reduced by approximately 40% of wild-type IHCs (Stalmann *et al*, 2021; Al-Moyed *et al*, 2019). Importantly, the dual-

AAV approach was effective even in mature cochleae, suggesting a broad therapeutic window (Akil *et al*, 2019).

4.7.2 Recombination strategies in dual-AAV approaches

To overcome AAV's limited packaging capacity, several recombination strategies have been developed to enable delivery of large genes such as *OTOF*. These include trans-splicing**,** overlapping homologous recombination**,** hybrid systems**,** and oversize AAVs**.**

Trans-splicing divides the target gene between two AAV vectors, each containing a splice donor (SD) or splice acceptor (SA) signal. Following co-transduction, vector genomes concatemerize via ITRs, enabling the splicing machinery to generate a full-length mRNA transcript right after mRNA transcription (Fig. 7) (Trapani *et al*, 2014). In the retina, expression after delivery reached in vivo around ~40% of endogenous protein levels (Reich *et al*, 2003). Trans-splicing has been applied to deliver large genes such as *Abca4*, *Myo7a*, and *Otof* in either retinal or cochlear gene therapy contexts in animal models (Trapani *et al*, 2014; Al-Moyed *et al*, 2019; Akil *et al*, 2019).

The overlapping homologous recombination strategy uses dual AAV vectors with overlapping homologous sequences to promote endogenous recombination. Unlike trans-splicing, it does not require splicing elements but relies on the host's homologous recombination machinery (Fig. 7) (Trapani *et al*, 2014). Its efficiency is limited in post-mitotic cells, such as neurons, due to low intrinsic recombination activity (Trapani *et al*, 2014; Datta *et al*, 2024). Reduced expression efficacy has been observed in studies targeting *Myo7a* delivery (Trapani *et al*, 2014).

Hybrid strategies combine trans-splicing with a highly recombinogenic bridging sequence, such as fragments of alkaline phosphatase (AP) or a F1 phage recombinogenic region (AK), to enhance genome recombination (Fig. 7) (Trapani *et al*, 2014). These vectors show in some cases worse and in some cases improved performance over conventional trans-splicing and are suitable for delivering large genes like *Abca4*. Bridging sequences of 0.26–0.44 kb preserve recombination efficiency while maximizing vector genome capacity (Trapani *et al*, 2014; Ghosh *et al*, 2011). This method has also been applied to *Otof* gene delivery in the inner ear, yielding outcomes comparable to trans-splicing (Al-Moyed *et al*, 2019).

The oversize AAV approach bypasses recombination by forcibly packaging genomes exceeding the canonical ~4.7 kb limit, up to ~6 kb (Fig. 7) (Grieger & Samulski, 2005; Wu *et al*, 2007; Allocca *et al*, 2008). These vectors are heterogeneous, often containing incomplete sequences. Transgene expression depends on intracellular reassembly through overlapping regions. While less technically complex than dual-AAV strategies, this approach offers lower reconstitution efficiency (Trapani, 2019; Trapani *et al*, 2014). Oversize AAV vectors have shown therapeutic benefit in preclinical models of Stargardt disease through delivery of *Abca4* (Allocca *et al*, 2008). Expression efficiency improves with longer overlaps and when genome size moderately exceeds (~5–5.2 kb) rather than far exceeds the packaging limit (Dong *et al*, 2010; Lai *et al*, 2010; Wang *et al*, 2012). In the context of *Otof* delivery, overloaded AAVs were used to introduce the full-length coding sequence into cochleae of knockout mice, resulting in partial hearing restoration (Rankovic *et al*, 2021).

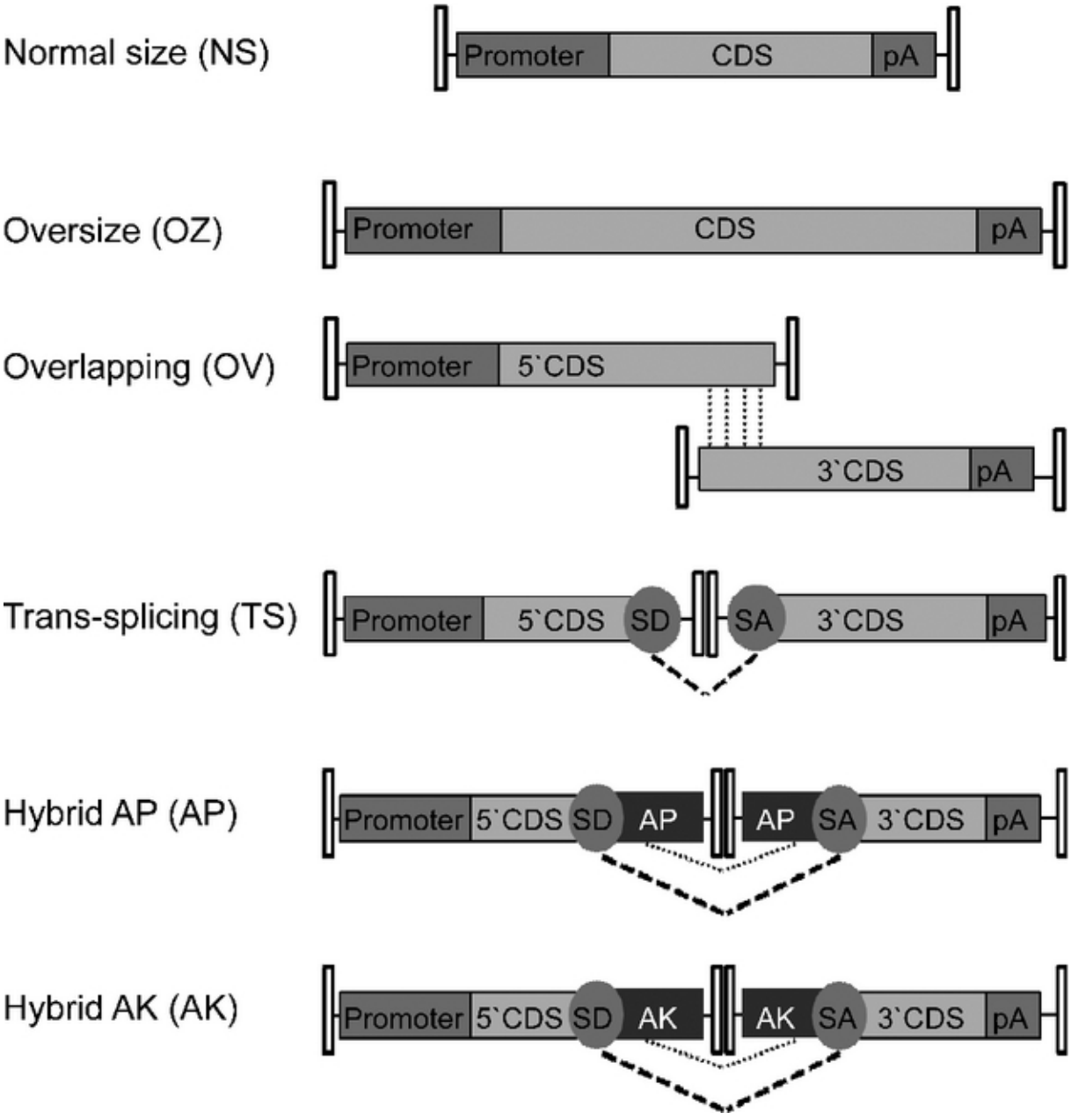
Normal size (NS)
Promoter
CDS
pA
Oversize (OZ)
Promoter
CDS
pA
Overlapping (OV)
Promoter
5`CDS
3`CDS
pA
Trans-splicing (TS)
Promoter
5`CDS
SD
SA
3`CDS
pA
Hybrid AP (AP)
Promoter
5`CDS
SD
AP
AP
SA
3`CDS
pA
Hybrid AK (AK)
Promoter
5`CDS
SD
AK
AK
SA
3`CDS
pA

Figure 7 - Schematic overview of gene therapy vector strategies for delivering large coding sequences exceeding the packaging capacity of AAVs. Normal size: A conventional single-vector design containing a promoter, coding sequence (CDS), and polyadenylation signal (pA) within the AAV packaging limit. **Oversize:** A single-vector approach with an oversized CDS that surpasses the AAV packaging capacity, potentially compromising efficiency. **Overlapping:** A dual-vector strategy in which the CDS is split into 5′ and 3′ fragments (5′CDS and 3′CDS), each delivered separately with overlapping regions to facilitate homologous recombination. **Trans-splicing (TS):** A dual-vector system incorporating splicing elements: the first vector includes the 5′CDS and a splice donor (SD), while the second includes a splice acceptor (SA), the 3′CDS, and a pA signal. **Hybrid AP:** A modified trans-splicing strategy that includes AAV-specific pairing sequences flanking the SD and SA sites to enhance vector co-localization and transcript reconstitution. **Hybrid AK:** A similar dual-vector approach using alternative pairing elements (AK) instead of AP to support efficient recombination. In all constructs, ITRs are indicated at both ends to denote AAV genome boundaries. Adapted from (Trapani *et al*, 2014).

4.7.3 Inteins

Inteins are genetic elements found in unicellular organisms that are transcribed and translated as internal polypeptide segments within host proteins (Mills *et al*, 2014; Novikova *et al*, 2014). Following translation, they catalyse their own excision from the precursor protein through a posttranslational process, leaving no amino acid modifications in the mature protein product. This protein splicing mechanism is energy-independent and does not require exogenous, host-specific proteases or cofactors (Mills *et al*, 2014; Novikova *et al*, 2014).

Intein activity is highly context-dependent, relying on specific peptide sequences flanking the ligation junction, referred to as the N- and C-exteins, for efficient trans-splicing. A critical requirement is the presence of a thiol- or hydroxyl-containing amino acid (Cys, Ser, or Thr) as the first residue of the C-extein (Shah *et al*, 2013). Split inteins, a subclass of inteins, are expressed as two separate polypeptides attached to distinct host proteins. These fragments mediate trans-splicing, thereby producing a single, contiguous polypeptide (Li, 2015).

The intein-based dual-AAV strategy utilizes split intein-mediated protein trans-splicing to bypass the DNA packaging constraints of AAV vectors. In this system, the coding sequence of a large target gene is divided between two AAV vectors. Each vector carries one half of the protein fused to a short split intein sequence, commonly derived from naturally occurring inteins such as Npu DnaE or Ssp DnaE (Tornabene *et al*, 2019).

Upon co-expression within the target cell, the split inteins facilitate the post-translational ligation of the two protein fragments, excising themselves in the process and yielding a functional, full-length protein (Tornabene *et al*, 2019).
A key advantage of the intein-based approach is its independence from DNA or RNA recombination processes, which are typically inefficient in post-mitotic cells, such as photoreceptors. This method achieved higher levels of functional protein expression compared to conventional dual-AAV strategies (Tornabene *et al*, 2019). The intein-based dual-AAV strategy was successfully used already in retinal (e.g. Stargardt disease) (Tornabene *et al*, 2019; Ferla *et al*, 2025) and inner ear studies (*Otof* knockout mice) (Tang *et al*, 2023).

4.8 *OTOF* gene therapy clinical studies

Recent clinical trials have demonstrated promising outcomes for gene therapy targeting *OTOF*-related congenital hearing loss (DFNB9), marking a significant shift toward curative approaches in auditory medicine. Multiple strategies employing AAV vectors have entered Phase 1/2 clinical evaluation, each employing tailored delivery systems and therapeutic constructs to restore otoferlin expression and auditory function (Reisinger & Trapani, 2024; see also clinitrial.gov).

In the Regeneron's CHORD trial the first treated child (10 months old) achieved near-normal auditory thresholds across 0.25–2.0 kHz by 48 weeks post-injection. Speech perception, including recognition of common words (e.g., "mommy," "cookies"), persisted through 72 weeks. ABR testing confirmed objective recovery of auditory function (Regeneron, 2025)

In the Chinese bilateral AAV1-hOTOF trial, five children (one to 18 years) with biallelic *OTOF* mutations were treated with 1.5×10^{12} vector genomes (vg) per ear via round window injection. All participants regained bilateral hearing, with average ABR thresholds improving from >95 dB to 50-85 dB. In addition, the participants demonstrated partially restored speech perception and sound localization abilities (Wang *et al*, 2024a).

In the Sensorion's AUDIOGENE Trial the initial cohort (three patients) tolerated surgery without serious adverse events therefore, the data monitoring committee approved escalation to a higher-dose cohort. Here, the strategic goal is to capitalize on early developmental neuroplasticity to promote optimal speech and auditory processing outcomes (Gullapalli, 2024).

In the Akouos/Eli Lilly's AK-OTOF-101 Trial dual AAVAnc80 vector system was engineered and delivered to children of an age between two and 17. The objective of this study is to assess safety, tolerability and efficacy of AK-OTOF in restoring hearing in individuals. The first participant (an eleven-year-old boy with congenital deafness) achieved thresholds of 20-65 dB HL across the tested frequencies (normal range at some frequencies) within 30 days post-treatment. Furthermore, there were no serious adverse events or dose-limiting toxicities reported. Some mild adverse events (e.g. transient lymphocyte elevation) were resolved without intervention (Vishnu, 2024).

4.9 RAB proteins

RAB proteins are a family of small GTPases within the Ras (reticular activation system) superfamily, playing essential roles in regulating membrane trafficking, a critical process for maintaining cellular organization and function (Schwartz *et al*, 2007). These proteins govern various stages of vesicular transport, including vesicle formation, cargo selection, membrane fusion, and recycling (Stenmark, 2009). Over 60 RAB isoforms are present in humans, each exhibiting organelle- and pathway-specific distribution (Schwartz *et al*, 2007; Pereira-Leal & Seabra, 2001; Zerial & McBride, 2001).

RAB proteins are peripheral membrane proteins, anchored to membranes via prenyl groups, typically geranylgeranyl moieties, covalently attached to cysteine residues at their C-terminus (Stenmark, 2009). This lipid modification enables RAB proteins to interact with membranes while maintaining solubility in the cytosol (Ullrich *et al*, 1993). Rab escort proteins (REPs) facilitate the delivery of RAB proteins to their target membranes by shielding their hydrophobic lipid anchors in the cytosol (Seabra, 1996; Shen & Seabra, 1996). Upon activation, RAB proteins cycle between two conformational states: GDP (guanosine disphosphate)-bound (inactive) and GTP (guanosine triphosphate)-bound (Pfeffer, 2005). The interconversion between these states is regulated by guanine nucleotide exchange factors (GEFs), which promote GDP-to-GTP exchange, and GTPase-activating proteins (GAPs), which stimulate GTP hydrolysis to return the proteins to their inactive state (Delprato *et al*, 2004).

4.10 RAB proteins in the inner ear

RAB proteins play integral roles in the cellular processes of the inner ear, contributing to cilia formation, protein trafficking, and auditory function. These functions are critical for maintaining hearing and balance, with RAB proteins ensuring the proper development and operation of sensory cells in the inner ear.

RAB11A for example plays a crucial role in the formation and maintenance of cilia in the vestibular organ of the inner ear (Chen *et al*, 2021). Localized to the basal body, Rab11a regulates cilia development by coordinating intraflagellar transport and planar cell polarity signalling pathways. This coordination ensures the correct structural organization of hair cell cilia, which are essential for mechanoelectrical transduction (Chen *et al*, 2021).

Furthermore, RAB8B is interacting with otoferlin, suggesting that RAB8B-mediated trafficking of synaptic vesicles is crucial for sound signal transmission (Heidrych *et al*, 2008). Nevertheless, apart from few examples, the specific role of RAB proteins in the inner ear has not yet been investigated.

4.11 RAB4B

RAB4B is primarily localized to early and recycling endosomes, where it functions in regulating the fast-recycling pathway of cargo back to the plasma membrane (in HeLa cells expressing murine Rab4b) (Perrin *et al*, 2013). In cooperation with RAB5, RAB4B helps maintain the balance between cargo influx and efflux within early endosomes,

ensuring the efficient recycling of proteins and lipids to the cell surface (Krawczyk *et al*, 2007; Perrin *et al*, 2013).

Additionally, RAB4B interacts with RUFY1 (also known as RABIP4), a dual effector that coordinates endosomal tethering and fusion, further supporting RAB4B's involvement in membrane trafficking (Perrin *et al*, 2013). Furthermore, RAB4B is thought to regulate vesicle budding and fusion, particularly during the sorting of RAB4 and RAB11 in recycling endosomes (also called RAB4 to RAB11 transition). Rab4 is primarily involved in fast recycling pathways, facilitating the rapid return of specific cargos directly from early endosomes to the plasma membrane (Li *et al*, 2008; Wandinger-Ness & Zerial, 2014; Wilson *et al*, 2023). In contrast, Rab11 mediates slow recycling, functioning predominantly through perinuclear recycling endosomes to support a more prolonged and regulated route back to the cell surface (Li *et al*, 2008; Wandinger-Ness & Zerial, 2014; Wilson *et al*, 2023). Upon internalization, cargos such as receptors may first enter Rab4-positive early endosomes, where they are either quickly recycled or sorted for a slower recycling pathway. In the latter case, these cargos transition to Rab11-positive compartments (Wilson *et al*, 2023; Li *et al*, 2008). During this transition, vesicular or tubular intermediates may transiently exhibit both Rab4 and Rab11, forming Rab4+/Rab11+ structures (Ward *et al*, 2005; Li *et al*, 2008). These hybrid compartments subsequently undergo segregation, with Rab4 and Rab11 forming distinct domains that eventually separate (Ward *et al*, 2005). This process results in the generation of Rab11-enriched vesicles, which are then directed toward the plasma membrane. This transition is vital for maintaining the morphology of recycling compartments and ensuring the efficient trafficking of membrane-bound cargo (Ward *et al*, 2005).

In adipocytes, RAB4B is essential for the trafficking of GLUT4, where, under basal conditions, RAB4B ensures the intracellular retention of GLUT4. However, upon insulin stimulation, RAB4B facilitates the translocation of GLUT4 to the cell membrane, which is critical for glucose uptake. Dysregulation, of RAB4B (e.g. downregulation as observed in obese diabetic humans and mice) can impair GLUT4 trafficking, contributing to insulin resistance and metabolic disorders (Kaddai *et al*, 2009).

Despite being encoded by distinct genes, *RAB4A* and *RAB4B* have very high sequence identity (~85% identical amino acid sequence). Nevertheless, comprehensive profiling of Rab-mediated trafficking networks strongly indicates that Rab4b and Rab4a may serve distinct biological functions (Gurkan *et al*, 2005). This is likely due to differences in their respective levels of enrichment, as well as those of their various interaction partners, across different cell types (Perrin *et al*, 2013).

In a cohort of five patients from Tübingen and Heidelberg with progressive hearing loss, a dominantly inherited point mutation in the *RAB4B* gene was identified. These patients experienced increasing difficulties with speech comprehension despite only moderately elevated hearing thresholds. Although *RAB4B* has not yet been associated with hearing disorders, its potential role in the inner ear remains to be explored.

4.12 Aim of projects

4.12.1 Characterization of the Otof-p. KL>M mouse line

The protein otoferlin is essential for synaptic transmission from cochlear IHCs to SGNs, the primary neurons in the auditory pathway. Mutations in the *OTOF* gene, which encodes otoferlin, result in autosomal recessive prelingual hearing loss classified as DFNB9. This form of hearing impairment is typically severe to profound. Otoferlin is characterized by multiple C2 domains and a unique phospholipid-binding C2-FerA domain. Although the C2-FerA domain has been shown to bind Ca^{2+} and phospholipids, its specific functional role in hearing remains unclear.

The aim of the Otof-p. KL>M mouse line characterization project was to investigate the physiological relevance of the C2-FerA domain of otoferlin. To this end, a variety of techniques were employed, including auditory ABR measurements, DPOAE recordings, immunostaining of otoferlin and synaptic markers in IHCs, and proximity ligation assays. As no published mouse models with targeted mutations in the FerA domain currently exist, the characterization of this mouse line provides the first insights into the functional significance of this domain in auditory processing.

4.12.2 AAV in vitro transduction on organs of Corti

Several gene therapy approaches in otoferlin-deficient mouse models, as well as early clinical trials involving patients with *OTOF* mutations, have demonstrated that dual-AAV gene therapy can effectively deliver a functional *OTOF* coding sequence to the inner ear. However, there remains considerable potential for further optimization.

The primary aim of this project was to establish and optimize small-scale AAV production. To this end, various steps in the AAV production process, such as transfection and harvesting, were systematically optimized by evaluating and comparing different methodological approaches.

Subsequently, an in vitro AAV transduction assay for organs of Corti was developed to serve as a serotype pre-screening platform prior to conducting in vivo experiments. This method was used to evaluate the efficiency of different AAV serotypes in transducing IHCs and OHCs, both in the context of single-AAV and dual-AAV delivery systems.

4.12.3 Rab4b in mouse inner ear

In five patients from Tübingen and Heidelberg presenting with progressive hearing loss, a dominantly inherited point mutation in the *RAB4B* gene, encoding the Ras-related protein RAB4B, was identified. These individuals exhibited increasing difficulties with speech comprehension despite only moderately elevated hearing thresholds. Notably, *RAB4B* has not previously been implicated in hearing disorders.

The aim of this project was to investigate the potential role of RAB4B in the inner ear. To this end, immunohistochemistry and RNA Scope in situ hybridization were employed to assess whether Rab4b is generally expressed in inner ear structures. Additionally, a genetically modified mouse line carrying the T64M mutation, identified in the five patients, was generated to serve as a model for further functional characterization of Rab4b in auditory physiology.

5. Material and Methods

5.1 C2-FerA domain protein structure prediction

Wild type and KLM C2-Fer domain (Otoferlin *Homo sapiens* amino acids 606 (K) - 925 (F))protein structure were predicted using the RoseTTAFold2 (Baek *et al*, 2021) via Neurosnap Inc. - Computational Biology Platform for Research. Wilmington, DE, 2022. https://neurosnap.ai/ (predictions performed on 04.12.2024).

5.2 Study approval and animals

Animal handling and experiments were approved by the Veterinary Services of the University of Tübingen and the Animal Care, the Ethics Committee of the Regional Government of Baden-Württemberg, Germany, and by LAVES Hannover, Germany and were performed in accordance with national and institutional guidelines. Mice were housed in the pathogen-free animal facility of the Department of Otorhinolaryngology, University Hospital of Tübingen.

The mouse line C57BL/6N-*Otof*^{em2}Erei/Erei (KL>M) with a c.delAGC/p.K824L825>M mutation was generated by CRISPR/Cas9 endonuclease treatment and a random deletion during non-homologous end-joining. Generation of mice was performed essentially as described (Segelcke *et al*, 2021; Yang *et al*, 2014). Two guide RNAs (gRNAs) were used simultaneously: 5’ ACACTGTTCGGGACAAGCTGAGG-3’ and 5’-GTAGCTTCTGCAGAAAGTTC-3'. Both gRNAs and the recombinantly expressed CRISPR/Cas9 enzyme were microinjected into mouse zygotes of C57BL/6N background and these were transferred into dams. Sequencing of the offspring revealed one mouse homozygous for the c.delAGC/p.K824L825>M mutation, which was selected for further breeding and analysis.

5.3 Genotyping

5.3.1 Lysis and genotyping polymerase chain reaction (PCR)

Ear punches, tails, or toe samples (only Rab4b samples from Switzerland) were lysed, and genomic DNA was isolated and purified using the nexttec™ 1-step DNA Isolation Kit for Tissue and Cells according to the manufacturer's instructions (10N. 904, nexttec Biotechnologie GmbH, Leverkusen, Germany).

A PCR mixture was prepared according to Table 1, and the PCR cycler program was executed as outlined in Table 2. The PCR products (5 µL product + 1 µL 6X DNA gel loading dye (R0611, Thermo Scientific, Waltham, United States)) were analysed following agarose gel electrophoresis. Subsequently, GELRED® nucleic acid gel stain (1:10,000, 41003, Biotium, Fremont, United States) was added, and the results were documented using the E-Box VX 5 with UV-light illumination (Vilber Lourmat, Eberhardzell, Germany).

Table 1 - Genotyping PCR mix composition.

Ingredient	Volume [µL]
H_2O	6.2
11.1x Buffer (see also Sup. Tab. 35)	0.9
DMSO	0.5
Primer 1 (20 µM)	0.1
Primer 2 (20 µM)	0.1
DreamTaq DNA Polymerase	0.2

Table 2 - Genotyping PCR cycler conditions.

Step	Temperature [°C]	Time [min:sec]
Initial Denaturation	94	03:00
35 Cycles		00:30
Denaturation	94	00:10
Annealing	60 (depending on primers Tm)	00:30 sec
	72	
Extension		01:00
Final Extension	72	07:00
Hold	4	-

The following primers were used for amplification:

Otoferlin project:

For wild type:

Primer 1 (G9): 5'-GGTGGCTAAGTCCTGGCTCTTC-3'

Primer 2 (G18): 5'-TCTGGCATGACCTCAGCTTGTC-3'

For the Otof-p. KL>M mutants:

Primer 1 (G9): 5'-GGTGGCTAAGTCCTGGCTCTTC-3'

Primer 3 (G19): 5'-AAGTTCTGGCATGACCTCATGTC-3'

Both mutant and wild-type amplification give a product of approximately 380 bp. An annealing temperature of 61°C for ear punches and 62°C for tails was used.

Rab4b project

For wild type:

Primer 1 (G22): 5'-GAAACCGCTCCTGGCCAGCagtG-3'

Primer 2 (G23): 5'-CAGGTGGGGTAGGTAGCAGGTACCATTGAC-3'

For the T64M mutants:

Primer 1 (G23): 5'-CAGGTGGGGTAGGTAGCAGGTACCATTGAC-3'

Primer 2 (G25): 5'-GAAACCGCTCCTGGCCAGCcatG-3'

Both mutant and wild-type amplification give a product of approximately 300 bp. An annealing temperature of 68°C was used.

5.3.2 DNA sequencing of potential Rab4b mutants

After sample lysis using the nexttec™ 1-step DNA Isolation Kit for Tissue and Cells, a second PCR was conducted to analyse the DNA sequence of potential mutant mice. Primers were designed to anneal approximately 300 bp upstream and 300 bp downstream of the T64M mutation site. The expected amplified DNA fragment is approximately 600 bp in the case of a successful T64M mutation. In knockout mice, the fragment may be shorter. The following primers were used for DNA amplification:

Primer 1 (G21): 5'-CTTCTCCTTCACCCTCTCTCTG-3'

Primer 2 (G23): 5'- CAGGTGGGGTAGGTAGCAGGTACCATTGAC-3'

The PCR mixture was prepared as previously described in Table 1. The same PCR cycler program outlined in Table 2 was used, with an annealing temperature of 60°C. PCR products (5 µL product + 1 µL 6X DNA gel loading dye) were analysed following

agarose gel electrophoresis. Subsequently, GELGREEN® nucleic acid gel stain (1:10 000) (41005, Biotium, Fremont, United States) was added, and the results were documented using the Blue Light LED Illuminator BL star9 (Analytik Jena, Jena, Germany). Successfully amplified DNA bands were excised from the agarose gel, purified using the innuPREP DOUBLEpure Kit (10755-786, Analytik Jena, Jena, Germany), and sent for sequencing to Eurofins Genomics (Ebersberg, Germany) with the composition specified in Table 3.

Table 3 - Sequencing ingredient composition for genotyping.

Ingredient	Volume [µL]	Sample Concentration
PCR Product	5 µL	5 ng/µL
Primer	5 µL	5 pmol/µL

The following primers were used to sequence the Rab4b DNA fragment:

Primer 1 (G27): 5'-GCTGATATGCTGAGACTAGATTCTCCAGG-3'

Primer 2 (G28): 5'-CTAGTACTATAGGCTTGCCTCTAGCTTTGG-3'

Successful mouse mutants were further used for breeding.

5.4 Cloning

5.4.1 Planning

Cloning design was carried out using the cloud-based platform Benchling (Benchling, San Francisco, United States). All cloning steps were performed via restriction enzyme-based cloning (Fig. 8).

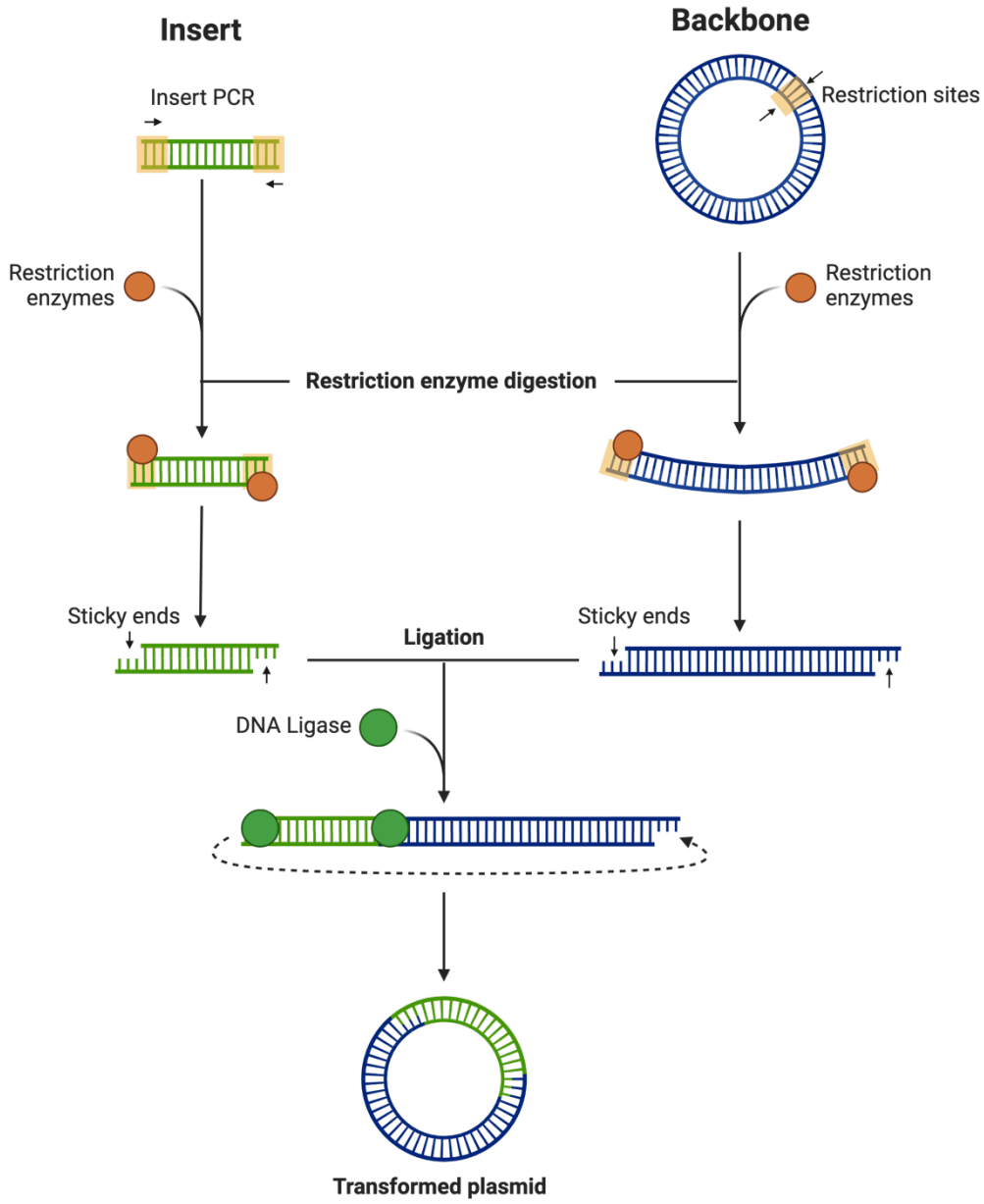

Figure 8 - Restriction enzyme cloning procedure. For restriction enzyme-based cloning, the insert is amplified via PCR using primers that contain the recognition sites of the required restriction enzymes. Subsequently, both the amplified insert and the plasmid backbone are enzymatically digested and ligated, resulting in the formation of the desired recombinant plasmid. Created with biorender.com.

The final plasmids (pXS6, pXS6.1, pXS10, pXS10.1, pXS11, and pDGM-PHP.B) were utilized for AAV production. The plasmid pXS11 contains a CMV promoter, GFP (Green Fluorescent Protein) as a reporter, a miniWPRE (Woodchuck Hepatitis Virus

Posttranscriptional Regulatory Element), and a bGH (bovine growth hormone) sequence, all flanked by the ITR sites of AAV2 (Fig. 9).

Figure 9 - GFP-plasmid (pXS11) construction. The GFP plasmid comprises a CMV promoter, GFP as a reporter gene, a miniWPRE element (which enhances the expression of genes delivered by viral vectors), and a bGH polyadenylation signal (which facilitates gene expression). These components are flanked by the ITRs of AAV2. Created with biorender.com.

Both plasmids, pXS6 and pXS6.1, contain a CMV promoter, a BFP (Blue Fluorescent Protein) reporter, a P2A sequence, a Kozak sequence, and a 5′ m*Otof* element (pXS6: up to position 783, pXS6.1: up to position 917), followed by the N-intein sequence of the GP41-1 intein, as well as the miniWPRE and bGH sequences. All elements are flanked by the ITRs of AAV2 (Fig. 10).

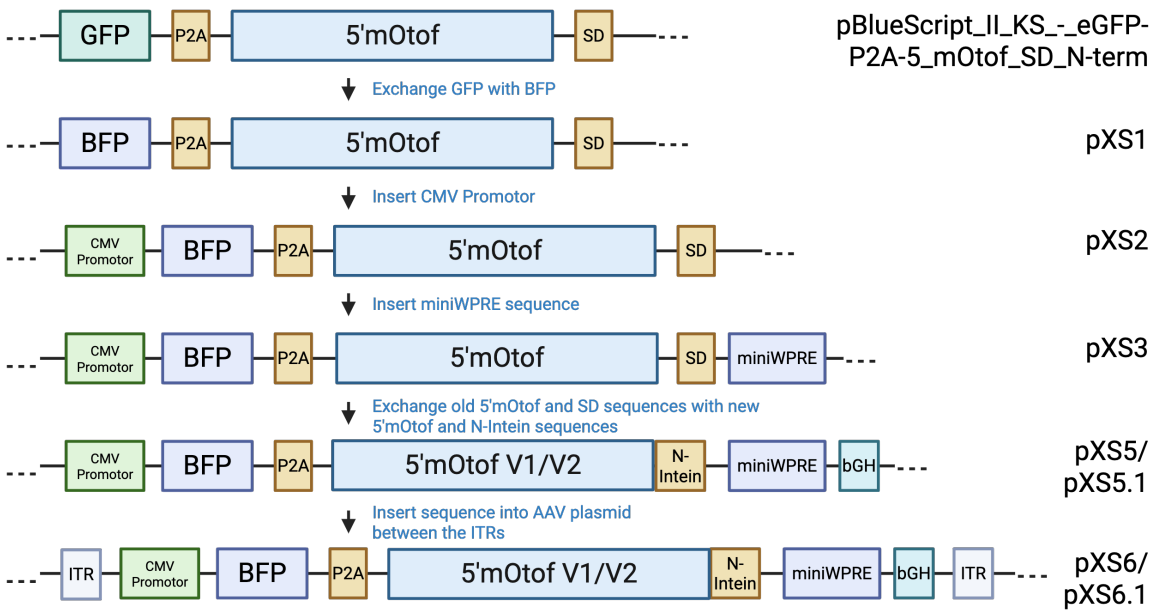

Figure 10 - Cloning history of pXS6 and pXS6.1. To construct the required plasmid (pXS6 and pXS6.1) containing the N-terminal portion of the m*Otof* coding sequence, followed by an N-Intein sequence, five distinct steps were performed. First, the GFP sequence was substituted with a BFP sequence. In the subsequent steps, a CMV promoter and the miniWPRE sequence were introduced. Finally, the previous version of the 5' m*Otof* sequence was replaced with a new version, which also includes the N-Intein sequence, and the construct was inserted into an AAV plasmid between the ITRs of AAV2.Created with biorender.com.

The plasmids pXS10 and pXS10.1 contain a CMV promoter, the C-Intein sequence of intein GP41-1, followed by the 3' m*Otof* sequence (pXS10: from position 784, pXS10.1: from position 918), the miniWPRE, and the bGH sequence, all flanked by the ITRs of AAV2 (Fig. 11).

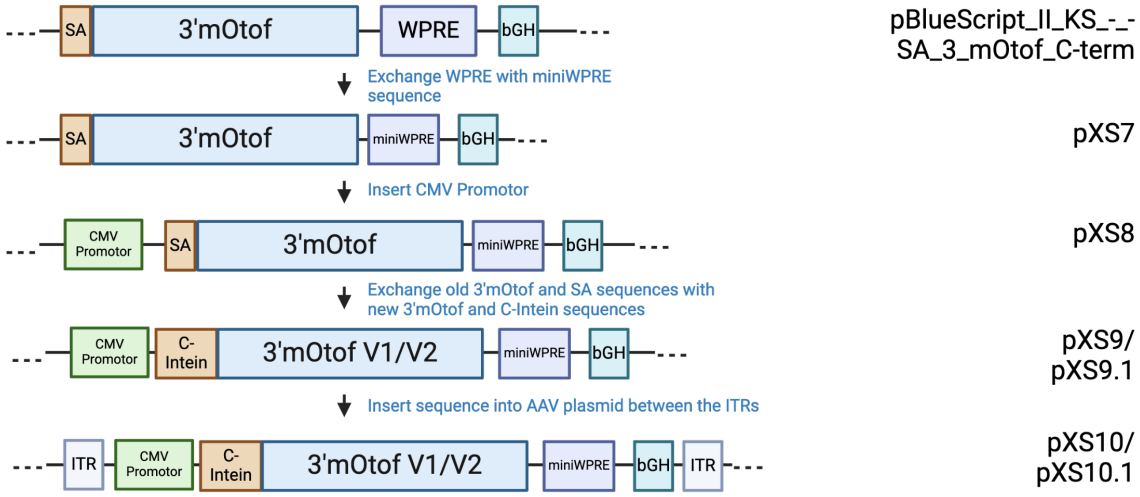

Figure 11 - Cloning history of pXS10 and pXS10.1. To construct an AAV plasmid containing the C-Intein sequence followed by the C-terminal m*Otof* sequence, the following steps were undertaken. First, the WPRE sequence was substituted with the shorter miniWPRE sequence in the pBlueScript_II_KS_-_-SA_3_mOtof_C-term plasmid (constructed by Hanan Al-Moyed). Subsequently, the CMV promoter sequence was inserted, and the previous N-terminal m*Otof* sequence was replaced with a new version that also includes the C-Intein sequence at the beginning. Finally, the modified construct was inserted into an AAV plasmid between the ITRs of AAV2. Created with biorender.com.

For the pDGM-PHP.B plasmid, the AAV6 capsid sequence from the pDGM6 plasmid (110660, Addgene, Watertown, United States) was replaced with the capsid sequence of PHP.B from plasmid pUCmini-iCAP-PHP.B (103002, Addgene, Watertown, United States). This modification was made to enable double transfection instead of triple transfection for AAV production (see also AAV production).

5.4.2 PCR for insert generation

For the insert amplification PCR was performed using a proofreading Q5 High-Fidelity DNA Polymerase (M0491S, New England BioLabs, Ipswich, United States) with the following reaction setup (Tab. 4).

Table 4 - Q5 high fidelity polymerase PCR components.

Component	25 µL Reaction	Final Concentration
5X Q5 Reaction Buffer	5 µL	1X
10 mM dNTPs	0.5 µL	200 µM
10 µM Forward Primer	1.25 µL	0.5 µM
10 µM Reverse Primer	1.25 µL	0.5 µM
Template DNA (1:1000 diluted plasmids)	1 µL	<1000 ng
Q5	0.25 µL	0.02 U/µL
Nuclease-Free H_2O	To 25 µL	-

The primers were designed to include the required restriction enzyme recognition sites at the 5' end of the sequence (for primer sequences, see supplement, Tab 29). The following thermocycling conditions were used for insert amplification (Tab 5).

Table 5 - Thermocycling condition for Q5 DNA polymerase reactions.

Step	Temperature [°C]	Time [min:sec]
Initial Denaturation	98	00:30
30 Cycles	98	00:10
	50-72 (depending on primers Tm)	00:10
	72	00:20-00:30 sec/kb
Final Extension	72	02:00
Hold	4	-

PCR products (5 µL product + 1 µL DNA gel loading dye 6X) were analysed following agarose gel electrophoresis, staining with GELRED® nucleic acid gel stain (1:10 000), and documented using the E-Box VX 5. Correct PCR products were subsequently purified using the innuPREP DOUBLEpure Kit.

5.4.3 Overlap PCR

To generate the miniWPRE, 5' m*Otof*-N-Intein, and C-Intein-3' m*Otof* sequences, overlap PCR was performed to eliminate any gap between the two sequence parts. For this purpose, specific primers were designed, as shown in Fig. 12.

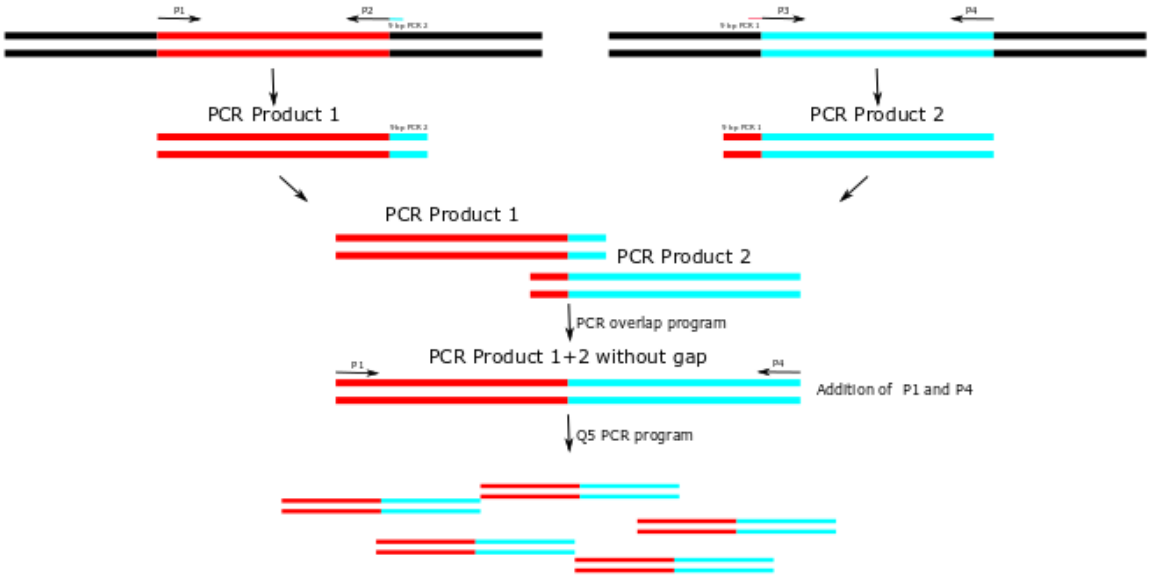

Figure 12 - Overlap PCR steps overview. For overlap PCR, four primers are required. A standard forward primer is used for the first PCR product, along with a reverse primer that includes the first nine base pairs of the second PCR product. For the second PCR product, a forward primer is needed that incorporates the last nine base pairs of the first PCR product, in addition to a standard reverse primer. After amplification, the two PCR products will have an 18-base pair overlap, resulting in a final PCR product that contains both sequences without any gap. This long sequence can then be further amplified using a standard PCR program.

One forward primer for the first PCR product was designed to start at the beginning of the desired region, while the reverse primer started at the end of the region, incorporating nine base pairs that overlap with the first nine base pairs of the second PCR product. The forward primer for the second PCR product included an overlap of nine base pairs with the last nine base pairs of the first PCR product, and the reverse primer overlapped with the end of the desired sequence. The PCRs for both sequences were performed as described previously (5.4.2 PCR for insert generation). To overlap the two sequences, the mix was prepared as outlined in Tab. 6, and a three-step thermocycling program was executed (Tab. 7).

Table 6 - Overlap PCR mix components.

Component	25 µL reaction
5X Q5 Reaction Buffer	5 µL
10 mM dNTPs	0.5 µL
PCR Product 1	5 µL
PCR Product 2	5 µL
Q5 High-Fidelity DNA Polymerase	0.25 µL
Nuclease-Free H_2O	6.75 µL
10 µM Forward Primer of PCR product 1 (added after overlap step)	1.25 µL
10 µM Reverse Primer of PCR product 2 (added after overlap step)	1.25 µL

Table 7 - Thermocycling condition for the overlap PCR step.

Temperature [°C]	Time [min:sec]
94	05:00
37	05:00
72	05:00
4	-

The forward primer of PCR product one and the reverse primer of PCR product two were included in the reaction mix, and the Q5 PCR cycler program was run as outlined in Tab. 5. PCR products (5 µL product + 1 µL DNA gel loading dye 6X) were analysed following agarose gel electrophoresis, staining with GELRED® nucleic acid gel stain (1:10 000), and documented using the E-Box VX 5. Correct PCR products were subsequently purified using the innuPREP DOUBLEpure Kit.

5.4.4 Insert and backbone digestion

For insert and backbone digestion, Fast Digest restriction enzymes (Thermo Fisher Scientific, Waltham, United States) were used (for the list of restriction enzymes, see supplement, Tab. 28). The following reaction mixture was prepared at room temperature (Tab. 8). The reaction mix was gently mixed, spin down, and incubated at 37°C in a thermocycler for 5 minutes (temperature and duration may vary depending on the enzyme used). Digestion products were analysed following agarose gel electrophoresis, staining with GELRGREEN® nucleic acid gel stain (1:10 000), and documented using the Blue Light LED Illuminator BL Star9. Correct backbone and insert digestion products were purified using the innuPREP DOUBLEpure Kit (Analytik Jena, Jena, Germany).

Table 8 - Insert and backbone digest components.

Component	Volume	
	Plasmid DNA (Backbone)	PCR Product (Insert)
Nuclease-free H_2O	15 µL	16 µL
10X Fast Digest Green Buffer	2 µL	3 µL
DNA	2 µL (up to 1 µg)	10 µL (up to 0.2 µg)
Fast Digest Enzyme	1 µL	1 µL
Total Volume	20 µL	30 µL

5.4.5 Ligation

For the ligation step, Thermo Scientific T4 DNA Ligase (EL0011, Thermo Fisher Scientific, Waltham, United States) was used, and the following reaction mixture for sticky-end ligation was prepared as outlined in Tab. 9. The mixture was incubated at 22°C for 10 minutes, after which the ligase was inactivated at 70°C for 5 minutes. In

some cases, ethanol precipitation was performed following ligase inactivation. For this, 0.1 volume of sodium acetate (6773.2, Roth, Karlsruhe, Germany, pH 5.8) (2 µL in 20 µL ligation mix) and 3 volumes of 100% ethanol (A3678.1000, Applichem, Darmstadt, Germany, 6 µL in 20 µL ligation mix) were added to the ligation mixture and incubated at -20°C for one hour to overnight. After incubation, the mixture was centrifuged for one hour at maximum speed at 4°C. A washing step with 50 µL of 70% ethanol was followed by another centrifugation step for 15 minutes at maximum speed and 4°C. Finally, the pellet was dried and resuspended in 4-10 µL of ddH_2O.

Table 9 - Sticky-end ligation reaction mixture.

Digested Backbone (linear vector DNA)	20-100 ng
Digested Insert DNA	1:1 to 5:1 molar ratio over vector
10x T4 DNA Ligase buffer	2 µL
Thermo Scientific T4 DNA Ligase	1 U
Nuclease-free H_2O	Up to 20 µL
Total Volume	20 µL

5.4.6 Electroporation

For the electroporation of pXS6, pXS6.1, pXS10, pXS10.1, and pXS11 plasmids (which contain integrated ITR sites), SURE Electroporation-Competent Cells (200227, Agilent Technologies, Santa Clara, United States) were used. For all other plasmids, XL1-Blue Electroporation-Competent Cells (200228, Agilent Technologies, Santa Clara, United States) were employed. A sterile electroporation cuvette (PP38.1, Carl Roth, Karlsruhe, Germany), two sterile microcentrifuge tubes, and 1000 µL of LB medium (110285, Merck, Darmstadt, Germany) were pre-chilled on ice. The Micro Pulser Electroporator (Bio-Rad Laboratories, Hercules, United States) was set to

program ‘EC1 Bacteria’. The electrocompetent cells were thawed on ice, gently mixed, and 40 µL was transferred into one of the microcentrifuge tubes. To this, 1.4 µL of the ligation mixture was added and gently mixed. The cell-DNA mixture was then transferred into the electroporation cuvette and placed into the Micro Pulser Electroporator. After a single pulse, 1000 µL of LB medium were added, and the mixture was incubated on ice for 1-2 minutes. Subsequently, the sample was incubated for one hour at 37°C with shaking at 550 rpm. Following centrifugation at 6000 rpm for one minute, approximately 800 µL of LB medium were removed, and the pellet was resuspended in the remaining LB medium. The resuspended cells were then plated onto a LB-Agar plate (10 cm, 110283, Merck, Darmstadt, Germany) containing Carbenicillin (100 mg/mL, 6344.2, Carl Roth, Karlsruhe, Germany) and incubated overnight at 37°C. Four to eight colonies were picked using a pipette tip and transferred into a culture tube containing 4 mL of LB medium (with Carbenicillin, 100 mg/mL). The culture was incubated overnight at 37°C with shaking at 150 rpm. Plasmid DNA was isolated using the GeneJET Plasmid Miniprep Kit (K0502, Thermo Fisher Scientific, Waltham, United States).

5.4.7 Test digestion and sequencing

A test digestion was performed on all extracted plasmids to identify the correct ones. The digestion was carried out using the same mixture as in the backbone digestion described previously (Tab. 9). Plasmids with the correct DNA bands were sent for sequencing to Eurofins Genomics (Ebersberg, Germany) with the desired mixture (Tab. 10). The sequencing results were analysed using the Benchling platform. A glycerol stock (800 µL bacterial culture and 200 µL glycerol) was prepared for each correct plasmid and stored at -80°C.

Table 10 - Sequencing ingredient composition for cloning.

Ingredient	Volume [µL]	Sample Concentration
Plasmid	5 µL	50-100 ng/µL
Primer	5 µL	5 pmol/µL

5.4.8 Mega plasmid purification

All plasmids used for AAV production (pXS6, pXS6.1, pXS10, pXS10.1, pXS11, pDGM6, pDGM-PHP.B, iCapminPHP.B, pAdDeltaF6, and pUCiCapminPHP.eB) were isolated and purified using the PureLink™ Expi Endotoxin-Free Mega Plasmid Purification Kit (A31232, Thermo Fisher, Waltham, United States) following the manufacturer's protocol. The final plasmid concentrations are provided in Tab. 31 (supplement).

5.5 AAV production

The AAV production steps, including transfection, cell type selection, harvesting, and purification, were optimized (Fig. 13). Several AAVs were produced for different experiments using the optimized protocol. For the AAV production optimization and in vitro transduction experiments on wild-type organs of Corti, GFP AAVs with serotypes AAV6, PHP.B, and PHP.eB were produced both in purified and non-purified forms. For the in vitro transduction experiments on otoferlin knockout organs of Corti, AAVs with the serotypes AAV6, PHP.B, and PHP.eB, as well as the two different *Otof* versions, were produced in a non-purified form.

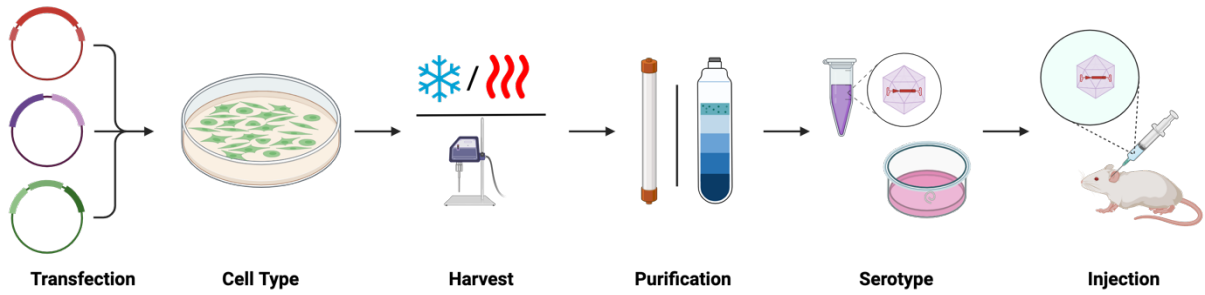

Figure 13 - AAV production and optimisation steps. Various steps in the AAV production process were planned for optimization. First, the transfection method was optimized by comparing calcium phosphate transfection to Turbofect transfection. Additionally, two different HEK cell lines (AAV-293 and HEK293T) were tested. For AAV harvesting, the freeze/thaw method was compared to sonication in a water bath. Furthermore, two different purification methods were tested: Iodixanol gradient and purification using an AAVX pre-packed column. These optimization steps were carried out to achieve a higher AAV titer and improved vector quality, which would then be used for in vitro experiments and, ultimately, in vivo studies with the produced vectors.

5.5.1 Cell culture

5.5.1.1 Thawing of frozen cells

One cryovial containing frozen HEK293T cells (kindly provided by AG Vona) or AAV-293 cells (240073, Agilent Technologies, Santa Clara, United States) was thawed by gentle agitation in a 37°C water bath for 1-2 minutes. The cell suspension was then transferred into a 50 mL centrifuge tube containing 5 mL of complete DMEM (10% FBS (A5256701, Thermo Fisher Scientific, Waltham, United States), 1% Penicillin/Streptomycin (15140122, Thermo Fisher Scientific, Waltham, United States)), high glucose, GlutaMAX™ Supplement (11965092, Thermo Fisher Scientific, Waltham, United States). After centrifugation at 1000 g for 5 minutes, the growth medium was removed by aspiration. The cells were resuspended in 10 mL of fresh complete DMEM by gently pipetting up and down and then transferred to a 75-cm² tissue culture flask. The flask was placed in an incubator at 37°C with 5% CO2.

5.5.1.2 Cell passaging

For cell passaging, sterile complete DMEM medium, PBS (14040133, Thermo Fisher Scientific, Waltham, United States), and 0.25% trypsin-EDTA (25200072, Thermo Fisher Scientific, Waltham, United States) were pre-warmed in a 37°C water bath. The growth medium was removed by aspiration, and the cells were washed with 10 mL of sterile PBS. The cells were then trypsinized for approximately 3 minutes at 37°C in 2 mL of 0.25% trypsin-EDTA and subsequently diluted in 8 mL of complete DMEM medium to inactivate the trypsin. The appropriate volume of the cell suspension was transferred to a new 75-cm² tissue culture flask containing 10 mL of complete DMEM medium. The flask was placed in an incubator at 37°C with 5% CO2. Cell confluence was maintained at 50% by passaging the cells twice a week (Monday at a 1:10 dilution and Thursday at a 1:20 dilution).

5.5.1.3 Freezing of cells for a liquid nitrogen stock

For the liquid nitrogen stock, only healthy log-phase cells were collected. The complete DMEM culture medium was removed, and the cells were washed with 10 mL of pre-warmed, sterile PBS. The cells were trypsinized for approximately 3 minutes at 37°C in 2 mL of 0.25% trypsin-EDTA and then diluted in 8 mL of complete DMEM medium to inactivate the trypsin. The cells were counted using a hemocytometer (Neubauer Zählkammer improved), and the required volume of the cell suspension was centrifuged at 500 g for 5 minutes at room temperature. The growth medium was removed by aspiration, and the cells were resuspended in freezing medium (50% DMEM, high glucose, GlutaMAX™ Supplement, 40% heat-inactivated FBS, and 10% DMSO (D8418, Merck, Darmstadt, Germany)) to achieve a final concentration of 1×10^6 cells/mL. Aliquots of 1 mL were dispensed into cryovials. The cell aliquots were gradually frozen by placing the vials in a Mr. Frosty (5100-0001, Nalgene, Rochester,

United States) at -80°C overnight. The vials were then transferred to liquid nitrogen the following day for long-term storage.

5.5.2 Transfection

For the transfection step, two different methods, calcium phosphate transfection and Turbofect transfection, were used and compared to determine if one method resulted in a higher viral titer. Only the calcium phosphate transfection method was used for the production of AAVs used in experiments (e.g., in vitro transduction on the organ of Corti).

5.5.2.1 Calcium phosphate transfection

Twenty-four hours prior to transfection, 1.5×10^6 cells per 10 cm plate (either AAV-293 or HEK293T cells, depending on the experiment) were inoculated in complete DMEM. The following day, the cells were transfected. For one 10 cm plate, 428 µL of sterile H_2O, 62 µL of 2M $CaCl_2$, and 15 µg of DNA were mixed by vortexing. For the DNA, a molar ratio of 1:1:1 (Rep/Cap: pHelper: Transfer Plasmid) was used for triple transfection, and a molar ratio of 2:1 (pDGM-Plasmid: Transfer Plasmid) was used for single transfection. Next, 500 µL of sterile 2X HBS (50 mM HEPES, 10 mM KCl, 12mM Glucose, 280 mM NaCl, 1.5 mM Na_2PO_4) were added dropwise while aerating the mixture. 1 mL of the final mix was then added around the cell culture plate and mixed gently. The plate was returned to the incubator (37°C, 5% CO_2). Twelve to sixteen hours after transfection, the medium was gently aspirated, and fresh, pre-warmed complete medium was applied to the cells.

5.5.2.2 Turbofect transfection

Twenty-four hours prior to transfection, 1 × 10^6 cells per 10 cm plate (either AAV-293 or HEK293T cells, depending on the experiment) were inoculated in complete DMEM. The following day, 10 µg of DNA were diluted into 1000 µL of serum-free DMEM. For triple transfection, a molar ratio of 1:1:1 (Rep/Cap: pHelper: Transfer Plasmid) was used, and for single transfection, a molar ratio of 2:1 (pDGM-Plasmid: Transfer Plasmid) was applied. The Turbofect transfection reagent (R0533, Thermo Fisher, Waltham, United States) was briefly vortexed, and 30 µL were added to the diluted DNA. The mixture was immediately vortexed to ensure proper mixing. After incubation for 15-20 minutes at room temperature, 1000 µL of the transfection reagent/DNA mixture was added dropwise to the plate with cells. The plate was gently rocked to achieve even distribution of the complexes immediately after adding the transfection reagent. The cells were incubated at 37°C with 5% CO_2 for 48 hours.

5.5.3 AAV harvest

Similar to the transfection step, two different methods for harvesting were compared to determine which resulted in a higher viral titer: the freeze/thaw method and the sonication method. Only the sonication method was used to produce the AAVs for experiments (e.g., in vitro transduction on the organ of Corti).

5.5.3.1 Freeze/thaw method

The culture medium was carefully removed without disturbing the cells, and 10 mL of sterile PBS were added to the plate. Cells were harvested in a 50 mL centrifugation tube 48 hours after transfection and centrifuged for 15 minutes at 2500 rpm. The cell pellet was resuspended in 1 mL sterile lysis buffer (50 mM Tris-HCl (9090.2, Roth,

Karlsruhe, Germany), pH 8.0, 150 mM NaCl (1.06404.1000, Merck, Darmstadt, Germany)) and transferred into a 1.5 mL centrifugation tube. The cell suspension was frozen in liquid nitrogen and immediately thawed in a 37°C water bath for five cycles. After a centrifugation step of 10 minutes at 13 200 rpm, the supernatant containing the AAVs was transferred into a fresh 1.5 mL centrifugation tube.

For benzonase treatment, the respective amount of 10x Benzonase buffer (500 mM Tris-HCl, pH 8.0, 10 mM $MgCl_2$ (28305, Serva, Heidelberg, Germany), 1 mg/mL BSA (A2153-50G, Sigma, Burlington, United States)) to make 1x buffer, and 250 units of Benzonase (101697, Merck, Darmstadt, Germany) were added to the AAV solution and incubated for 30 minutes at 37°C. The AAV solution was either stored at -80°C or concentrated using an Amicon Ultra Centrifugal Filter (100 kDa MWCO, UFC510008, Merck, Darmstadt, Germany). To concentrate the solution, the volume of the viral preparation was increased to 15 mL with sterile PBS, transferred to the centrifugal filter tube, and centrifuged for 40 minutes at 4000 g to reduce the volume to approximately 141 µL. The concentrated AAV solution was transferred to a fresh 1.5 mL centrifugation tube and stored at -80°C.

5.5.3.2 Sonication method

The culture medium was carefully removed without disturbing the cells, and 10 mL of sterile PBS was added to the plate. Cells were harvested in a 50 mL centrifugation tube 48 hours after transfection and centrifuged for 15 minutes at 2500 rpm. The cell pellet was resuspended in 1 mL sterile lysis buffer and transferred into a 1.5 mL centrifugation tube. The cell suspension was sonicated for 5 minutes at 37°C in a Bandelin Sonorex Digitec sonication water bath (Bandelin, Berlin, Germany).

After a centrifugation step of 10 minutes at 13 200 rpm, the supernatant containing the AAVs was transferred into a fresh 1.5 mL centrifugation tube.

For benzonase treatment, the appropriate amount of 10x Benzonase buffer was added to make a 1x solution, along with 250 units of Benzonase, and the mixture was incubated for 30 minutes at 37°C. The AAV solution was either stored at -80°C, purified or concentrated using an Amicon Ultra Centrifugal Filter (100 kDa MWCO). To concentrate the solution, the volume of the viral preparation was increased to 15 mL with sterile PBS, transferred to the centrifugal filter tube, and centrifuged for 40 minutes at 4000 g to reduce the volume to approximately 141 µL. The concentrated AAV solution was transferred to a fresh 1.5 mL centrifugation tube and stored at -80°C.

5.5.4 Purification

For all AAV purifications, the POROS™ GoPure™ AAVX Pre-packed Column (A36652, Thermo Fisher, Waltham, United States) in combination with the Ismatec Reglo ICC peristaltic pump (Isamatec SA; Glattburg, Switzerland) was used. The column was pre-equilibrated with 10 mL of 1x TBS (Tris-buffered saline; pH 7.6; 50 mM Tris-HCl, pH 7.6; 150 mM NaCl) at 25 rpm. The lysate was then loaded onto the column at a speed of 7 rpm and washed with 10 mL of 1X TBS at 25 rpm. Three additional washing steps followed: 5 mL of 2X TBS (25 rpm), 10 mL of 20% ethanol (25 rpm), and 10 mL of 1X TBS (25 rpm).

The bound AAV was eluted using 10 mL of low-pH buffer (0.2 M glycine (3790.2, Roth, Karlsruhe, Germany) in 1X TBS, 0.01% (v/v) Pluronic F-68, pH 2.5) at 15 rpm in an up-flow direction. The eluted solution was neutralized by adding 1 M Tris-HCl to one-tenth of the fraction volume directly into the fraction collection tube prior to elution.

Following this, the column was washed with 10 mL of 1X TBS (25 rpm) and regenerated with 15 mL of 6M guanidine-HCl (A1499.1000, Applicam, Darmstadt,

Germany) at a flow rate of 15 rpm. After two additional washing steps with 10 mL of 20% ethanol and 10 mL of 1X TBS (25 rpm), the column was filled with 0.1M sodium phosphate (71640, Fluka, Buchs, Switzerland) in 20% ethanol (pH 7.0) and stored at 4°C.

The AAV solution was concentrated using an Amicon Ultra Centrifugal Filter (100 kDa MWCO). The volume of the viral preparation was increased to 15 mL with sterile PBS, transferred to the centrifugal filter tube, and centrifuged for 40 minutes at 4000 g to reach a volume of approximately 141 µL. The concentrated AAV solution was transferred to a fresh 1.5 mL centrifugal tube and stored at -80°C.

5.5.5 RT-PCR

To determine the AAV concentration, RT-PCR was performed. The AAV solution was first treated with DNase (12185010, PureLink™ DNase, Thermo Fisher, Waltham, United States) to eliminate any contaminating plasmid DNA that may have been carried over from the production process. To do this, 5 µL of the AAV sample, 39 µL of H2O, 5 µL of 10X DNase buffer, and 1 µL of DNase were gently mixed together and incubated for 30 minutes at 37°C. The samples were then transferred to ice and diluted according to the dilution scheme outlined in Tab. 11.

Table 11 - Dilution series for AAV quantification.

Dilution Series	Sample	Nuclease free H_2O	Dilution factor	Total dilution
Dilution 1 (DNase step)	5 µL AAV stock	45 µL	10X	10X
Dilution 2	5 µL Dil. 1	95 µL	20X	200X
Dilution 3	20 µL Dil. 2	80 µL	5X	1000X
Dilution 4	20 µL Dil. 3	80 µL	5X	5000X
Dilution 5	20 µL Dil. 4	80 µL	5X	25000X
Dilution 6	20 µL Dil. 5	80 µL	5X	125000X
Dilution 7	20 µL Dil. 6	80 µL	5X	625000X
Dilution 8	20 µL Dil. 7	80 µL	5X	3125000X

If the sample was expected to have a titer of $<1 \times 10^{12}$ GC/mL, dilutions 3-6 were used, whereas for samples with a titer of $>3 \times 10^{13}$ GC/mL, dilutions 5-8 were applied. For the standard, a dilution series of the plasmid pXS11 was prepared using the following calculations:

$$5014\ bp\ *650\ \frac{daltons}{bp} = 3.27 * 10^6\ \frac{g}{mol}$$

$$\frac{1.1044\ \frac{\mu g}{\mu L} * \frac{1\ g}{10^6}}{3.27 * 10^6 \frac{g}{mol}} = 3.38 * 10^{-13}\ \frac{moles}{\mu L}$$

$$3.38 * 10^{-13}\ \frac{moles}{\mu L} * 6.022145 * 10^{23}\ \frac{molecules}{mol} = 2.04 * 10^{11}\ \frac{molecules}{\mu L}$$

To obtain a solution of $2 * 10^9\ \frac{molecules}{\mu L}$:

$$\frac{2.04*10^{11}\ \frac{molecules}{\mu L}}{2*10^9\ \frac{molecules}{\mu L}} = 101.77X \text{ dilution}$$

$$\rightarrow \frac{100\ \mu L}{101.77} = 0.983\ \mu L\ of\ pXS11 \text{ in } 99.017\ \mu L\ H_2O$$

The dilution series was prepared according to Tab. 12.

Table 12 - Dilution series for the standard.

	Volume [µL] of sample	Volume of H_2O [µL]	Molecules per µL
Dilution 1	0.983 of stock	99.017	$1*10^9$
Dilution 2	10 of Dil. 1	90	$1*10^8$
Dilution 3	10 of Dil. 2	90	$1*10^7$
Dilution 4	10 of Dil. 3	90	$1*10^6$
Dilution 5	10 of Dil. 4	90	$1*10^5$
Dilution 6	10 of Dil. 5	90	$1*10^4$
Dilution 7	10 of Dil. 6	90	$1*10^3$

A solution containing primers and PowerUp SYBR™ Mastermix (A25742; Thermo Fisher, Waltham, United States) was prepared according to the specifications in Tab. 13, in the required volume based on the number of plate wells needed.

Table 13 - Master mix composition for AAV quantification via RT-PCR.

Reagent	Volume (1X) [µL]
PowerUp SYBR Mastermix	10
100 µM Forward Primer	0.15
P68 RT-PCR_CMV_Promotor_for [59.44°C]	
100 µM Reverse Primer	0.15
P69 RT-PCR_CMV_Promotor_rev [60.00°C]	
Nuclease Free Water	4.7

In a 96-well plate, 5 µL of each standard or sample and 15 µL of master mix were loaded in triplicates. The plate was sealed with transparent film and centrifuged at 3000 rpm for 2 minutes to ensure the sample was at the bottom of the wells. The protocol outlined in Tab. 14 was then run on a LightCycler 480 (Roche, Basel, Switzerland).

Table 14 - RT-PCR program for AAV titer quantification.

	Temperature [°C]	**Time**	
UDG activation	50	2 min	
Dual-Lock DNA Polymerase	95	2 min	
Denature	95		
Anneal	55		X40
Extension	72 → Signal Detection		

Data analysis was performed using Microsoft Excel (Microsoft, Redmond, United States). The physical titer of the samples (viral genomes per mL) was determined based on the standard curve and the corresponding sample dilutions.

5.6 Hearing measurements

Hearing function was assessed by DPOAE and ABR in a soundproof chamber (IAC 400-A, Industrial Acoustics Company GmbH, Niederkrüchten, Germany) as previously described (Marchetta *et al*, 2022) at three different ages: one, six, and twelve months.

Mice were anesthetized with an intraperitoneal injection of a mixture of fentanyl (0.05 mg/kg body weight, 06143427, Fentanyl-Hameln, Hameln Pharma plus, Hameln, Germany), midazolam (5 mg/kg body weight, 4991909, Midazolam-Hameln®; Hameln Pharma plus, Hameln, Germany), medetomidine (0.5 mg/kg body weight, 1901022, Sedator®, Albrecht, Aulendorf, Germany), and atropine sulfate (0.2 mg/kg body weight, 2192616, B. Braun, Melsungen, Germany), diluted with water ad. inj. (06178414, Ampuwa, Fresenius KABI, Bad Homburg, Germany) to a total injection volume of 10 mL per kg body weight. Additional doses of anaesthetic were administered as required.

To maintain ocular hydration, an ointment (01578675, Bepanthen, Bayer AG, Leverkusen, Germany) was applied. During the measurements, the animals were positioned prone. Electrocardiography was monitored, and a heated blanket was used to maintain the body temperature at approximately 37°C.

For DPOAE measurements, anesthetized wild-type or mutant mice were placed on a pre-warmed resting pad (37°C) in the soundproof chamber, and an acoustic coupler was carefully placed in the ear canal. The cubic 2f1 - f2 DPOAE was measured for frequencies (f) with f2 = 1.24 × f1 and levels (L) with L2 = L1 - 10 dB using a sensitive microphone inside the coupler (MK231, Microtech Gefell, Gefell, Germany, Preamplifier B&K 2669C, Bruel & Kjaer, Naerum, Denmark). The stimuli pair contained frequencies between f2 = 4.0 to 32.0 kHz, with L2 either constantly at 50 dB SPL

(Sound Pressure Level; DP-gram) or increasing from -5 to 65 dB SPL in 5 dB steps (I/O growth function).

ABR, evoked by short-duration sound stimuli, represents the summed activity of neurons in various anatomical structures along the ascending auditory pathway (Burkard *et al*, 2007) and was measured by averaging the evoked electrical responses recorded via subcutaneous cranial electrodes. In brief, ABR thresholds were elicited using click (100 µs), noise (1 ms duration), or pure-tone stimuli (3 ms duration, with a 1 ms cosine squared rise and fall envelope, covering frequencies from 2 to 45.2 kHz).

All animals were sacrificed by decapitation at the end of the hearing measurements for subsequent immunostaining of the organ of Corti.

5.7 AAV in vitro transduction on organ of Corti cultures

For the AAV in vitro transduction on organ of Corti cultures, wild-type P7-P9 animals were euthanized by decapitation, and the cochleae were removed from the temporal bone. The apical and midbasal parts of the organ of Corti were excised in sterile dissection solution (HBSS (14025050, Thermo Fisher, Waltham, United States) + 1% 1M HEPES (Company)) and transferred to a culture insert well (80369, ibidi, Fitchburg, United States) containing 50 µL DMEM/F12 + GlutaMax (10565018, Thermo Fisher, Waltham, United States) + 5% FBS + 50 µg/mL Ampicillin (Company) medium (Fig. 14). The culture inserts were pre-positioned on sterile glass slides and placed into a sterile 10 cm plate containing 3-4 mL sterile ddH_2O. The plate with the organs was then placed in an incubator at 37°C and 5% CO_2 overnight.

The following day, 1 × 10^{10} VG of the appropriate AAV were added to the culture inserts with 50 µL of fresh culture medium. After 24 hours and 48 hours, the medium was replaced with fresh culture medium. The organs of Corti were fixed with 4% PFA (P733.1, Roth, Karlsruhe, Germany) 72 hours after AAV addition for one hour at 4°C. The organs were washed three times with PBS. Immunostaining procedures followed as described in the "Tissue Preparation and Immunohistochemistry" section.

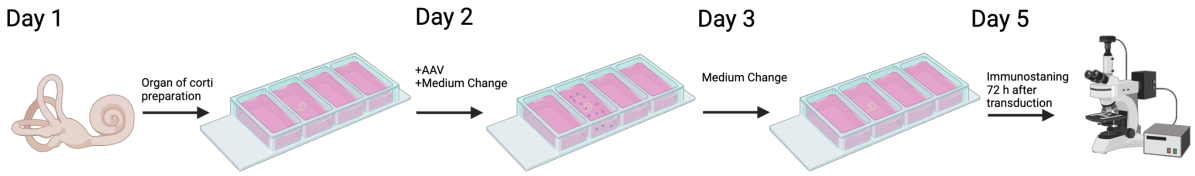

Figure 14 - Experimental setup and procedure of in vitro culture transduction experiment. For the AAV in vitro transduction experiments, the cochleae of wild-type P7-P9 mice were removed from the temporal bone, and the apical and midbasal parts of the organ of Corti were excised. These sections were then placed in a culture insert well containing 50 µL of medium. The following day, the AAVs to be tested were added to the medium after a medium change. On days three and four, the medium was changed again. Finally, 72 hours after AAV addition, the organs were fixed and stained to assess the transduction rates, particularly in the IHCs and OHCs.

5.8 Tissue preparation and immunohistochemistry

Tissue preparation and immunostaining were performed as described by Strenzke *et al*, (2016). Wild-type and Otof-p. KL>M mice were euthanized via CO_2 exposure. After decapitation, the cochleae were carefully removed from the temporal bone. The upper part of the bony shelf was excised, and the round window was perforated. The cochleae were then fixed in 4% PFA in PBS for one hour on ice. After three PBS washes, the cochleae were decalcified in 200 mM EDTA (at 4°C) for 1-3 hours, depending on the age of the mice. Wholemounts of the organ of Corti were excised and blocked in donkey serum dilution buffer (DSDB, containing 16.67% Donkey Serum

(D9663-10mL, Merck, Darmstadt, Germany), 20 mM phosphate buffer, 0.45 M NaCl, and 0.3% Triton X-100) for one hour at room temperature. Primary antibodies (as detailed in Tab. 15, 17 and 19) were diluted in DSDB and incubated with the organ of Corti overnight at 4°C. The anti-otoferlin antibody required additional pre-incubation at 37°C for one hour. After three washes with wash buffer (20 mM phosphate, 0.3% Triton X-100 (1.08603.1000, Merck, Darmstadt, Germany), 0.45 M NaCl), secondary antibodies (as listed in Tab. 16, 18, and 20) were applied and incubated for one hour at room temperature. After three washes in wash buffer and 5 mM phosphate buffer, the organs of Corti were mounted in mowiol (0713.1, Carl Roth, Karlsruhe, Germany). Wild-type and mutant organs of Corti were stained simultaneously for comparison.

Table 15 - Primary antibodies used for the otoferlin project.

Antibody	Dilution	Additional Information
Mouse anti-Otoferlin	1:400	ab53233, Abcam, Cambridge, United Kingdom
Rabbit anti-VGlut3	1:400	135 203, Synaptic Systems, Göttingen, Germany
Mouse anti-Ctbp2	1:200	612044, BD Biosciences, Franklin Lakes, United States
Rabbit anti-Shank1a	1:300	RA19016, Neuromics, Edina, United States
Goat anti-Calretinin	1:200	CG1, Swant, Burgdorf, Switzerland

Table 16 - Secondary antibodies used for the otoferlin project.

Antibody	Dilution	Additional Information
Donkey anti-mouse Alexa546	1:200	A11056, Thermo Fisher, Waltham, United States
Donkey anti-rabbit Alexa488	1:200	711-546-152, Jackson ImmunoResearch, Philadelphia, United States
Donkey anti-mouse Alexa546	1:200	A11056, Thermo Fisher, Waltham, United States
Donkey anti-goat Alexa647	1:400	A32849, Thermo Fisher, Waltham, United States

Table 17 - Primary antibodies used for the AAV in vitro transduction project.

Antibody	Dilution	Additional Information
Guinea Pig anti-Parvalbumin	1:500	195004, Synaptic Systems, Göttingen, Germany
Chicken anti-GFP	1:200	ab13970, Abcam, Cambridge, United Kingdom
Mouse anti-Otoferlin	1:400	ab53233, Abcam, Cambridge, United Kingdom
Goat anti-HA-Tag	1:200	A190-138A, FORTIS Life Sciences, Boston, United States
Rabbit anti-Myo7a	1:400	25-6790, Proteus Biosciences Inc., Ramona, United States

Table 18 - Secondary antibodies used for the AAV in vitro transduction project.

Antibody	Dilution	Additional Information
Donkey anti-Guinea pig BV421	1:50	706-675-148, Jackson ImmunoResearch, Philadelphia, United States
Donkey anti-Chicken Alexa647	1:200	703-605-155, Jackson ImmunoResearch, Philadelphia, United States
Donkey anti-Mouse Alexa546	1:200	A10036, Thermo Fisher, Waltham, United States
Donkey anti-Goat Alexa488	1:200	A-11055, Thermo Fisher, Waltham, United States
Donkey anti-Rabbit Alexa647	1:800	711-606-152, Jackson ImmunoResearch, Philadelphia, United States

Table 19 - Primary antibodies for the Rab4 immunostainings.

Antibody	Dilution	Additional Information
Guinea Pig anti-Vglut3	1:400	135 204, Synaptic Systems, Göttingen, Germany
Goat anti-Oncomodulin	1:200	PA5-4782, Thermo Fisher, Waltham, United States
Mouse anti-Neurofilament 200	1:800	N0142-100UL, Sigma-Aldrich, St. Louis, United States
Rabbit anti-Rab4b	1:200	OSR00343W, Thermo Fisher, Waltham, United states
Rabbit anti-Rab4a	1:50	ET1602-15, BIOZOL, Hamburg, Germany

Table 20 - Secondary antibodies for the Rab4 immunostaining.

Antibody	Dilution	Additional Information
Donkey anti-Guinea pig Alexa488	1:100	706-545-148, Jackson ImmunoResearch, Philadelphia, United States
Donkey anti-Mouse Alexa546	1:200	A10036, Thermo Fisher, Waltham, United States
Donkey anti-Goat BV421	1:50	705-675-147 Jackson ImmunoResearch, Philadelphia, United States
Donkey anti-Rabbit Alexa647	1:800	711-606-152, Jackson ImmunoResearch, Philadelphia, United States

5.9 Proximity ligation assay

Prior to the proximity ligation assay (PLA), apical and midbasal turns of P14-P16 wild-type and Otof-p. KL>M mice were dissected in HBSS buffer without Ca^{2+}. After dissection, the organs of Corti from both wild-type and Otof-p. KL>M mice were treated under two different conditions. The first condition involved incubation in HBSS buffer

without Ca^{2+} (5.36 mM KCl (1.05001.0250, Merck, Darmstadt, Germany), 141.7 mM NaCl, 1 mM $MgCl_2$, 0.5 mM $MgSO_4$ (1.05886.0500, Merck, Darmstadt, Germany), 10 mM HEPES (A1070.0100, ApliChem, Darmstadt, Germany), 3.4 mM L-glutamine (G8540-100G, Sigma, Burlington, United States) 6.9 mM D-glucose (G8270-100G, Sigma, Burlington, United States); Rest) at 37°C for one minute (Rest 1'). The second condition involved incubation in HBSS with high K^+ (65.36 mM KCl, 79.7 mM NaCl, 1 mM $MgCl_2$, 0.5 mM $MgSO_4$, 10 mM HEPES, 3.4 mM L-glutamine, 6.9 mM D-glucose, 2 mM $CaCl_2$) at 37°C for one minute (Stim 1'). After the respective treatments, the organs of Corti were immediately fixed in 4% PFA for 60 minutes at 4°C. The PLA assay was performed using the Duolink In Situ Red Mouse/Rabbit Kit, according to the manufacturer's protocol (DUO92101, Merck, Darmstadt, Germany), with modifications as described previously (Cepeda *et al*, 2019). The antibodies used are listed in Tab. 21.

Table 21 - Primary and secondary antibodies used for the otoferlin PLA.

Antibody	Dilution	Additional Information
Mouse anti-Otoferlin	1:400	ab53233, Abcam, Cambridge, United Kingdom
Rabbit anti-Calbindin	1:300	CB-38a, Swant, Burgdorf Switzerland
Goat anti-Calretinin	1:200	CG1, Swant, Burgdorf, Switzerland
Donkey anti-goat Alexa 488	1:200	A-11055, Thermo Fisher, Waltham, United States

5.10 RNA Scope

RNA Scope is an advanced in situ hybridization technique that utilizes a unique double-Z probe design to detect specific RNA molecules within fixed cells with single-molecule sensitivity. The method involves a series of hybridization steps and signal amplification cascades, enabling the visualization of target RNA as distinct punctate dots under a

microscope. This approach allows for quantitative analysis of gene expression with high specificity and minimal background noise.

In this study, RNA Scope was employed to identify Rab4b and Rab4a RNA in the inner ear of wild-type mice. For this purpose, either cochlear cryosections or whole mounts of the organ of Corti were prepared.

5.10.1 Cryosections

For cryosection preparation, a P29 wild-type BL6 animal was euthanized by CO_2 exposure. After decapitation, the cochleae were removed from the temporal bone, the upper part of the bony cochlea was removed, and the round window was perforated. The cochleae were fixed in 4% PFA in PBS for 24 hours at 4°C. After three PBS washes, the cochleae were decalcified in 200 mM EDTA (pH 7.4) for 24 hours at 4°C. The cochleae were then transferred to a 25% sucrose (1.07651.100, Merck, Darmstadt, Germany) solution in 1X PBS and stored on a rotating shaker overnight at 4°C. Afterward, the cochleae were placed in small caps made of aluminium foil containing TissueTek OCT medium (4583, Sakura Finetek Europe, Alphen aa den Rijn, Netherlands) and gently shaken for one hour to ensure that the medium penetrated the cochlear coils. The caps with the cochleae were placed at -20°C overnight. 16 µm thick sections were cut (at -30°C) and placed on Super Frost slides (1255015, Thermo Scientific, Waltham, United States) and stored at -80°C.

For RNA Scope staining, the slides were first incubated for 10 minutes at room temperature, and a hydrophobic barrier was drawn tightly around the tissue. After one wash, the tissues were post-fixed for 10 minutes with 4% PFA at room temperature, washed with 1X PBS, and treated with hydrogen peroxide for 10 minutes. Protease III (322335, RNAscope® H2O2 and Protease Reagents Kit, ACD BIO, Newark, United

States) was added and incubated at 40°C for one hour under moist conditions. After washing again with 1X PBS for 10 minutes, the probe mix (C3: Rab4b (1304821, ACD BIO, Newark, United States) 1:50 in C1: Rab4a (1304811-C1, ACD BIO, Newark, United States)) was applied to the tissue and incubated for two hours at 40°C under moist conditions. Two washing steps with 1X PBS for 10 minutes at room temperature followed. The amplification step involved three incubation steps, starting with v2 Amp1 and v2 Amp2 (323110, RNAscope® Multiplex Fluorescent Detection Reagent VL, ACD BIO, Newark, United States), each incubated for 30 minutes at 40°C, followed by v2 Amp3 (323110, RNAscope® Multiplex Fluorescent Detection Reagent VL, ACD BIO, Newark, United States) for 15 minutes at 40°C. After the three steps, two washing steps with 1X RNA Scope wash buffer (310091, RNAscope® Wash Buffer, ACD BIO, Newark, United States) for 5 minutes at room temperature were performed. HRP-C1 solution was then applied to the tissue, incubated at 40°C for 15 minutes, and washed twice with 1X RNA Scope wash buffer (five minutes at room temperature). Following a 30-minute incubation at 30°C with TSA Vivid Fluorophore 520 (1:1500), two additional washing steps were performed. Finally, the HRP blocker (323110, RNAscope® Multiplex Fluorescent Detection Reagent VL, ACD BIO, Newark, United States) was added, incubated for 15 minutes at 40°C, and washed twice (1X RNA Scope wash buffer, 5 minutes at room temperature). The same procedure was repeated for HRP-C3 (323110, RNAscope® Multiplex Fluorescent Detection Reagent VL, ACD BIO, Newark, United States) and TSA Vivid Fluorophore 570 (323110, RNAscope® Multiplex Fluorescent Detection Reagent VL, ACD BIO, Newark, United States).

After RNA Scope staining, immunostaining with various Rab4a and Rab4b antibodies followed as previously described (5.8 Tissue preparation and immunohistochemistry), starting with the DSDB blocking step.

Table 22 - Primary antibodies used after RNA Scope staining.

Antibody	Dilution	Additional Information
Goat anti Calretinin	1:200	CG1, Swant Burgdorf, Switzerland
Guinea Pig anti VGlut3	1:400	135 204, Synaptic Systems, Göttingen, Germany
Rabbit anti Rab4b (Thermo Fisher)	1:200	OSR00343W, Thermo Fisher, Waltham, United States
Rabbit anti Rab4b (Abcam)	1:80	AB179948, Abcam, Cambridge, United Kingdom
Rabbit anti Rab4a (Proteintech)	1:50	10347-1-AP, Proteintech, San Diego, United States
Rabbit anti Rab4a (BIOZOL)	1:50	ET1602-15, BIOZOL, Hamburg, Germany

Table 23 - Secondary antibodies used after RNA Scope staining.

Antibody	Dilution	Additional information
Donkey anti goat BV421	1:50	705-675-147, Jackson ImmunoResearch, West Grove, United States
Donkey anti guinea pig BV421	1:50	706-675-148, Jackson ImmunoResearch, West Grove, United States
Donkey anti goat 546	1:200	A-11056, Thermo Fisher, Waltham, United States
Donkey anti rabbit Alexa 647	1:800	711-606-152, Jackson ImmunoResearch, West Grove, United States

5.10.2 Whole mounts

For whole mount preparations, wild-type BL6 mice (at one, six, and twelve months of age) were euthanized by CO_2 exposure. After decapitation, the cochleae were carefully extracted from the temporal bone. The upper portion of the cochlear bony shelf was removed, and the round window was perforated. The cochleae were then fixed in 4% PFA in PBS for 24 hours. Following three PBS washes, the cochleae were decalcified in 200 mM EDTA for 1-3 hours (at 4°C), depending on the age of the mice. Whole mounts of the organ of Corti were excised and placed on a 24-well plate covered with

parafilm. The RNA Scope staining procedure was carried out as previously described (5.10 RNA Scope).

For the six- and twelve-month-old mice, the C1 and C3 probes were applied to separate whole mounts. Specifically, the C3 probe (Rab4b) was diluted 1:1500 in probe diluent (323110, RNAscope® Multiplex Fluorescent Detection Reagent VL, ACD BIO, Newark, United States). Additionally, the amplification steps involving HRP-C1/C3 and TSA Vivid Fluorophore 520/570 were performed separately on the two different whole mounts. After RNA Scope staining, immunostaining with Rab4a and Rab4b antibodies was conducted as described previously (5.8 Tissue preparation and immunohistochemistry), beginning with the DSDB blocking step. The same antibodies as those used in cryosection staining were applied (Tab. 22 and 23).

5.11 Microscopy

5.11.1 Otoferlin project

Confocal images were obtained using a Leica Stellaris 5 microscope (Leica; Wetzlar, Germany) with a 40× glycerol immersion objective (NA: 1.25, 2× zoom, laser speed 600) for otoferlin and hair cell imaging, and a 63× glycerol immersion objective (NA: 1.3, 1.4× zoom, laser speed 600) for synapse imaging. The imaging was performed using a white light (485-685 nm) and a diode laser (421 nm) (Used wavelengths: 488 nm (VGlut3, Shank1a), 546 nm (Otoferlin, Ctbp2), and 647 nm (Calretinin). Z-stack images were captured with a step size of 0.3 µm.

Overview images were acquired using a Zeiss Axioplan 2 fluorescence microscope equipped with a 10× (NA: 0.45) or a 20× (NA: 0.8) air objective.

5.11.2 In vitro transduction project

Confocal images were obtained using a Leica Stellaris 5 microscope (Leica; Wetzlar, Germany) with a 10× air objective (NA: 0.3, 1× zoom, laser speed 400) for overview images of the organ of Corti, and a 40× glycerol immersion objective (NA: 1.25, 2× zoom, laser speed 600) for hair cell imaging. The imaging was performed using a white light (485-685 nm) and a diode laser (421 nm) (Used wavelengths: 421 nm (Parvalbumin), 488 nm (AAV-GFP), and 647 nm (antiGFP)). Z-stack images were acquired with a step size of 0.3 µm.

5.11.3 Rab4b project

Confocal images were acquired on a Leica Stellaris 5 microscope (Leica; Wetzlar, Germany) using a 20× glycerol immersion objective (NA: 0.75, 1.4× zoom, laser speed 400) for overview images of the organ of Corti, and a 40× glycerol immersion objective (NA: 1.25, 1× zoom, laser speed 400) for hair cell imaging. The following wavelengths were used: 421 nm (Calretinin, VGlut3), 488 nm (Rab4b- or Rab4a-RNA, depending on the experiment), 546 nm (Rab4a-RNA), and 647 nm (Rab4b or Rab4a proteins, depending on the experiment). Z-stack images were acquired with a step size of 0.3 µm. Overview images of cryosections were captured using a Zeiss Axioplan 2 fluorescence microscope with a 10× (NA: 0.45) or a 20× (NA: 0.8) air objective.

5.12 Data analysis

5.12.1 Otoferlin project

To compare fluorescence intensity, image files were loaded into ImageJ (NIH, Bethesda, MD, USA), and maximum intensity projections were generated. The fluorescence intensity of each inner IHC was calculated using ImageJ. Background

fluorescence was subtracted from the IHC intensity values. Fluorescence results from Otof-p. KL>M animals were compared to the mean fluorescence intensity of the concurrently stained wild-type animals.

Inner and outer hair cells were counted manually. The length of each segment of the organ of Corti (apical or basal) was measured along the IHCs. Inner and outer hair cells were counted if calretinin or Vglut3 staining was positive.

Synapses were counted only when both pre-synaptic (Shank1a and Ctbp2) and post-synaptic markers, as well as the inner hair cell marker (calretinin), were visible.

5.12.2 In vitro experiments

Image files were loaded into ImageJ (NIH, Bethesda, MD, USA), and maximum intensity projections were generated to analyse the transduction rate of each GFP AAV. Inner and outer hair cells were counted manually. Hair cells were considered transduced only if a clear AAV-GFP signal was observable.

5.12.3 Rab4b project

Image files were loaded into ImageJ (NIH, Bethesda, MD, USA), and maximum intensity projections were generated to identify the locations of Rab4b and Rab4a proteins or RNA in the inner ear of wild-type mice.

5.13 Statistical analysis

All data are presented as mean ± SD or SEM. Statistical analysis was performed using Brown-Forsythe and Welch ANOVA tests, followed by Dunnett's T3 multiple comparison test, or 2-way ANOVA followed by Šídák's multiple comparison test. All

calculations were conducted using GraphPad Prism 10 (GraphPad Software, La Jolla, CA, USA). A p-value of ≤ 0.05 was considered statistically significant.

6. Results

6.1 Characterization of the Otof-p. KL>M mouse line

The Otof-p. KL>M mouse line carries a three-base-pair deletion, resulting in the replacement of lysine 824 and leucine 825 with methionine in the C2-FerA domain of otoferlin. To better understand the significance and function of the C2-FerA domain, the Otof-p. KL>M mouse line was characterized through various experiments, including protein structure prediction, hearing measurements, otoferlin immunostaining, proximity ligation assays (PLAs), as well as IHC and OHC quantification.

6.1.1 3D structure prediction of the wild type and Otof-p. KL>M C2-FerA domain.

The pK824L825>M resides in the FerA domain, which is part of the loop region of a (presumed) C2 domain (Fig. 15A). This unconventional C2-domain was first time predicted by Alpha2Fold and RoseTTAFold (Dominguez *et al*, 2022) which however has no obvious lipid-binding or Ca^{2+} binding residues (Harsini *et al*, 2019). However, the four-helix bundle fold has been implicated in Ca^{2+} and phospholipid binding (Harsini *et al*, 2018; Dominguez *et al*, 2022).

To see if the pK824L825>M mutation affects the 3D structure of otoferlin's C2-FerA domain, RoseTTAFold2 server was used to predict the 3D structure of the wild type and mutated C2-FerA domains (Fig. 15B & C). Indeed, the mutation disrupts one a-helix fold of the FerA domain (Fig. 15C) resulting in a longer unstructured loop between a-helix c and a-helix d compared to the wild-type version (Fig. 15B).

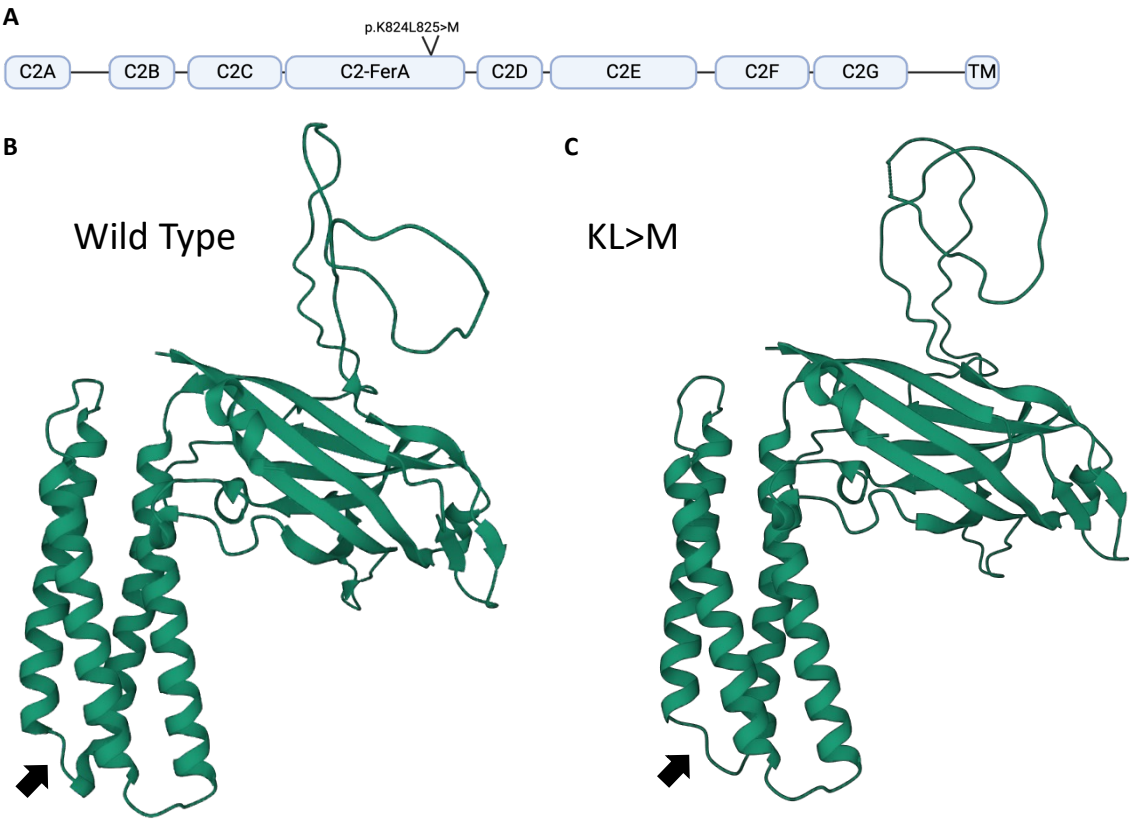

Figure 15 – Experimental plan and 3D structure prediction of the C2-FerA domain. A. Position of the KL>M mutation in the otoferlin sequence. B.-C. 3D structure prediction of the human wild type and KL>M otoferlin C2-FerA domain. Structure prediction was performed by using the RoseTTAFold2 via Neurosnap Inc.

6.1.2 ABRs decline with aging in Otof-p. KL>M mice.

First, to analyse if the Otof-p. KL>M mutation impacts hearing in mice, we performed ABR measurements at three different ages (one, six, and twelve months) and compared them to wild type mice (Fig. 16). Auditory thresholds in response to click or white noise stimuli were not significantly different compared to wild-type mice at one month of age (Fig. 16B & C; thresholds for click stimuli: 23±6 dB SPL for Otof-p. KL>M and 23±2 dB SPL for wild type mice; noise stimuli: 16±6 dB SPL for Otof-p. KL>M and 17±2 dB SPL for wild type mice). Six-month-old Otof-p. KL>M and wild-type mice exhibited no significant difference in response to click and noise stimuli (Fig. 16B & C;

thresholds for click stimuli: 25±5 dB SPL for Otof-p. KL>M and 27±5 dB SPL for wild type mice; noise stimuli: 19±3 dB SPL for Otof-p. KL>M and 18±5 dB SPL for wild type mice). In contrast, at twelve months, Otof-p. KL>M mice revealed a significant threshold shift of ~15 dB SPL in response to click (Fig. 16B) and ~17 dB SPL in response to noise stimuli (Fig. 16C) compared to wild type mice of the same age (thresholds for click stimuli: 47±8 dB SPL for Otof-p. KL>M and 32±4 dB SPL for wild type mice; noise stimuli: 44±8 dB SPL for Otof-p. KL>M and 27±4 dB SPL for wild type mice).

The elevated thresholds were also observable in ABRs elicited by tone burst stimuli of twelve-month-old mice (Fig. 16F), but not in younger mice (Fig. 16D & E). One-month-old Otof-p. KL>M mice exhibited no significant differences in response to any measured frequency compared to wild type. This was also similar in six-month-old mice, with only a small difference at the 16 kHz (Sidak's multiple comparisons test: P = 0.0083) response. For high and low frequencies, some responses were not detectable in six-month-old mice (Fig. 16E). This was also the case in twelve-month-old mice, with even fewer detectable signals in Otof-p. KL>M mice. In mutant mice, no brainstem responses were detectable for 2, 2.8, 22, 32, and 45 kHz in all mice tested. Also, for wild type mice, no responses were collectable at 32 and 45 kHz, however, in contrast to mutants, wild type mice showed signals at lower frequencies (2 and 2.8 kHz; Fig. 16F). In twelve-month-old mice with detectable signals, these were elicited by significantly higher sound pressure levels (Fig. 16F)

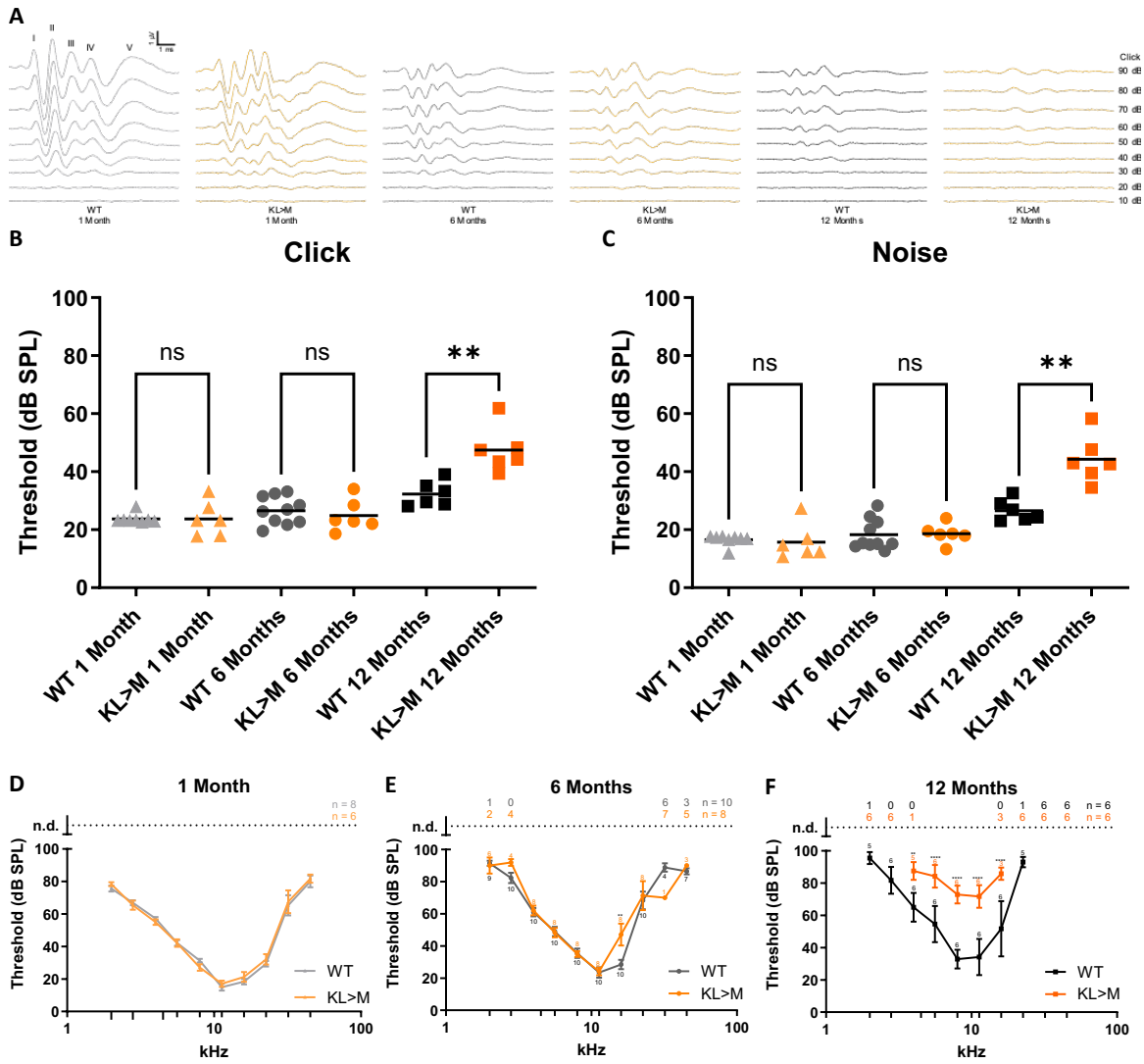

Figure 16 - Auditory brain stem responses of Otof-p. KL>M mice at different ages compared to wild type. A. ABR wave traces in respond to click sound stimuli Otof-p. KL>M compared to wild type in one, six and twelve-month-old mice. **B.** ABR click sound thresholds with 100 µs stimulus. One, six and twelve-month-old Otof-p. KL>M mice compared to wild type mice of the same age. Brown-Forsythe and Welch ANOVA tests followed by Dunnett's T3 multiple comparisons tests: WT vs Otof-p. KL>M 1 month P= >0.999. WT vs Otof-p. KL>M 6 months P = 0.8958. WT vs Otof-p. KL>M 12 months P = 0.0086. **C.** Noise ABR threshold with 1 ms stimulus. One, six and twelve-month-old Otof-p. KL>M mice compared to wild type mice of the same age. Brown-Forsythe and Welch ANOVA tests followed by Dunnett's T3 multiple comparisons tests: WT vs Otof-p. KL>M 1 month P= >0.9823. WT vs Otof-p. KL>M 6 months P = 0.9981. WT vs Otof-p. KL>M 12 months P = 0.0052. **D. – F.** Tone burst ABR threshold for different frequencies. Otof-p. KL>M mice compared to wild type in one (D.) six (E.) and 12 month (F.) old mice. Two-way ANOVA followed by Sidak's multiple comparisons test: C. P = 0.6368, D. P = 0.4845, E. P = <0.0001. The number of the non-detected signals is written above the 100 dB line. Otof-p. KL>M and wild type mice of the same age were measured in pairs on the same day and the same setup.

As described previously, ABR wave amplitudes in response to click stimuli (10-90 dB SPL stimuli) decline over time, particularly in mice with C57BL/6N background which develop significant hearing loss by 6-15 months (Dong *et al*, 2018; Someya *et al*, 2009; Johnson *et al*, 2017). This was indeed the case both for wild-type and Otof-p. KL>M mice (Fig. 17). In addition, we observed a marked reduction of ABR wave amplitudes in Otof-p. KL>M mice already at the age of one month (Fig. 17A & D). Wave I, which is the summed action potentials in the auditory nerve, is significantly lower in Otof-p. KL>M mice at all three age groups (Fig. 17A-C). Additionally, the summed amplitudes of waves II-V are significantly lower in Otof-p. KL>M mice at all three age groups, indicating an altered signal transmission in the auditory pathway, already observable in young mice (Fig. 17 D-F). In contrast to the wave amplitudes, the ABR wave latencies were not different in one-month-old Otof-p. KL>M or wild-type mice, indicating that there is no delay in signal transduction (Fig. 17G).

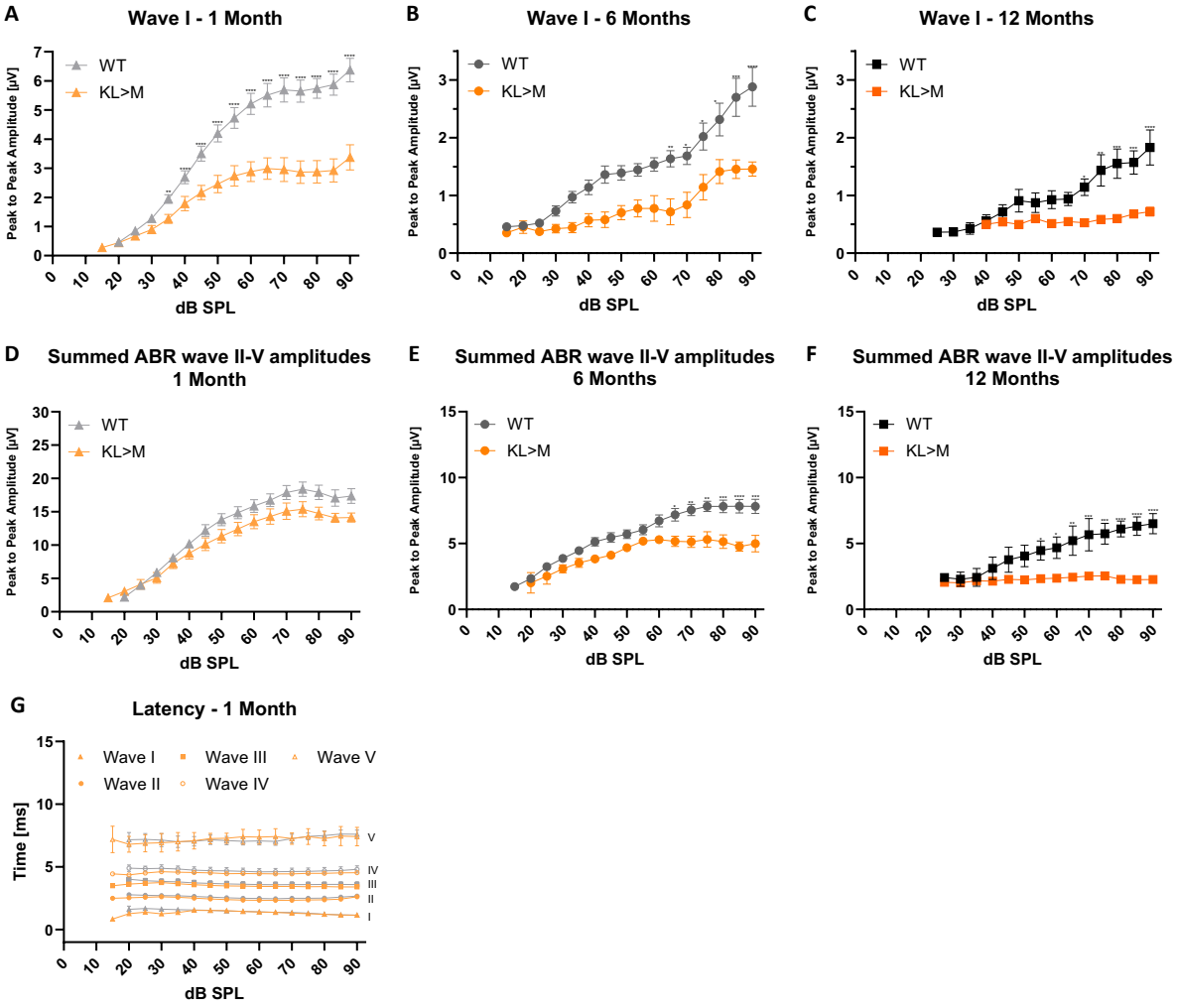

Figure 17 - Wave amplitudes and latencies of click auditory brain stem responses Otof-p. KL>M mice compared to wild type. 100 µm stimuli. **A. – C** Wave I amplitudes in response to 10-90dB SPL click stimuli of one, six and twelve months old Otof-p. KL>M mice compared to wild type. 2way Anova: A. P = <0.0001, B. P = 0.0439, C. P = 0.0092. **D.-F** Summed ABR waves II-IV amplitudes of one, six- and twelve-months old mice. 2way Anova: D. P = 0.6213, E. 0.0609, F. P = 0.0159. **G.** Waves I-V latencies of one-month old mice. G. Wave I P = 0.0679, Wave II P = >0.9999, Wave III P = >0.9999, Wave IV P = 0.9980, Wave V P = 0.7170. Data were analyzed only if waves were detectable.

6.1.3 The Otof-p. KL>M mutation has age dependent effects on the otoferlin levels of IHCs

To determine the otoferlin levels in IHCs, Otof-p. KL>M and wild type organs of Corti were stained at three different ages (one, six, and twelve months) with an anti-otoferlin antibody and an anti-Vglut3 antibody (as an IHC marker). Fluorescence imaging was

performed with the same confocal microscope settings for each wild type – Otof-p. KL>M pair. While the Vglut3 signal seemed not to change, otoferlin levels decreased over time (Fig. 18A). IHCs in one-month-old mice had the same levels of otoferlin, while IHCs of six-month-old Otof-p. KL>M mice had ~15% less and twelve-month-old ones ~23% less otoferlin compared to wild types of the same age (Dunnett's T3 multiple comparisons test: one-month vs six months: P = 0.0099, one-month vs twelve months: P = 0.0002, Fig. 18B).

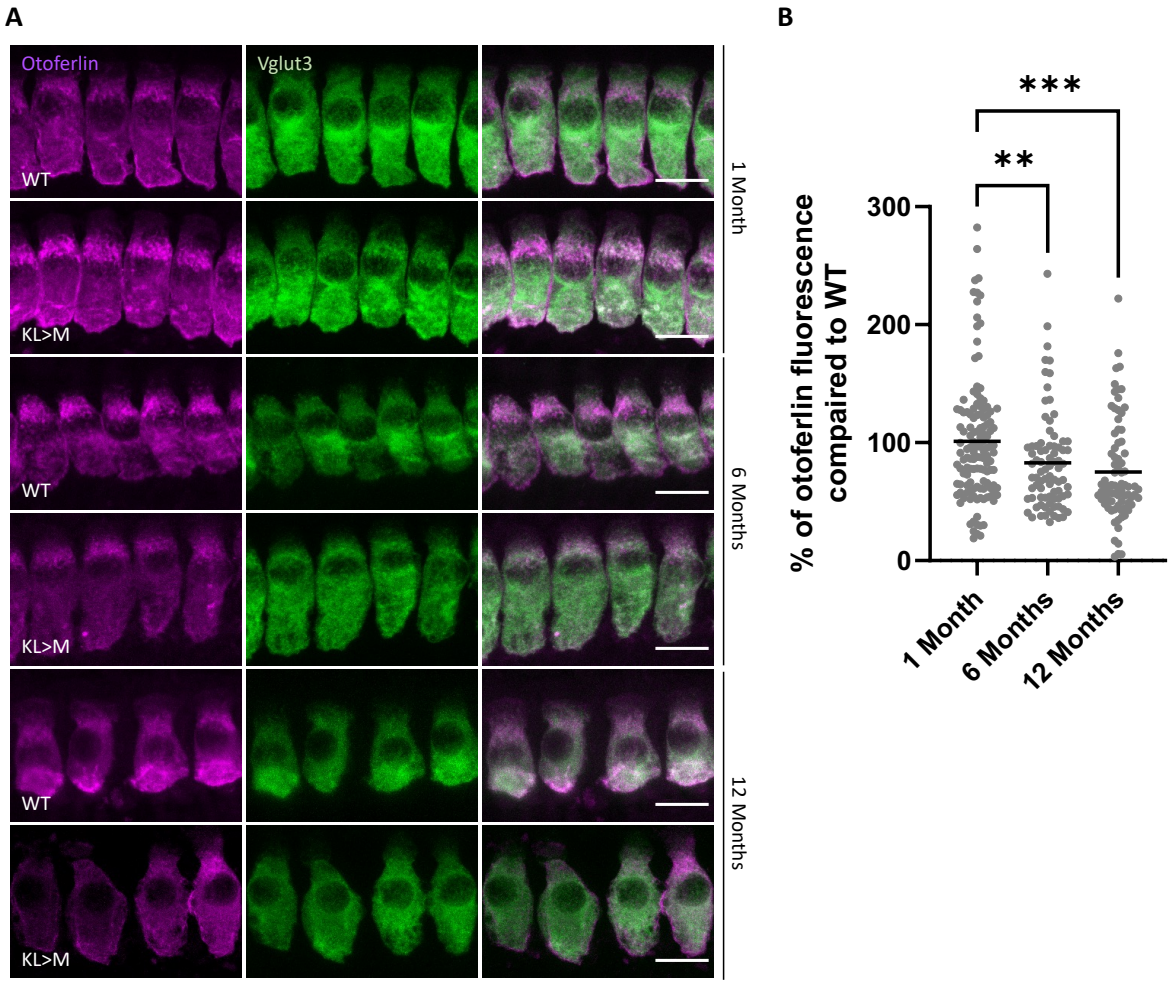

Figure 18 - Otoferlin levels of Otof-p. KL>M mice compared to wild type. A. Otof-p. KL>M Otoferlin and Vglut3 fluorescence compared to wild type. Otoferlin fluorescence and analysis was performed simultaneously in wild type and Otof-p. KL>M mice of the same age. Maximum intensity projections of optical sections. Scale bars: 5 µm. **B.** Relative otoferlin amount in IHCs of one, six- and twelve-months old mice compared to wild type. Otof-p. KL>M organs of Corti were always stained and analyzed together with one wild type sample. The percentage of Otof-p. KL>M otoferlin was calculated in relation to its particular wild type control. The background was subtracted from the mean otoferlin fluorescence. Dunnett's T3 multiple comparisons test: one vs six months P = 0.0313, 1 vs 12 months P = 0.0006.

6.1.4 Otof-p. KL>M mice exhibit an age dependent IHC loss

It is known that *Otof* knockout mice exhibit an increased and age-dependent IHC loss (Stalmann *et al*, 2021). Therefore, we wanted to check if the Otof-p. KL>M mutation is also affecting the IHCs in a similar way. Immunostainings for IHCs and OHCs were

performed and their number counted in both the apical and midbasal/basal regions of the organ of Corti.

Indeed, Otof-p. KL>M mice exhibited an age-dependent alteration in the number of IHCs (Fig. 19). While one-month-old mice demonstrate no significant difference, six- and twelve-month-old Otof-p. KL>M mice have significantly reduced numbers of IHCs. Six-month-old Otof-p. KL>M mice have about eight cells/mm fewer in the apical turn and ~32 cells/mm fewer in the midbasal/basal turn compared to wild type. Twelve-month-old mice revealed an even greater difference in the apical turn with ~16 IHCs/mm fewer and ~27 IHCs/mm fewer in the midbasal/basal part of the organ of Corti compared to wild type organs of the same age. This indicates that the basal part (sensing high frequencies) of the organ of Corti is more affected than the apical part (sensing low frequencies; Fig. 19C-D). In contrast, OHCs numbers did not exhibit any significant differences at any age (Fig. 19E).

Similar to the otoferlin levels, the number of IHCs was significantly lower compared to wild type mice, but only in older mice (six- and twelve-month-old, Fig. 19C & D). This indicates that the loss of IHCs could contribute to the threshold shift and the ABR wave amplitude decline observed in the ABR measurements (Fig. 16 & 17).

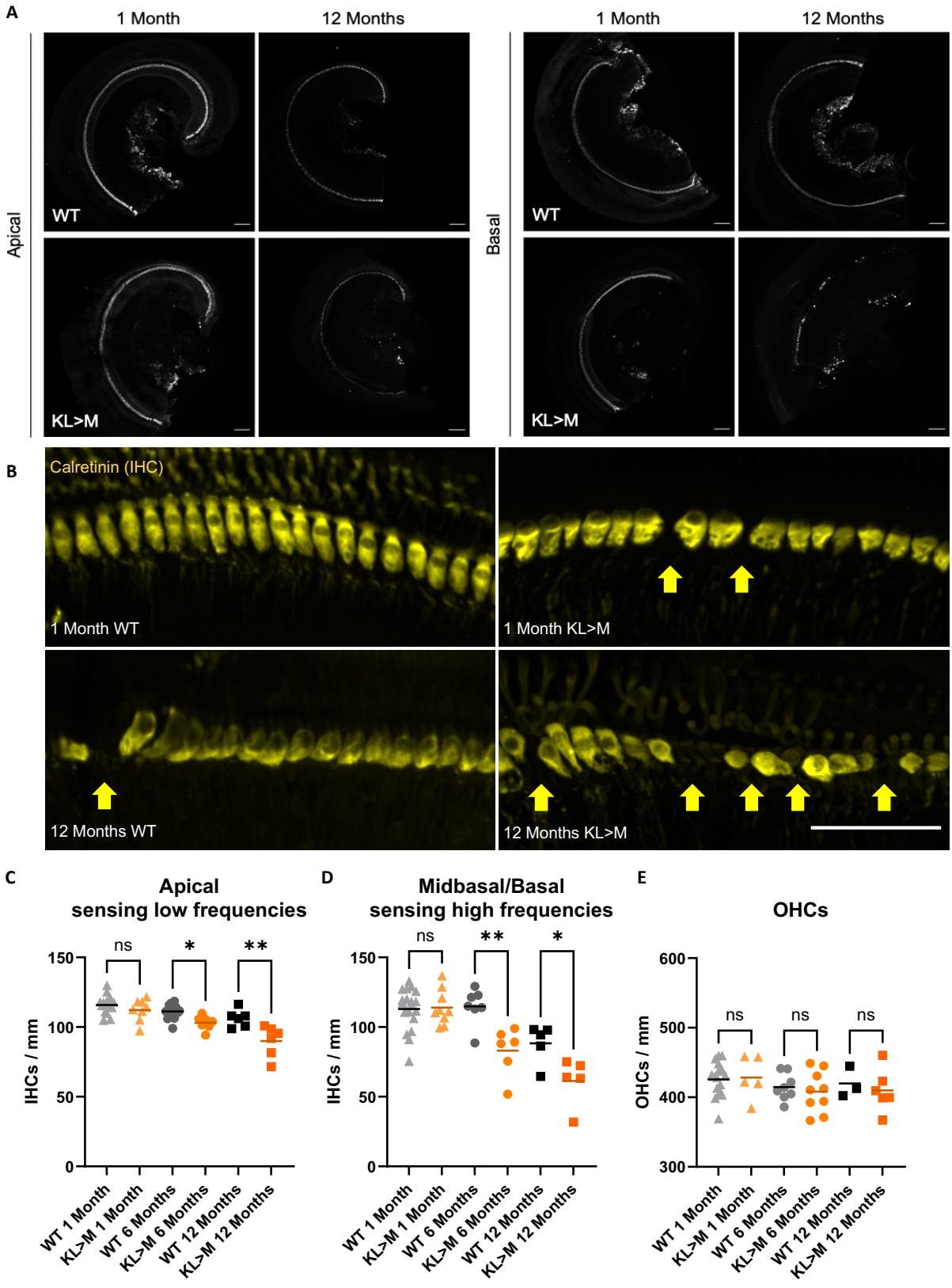
A
1 Month
12 Months
1 Month
12 Months
Apical
Basal
WT
KL>M
WT
KL>M
B
Calretinin (IHC)
1 Month WT
1 Month KL>M
12 Months WT
12 Months KL>M
C
Apical
sensing low frequencies
IHCs / mm
150
100
50
0
ns
*
**
WT 1 Month
KL>M 1 Month
WT 6 Months
KL>M 6 Months
WT 12 Months
KL>M 12 Months
D
Midbasal/Basal
sensing high frequencies
IHCs / mm
150
100
50
0
ns
**
*
WT 1 Month
KL>M 1 Month
WT 6 Months
KL>M 6 Months
WT 12 Months
KL>M 12 Months
E
OHCs
OHCs / mm
600
500
400
300
ns
ns
ns
WT 1 Month
KL>M 1 Month
WT 6 Months
KL>M 6 Months
WT 12 Months
KL>M 12 Months

Figure 19 - IHC and OHCs loss of Otof-p. KL>M mice compared to wild type. A. Calretinin IHC staining in Otof-p. KL>M and wild type organs of Corti. Otof-p. KL>M and wild type mice of the same age were simultaneously stained with an anti-calretinin antibody. Maximum intensity projections of optical sections. Scale bars: 10 µm. **B.** Calretinin IHC staining at higher magnification. One- and twelve-months old Otof-p. KL>M and wild type were simultaneously stained with an anti-calretinin antibody. Maximum intensity projections of optical sections. Scale bars: 5 µm. Yellow arrows indicate missing IHCs. **C.** Number of IHCs of the organ of Corti apical part in Otof-p. KL>M and wild type mice of different ages. IHCs were counted after calretinin staining. Sidak's multiple comparison test: 1 month P = 0.6147, 6 months P = 0.0368, 12 months P = 0.0011. **D.** Number of IHCs of the organ of Corti midbasal/basal part in Otof-p. KL>M and wild type mice of different ages. Sidak's multiple comparison test: 1 month P = 0.8697, 6 months P = 0.0039, 12 months P = 0.0397. **E.** Number of outer hair cells of the organ of Corti (pooled results of apical, midbasal and basal part) in KL>M and wild type mice of different ages. Outer hair cells were counted after calretinin staining. Sidak's multiple comparison test: 1 month P = 0.9997, 6 months P = 0.9618, 12 months P = 0.9993.

6.1.5 Otof-p. KL>M show normal DPOAE thresholds.

DPOAE measurements were performed, and the thresholds were analysed (Fig. 20). Here, we did not observe any significant difference in the DPOAE thresholds at any frequency stimulus response (Fig. 20A-C). This also fits with the not altered number of OHCs in the organ of Corti (Fig. 19E) and indicates that the OHC function is not affected by the Otof-p. KL>M mutation.

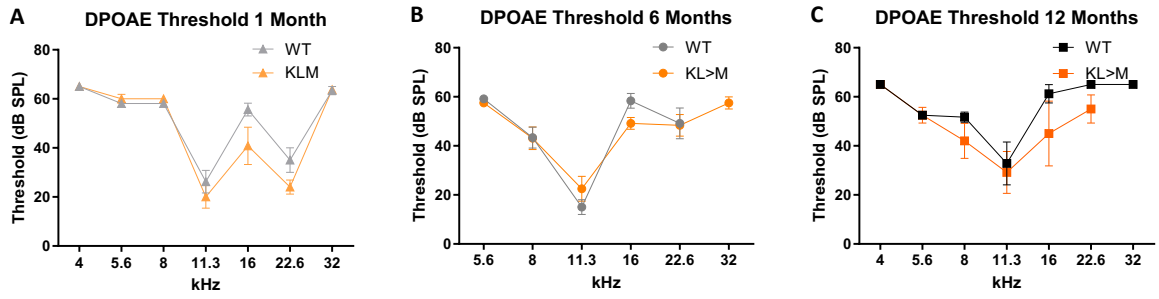

Figure 20 – DPOAE threshold in Otof-p. KL>M mice compared to wild-types. A. DPOAE thresholds of one month old Otof-p. KL>M and wild type mice. Two-way ANOVA: P = 0.3137. **B.** DPOAE thresholds of six months old Otof-p. KL>M and wild type mice. Two-way ANOVA: P = 0.7694. **C.** DPOAE thresholds of twelve months old Otof-p. KL>M and wild type mice. Two-way ANOVA: P = 0.1238.

6.1.6 Twelve-month-old mice have a reduced number of IHC synapses

Otoferlin plays a critical role in the function of IHC synapses and is also important for proper synapse maturation (Stalmann *et al*, 2021). To test if the pK824L825>M mutation alters synapse numbers and structure, immunostainings for post- and presynapses of organ of Corti IHCs were performed in one-, six-, and twelve-month-old Otof-p. KL>M and wild type mice (Fig. 21A).

While each IHC of one- and six-month-old Otof-p. KL>M mice formed on average 14 and 13 synapses, respectively, with no difference compared to wild types of the same age, twelve-month-old Otof-p. KL>M IHCs had about ~one synapse fewer than wild type IHCs (Fig. 21B). Interestingly, twelve-month-old wild type mice seemed to have a higher number of synapses compared to six-month-old wild types. As this appeared very untypical, also the number of low-synapse IHCs was examined (IHCs with fewer than ten synapses; Tab. 24).

Otof-p. KL>M mice revealed a higher percentage of low-synapse IHCs at all three age groups. One-month-old mice had around 6% (individual experiments: 23%, 0%, 0%, 0%), six-month-old mice had 21% (individual experiments: 5%, 53%, 2%, 23%), and twelve-month-old mice had 28% (individual experiments: 18%, 83%, 11%, 0%) low-synapse IHCs. In contrast, one-month-old wild type mice had around 2% (individual experiments: 2%, 2%, 5%, 0%) low-synapse IHCs. The percentage increased in six-month-old mice to 16% (individual experiments: 6%, 26%, 0%, 2%, 46%) but decreased again to 8% (individual experiments: 10%, 7%, 8%) in twelve-month-old mice, indicating that many of the low-synapse IHCs likely die between the age of six and twelve months. However, it must be mentioned that the individual experiments showed often high variability.

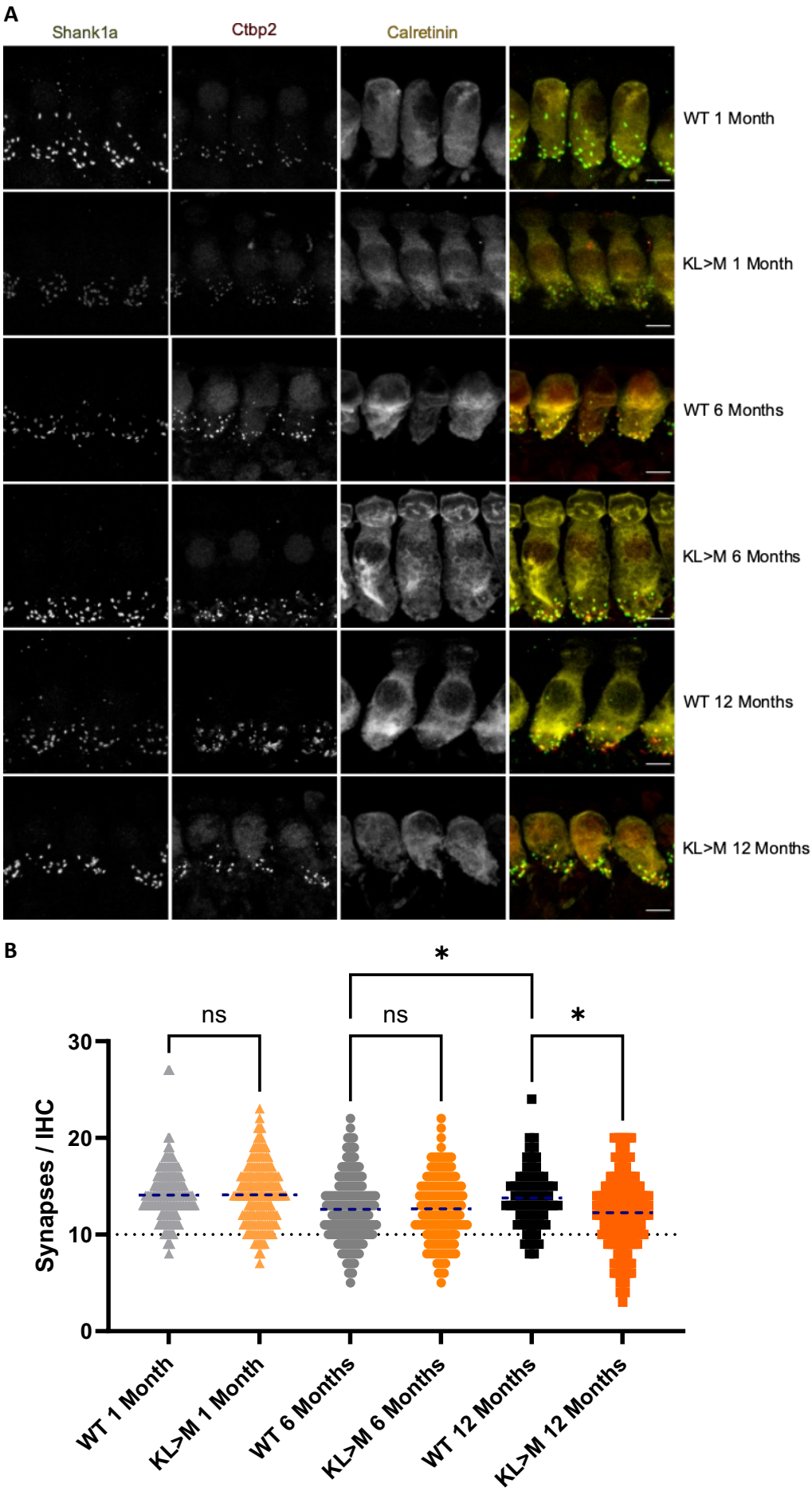
A
Shank1a
Ctbp2
Calretinin
WT 1 Month
KL>M 1 Month
WT 6 Months
KL>M 6 Months
WT 12 Months
KL>M 12 Months
B
*
ns
ns
*
Synapses / IHC
30
20
10
0
WT 1 Month
KL>M 1 Month
WT 6 Months
KL>M 6 Months
WT 12 Months
KL>M 12 Months

Figure 21 - Synapses of Otof-p. KL>M mice inner hair cells. A. Inner hair cell synapse staining of Otof-p. KL>M and wild type in one-, six- and twelve-month-old mice. Shank1a was used as a postsynaptic marker, Ctbp2 as a presynaptic marker and calretinin for the inner hair cell staining. Scale bars: 5 µm. **B.** Number of synapses stained in A of Otof-p. KL>M compared to wild type in one-, six- and twelve-month-old mice. Synapses were counted only if Shank1a was found adjacent to Ctbp2 spots and both were located within the calretinin-labelled IHCs. Kruskal-Wallis test followed by Dunn's multiple comparisons test: 1 month P = >0.9999, 6 months P = >0.9999, 12 months P = 0.0099. WT 6 months and WT 12 Months P = 0.0356.

Table 24 - Low synapse number cells in wild type and Otof-p. KL>M mice.

	1 Month		*6 Months*		*12 Months*	
	WT(n=4)	KL>M(n=4)	WT(n=5)	KL>M(n=4)	WT(n=3)	KL>M(n=3)
Total number of analysed cells	162	200	210	150	69	189
Number of low synapse number cells	4	10	33	29	6	41
% of low synapse number cells	2%	6%	16%	21%	8%	28%

6.1.7 Otof-p. KL>M mice show altered otoferlin/calbindin interaction

Ca^{2+} influx can be triggered in vitro by bathing the explanted organ of Corti tissue in a solution with high K^{+}. Thereby the cells depolarize and activate voltage gated Ca^{2+} channels, which in turn actives Ca^{2+} dependent kinases that phosphorylate otoferlin. Moreover, phosphorylated otoferlin augments the binding to calbindin (Meese *et al*, 2017; Cepeda *et al*, 2019). To determine if there is a difference in the otoferlin-calbindin interaction in Otof-p. KL>M mice compared to wild types, a PLA assay using antibodies

targeting the two proteins was performed (Fig. 22A). Interestingly, while there was no significant difference in fluorescence intensity between wild-type and Otof-p. KL>M IHCs under resting conditions (1 min in HBSS at 37°C), a significant decrease in fluorescence intensity was observed in Otof-p. KL>M IHCs under stimulation conditions (1 min in high K^+ HBSS at 37°C; Fig. 22B). This suggests that the mutation in the FerA domain may interfere with phosphorylation and calbindin binding in IHCs during stimulation.

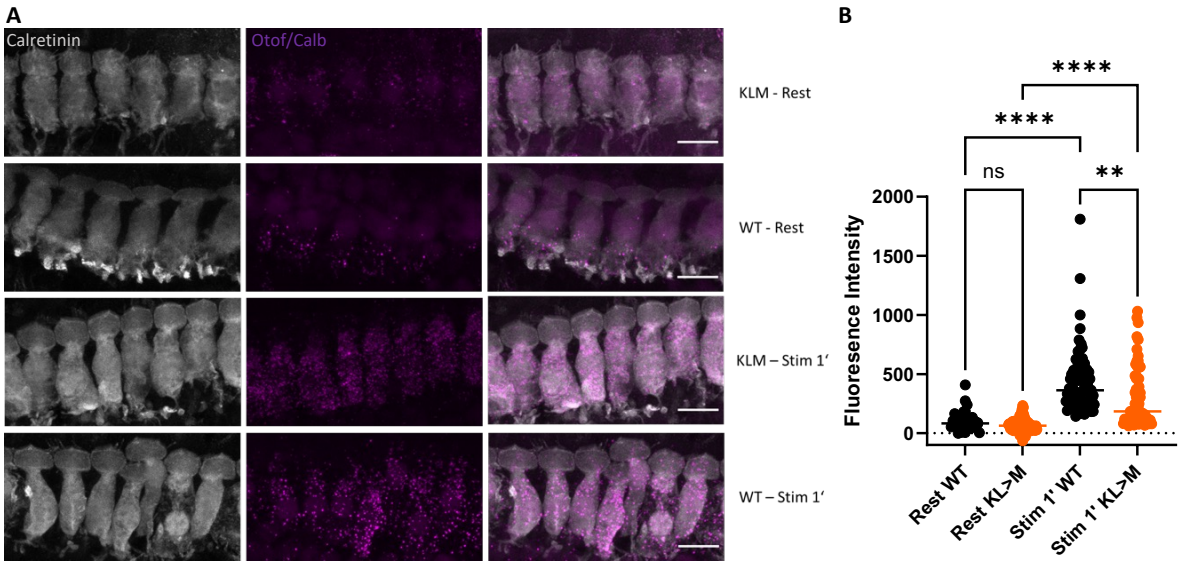

Figure 22 - Otoferlin/Calbindin proximity ligation assay on Otof-p. KL>M and wild type mice. A. PLA assay of Otoferlin/Calbindin interaction in IHCs of Otof-p. KL>M and wild type mice at P14-16. Calretinin antibody was used as an IHCs marker. Maximum intensity projections of optical sections. Scale bars: 10 µm. **B.** Otof/Calb PLA fluorescence intensity in Otof-p. KL>M and wild type IHCs in Rest and Stim 1' conditions. The background was subtracted from the mean Otof/Calb fluorescence. Sidak's multiple comparisons test: Rest WT vs Rest KL>M P = 0.8690, Rest WT vs Stim 1' WT P = <0.0001, Rest KL>M vs Stim 1' KL>M P = <0.0001, Stim 1' WT vs Stim 1' KL>M P = 0.0025.

6.2 AAV production optimization

To establish and optimize small-scale AAV production, various methods were tested across multiple production steps. These included different cell types for transfection, transfection reagents and methods, transfection duration, as well as two distinct purification approaches (Fig. 23). All experiments were conducted using the AAV6-GFP construct.

In the initial step of AAV production, two different HEK cell lines were evaluated: the standard HEK293T cells and the AAV-293 cell line, which is optimized for AAV packaging. The AAV-293 cells express E1 in trans, enabling AAV production using E1-deleted adenovirus vectors or a three-plasmid AAV helper-free system. Both cell lines exhibited high viral titers, with $1.38*10^{13}\pm2.9*10^{12}$ VG/mL in AAV-293 cells and $1.48*10^{13}\pm3.6*10^{12}$ VG/mL in HEK293T cells, demonstrating their suitability for transfection (Fig. 23A). However, all subsequent AAV productions were performed using AAV-293 cells due to their lower passage number and more recent cultivation compared to HEK293T cells.

Similarly, transfection optimization yielded high viral titers (Fig. 23B). The commercially available transfection reagent Turbofect resulted in $1.38*10^{13}\pm2.9*10^{12}$ VG/mL, whereas the calcium phosphate method achieved $1.73*10^{13}\pm2.8*10^{12}$ VG/mL. All further AAV productions were conducted using the calcium phosphate transfection method, as it offers comparable efficiency, ease of use, and lower costs compared to commercial reagents.

The optimal duration of transfection to AAV vector collection was also evaluated. Collecting vectors after 48 hours resulted in a higher concentration ($1.73*10^{13}\pm2.8*10^{12}$ VG/mL) compared to collection after 72 hours ($8.54*10^{13}\pm2.3*10^{12}$ VG/mL) (Fig. 23C).

To further optimize AAV production, different transfection strategies were tested. The pDGM plasmid, which contains the rep, cap, and helper genes necessary for AAV production, enabled the comparison of triple and double transfection approaches. Specifically, the AAV6 capsid gene in the pDGM6 plasmid was replaced with the PHP.B capsid gene. PHP.B vector production was performed using both the three-plasmid system (transgene plasmid [pXS11, GFP construct], pAAV-PHP.B Rep/Cap plasmid, and pAd-Helper plasmid) and the newly cloned pDGM-PHP.B vector in combination with the transgene plasmid (pXS11, GFP construct). Surprisingly, the triple transfection method resulted in a higher viral titer ($4.14*10^{11}\pm2.51*10^{11}$ VG/mL) compared to the double transfection method ($1.37*10^{11}\pm1.1*10^{10}$ VG/mL; Fig. 23 D). Consequently, triple transfection was used for all PHP.B and PHP.eB productions, while AAV6 production relied on double transfection due to the availability of only the pDGM6 plasmid.

Next, two harvesting methods were compared: the freeze-thaw method (several cycles of freezing in liquid nitrogen followed by thawing in a 37°C water bath) and sonication (five minutes in a sonication water bath). Sonication resulted in a slightly higher titer ($2.17*10^{13}\pm3.5*10^{12}$ VG/mL) compared to the freeze-thaw method ($1.38*10^{13}\pm2.9*10^{12}$ VG/mL; Fig. 23E). Sonication was preferred for subsequent productions due to its ease of use and reduced impact on viral integrity.

Additionally, two purification methods were evaluated: iodixanol gradient purification and affinity chromatography using the AAVX POROS column. The iodixanol gradient

method (performed by MD student Niklas Keppeler) resulted in an ~97% loss of AAV particles, indicating inefficiency for small-scale AAV production (Fig. 23F). In contrast, affinity chromatography purification was assessed by measuring the concentrations of three AAV capsids before and after purification. The purified and unpurified AAV6 samples exhibited similar titers ($6.15*10^{10}\pm7.72*10^{10}$ VG/mL unpurified and $7.45*10^{10}\pm9.77*10^{10}$ VG/mL purified, Fig. 23G), indicating no significant loss as the solutions were concentrated to the same volume (~150 µL). However, for PHP.B vectors, the unpurified sample had a titer of $4.10*10^{12}\pm1.8*10^{11}$ VG/mL, whereas the purified solution contained $5.51*10^{11}\pm1.82*10^{11}$ VG/mL, corresponding to an overall loss of ~87% (at same volume of ~150 µL). Interestingly, the opposite trend was observed for PHP.eB vectors, where the purified sample exhibited a higher titer ($2.95*10^{11}\pm3.95*10^{11}$ VG/mL) than the unpurified sample ($4.07*10^{11}\pm5.2*10^{10}$ VG/mL; Fig. 23G). It should be noted that the unpurified solution could not be concentrated to the same volume as the purified sample, which explains the higher concentration in the purified sample (same number of viral genomes result to lower titer with increasing volume). Despite the feasibility of purification using the AAVX column, AAVs intended for in vitro experiments were not purified to maintain higher concentrations, which were necessary for experimental procedures.

The final step in AAV production was concentration, performed using a 100 kDa Amicon Ultra Centrifugal Filter tube. To assess potential AAV particle loss during this step, AAVs were harvested and resuspended in ~150 µL PBS or diluted to 15 mL before being concentrated back to ~150 µL via centrifugation using the filter unit. Both methods yielded comparable titers ($6.26*10^{12}\pm6.2*10^{11}$ VG/mL before concentration and $6.26*10^{12}\pm9.1*10^{11}$ VG/mL after concentration; Fig. 23H), indicating that the

concentration filter unit effectively concentrates AAV solutions while removing residual contaminants such as proteins or other particles.

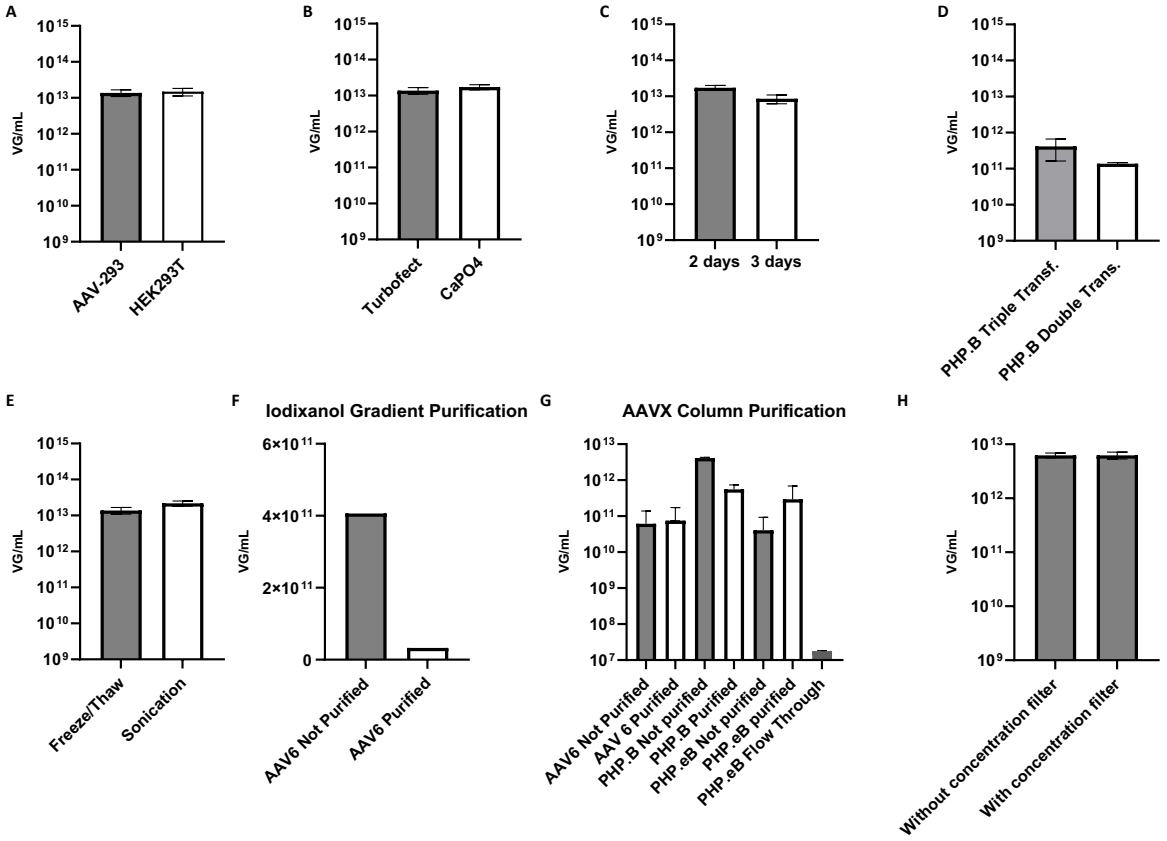

Figure 23 - RT-PCR results of each AAV production optimization step. A. AAV6-GFP titer two days after transfection inAAV293 and HEK293T cells. **B.** AAV6-GFP titer two days after transfection with the Turbofect transfection reagent and the $CaPO_4$ transfection method in AAV-293 cells. **C.** AAV6-GFP titer, two and three days after $CaPO_4$ transfection in AAV-293 cells. **D.** PHP.B-GFP titer two days after triple and double $CaPO_4$ transfection. **E.** AAV6-GFP titer two days after $CaPO_4$ transfection with the freeze/thaw and the sonication harvesting method. **F.** AAV6-GFP titer before and after purification with the iodixanol gradient purification method (Data kindly provided by MD student Niklas Keppeler). **G.** AAV6-GFP, PHP.B-GFP and PHP.eB-GFP titer before and after affinity chromatography purification with the AAVX Poros column. **H.** AAV6-GFP titer before and after using the 100 kDa Amicon Ultra Centrifugal Filter for AAV concentration. Error bars represent the standard deviation.

6.3 AAV in vitro transduction in the organ of Corti

Gene therapy for the inner ear is receiving increasing attention, with the first patients already treated using an AAV-based gene therapy approach targeting mutations in the

OTOF gene. However, there remains significant potential for improvement. Not only in the field of hearing research but also in other biomedical areas, efforts are underway to develop AAV variants with enhanced transduction efficiency in target tissues and cells.

In the context of *OTOF* gene therapy, the primary target cells in the inner ear are the sensory cells of the organ of Corti, specifically the inner hair cells (IHCs) and outer hair cells (OHCs). This study introduces a novel in vitro method to assess the transduction efficiency of different AAV variants in the organ of Corti. In this approach, organs of Corti are cultured in cell culture insert wells and transduced with the AAVs of interest. Three days post-transduction, the tissue is stained to evaluate the efficiency of the viral vectors.

The objective of this method is to serve as a pre-screening tool to identify the most effective AAV variant (in terms of transduction rate, specificity, etc.) before proceeding to in vivo experiments. This approach offers three major advantages: it reduces the number of animals required, is less time-consuming than in vivo studies, and is relatively simple to perform.

6.3.1 In vitro transduction with AAV6, PHP.B and PHP.eB

In order to see if the new in vitro method works, proof of concept experiments was first required. To achieve this, three different AAVs carrying GFP as a reporter were produced. For these initial experiments, the AAV6 variant (used in previous in vivo studies by Al-Moyed *et al*, 2019), as well as the AAV9-derived variants PHP.B and PHP.eB (which are known to be efficient in the inner ear), were selected.

To verify the functionality of the produced AAVs, they were tested on HEK293T cells. The cells were plated in culture insert wells, as described earlier for the organ of Corti (Chapter 5.7), using the same medium volume and an equal number of viral particles ($1x10^{10}$ VG). Staining of the cells revealed that the GFP-AAVs were indeed able to successfully transduce HEK293T cells (Fig. 24).

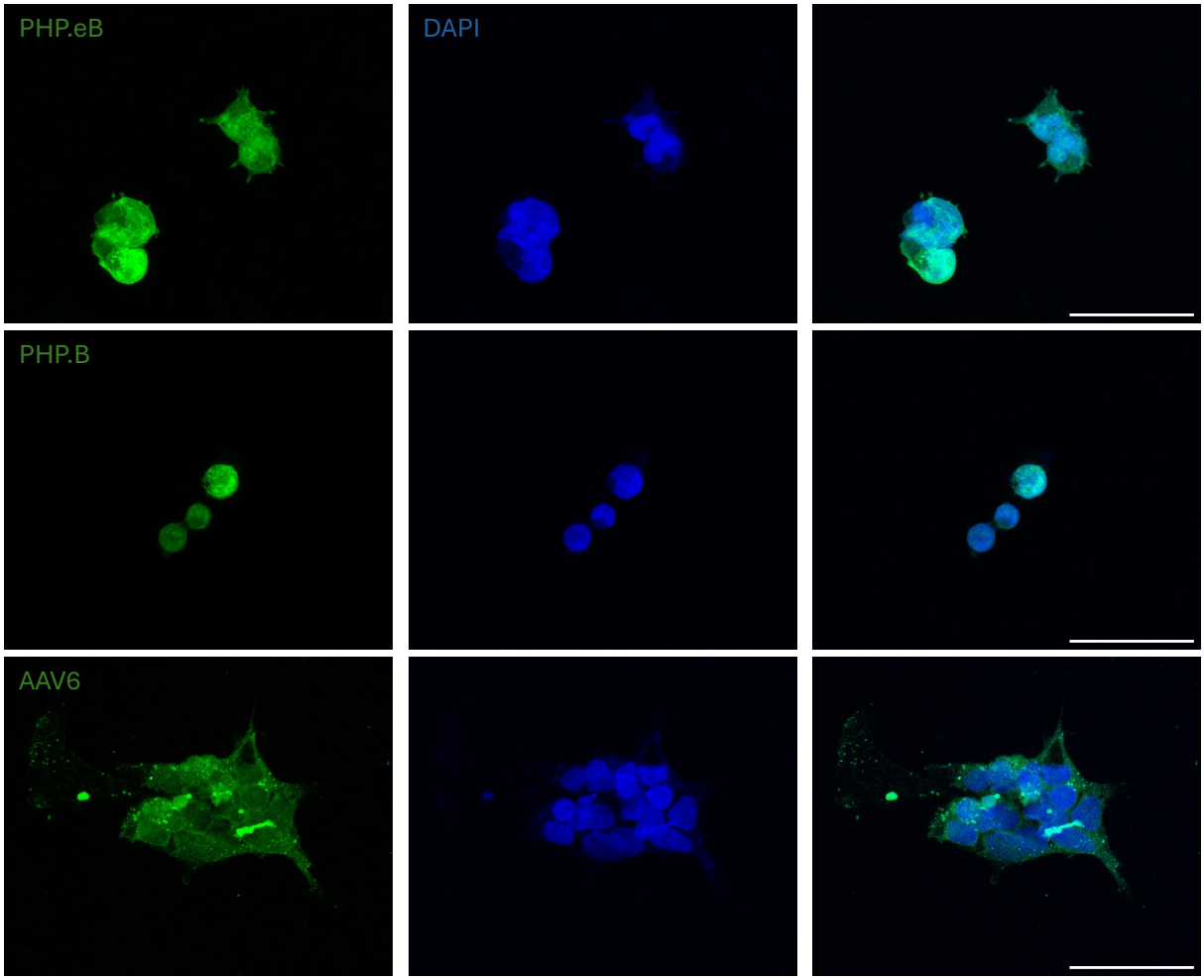

Figure 24 - AAV6-GFP, PHP.B-GFP and PHP.eB-GFP transduction on HEK cells. All three serotypes (AAV6, PHP.B and PHP.eB) were able to transduce HEK cells in which GFP was expressed after transduction. Cells were fixed 72 h after AAV addition and stained with DAPI for easier localization. Maximum intensity projections of optical sections. Scale bars 50 µm.

Next, the three AAV variants were tested in in vitro cultures of mouse organs of Corti, and the transduction rate in IHCs and OHCs was determined.

AAV6-GFP successfully transduced both IHCs and OHCs. However, the GFP signal was not limited to the sensory cells. Notably, high signal intensity was observed in the stria vascularis (Fig. 25). The transduction rate in IHCs was relatively low, with 6.44 ± 1.77% in the apical turn and 19.4 ± 8.2% in the midbasal turn (Fig. 29A). Similarly, OHCs exhibited a higher transduction rate in the midbasal turn at 29.4 ± 7.4%, while in the apical turn, it was 13.8 ± 7.1% (Fig. 29B).

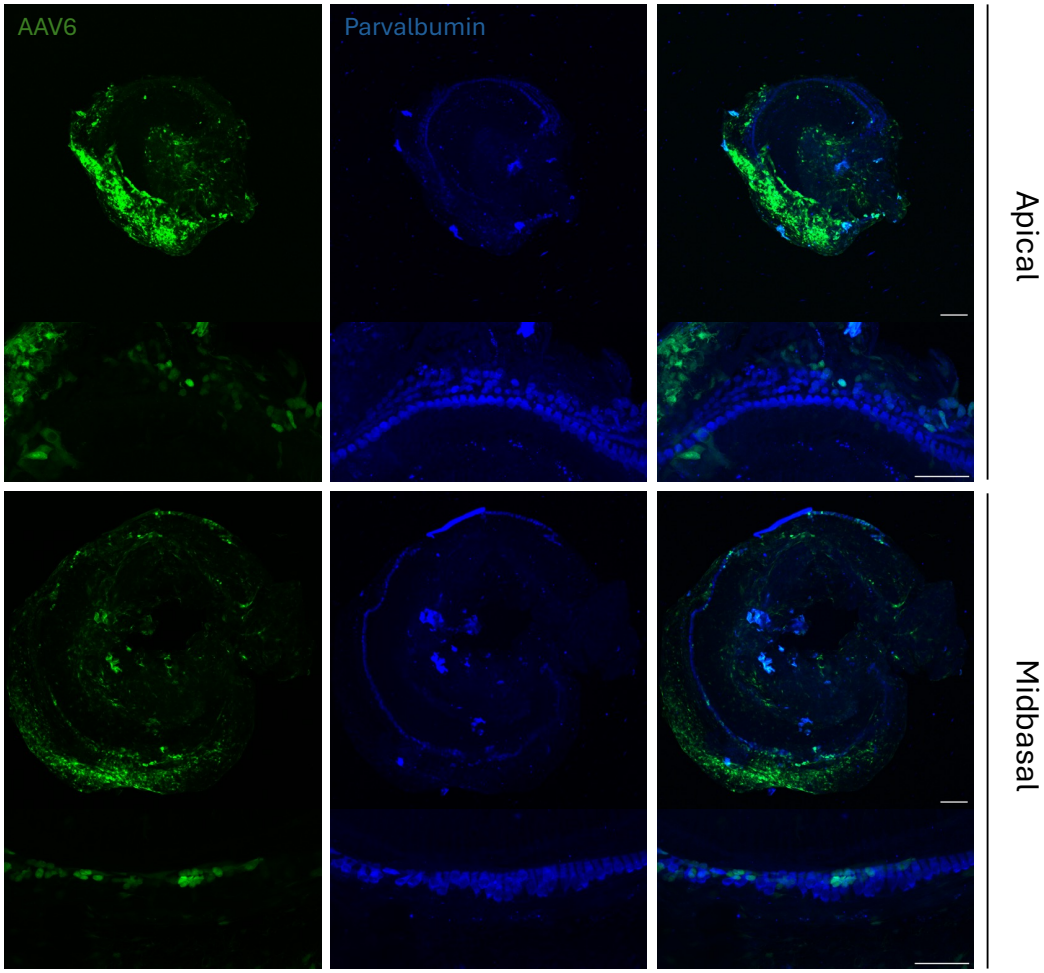

Figure 25 - AAV6-GFP in vitro transduction on P7 wild type organ of Corti. AAV6-GFP transduced IHCs and OHCs with low transduction rates. The stria vascularis shows also high GFP expression. The transduction was distributed all over the organ of Corti. The

apical and midbasal turns of the organ of Corti were fixed 72 h after AAV addition and stained against parvalbumin for IHCs and OHCs localization. Maximum intensity projections of optical sections. Scale bars 100 µm for organ of Corti overview image and 50 µm for IHCs and OHCs image.

The AAV9-derived variant PHP.B was also able to transduce both IHCs and OHCs. Unlike AAV6, this variant did not show any GFP signal in the stria vascularis. However, the signal was still not confined to the sensory cells (Fig. 26). The transduction rates in IHCs and OHCs were higher compared to AAV6. Interestingly, while the transduction rates were very similar in the apical turn between IHCs and OHCs, in the midbasal turn, the rate was higher in OHCs. In the apical turn, the transduction rate was 54.9 ± 20.3% in IHCs and 53.0 ± 18.1% in OHCs. In the midbasal turn of the organ of Corti, a transduction rate of 37.9 ± 20.2% was observed in IHCs and 69.0 ± 26.8% in OHCs (Fig. 29).

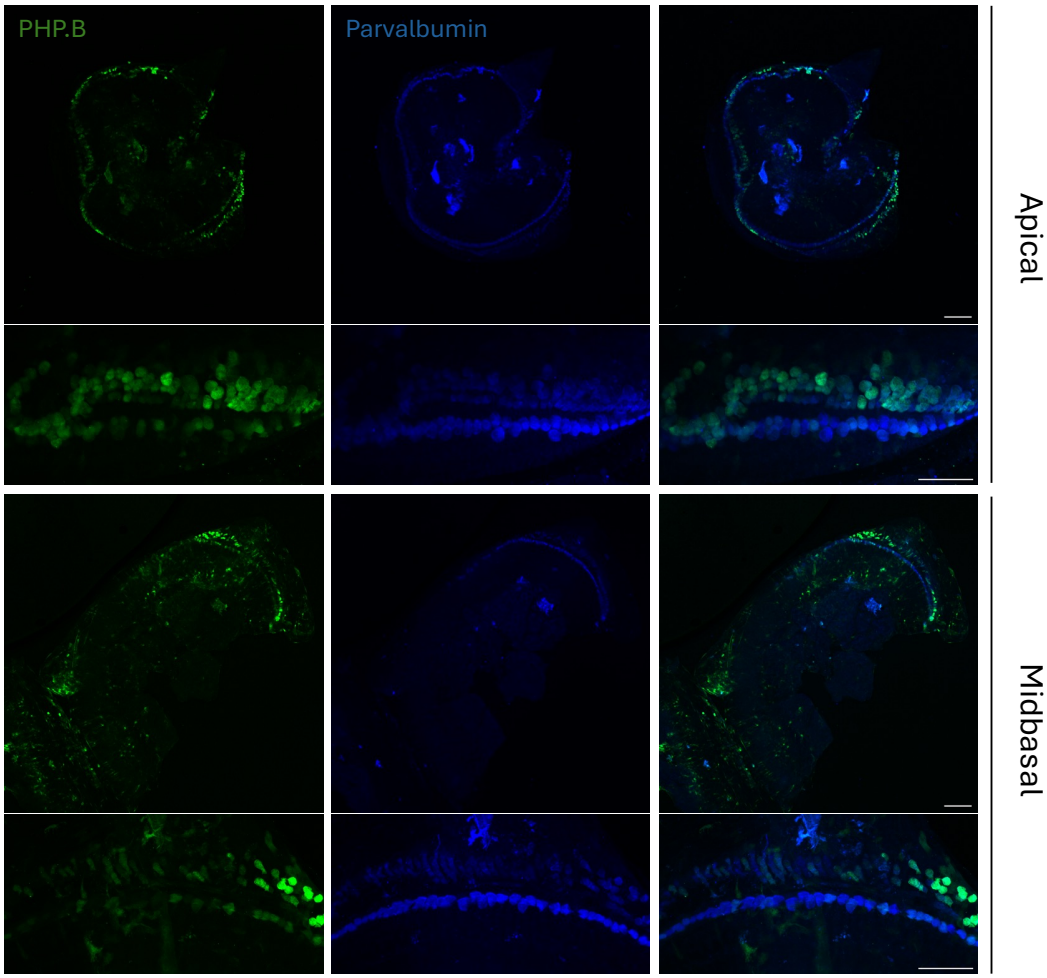

Figure 26 - PHP.B-GFP in vitro transduction on P7 wild type organ of Corti. PHP.B-GFP transduced IHCs and OHCs with higher transduction rates in OHCs. GFP expression is also observable in the SGNs region of the organ of Corti. The apical and midbasal turn of the organ of Corti were fixed 72 h after AAV addition and stained with antibodies against parvalbumin for IHCs and OHCs localization. Maximum intensity projections of optical sections. Scale bars 100 µm for organ of Corti overview image and 50 µm for IHCs and OHCs image.

Like the other two variants, PHP.eB was able to transduce both IHCs and OHCs. Interestingly, the GFP signal was restricted to the sensory cells (Fig. 27). Compared to the other variants, PHP.eB demonstrated the highest transduction rates in the sensory cells, both in the apical and midbasal turns. In IHCs, PHP.eB achieved a transduction rate of 79.0 ± 11.6% in the apical turn and 93.8 ± 10.8% in the midbasal

turn (Fig. 29A). Similarly, OHCs showed very high transduction rates, with 82.4 ± 14.3% in the apical turn and 94.2 ± 4.3% in the midbasal turn (Fig. 29B).

As expected, the control organs (treated with sterile PBS) showed no GFP signal (Fig. 28).

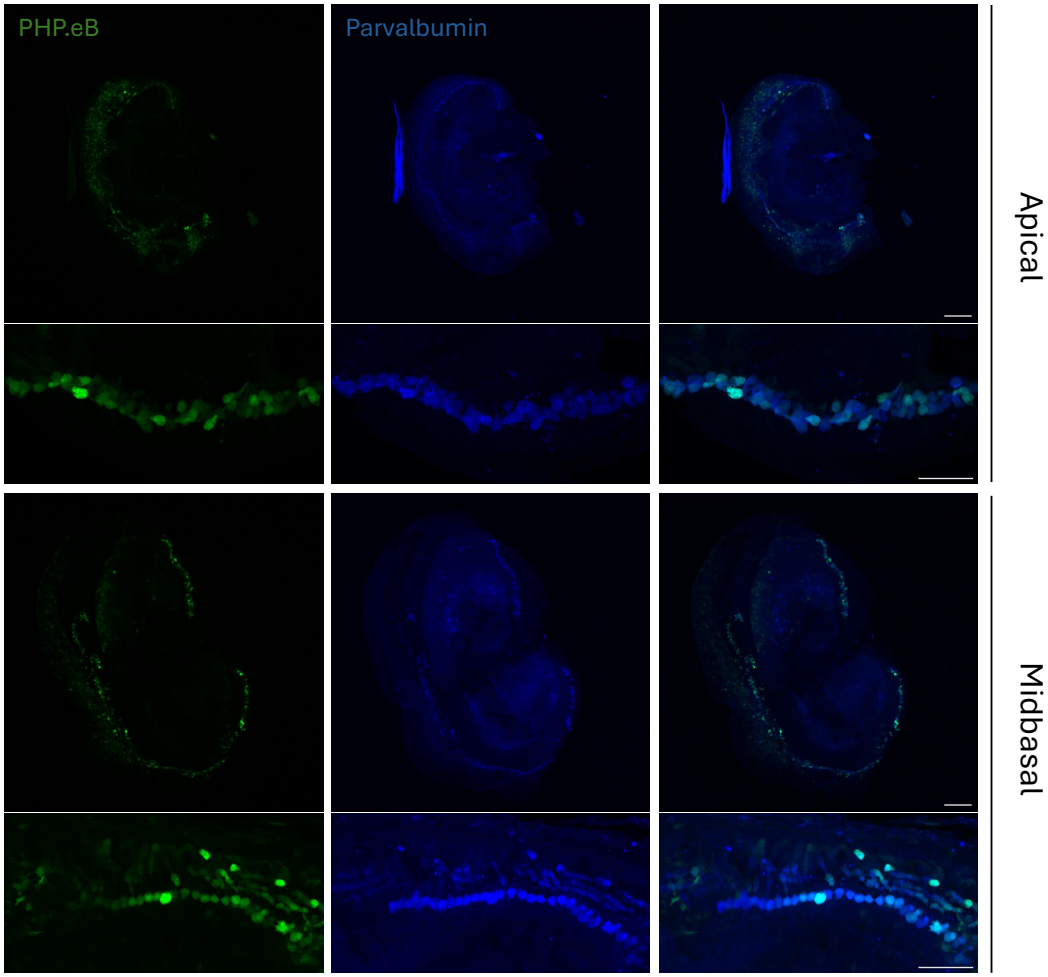

Figure 27 - PHP.eB -GFP in vitro transduction on P7 wild type organ of Corti. PHP.B-GFP successfully transduced IHCs and OHCs with very high transduction rates >95%. The signal was mainly restricted to the hair cells. The apical and midbasal turn of the organ of Corti were fixed 72 h after AAV addition and stained with antibodies against parvalbumin for IHCs and OHCs localization. Maximum intensity projections of optical sections. Scale bars 100 µm for organ of Corti overview image and 50 µm for IHCs and OHCs image.

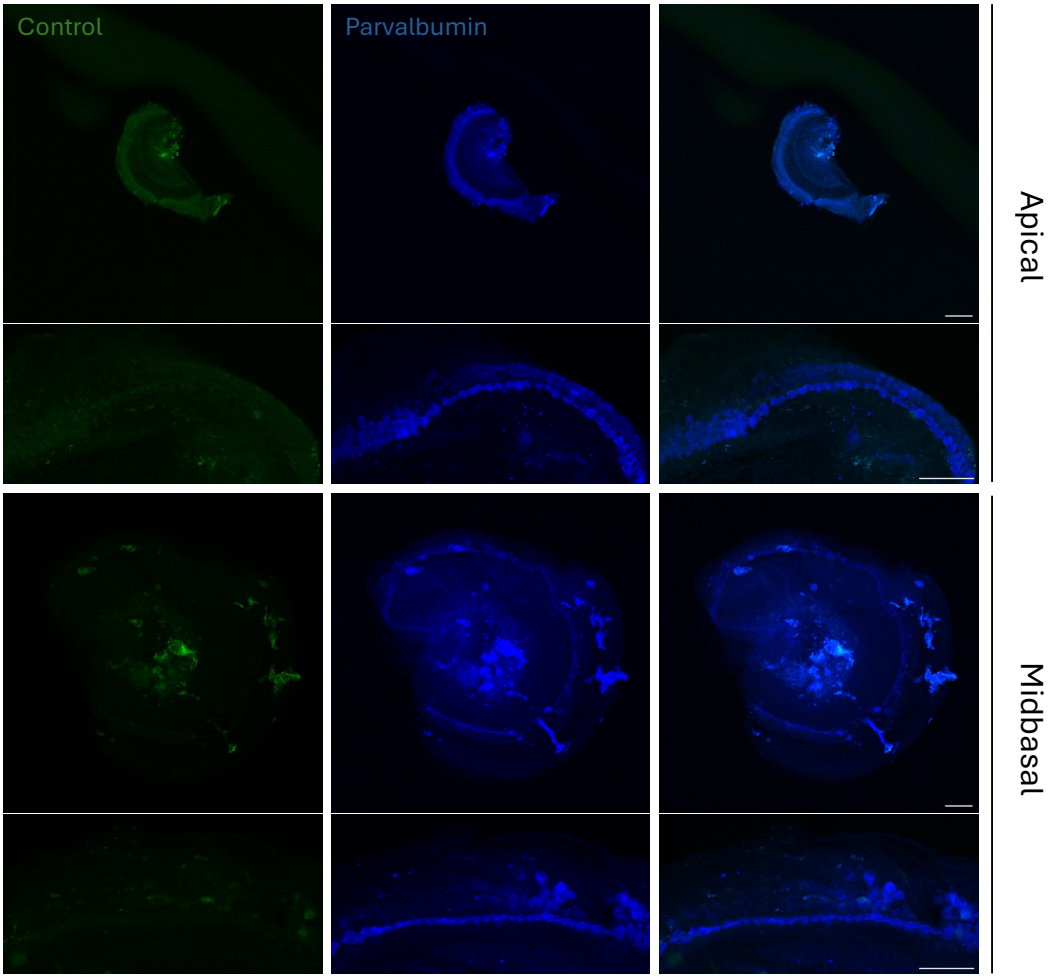

Figure 28 - Control for in vitro transduction on P7 wild type organ of Corti. The apical and midbasal turn of the organ of Corti were fixed 72 h after PBS (5 µL) addition and stained with antibodies against parvalbumin for IHCs and OHCs localization. Maximum intensity projections of optical sections. Scale bars 100 µm for organ of Corti overview image and 50 µm for IHCs and OHCs image.

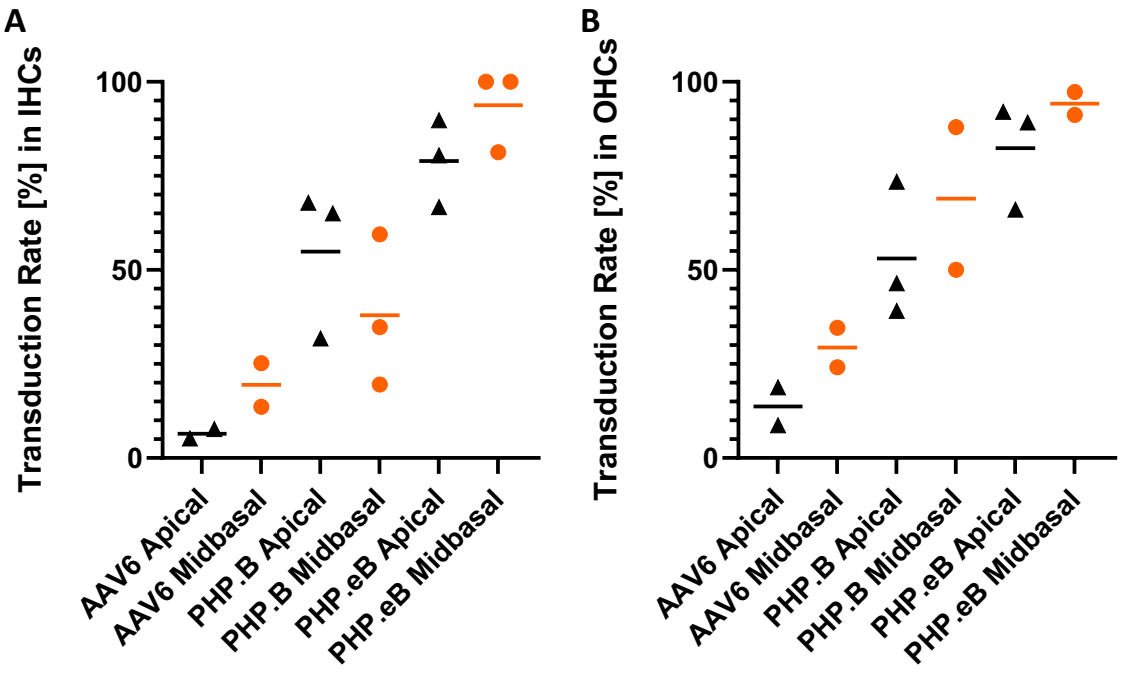

Figure 29 - Transduction rate of AAV6-GFP, PHP.B-GFP and PHP.eB-GFP in P7 in IHCs and OHCs wild type organs of Corti. A. Transduction rate of AAV6-GFP, PHP.B-GFP and PHP.eB-GFP in P7 in IHCs. The transduction rate was calculated by manually counting the number of GFP positive IHCs and dividing it with the total number of IHCs in separately in the apical and the midbasal turns of the organs of Corti. **B.** Transduction rate of AAV6-GFP, PHP.B-GFP and PHP.eB-GFP in P7 in OHCs. The transduction rate was calculated by manually counting the number of GFP positive OHCs and dividing it with the total number of OHCs in separately in the apical and the midbasal turns of the organs of Corti.

6.3.2 AAV in vitro transduction on organs of Corti with AAV variants from AG Michalakis

After successfully establishing the proof of concept for the in vitro AAV transduction experimental setup with the self-produced AAV variants (AAV6-GFP, PHP.B-GFP, and PHP.eB-GFP), the group of Prof. Stylianos Michalakis kindly provided five additional AAVs (AAV1 GL, AAV1 GLR, AAV2 PT, AAV2 RTAR, AAV9 GLR), all carrying GFP as a reporter protein. The capsids of these AAVs differ from their wild-type versions. These variations were either identified in databases/libraries or were deliberately engineered to enhance transduction efficiency in retinal cells. The aim of the following experiments was to determine whether these vectors could also transduce cells in the

organ of Corti, and if so, to assess their specificity and efficiency in transducing the sensory cells.

AAV1 GL successfully transduced both IHCs and OHCs. However, the transduction was not confined to the sensory cells. A strong GFP signal was observed throughout the organ of Corti, including in the regions of the stria vascularis and the spiral ganglion neurons (SGNs; Fig. 30). Interestingly, the transduction rates of AAV1 GL were higher in the midbasal turn compared to the apical turn in both IHCs and OHCs (Fig. 36). In IHCs, the transduction rate was 32.2 ± 0.3% in the apical turn and 60.8 ± 35.5% in the midbasal turn (Fig. 36A). In OHCs, AAV1 GL exhibited a transduction rate of 44.2 ± 9.4% in the apical turn and 86.0 ± 7.4% in the midbasal turn of the organ of Corti (Fig. 36B).

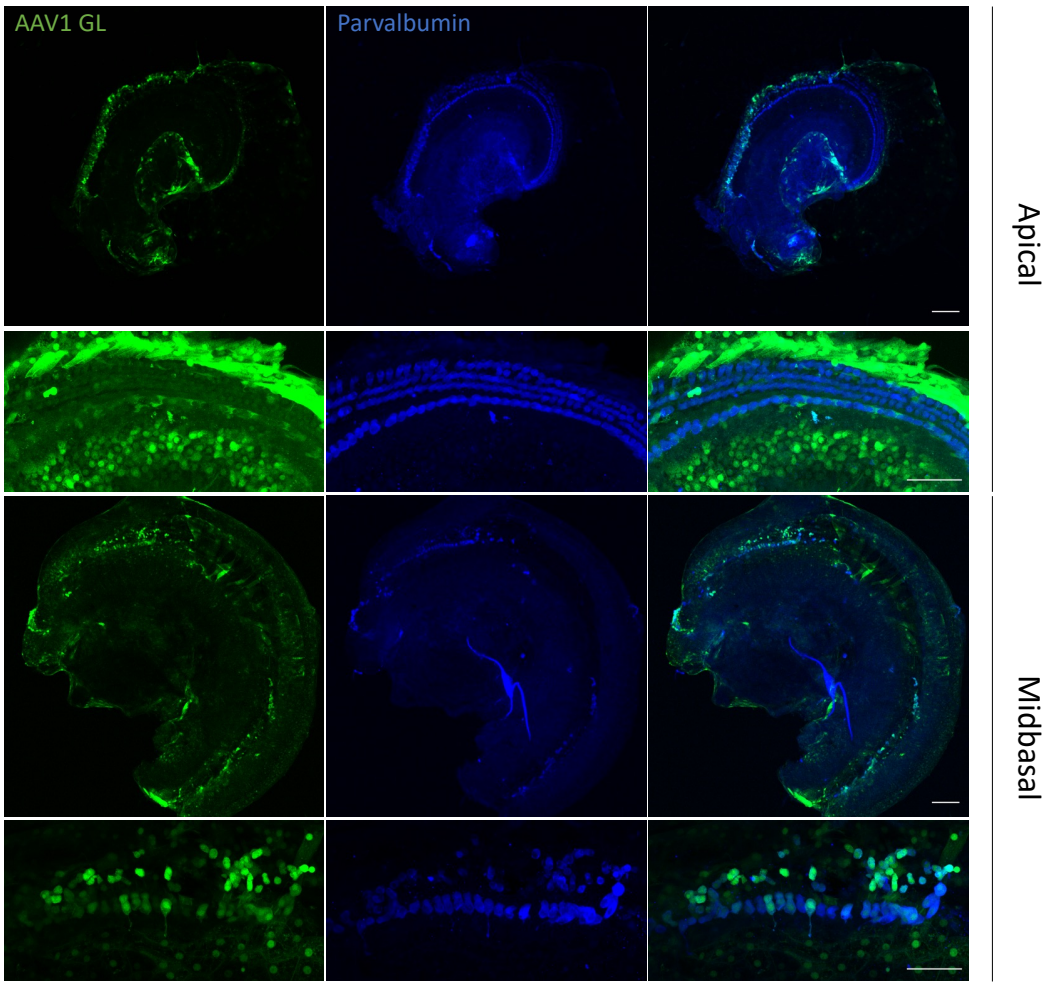

Figure 30 - AAV1 GL-GFP in vitro transduction on P9 wild type organ of Corti. AAV1 GL-GFP transduced IHCs and OHCs with higher transduction rates in the midbasal turn of the organ of Corti. GFP expression was distributed over the whole organ of Corti and was not restricted in the hair cells. The apical and midbasal turns of the organ of Corti were fixed 72 h after AAV addition and stained with antibodies against parvalbumin for IHCs and OHCs localization. Maximum intensity projections of optical sections. Scale bars 100 µm for organ of Corti overview image and 50 µm for IHCs and OHCs image.

Similar to AAV1 GL, AAV1 GLR was able to transduce both IHCs and OHCs, with the GFP signal being observable throughout the entire organ of Corti (Fig. 31). The transduction rates in both IHCs and OHCs were generally lower compared to AAV1 GL. However, unlike AAV1 GL, the transduction rates in the apical turn were higher, with 35.3 ± 9.7% in IHCs and 36.3 ± 15.9% in OHCs. In contrast, the transduction rates in the midbasal turn were lower, with 15.3 ± 15.0% of IHCs and 28.2 ± 3.9% of OHCs transduced (Fig. 36A & B).

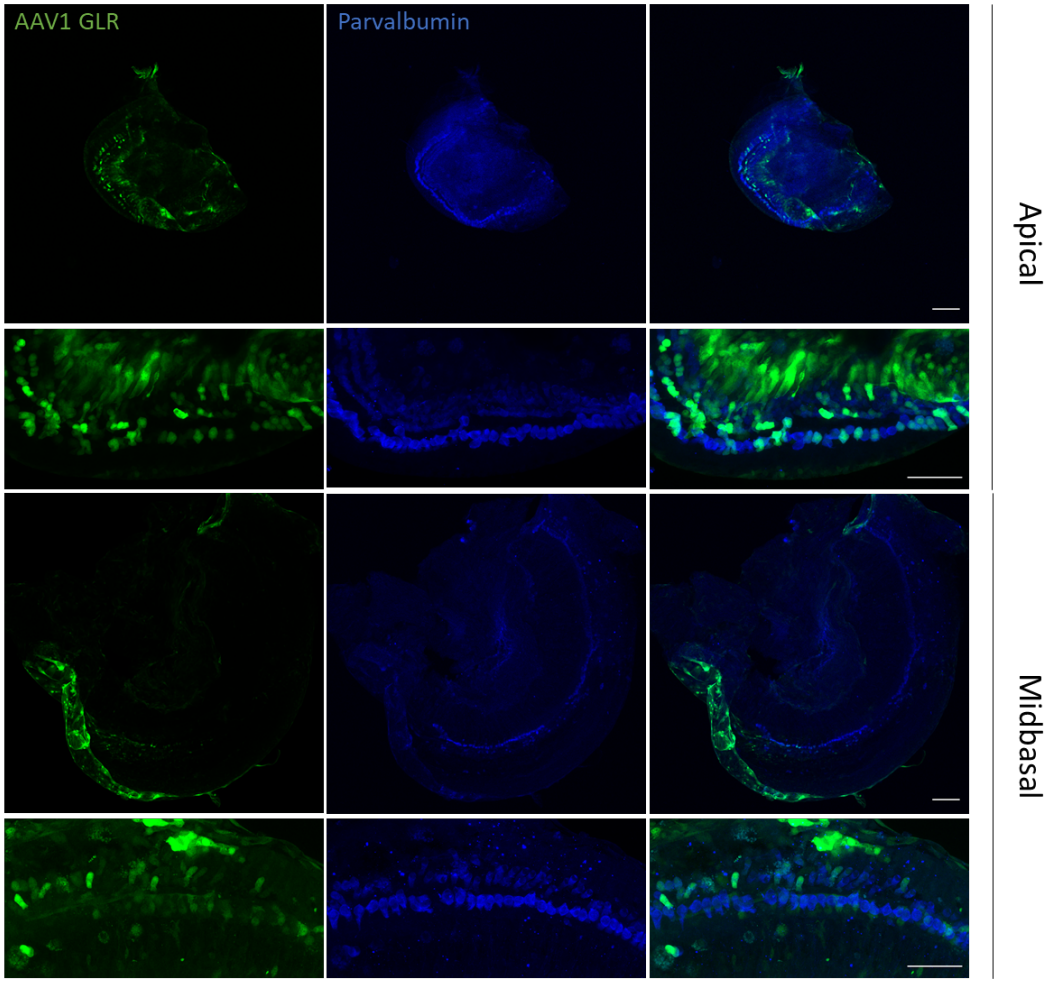

Figure 31 - AAV1 GLR-GFP in vitro transduction on P9 wild type organ of Corti. AAV1 GLR-GFP successfully transduced IHCs and OHCs with transduction rates <40%. In addition, the GFP signal was not restricted in the hair cells. The apical and midbasal turn of the organ of Corti were fixed 72 h after AAV addition and stained with antibodies against parvalbumin for IHCs and OHCs localization. Maximum intensity projections of optical sections. Scale bars 100 µm for organ of Corti overview image and 50 µm for IHCs and OHCs image.

AAV9 GLR, like the other variants, was able to transduce both IHCs and OHCs, with a GFP signal observed outside the sensory cells (Fig. 32). In contrast to the AAV1 GLR variant, which showed better transduction in the apical part, AAV9 GLR exhibited generally higher transduction rates in the midbasal part of the organ of Corti compared to the apical part. In the apical turn, IHCs had a transduction rate of 20.6 ± 15.7% (Fig.

36A), and OHCs had a transduction rate of 49.1 ± 42.0%. In the midbasal turn, the transduction rates were 46.6 ± 19.3% in IHCs and 71.9 ± 19.1% in OHCs (Fig. 36B).

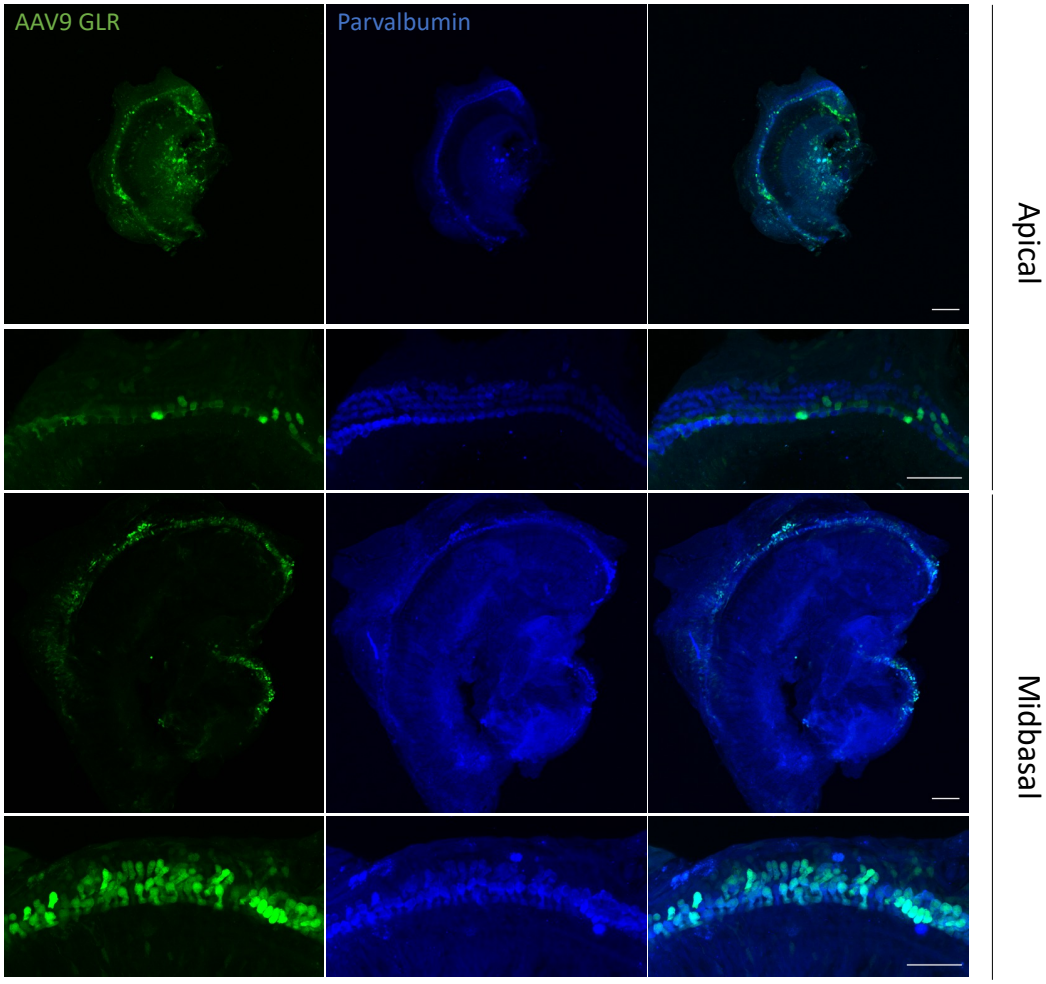

Figure 32 - AAV9 GLR-GFP in vitro transduction on P9 wild type organ of Corti. AAV9 GLR transduced IHCs and OHCs with better transduction rates in the midbasal part of the organ of Corti. GFP expression was not restricted in the hair cells. The apical and midbasal turns of the organ of Corti were fixed 72 h after AAV addition and stained with antibodies against parvalbumin for IHCs and OHCs localization. Maximum intensity projections of optical sections. Scale bars 100 µm for organ of Corti overview image and 50 µm for IHCs and OHCs image.

The two tested AAV2 variants (AAV2 PT and AAV2 RTAR) displayed notably different results in terms of their transduction efficiency. While both were able to transduce IHCs and OHCs, with the GFP signal being highly restricted to the hair cells (Fig. 33 and

34), their transduction rates varied significantly. AAV2 PT showed the highest transduction rates in both cell types and organ of Corti turns among all tested variants. In IHCs, AAV2 PT achieved a transduction rate of 96.8 ± 5.6% in the apical turn and 100% ± 0.0% in the midbasal turn (Fig. 36A). In OHCs, the transduction rate was 99.1 ± 1.6% in the apical turn and 96.7 ± 4.7% in the midbasal turn (Fig. 36B).

In contrast, AAV2 RTAR exhibited much lower transduction rates. In IHCs, the transduction rate was 15.5 ± 3.1% in the apical turn and 30.6 ± 26.5% in the midbasal turn (Fig. 36A), while in OHCs, it was higher, with 43.1 ± 21.7% in the apical turn and 47.9 ± 11.1% in the midbasal turn (Fig. 36B).

As expected, no GFP signal was observable in the control organ (addition of sterile PBS, Fig. 35).

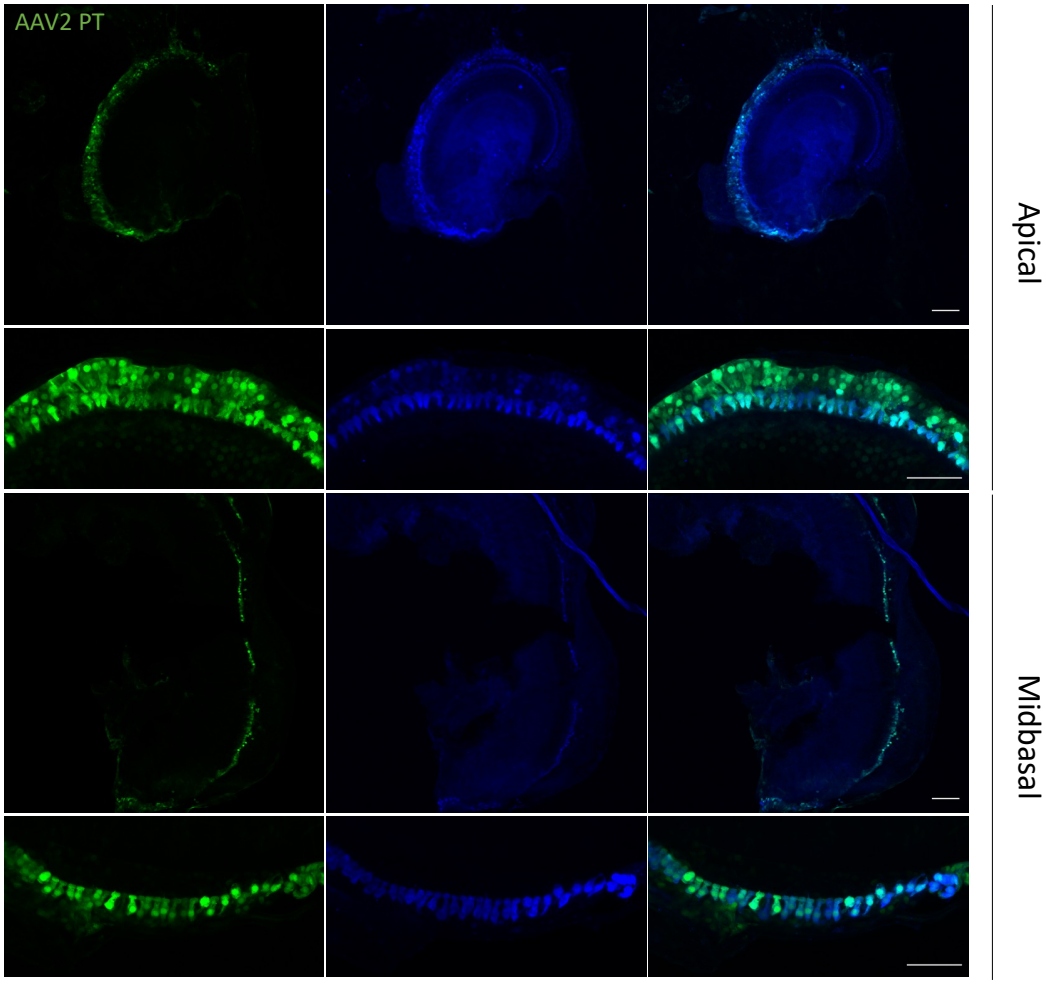

Figure 33 - AAV2 PT-GFP in vitro transduction on P9 wild type organ of Corti. AAV2 PT-GFP successfully transduced IHCs and OHCs with very the highest transduction rates pf all tested serotypes (>96%). In addition, GFP was only observable in the hair cells of the organ of Corti. The apical and midbasal turns of the organ of Corti were fixed 72 h after AAV addition and stained with antibodies against parvalbumin for IHCs and OHCs localization. Maximum intensity projections of optical sections. Scale bars 100 µm for organ of Corti overview image and 50 µm for IHCs and OHCs image.

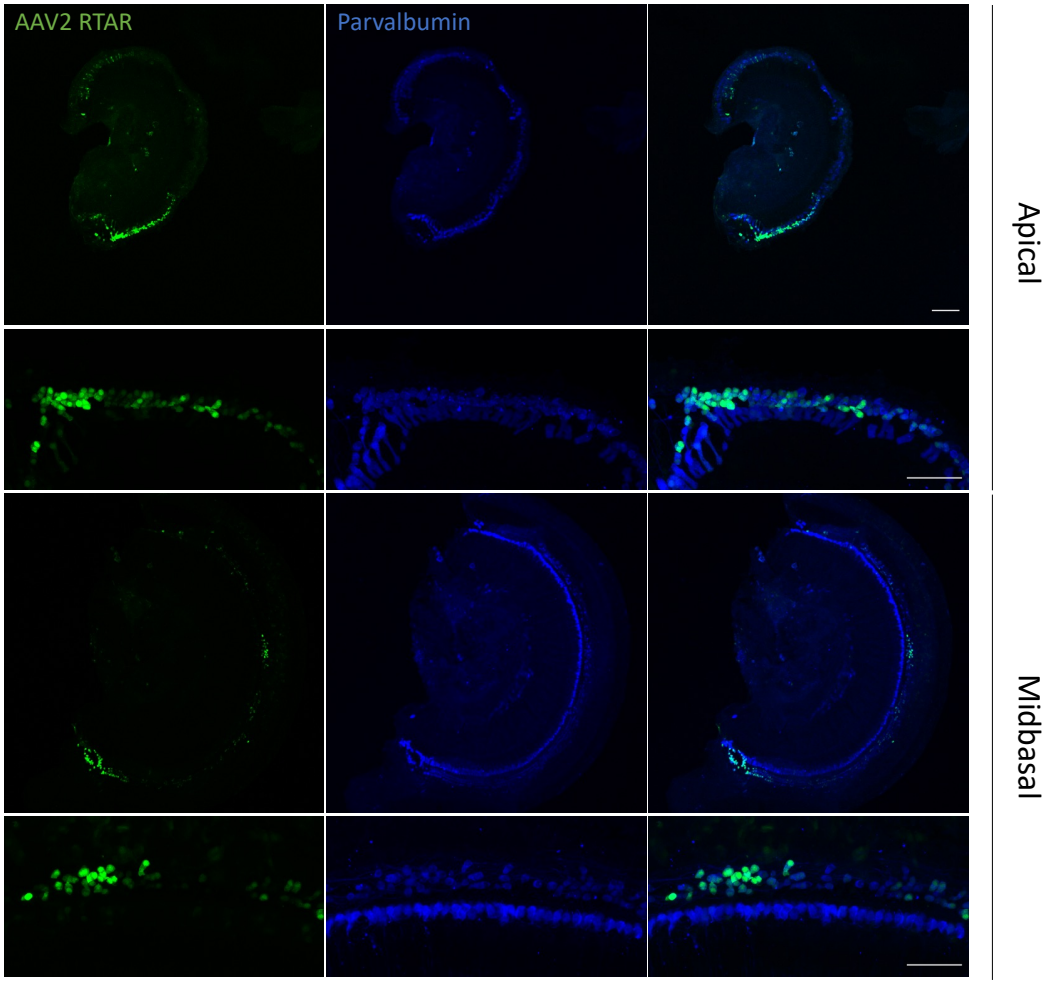

Figure 34 - AAV2 RTAR-GFP in vitro transduction on P9 wild type organ of Corti. AAV2 RTAR-GFP successfully transduced IHCs and OHCs with better transduction rates in OHCs. In addition, GFP expression was restricted to the hair cells of the Organ of Corti. The apical and midbasal turns of the organ of Corti were fixed 72 h after AAV addition and stained with antibodies against parvalbumin for IHCs and OHCs localization. Maximum intensity projections of optical sections. Scale bars 100 µm for organ of Corti overview image and 50 µm for IHCs and OHCs image.

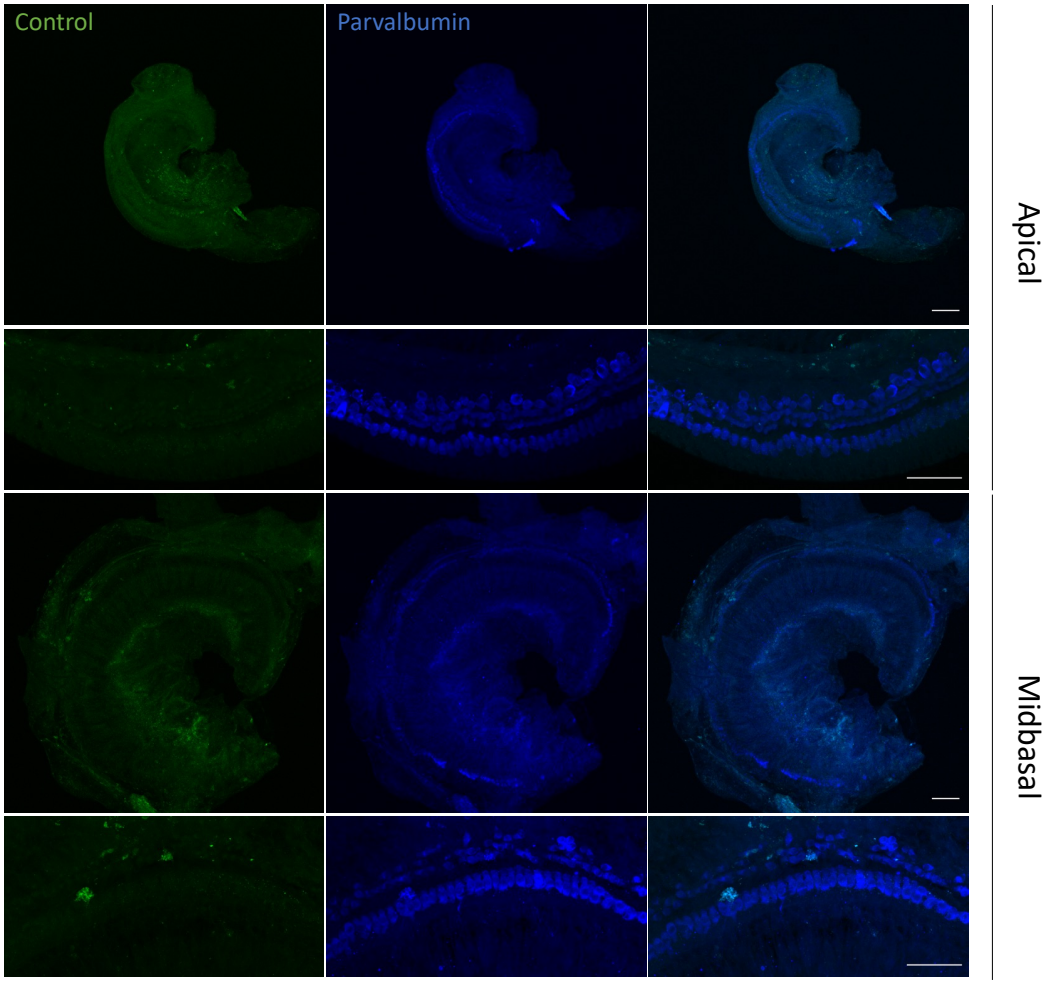

Figure 35 - Control of in vitro transduction on P9 wild type organ of Corti. The apical and midbasal turns of the organ of Corti were fixed 72 h after PBS (kindly provided by AG Michalakis; 5 µL) addition and stained with antibodies against parvalbumin for IHCs and OHCs localization. Maximum intensity projections of optical sections. Scale bars 100 µm for organ of Corti overview image and 50 µm for IHCs and OHCs image.

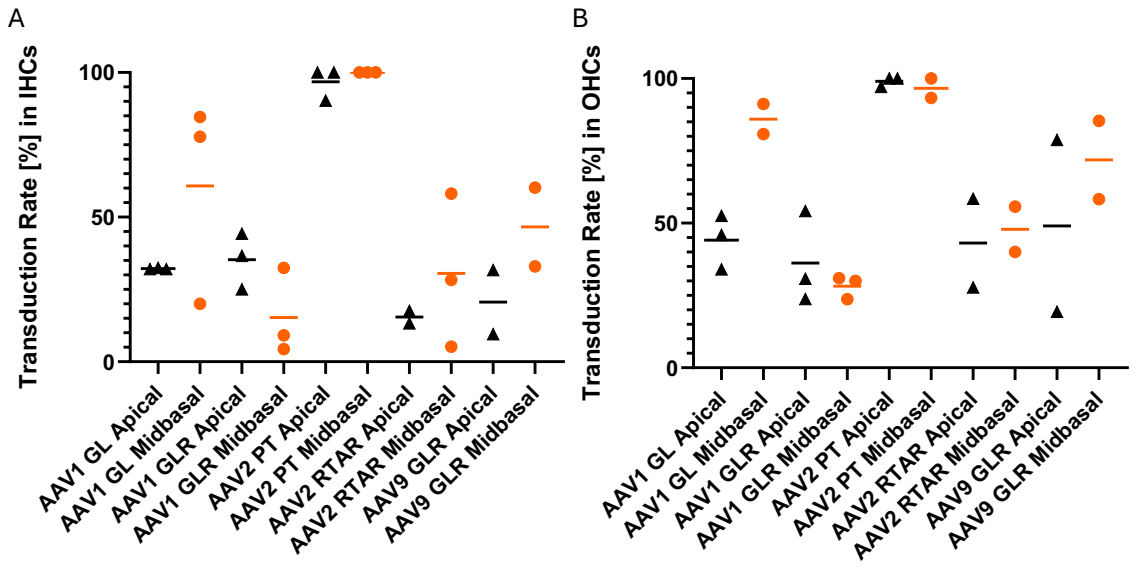

Figure 36 - Transduction rate of AAV1 GL-GFP, AAV1 GLR-GFP, AAV2 PT-GFP, AAV2 RTAR-GFP and AAV9 GLR-GFP in P7 in IHCs and OHCs wild type organs of Corti. A. Transduction rate of AAV1 GL-GFP, AAV1 GLR-GFP, AAV2 PT-GFP, AAV2 RTAR-GFP and AAV9 GLR-GFP in P9 in IHCs. The transduction rate was calculated by manually counting the number of GFP positive IHCs and dividing it with the total number of IHCs in separately in the apical and the midbasal turns of the organs of Corti. **B.** Transduction rate of AAV1 GL-GFP, AAV1 GLR-GFP, AAV2 PT-GFP, AAV2 RTAR-GFP and AAV9 GLR-GFP in P9 in OHCs. The transduction rate was calculated by manually counting the number of GFP positive OHCs and dividing it with the total number of OHCs in separately in the apical and the midbasal turns of the organs of Corti.

6.3.3 Dual AAV transduction in otoferlin knockout organ of Corti

After successfully testing the new AAV in vitro transduction method in the organ of Corti with single GFP AAVs, it was of interest to determine whether dual transduction could also be achieved in vitro. Previous in vivo studies (Al-Moyed *et al*, 2019; Akil *et al*, 2019) had already shown that dual AAV gene therapy is possible in otoferlin knockout mice in vivo, leading to partial hearing rescue. In line with the in vivo study by Al-Moyed *et al*, 2019, two different AAVs, each carrying a part of the mouse otoferlin coding gene, were produced. However, in contrast to the in vivo study, several modifications were made to the AAV plasmids for future experimental purposes. Specifically, the GFP gene was replaced by the BFP gene, and the WPRE sequence

was substituted with the shorter miniWPRE sequence to increase AAV capacity (Choi *et al*, 2014). Additionally, the recombination method was changed from a DNA-level approach (Dual-AAV-trans-splicing and Dual-AAV-Hybrid) to a protein-level recombination method using split inteins. Split inteins have previously been successfully tested in the retina and inner ear, leading to higher transduction rates and protein levels (Tornabene *et al*, 2019; Ferla *et al*, 2025; Tang *et al*, 2023).

Two versions of the AAV plasmid pairs were cloned, each splitting the otoferlin coding sequence at different locations (Version 1: position 783; version 2: position 917). The plasmid carrying the N-terminal otoferlin sequence included a BFP sequence, while the C-terminal otoferlin sequence carried an HA-tag. Both versions were produced with AAV6, PHP.B, and PHP.eB capsids. After successful production, all three capsids and both versions were tested for in vitro dual AAV transduction on HEK293T cells. To locate the N-terminal otoferlin part, a primary antibody specific to the N-terminal protein was used, and for the C-terminal otoferlin part, a primary antibody specific for the HA-tag was employed. All three tested capsids and both otoferlin versions were detectable in HEK293T cells. For all variations, BFP, N-terminal, and HA-tag signals were detectable, confirming that dual AAV transduction is indeed possible in HEK293T cells (Fig. 37).

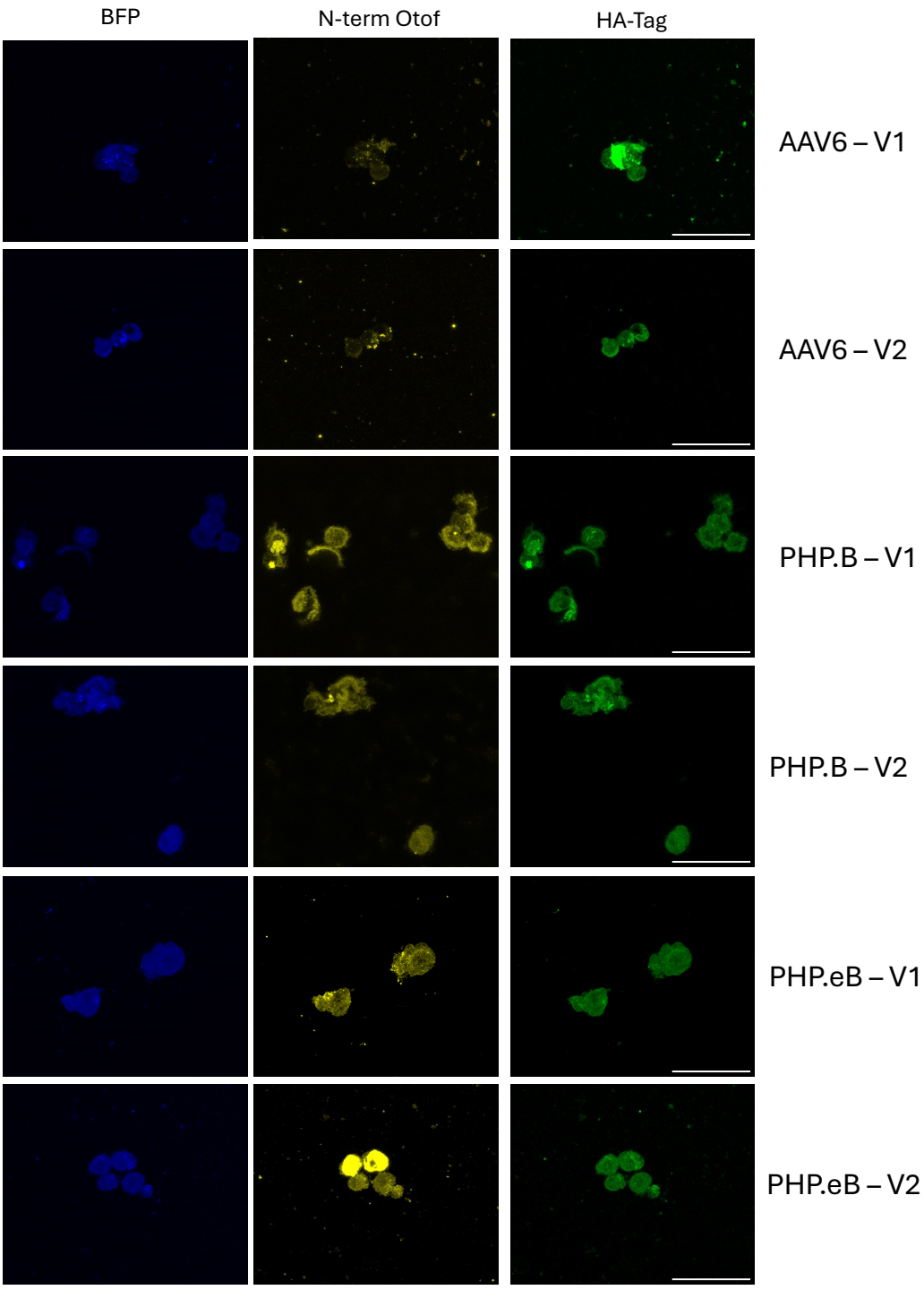
BFP
N-term Otof
HA-Tag
AAV6 – V1
AAV6 – V2
PHP.B – V1
PHP.B – V2
PHP.eB – V1
PHP.eB – V2

Figure 37 - Dual AAV in vitro transduction on HEK293T cells. Dual AAV transduction was successful in HEK cells with all three tested serotypes (AAV6, PHP.B and PHP.eB) and both *Otof* versions. BFP, N-term Otof and HA-Tag signals were detectable with all three capsids and both Otof split versions. Cells were fixed 72 h after AAV addition and stained with an antibody against the N-terminal part of otoferlin and a HA-Tag antibody (for localization of the C-terminal part of otoferlin). AAV6, PHP.B and PHP.eB carrying both split intein versions of otoferlin were transduced (Version 1: integration of the split intein at position 783; version 2: position 917) Maximum intensity projections of optical sections. Scale bars 50 µm.

Next, all dual AAV pairs were tested on mouse otoferlin knockout organs of Corti to evaluate whether dual AAV transduction is feasible in in vitro organ of Corti cultures. The AAV6 pair carrying version 1 of the *Otof* sequences exhibited both BFP and HA-Tag signals. However, no N-terminal *Otof* signal was detected in IHCs or OHCs. This observation suggests that, although both AAVs successfully entered the sensory cells, only the C-terminal otoferlin sequence was expressed (Fig. 38).

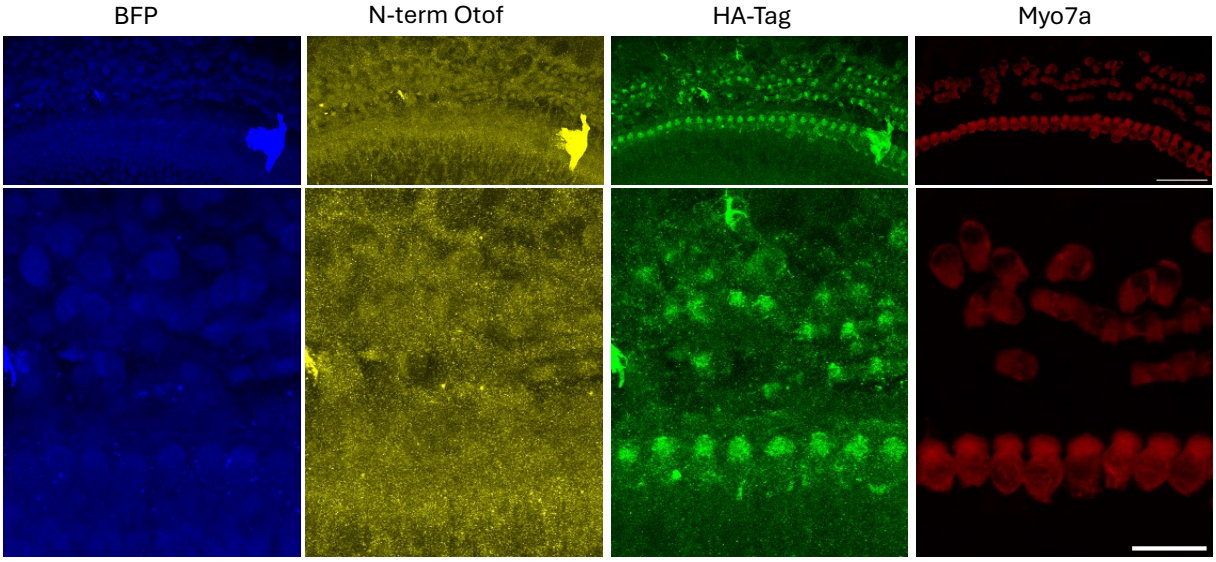

Figure 38 - Dual AAV6-*Otof* version 1 in vitro transduction on Otof knock-out organs of Corti. Dual AAV6 with *Otof* version 1 showed no N-term Otof expression but clear HA-Tag signal in IHCs and OHCs. Cells were fixed 72 h after AAV addition and stained with an N-term Otof (for localization of the N-term Otof) and an HA-Tag antibody (for localization of the C-term Otof). Maximum intensity projections of optical sections. Scale bars 50 µm overview of IHCs and OHCs and 20 µm for the zoomed image.

The AAV6 pair carrying version 2 of the *Otof* sequences did not exhibit any BFP, N-terminal Otof, or HA-Tag signal in either IHCs or OHCs. This suggests that neither AAV was able to transduce the sensory cells (Fig. 39).

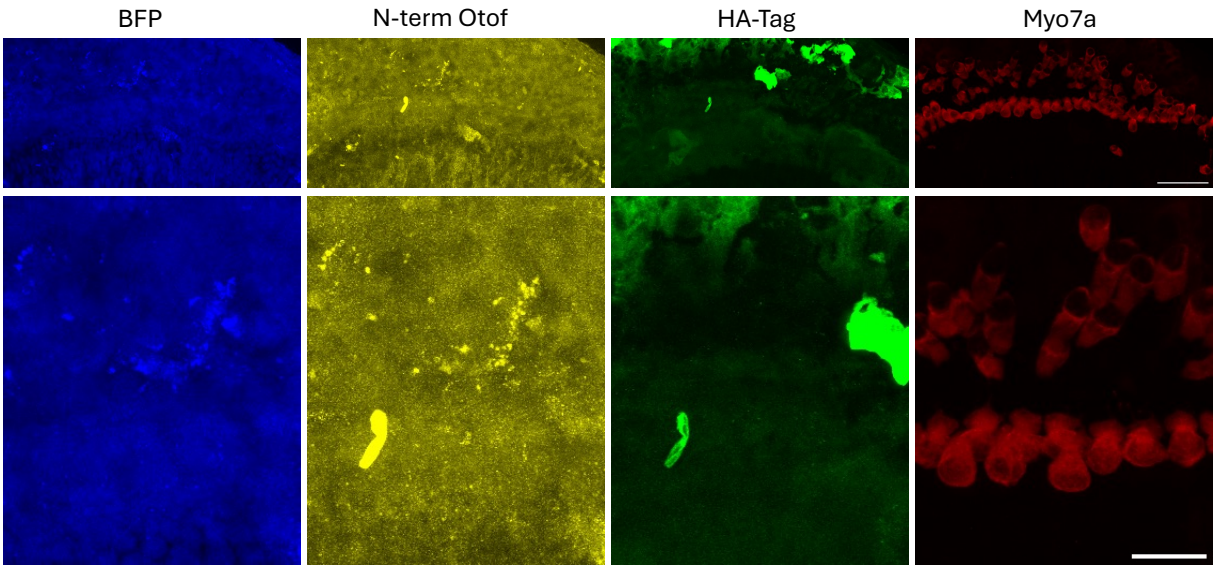

Figure 39 - Dual AAV6-*Otof* version 2 in vitro transduction on Otof knock-out organs of Corti. In dual AAV6 with *Otof* version 2 no N-term Otof or HA-Tag signal was observable. Cells were fixed 72 h after AAV addition and stained with an N-term Otof (for localization of the N-term Otof) and an HA-Tag antibody (for localization of the C-term Otof). Maximum intensity projections of optical sections. Scale bars 50 µm overview of IHCs and OHCs and 20 µm for the zoomed image.

In contrast, the PHP.B pair carrying version 1 of the *Otof* sequences exhibited BFP, N-terminal Otof, and HA-Tag signals in both IHCs and OHCs (Fig. 40). Although the N-terminal Otof signal was relatively weak, it was clearly detectable and co-localized with the BFP signal. Therefore, it can be concluded that dual AAV transduction was successful in this case.

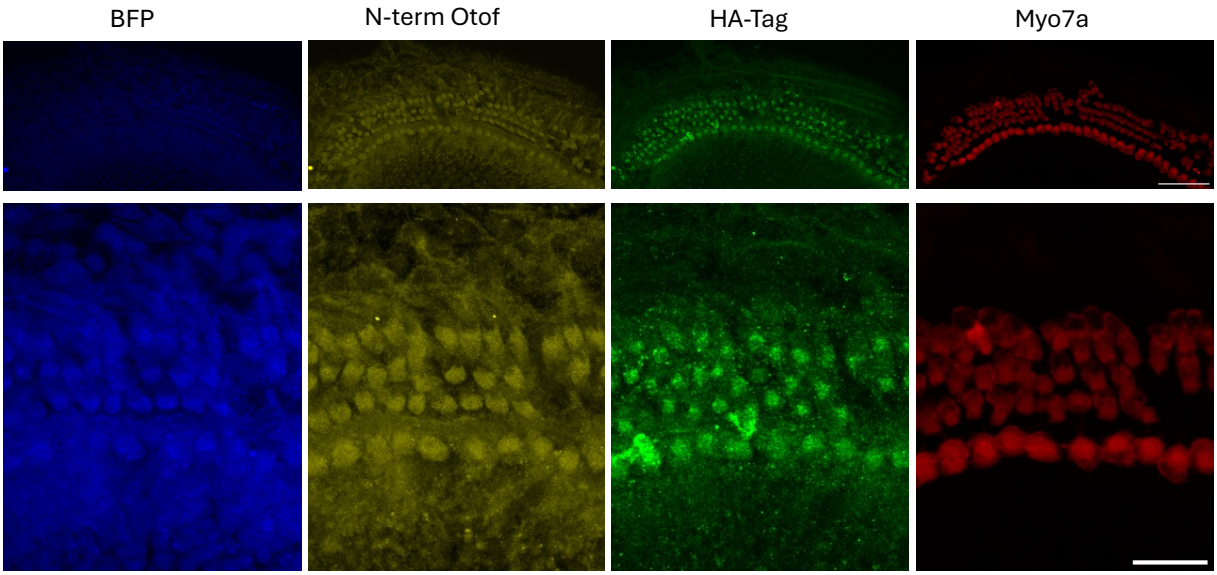

Figure 40 - Dual PHP.B-*Otof* version 1 in vitro transduction on Otof knock-out organs of Corti. Dual PHP.B with *Otof* version 1 revealed successful transduction of both AAVs with N-term Otof and HA-Tag expression in both IHCs and OHCs. Cells were fixed 72 h after AAV addition and stained with a N-term Otof (for localization of the N-term Otof) and a HA-Tag antibody (for localization of the C-term Otof). Maximum intensity projections of optical sections. Scale bars 50 µm overview of IHCs and OHCs and 20 µm for the zoomed image.

PHP.B carrying version 2 of the *Otof* sequences exhibited a clear HA-Tag signal and a faint, blurred N-terminal Otof signal in IHCs (OHCs were not detectable in the organ of Corti preparation). However, since no BFP signal was observed in IHCs, it remains unclear whether the N-terminal Otof signal originates from the expressed protein or represents background fluorescence (Fig. 41).

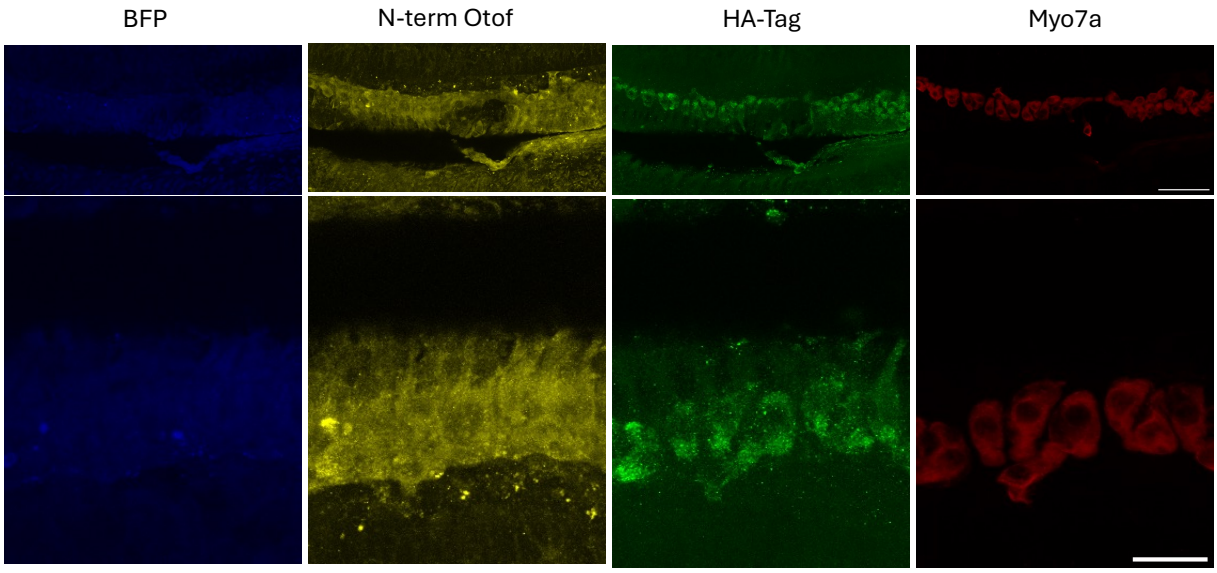

Figure 41 - Dual PHP.B-*Otof* version 2 in vitro transduction on Otof knock-out organs of Corti. Dual PHP.B with *Otof* version 2 showed HA-Tag expression in IHCs. In addition, blurred N-term Otof signal was observable in IHCs however, not in combination with BFP. Cells were fixed 72 h after AAV addition and stained with a N-term Otof (for localization of the N-term Otof) and a HA-Tag antibody (for localization of the C-term Otof). Maximum intensity projections of optical sections. Scale bars 50 µm overview of IHCs and OHCs and 20 µm for the zoomed image.

The PHP.eB pair carrying version 1 of the *Otof* sequences, similar to PHP.B version 1, exhibited BFP, N-terminal Otof, and HA-Tag signals in IHCs. Although the organ of Corti preparation was not in optimal condition, with only a few IHCs detectable, the observed signals were clear and strong. This indicates that, at least in IHCs, dual AAV transduction was successful (Fig. 42).

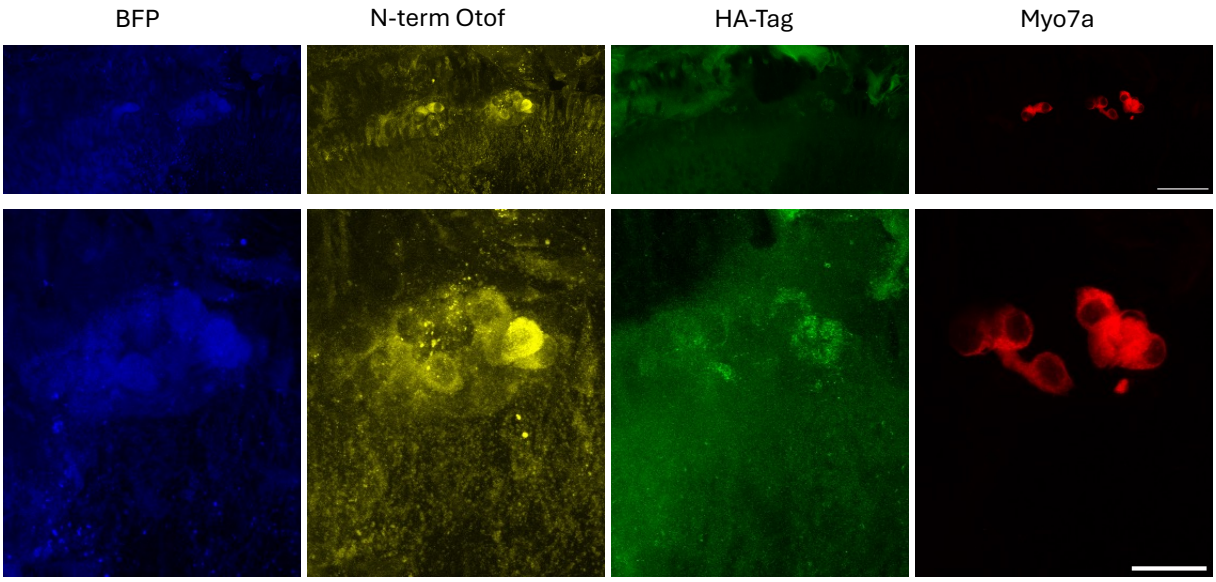

Figure 42 - Dual PHP.eB-*Otof* version 1 in vitro transduction on Otof knock-out organs of Corti. Dual PHP.eB with *Otof* version 1 revealed successful transduction of both AAVs with N-term Otof and HA-Tag expression in IHCs. Cells were fixed 72 h after AAV addition and stained with a N-term Otof (for localization of the N-term Otof) and a HA-Tag antibody (for localization of the C-term Otof). Maximum intensity projections of optical sections. Scale bars 50 µm overview of IHCs and OHCs and 20 µm for the zoomed image.

Similar to the PHP.B version 2 pair, the PHP.eB version 2 transduction exhibited HA-Tag, a very weak N-terminal Otof signal, and no detectable BFP signal. As previously mentioned, the absence of the BFP signal raises uncertainty regarding the success of dual AAV transduction. However, it is evident that the C-terminal Otof AAV successfully transduced the IHCs and OHCs (Fig. 43).

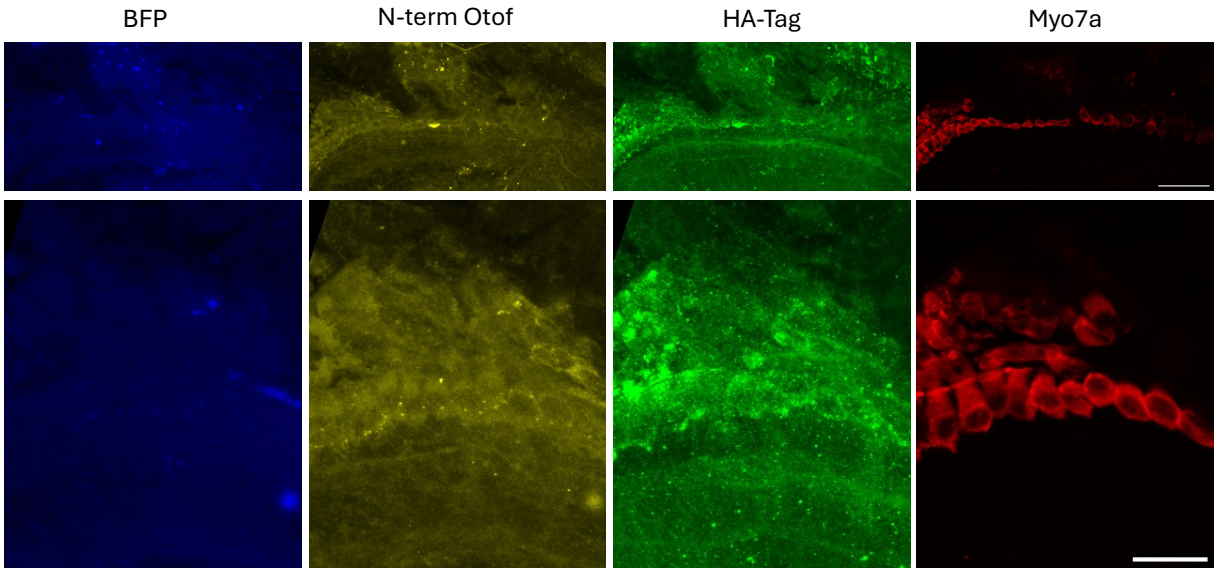

Figure 43 - Dual PHP.eB-*Otof* version 2 in vitro transduction on Otof knock-out organs of Corti. Dual PHP.eB with *Otof* version 2 showed HA-Tag expression in IHCs and OHCs. In addition, some weak N-term Otof signal was observable in IHCs and OHCs however, not in combination with BFP. Cells were fixed 72 h after AAV addition and stained with a N-term Otof (for localization of the N-term Otof) and a HA-Tag antibody (for localization of the C-term Otof). Maximum intensity projections of optical sections. Scale bars 50 µm overview of IHCs and OHCs and 20 µm for the zoomed image.

As presented in Table 25, PHP.B and PHP.eB carrying the version 1 *Otof* sequences demonstrated successful dual AAV transduction, with both N-terminal and C-terminal Otof signals detectable. Notably, the PHP.B capsid exhibited particularly strong and clear signals in both IHCs and OHCs.

In contrast, AAVs with the version 2 *Otof* sequences yielded less reliable results, especially regarding the N-terminal signals. Furthermore, none of the AAV6 pairs were able to transduce the sensory cells with both vectors.

Table 25 - Overview of the dual AAV in vitro transduction results on Otof knock-out organs of Corti.

	Version 1		Version 2	
	N-term Otof	HA-Tag	N-term Otof	HA-Tag
AAV6	✗	✓	✗	✗
PHP.B	✓	✓	(✓)	✓
PHP.eB	✓	✓	(✓)	(✓)

6.4 Rab4b in the mouse inner ear

Rab4b is a small GTPase involved in endocytic recycling and intracellular transport processes. However, its role and function in the inner ear remain unknown.

In five patients from Tübingen and Heidelberg with progressive hearing loss, a dominantly inherited point mutation in the *RAB4B* gene, encoding the Ras-related protein Rab4b, was identified. These patients experience increasing difficulties with speech comprehension, despite only moderately elevated hearing thresholds. To date, *RAB4B* has not been associated with hearing disorders.

To investigate whether this mutation is likely responsible for the patients' hearing loss, immunostaining and RNA Scope analysis were performed on cochlear cryosections and whole-mount organs of Corti from wild-type mice of different ages.

Rab4b shares a high degree of sequence identity with Rab4A, a member of the same protein family. Therefore, RNA Scope probes and antibodies targeting both Rab4b and Rab4a were utilized, with two different antibodies tested for each protein.

6.4.1 Cryosections of mouse cochlea

Cryosections of one-month-old mouse cochleae exhibited high RNA signals for both Rab4a and Rab4b in spiral ganglion neurons (SGNs), as well as in the stria vascularis. Additionally, RNA Scope punctae were detectable in both inner and outer hair cells (IHCs and OHCs), although the signal intensity was lower compared to that in the SGNs. Immunohistochemistry staining produced results similar to those observed with RNA Scope, with particularly strong signals in the SGNs and the stria vascularis. For Rab4b staining, the antibody from Thermo Fisher (Fig. 44) exhibited a stronger and

clearer signal than the one from Abcam (Fig. 45). Similarly, Rab4a staining demonstrated a strong signal, particularly in the SGNs and stria vascularis (Fig. 46 & 47). Both antibodies tested showed robust and comparable signals. However, while the BIOZOL antibody staining (Fig. 47) displayed a uniform signal distribution throughout the cells, the Proteintech antibody exhibited a punctate signal pattern (Fig. 46).

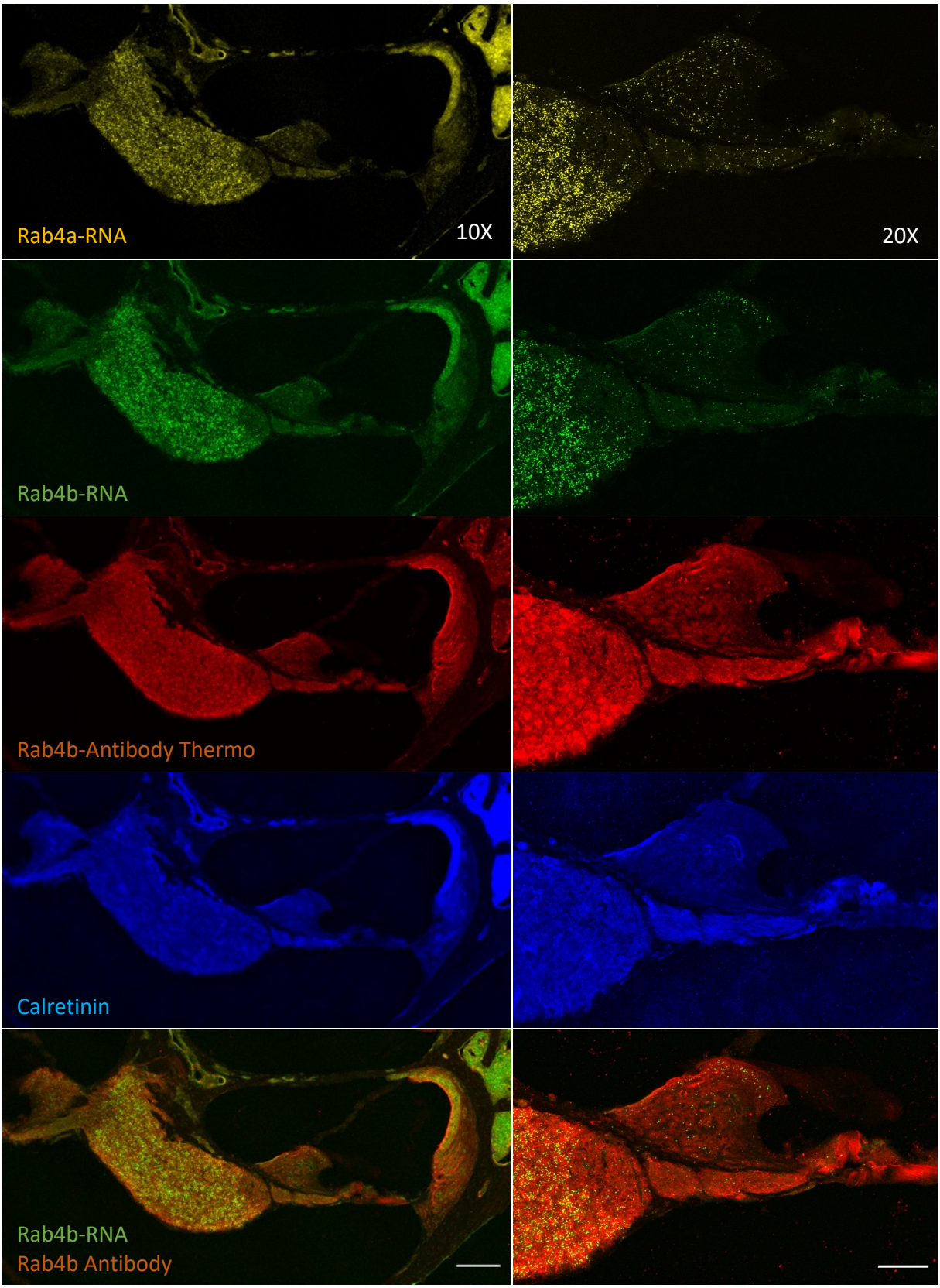
Rab4a-RNA
10X
20X
Rab4b-RNA
Rab4b-Antibody Thermo
Calretinin
Rab4b-RNA
Rab4b Antibody

Figure 44 - Rab4a and Rab4b RNA Scope staining and Rab4b immunostaining with the Thermo Fisher antibody in one-month-old wild type cochlear cryosections. The immunostaining protocol was performed after the RNA Scope staining with Rab4b specific antibodies from Thermo Fisher. Maximum intensity projections of optical sections. Scale bars 100 μm for the 10X and 50 μm for the 20X images.

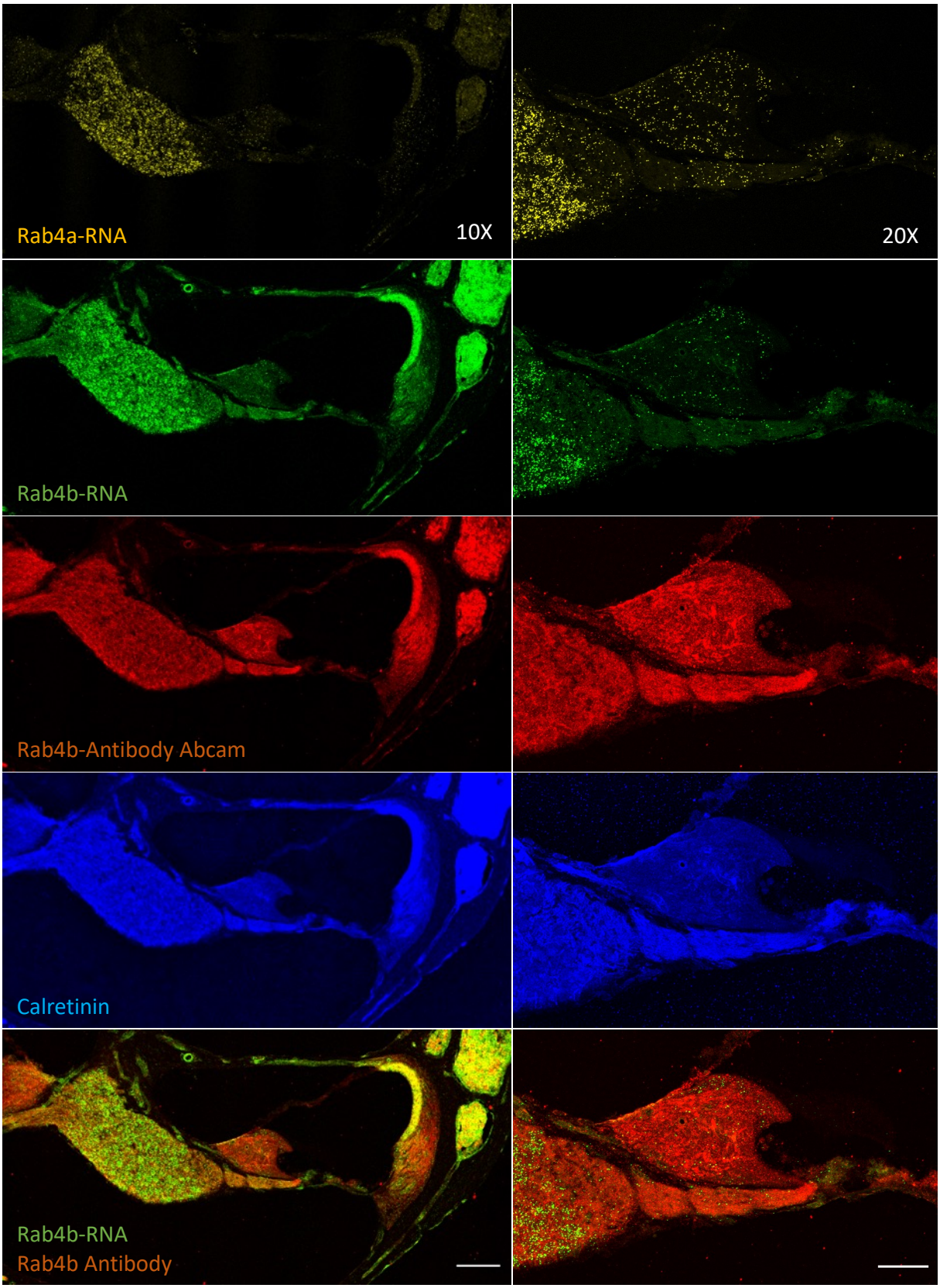

Figure 45 - Rab4a and Rab4b RNA Scope staining and Rab4b immunostaining with the Abcam antibody in one-month-old wild type cochlear cryosections. The immunostaining protocol was performed after the RNA Scope staining with Rab4b specific antibodies from Abcam. Maximum intensity projections of optical sections. Scale bars 100 µm for the 10X and 50 µm for the 20X images.

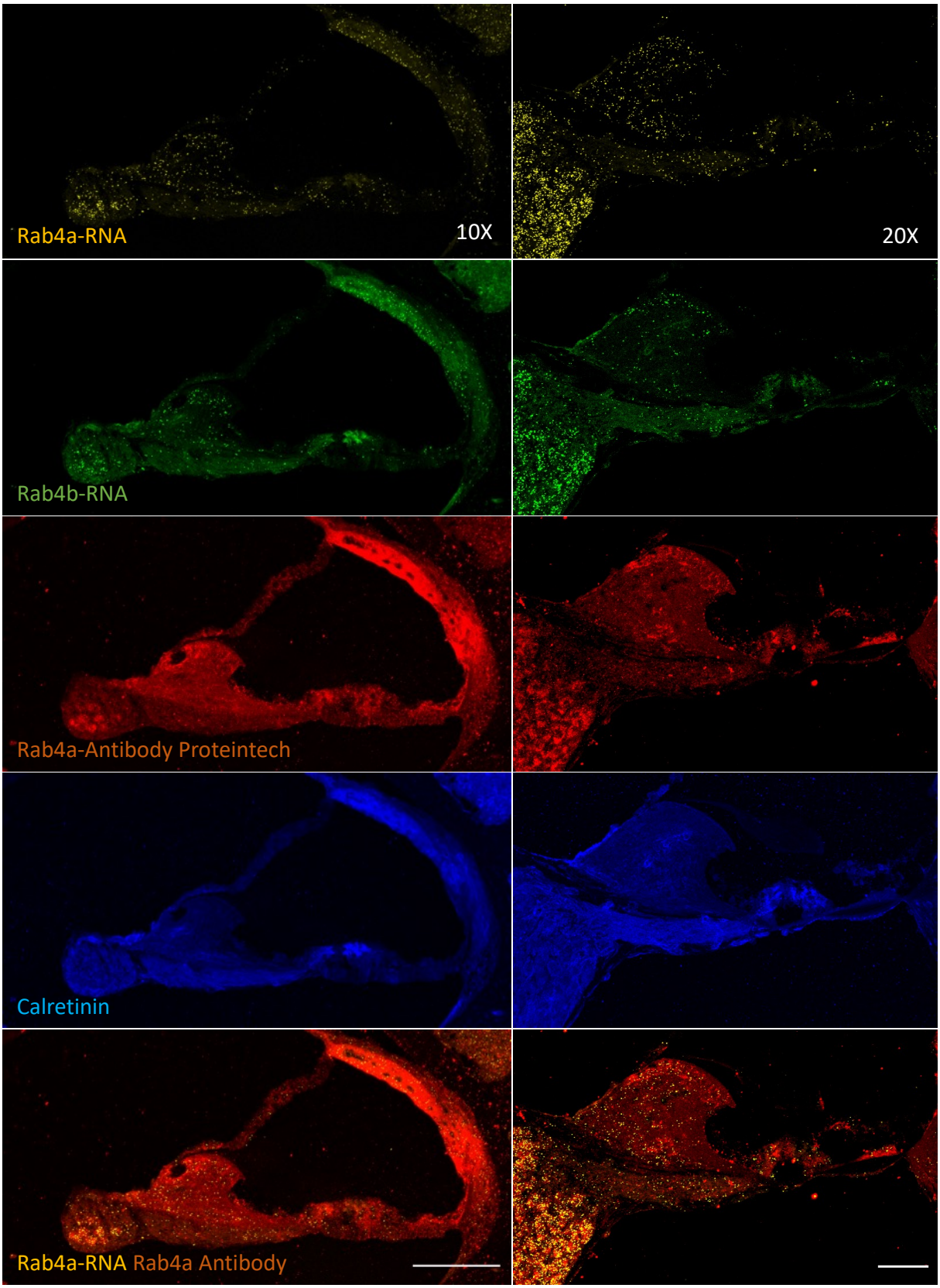
Rab4a-RNA
10X
20X
Rab4b-RNA
Rab4a-Antibody Proteintech
Calretinin
Rab4a-RNA Rab4a Antibody

Figure 46 - Rab4a and Rab4b RNA Scope staining and Rab4a immunostaining with the Proteintech antibody in one-month-old wild type cochlear cryosections. The immunostaining protocol was performed after the RNA Scope staining with Rab4a specific antibodies from Proteintech. Maximum intensity projections of optical sections. Scale bars 100 µm for the 10X and 50 µm for the 20X images.

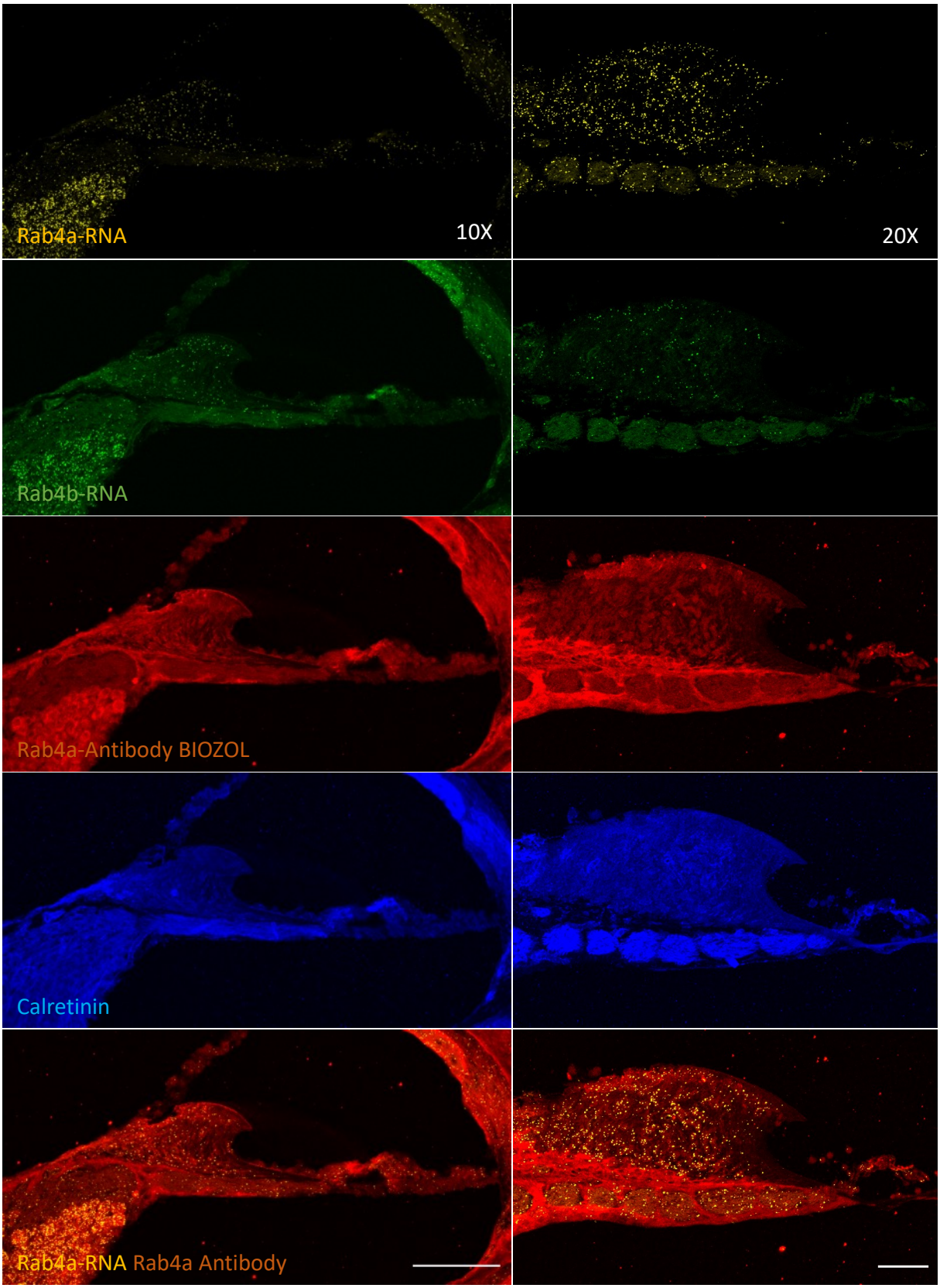

Figure 47 - Rab4a and Rab4b RNA Scope staining and Rab4a immunostaining with the BIOZOL antibody in one-month-old wild type cochlear cryosections. The immunostaining protocol was performed after the RNA Scope staining with Rab4a specific antibodies from BIOZOL. Maximum intensity projections of optical sections. Scale bars 100 µm for the 10X and 50 µm for the 20X images.

6.4.2 Whole mounts of mouse organs of Corti

Whole-mount RNA Scope followed by immunostaining in one-month-old wild-type mice revealed a strong Rab4b RNA signal (numerous punctae) in the SGNs, with some signal detected in both inner and outer hair cells (IHCs and OHCs). Immunohistochemical staining using the Thermo Fisher Rab4b antibody showed a clear signal in the OHCs and a weak signal in the IHCs. The Abcam antibody exhibited similar signal localization, although the intensity was notably weaker (Fig. 48).

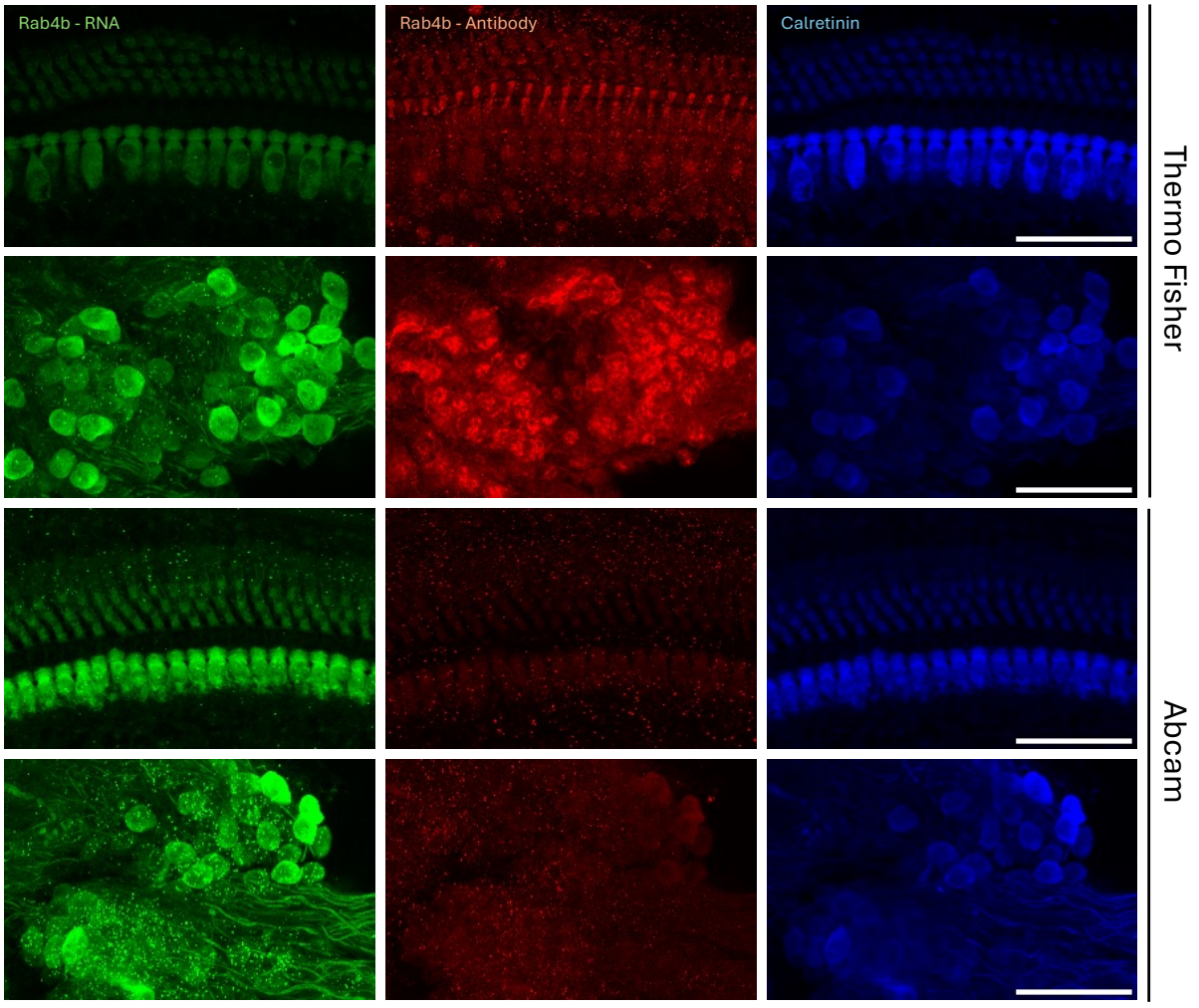

Figure 48 - Rab4b RNA Scope staining and immunostaining in one-month-old wild type organ of Corti whole mounts. The immunostaining protocol was performed after the RNA Scope staining with two different Rab4b specific antibodies (from Thermo Fisher and Abcam). Maximum intensity projections of optical sections. Scale bars 50 µm.

RNA Scope followed by immunostaining with Rab4a antibodies revealed RNA and protein signals in SGNs, IHCs, and OHCs, similar to the Rab4b results (Fig. 49). As observed in the cryosection staining (Fig. 46 & 47), the BIOZOL antibody for Rab4a displayed a signal that was uniformly distributed across the IHCs and OHCs, whereas the Proteintech antibody exhibited a punctate signal with more background staining (Fig. 49). Given that the Thermo Fisher antibody for Rab4a and the BIOZOL antibody for Rab4a yielded the most consistent staining results, only these two antibodies were selected for subsequent immunostaining experiments with whole mounts from six- and twelve-month-old mice.

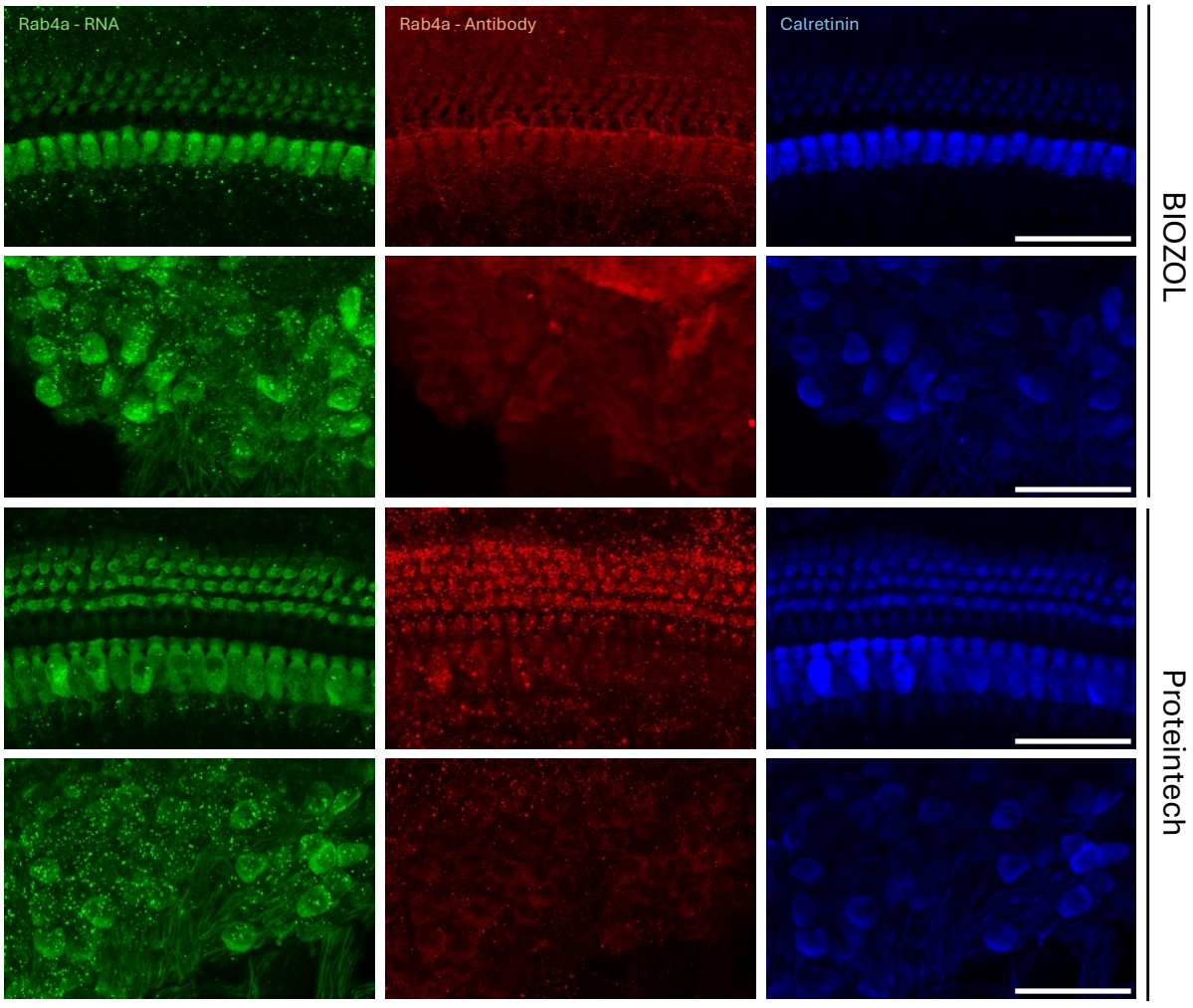

Figure 49 - Rab4a RNA Scope staining and immunostaining in one-month-old wild type organ of Corti whole mounts. The immunostaining protocol was performed after the RNA Scope staining with two different Rab4a specific antibodies (from Proteintech and BIOZOL). Maximum intensity projections of optical sections. Scale bars 50 µm.

To determine whether the RNA Scope protocol influences the Rab4a and Rab4b antibodies, only immunostaining was performed on whole mounts from one-month-old wild-type mice (Fig. 50). The Rab4b and Rab4a signals were found in the IHCs, OHCs, and SGNs, as described in the RNA Scope/Immunostaining experiments. Interestingly, for the Rab4b antibody (Thermo Fisher), the signal in the IHCs and OHCs appeared clearer, stronger, and less blurred compared to the staining following the RNA Scope protocol. Additionally, the signal in the SGNs was very clear and strong. The Rab4a signal appeared stronger in the OHCs and weaker in the IHCs and SGNs.

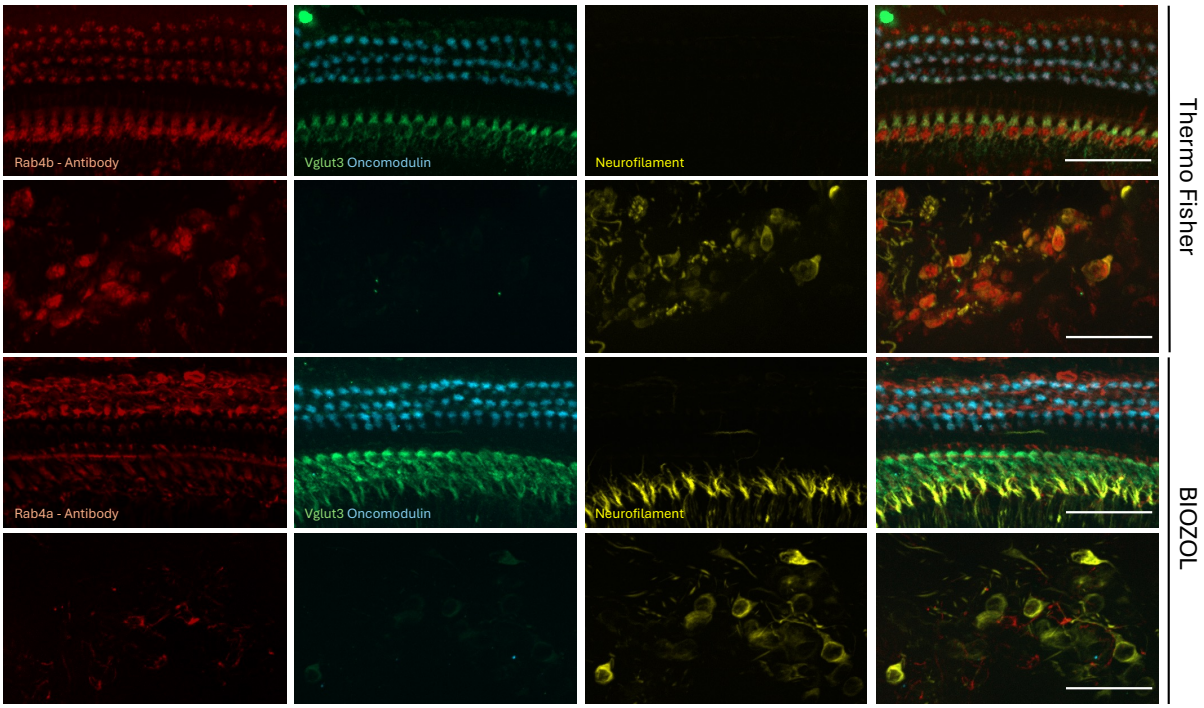

Figure 50 - Rab4a and Rab4b immunostaining in one-month-old wild type organ of Corti whole mounts. The immunostaining protocol with different the Thermo Fisher Rab4b specific and the BIOZOL Rab4a specific antibodies. The Vglut3 antibody was used to stain IHCs, the Oncomodulin antibody to stain OHCs and the Neurofilament antibody to stain the SGNs. Maximum intensity projections of optical sections. Scale bars 50 µm.

6.4.3 Rab4b and Rab4a in older wild type mice

Like the one-month-old mice, six-month-old (Fig. 51) and twelve-month-old mice (Fig. 52) showed RNA and protein signals for Rab4a and Rab4b in the IHCs, OHCs, and SGNs in both RNA Scope and immunostaining experiments. Notably, the Rab4b signal in the SGNs was very strong in both age groups. Interestingly, Rab4b protein expression appeared clearer and stronger in the IHCs of both six- and twelve-month-old mice compared to the one-month-old mice (Fig. 48, 49, 51 & 52).

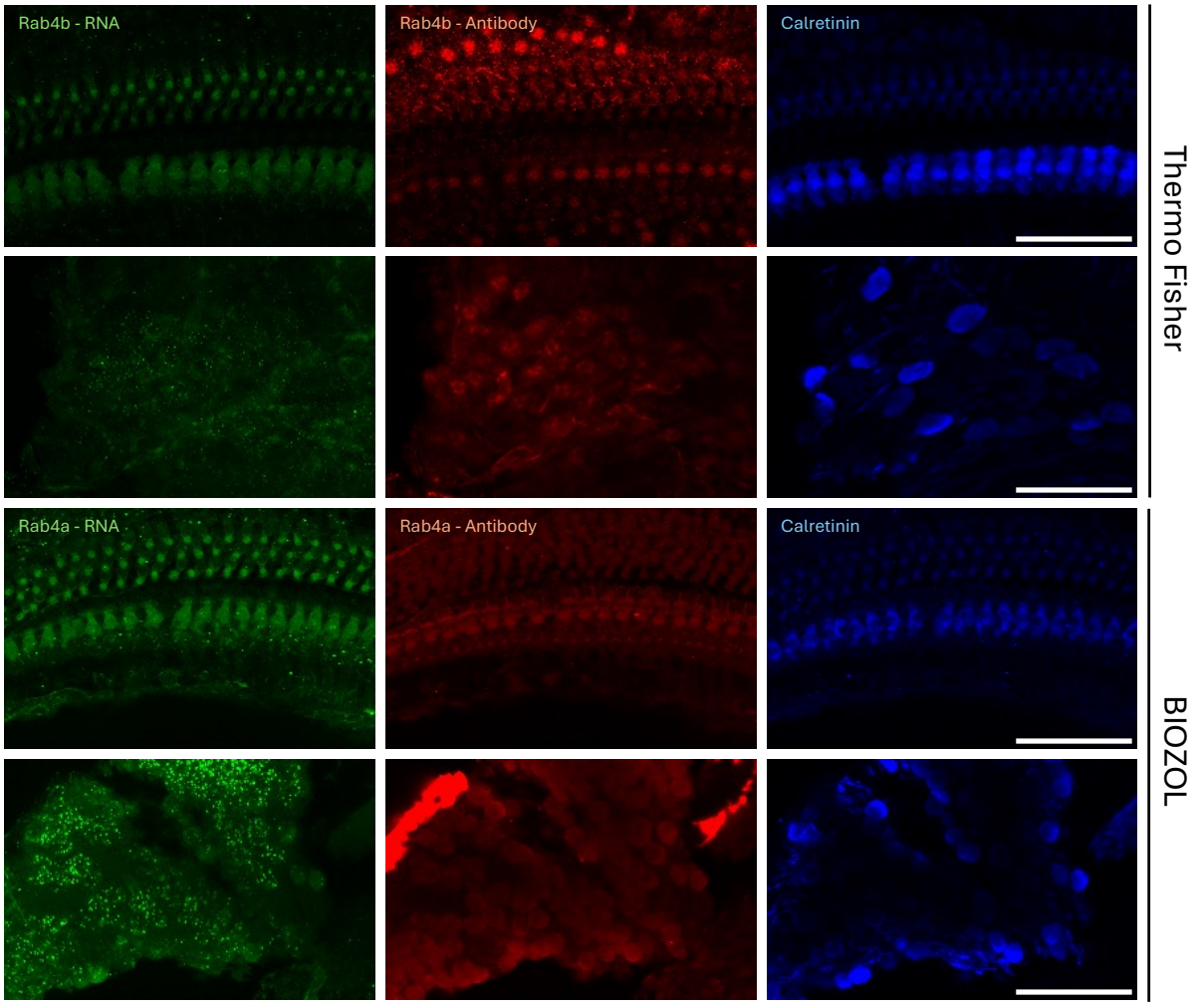

Figure 51 - Rab4a and Rab4b RNA Scope staining and immunostaining in six months old wild type organ of Corti whole mounts. The immunostaining protocol was performed after the RNA Scope staining. For the Rab4b immunostaining the Thermo Fisher antibody and for the Rab4a immunostaining the BIOZOL antibody was used. Maximum intensity projections of optical sections. Scale bars 50 µm.

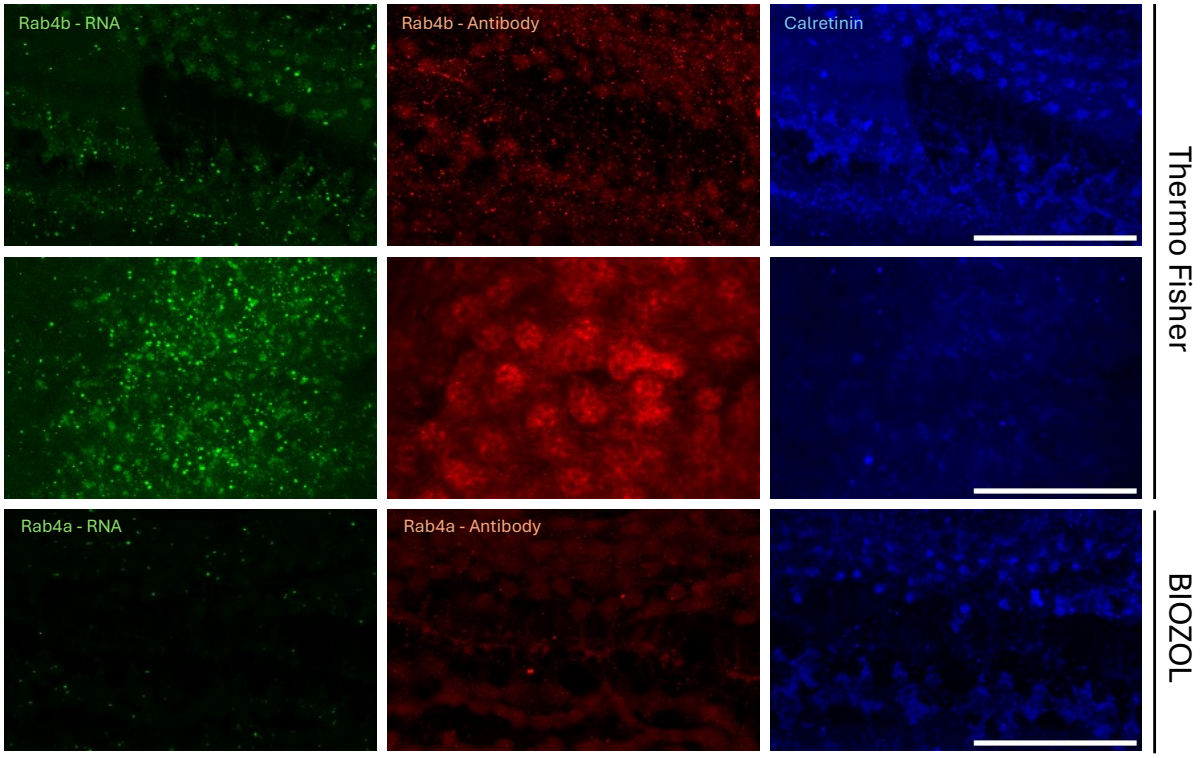

Figure 52 - Rab4a and Rab4b RNA Scope staining and immunostaining in twelve months old wild type organ of Corti whole mounts. The immunostaining protocol was performed after the RNA Scope staining. For the Rab4b immunostaining the Thermo Fisher antibody and for the Rab4a immunostaining the BIOZOL antibody was used. Maximum intensity projections of optical sections. Scale bars 50 µm.

6.4.3 Rab4b knockout and Rab4b T64M knockin mouse lines

To better understand the precise role of Rab4b in the inner ear and assess the importance of its function, two new mouse lines were planned: one carrying the T64M mutation, which was identified in patients, and a Rab4b knockout mouse line. The designed sgRNA and donor oligo (see also Supplement Tab. 36) were sent to the Department of Genetic Medicine and Development at the University of Geneva, where they attempted to generate these two mouse lines using CRISPR/Cas9 endonuclease treatment.

Upon receiving biopsies from the F1-generation offspring, genotyping was performed using two primer pairs: one specific to the wild-type sequence and the other specific to the sequence with the T64M mutation. The PCR results revealed that one animal (No. 03) was homozygous for the T64M mutation, four animals were heterozygous, showing both wild-type and T64M bands (No. 89, 90, 91, and 94), two animals exhibited a shorter band in addition to the wild-type band (No. 92 and 95), and one animal showed a wild-type band alongside a shorter T64M band (No. 96; Fig. 53 and Tab. 26).

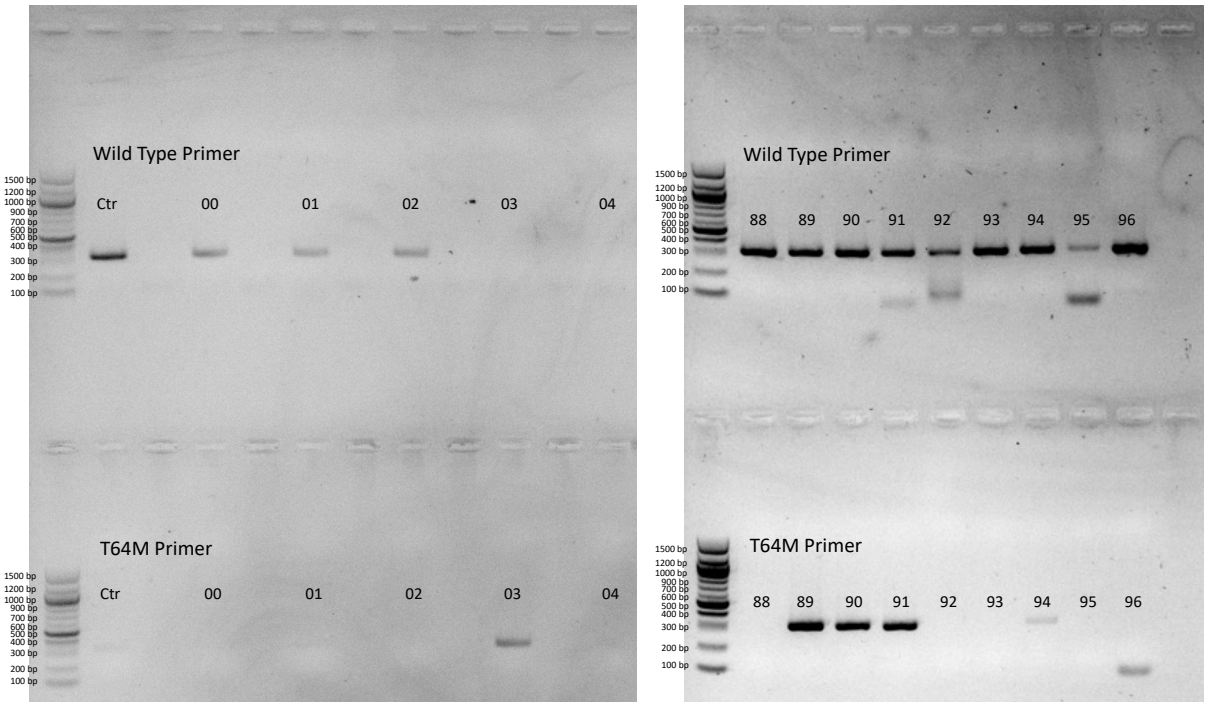

Figure 53 - Genotyping electrophoresis results of Rab4b T64M F1 generation mice. PCR amplification was performed following lysis and purification of the biopsies. Two different primer pairs were used for amplification: one that anneals exclusively to the wild-type sequence and another that anneals only if the T64M mutation is present. Wild-type animals exhibit a DNA band amplified solely by the wild-type primer pair, while T64M homozygous animals show a band amplified exclusively by the T64M primer pair. Heterozygous animals display bands in both PCR results. Potential Rab4b knockout animals may exhibit a shorter wild-type or T64M band.

Table 26 - Genotyping results of Rab4b T64M F1 generation mice.

00	***01***	***02***	***03***	***04***	***88***	***89***
WT	WT	WT	KI	No Signal	WT	WT/KI
90	**91**	**92**	**93**	**94**	**95**	**96**
WT/KI	WT/KI	WT/KO?	WT	WT/KI	WT/KO?	WT/KI short?

To verify that the mice carried the correct sequence, a longer PCR fragment of approximately 600 bp (300 bp upstream and 300 bp downstream of the T64M location) was amplified for the non-wild-type mice and sent for sequencing. An example of the sequencing results for a T64M homozygous and a wild-type animal is shown in Fig. 54. Unfortunately, amplification was not possible for animals 92, 95, and 96. However, for the T64M homozygous and heterozygous animals, the sequencing results confirmed the presence of the correct sequence, including the T64M mutation (sequencing result codes are provided in Supplement Tab. 33). The T64M homozygous, T64M heterozygous, and potentially heterozygous knockout animals were used for further breeding.

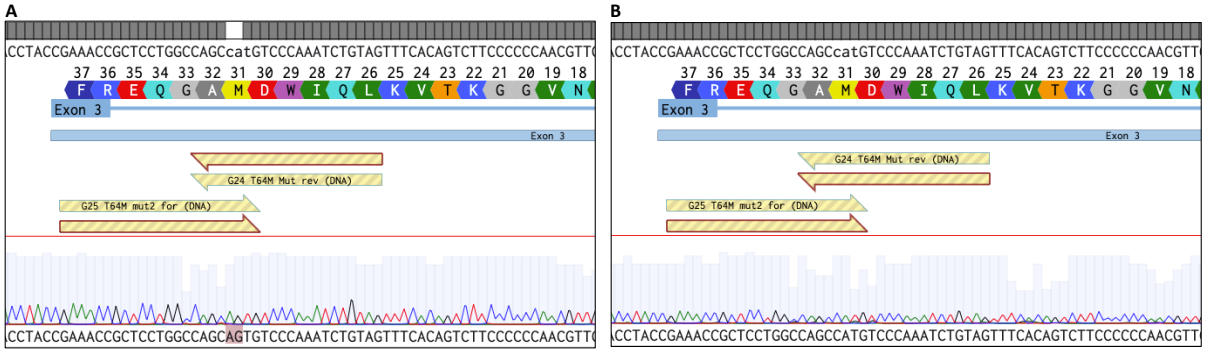

Figure 54 - Sequencing results example for wild type and Rab4b T64M mice. A. Sequencing result example of a wild-type animal. **B.** Sequencing result example of a homozygous Rab4b T64M animal. Sequencing results were analysed with the Benchling online alignment tool.

Genotyping results of the F2 generation revealed five T64M heterozygous animals and two potentially heterozygous Rab4b knockout mice (Fig. 55 Tab. 27). The heterozygous T64M animals exhibited both wild-type and T64M bands, while the knockout animals displayed only a wild-type band in the genotyping PCR. For all heterozygous (T64M and knockout) animals, PCR amplification of the longer fragment was performed (Fig. 56), and the product was sent for sequencing to confirm the presence of the correct and desired sequences.

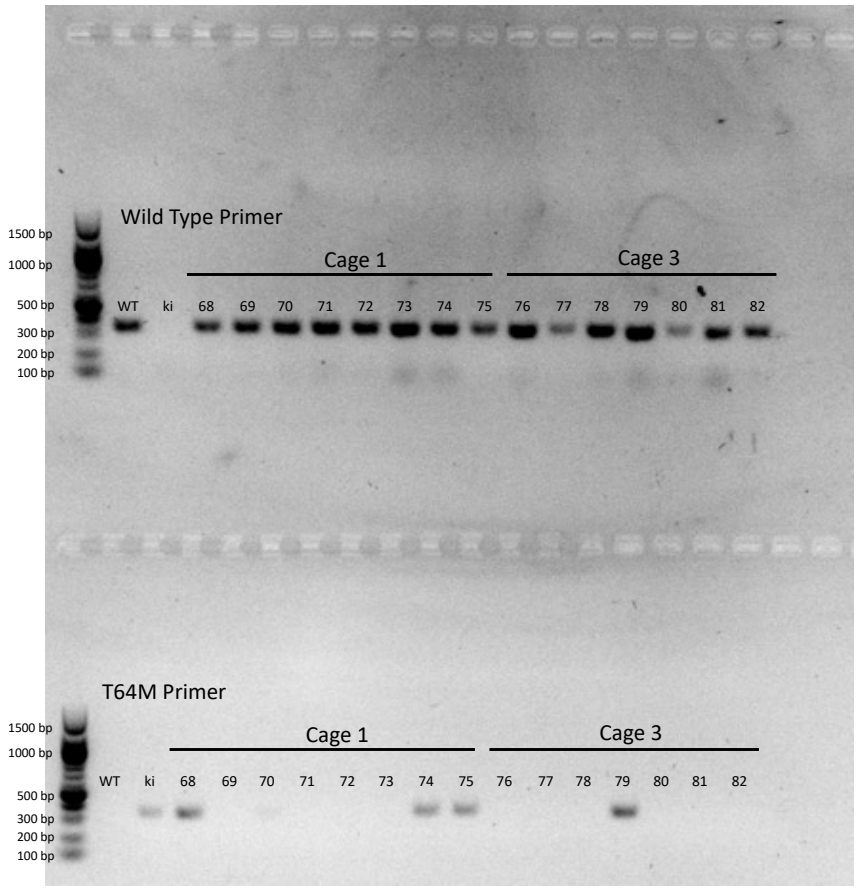

Figure 55 - Genotyping electrophoresis results of Rab4b T64M F2 generation mice. PCR amplification was performed following lysis and purification of the biopsies. Two different primer pairs were used for amplification: one that anneals exclusively to the wild-type sequence near the target position and the other that anneals only if the T64M mutation is present. Wild-type animals show a DNA band amplified only by the wild-type primer pair, while T64M homozygous animals exhibit a band amplified exclusively by the T64M primer pair. Heterozygous animals display bands in both PCR results. Potential Rab4b knockout animals may exhibit a shorter wild-type or T64M band.

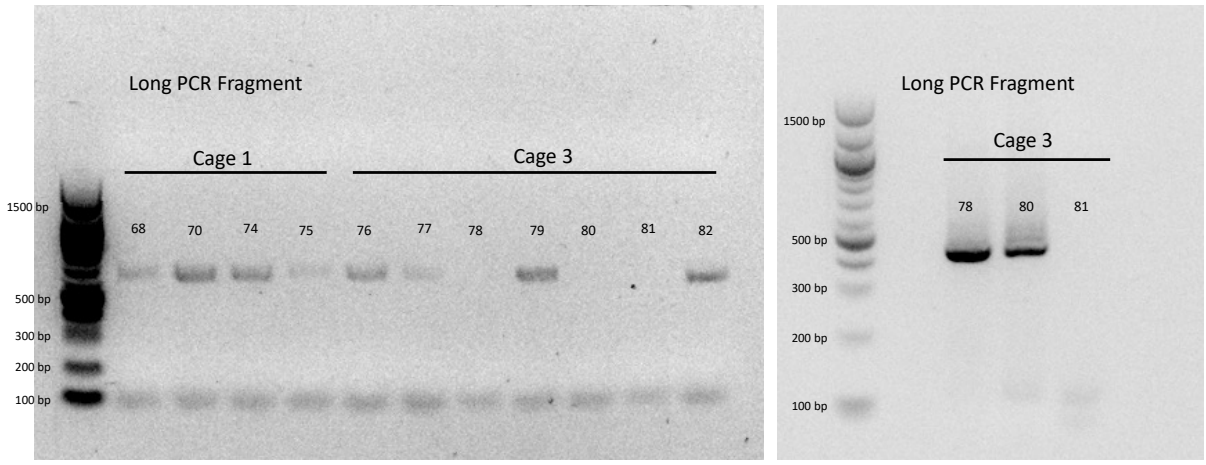

Figure 56 - Long fragment PCR amplification electrophoresis results of Rab4b T64M F2 generation mice. The primer pair for the long DNA fragment anneals approximately 300 bp upstream and 300 bp downstream of the T64M mutation, resulting in a 600 bp long DNA fragment. Rab4b knockout animals may also exhibit shorter fragments.

Table 27 - Genotyping results of Rab4b T64M F2 generation animals.

68	***69***	***70***	***71***	***72***	***73***	***74***	***75***
WT/KI	WT	WT/KI	WT	WT	WT	WT/KI	WT/KI
76	**77**	**78**	**79**	**80**	**81**	**82**	
WT	WT	WT/KO?	WT/KI	WT/KO?	WT	WT	

Sequencing results (sequencing results codes are provided in Supplement Tab. 34) confirmed that animals 68, 70, 74, 75, and 79 carry the T64M mutation. These mice can be used for further breeding and/or for the initial hearing measurements to determine whether the mutation already impacts hearing in heterozygous mice. Unfortunately, no sequence alterations were observed in animals 78 and 80, suggesting that these animals are likely wild-types.

7. Discussion

7.1 Characterization of the Otof-p. KL>M mouse line

Mutations in *OTOF* were occasionally found to cause mild to moderate progressive hearing loss (Vona *et al*, 2020; Yasunaga *et al*, 1999). Here, a mouse line with a three base pair deletion recapitulating this phenotype was analyzed.

Hearing measurements revealed an age-dependent hearing loss in response to click, noise, and tone burst stimuli, which was most evident at twelve months of age in Otof-p. KL>M mice. Interestingly, in humans most *OTOF* variants lead to congenital or early onset hearing impairment and only few (n=3) to progressive hearing loss (Vona *et al*, 2020).

The wave amplitudes of click measurements were already altered in one- and six-month-old Otof-p. KL>M mice, indicating that signal transduction is not functioning properly in Otof-p. KL>M mice, even in younger animals. Notably, wave I amplitude, which represents the activity of the auditory nerve, was significantly lower in Otof-p. KL>M mice. In contrast, DPOAE measurements revealed no differences between Otof-p. KL>M and wild type mice, which is consistent with the finding that the number of OHCs was not different between the genotypes.

Otof-p. KL>M mice show a decrease in otoferlin intensity in IHCs, an effect that is more pronounced in twelve-month-old mice. This decrease could result from pronounced degradation or less protein synthesis, or a combination of both. Depending on the localization and the physicochemical properties of the substituted or deleted amino acid residues, variants can significantly impair protein stability and promote protein degradation (Vona *et al*, 2020). Misfolding of one domain may also lead to proteasomal degradation of the entire mutated protein.

While twelve-month-old Otof-p. KL>M mice maintain otoferlin levels at approximately 75% of wild type levels, the *pachanga* mouse model for example, carrying a D1767G mutation in the C2F domain, exhibits reduced otoferlin levels, approximately 30% of normal levels in IHCs, likely due to misfolding and subsequent degradation (Pangrsic *et al*, 2010). Mice carrying the Ile515Thr missense mutation, which causes temperature-sensitive auditory synaptopathy (Varga *et al*, 2006), also revealed a reduction (~65%) of otoferlin levels in IHCs, presumably due to increased degradation of the mutated protein (Strenzke *et al*, 2016). The differences in otoferlin levels between the three mouse models could be due to their different effects in the protein misfolding. The D1767G mutation could for example lead to a more severe misfolding compared to the other two mutations.

Our experiments further showed that the Otof-p. KL>M mutation leads to IHC loss in six- and twelve-month-old mice. This also aligns with the fact that we did not observe any differences in otoferlin intensity or IHC numbers in one-month-old mice.

It is already known that otoferlin knockout mice exhibit age-dependent IHC loss, with an overall loss of 25% of IHCs compared to wild type mice (at 24 weeks). However, a more pronounced loss occurs in the basal regions of the cochlea (Stalmann *et al*, 2021). While the IHC loss was not as severe in Otof-p. KL>M mice (~85% apical and ~69% basal hair cells compared to wild-type at 12 months), we also observed a more pronounced loss in the midbasal/basal turn compared to the apical part of the organ of Corti.

We further observed an alteration in the number of synapses in twelve-month-old Otof-p. KL>M mice. *Otof* mutations can generally impact the IHC synapse in several ways, such as altering synaptic transmission, affecting vesicle dynamics, impairing synapse development and maintenance, and leading to progressive degeneration of auditory structures (Takago *et al*, 2018; Stalmann *et al*, 2021; Leclère & Dulon, 2023; Yin *et al*,

2023; Tsuzuki *et al*, 2023; Dulon *et al*, 2024). Nevertheless, we only observed a decrease in the number of synapses in twelve-month-old Otof-p. KL>M mice compared to wild-types of the same age. Interestingly, twelve-month-old wild-type IHCs revealed higher number of synapses compared to six-month-old wild-type IHCs. Upon closer examination of the number of cells with low synapse numbers, it can be hypothesized that the increased number of synapses in the twelve-month-old wild type mice is due to a loss of IHCs with low numbers of synapses, which may lead to cell death between six and twelve months, thus not being observable in the twelve-month-old wild type mice. Interestingly, Otof-p. KL>M mice generally exhibit more cells with low numbers of synapses, which suggests a synapse maintenance problem. This observation may contribute to the decrease in the wave I amplitude.

The FerA domain is a four-helix bundle fold, a characteristic structural element of the ferlin protein family. Structure predictions for the wild type and KL>M C2-FerA domain revealed a shortened α-helix in the membrane-binding region of the mutated structure, resulting in a longer flexible loop connecting two different α-helices. The FerA domain exhibits calcium-dependent phospholipid-binding activity, suggesting that its interaction with membranes is enhanced in the presence of Ca^{2+}, likely contributing to otoferlin's overall calcium sensitivity (Leclère & Dulon, 2023; Harsini *et al*, 2018).

The introduced mutation and the resulting shortened α-helix may disturb otoferlin's calcium-dependent membrane fusion, which could further explain the decreased wave I amplitude measured in Otof-p. KL>M mice at all three ages.

Interestingly, at least at young age, Otof-p. KL>M otoferlin can still be phosphorylated and interact with calbindin, forming a Ca^{2+}-dependent signaling complex that may regulate different modes of endocytosis (Cepeda *et al*, 2019). Nevertheless, this interaction is decreased (lower PLA fluorescence levels) under stimulation conditions which further proves that the structural changes disturb the mentioned otoferlin tasks.

In future, it would be interesting to prove that the α-helix is indeed shortened e.g. with circular dichroism spectroscopy or X-ray spectroscopy. However, crystallization of otoferlin is very challenging as to date only the C2A domain was successfully crystallized (Helfmann *et al*, 2011). Furthermore, it would also be interesting to perform gene therapy on those mice and see how efficient it is, in *Otof* models with progressive hearing loss.

Taken together, these findings underscore the critical role of the otoferlin C2-FerA domain in preserving IHC integrity and functional competence.

7.2 AAV production optimization

AAV production optimization was carried out with the aim of establishing a reliable small-scale AAV production protocol within our laboratory. This approach is advantageous due to its lower resource demands, transfection can be performed in just two to four 10-cm culture dishes, and shorter turnaround time compared to standard large-scale methods. During the optimization process, multiple production steps were evaluated, including transfection conditions, harvesting methods, and purification strategies. Key variables tested included different cell lines, transfection reagents and protocols, transfection duration, and two distinct purification approaches.

In the transfection optimization, both tested cell lines, AAV-293 and HEK293T, produced comparably high viral titers. The AAV-293 cell line was selected for the final protocol due to its specialization for AAV production and lower passage number. Similarly, both tested transfection reagents, Turbofect and $CaPO_4$, yielded high titers, but $CaPO_4$ was chosen for subsequent experiments due to its comparable efficiency, ease of use, and significantly lower cost.

The duration of transfection significantly impacted viral yield. Higher titers were observed when AAVs were harvested two days post-transfection, compared to three days. This difference may be attributed to increased cell death by day three, causing viral particles to accumulate in the discarded medium. As a result, all subsequent AAV preparations used a two-day transfection period.

Typically, AAV production requires three plasmids: the vector genome plasmid containing the ITR-flanked transgene, the Rep/Cap plasmid encoding replication and capsid proteins, and the adenoviral helper plasmid encoding E2a, E4orf6, and VA RNA genes (Wang *et al*, 2019). However, a simplified two-plasmid system also exists, which combines the Rep/Cap and helper functions into a hybrid helper plasmid (Grimm *et al*, 1998, 2003).This double transfection approach simplifies production and reduces cost while maintaining comparable titers (Tang *et al*, 2020), with some reports noting a 34–222% increase in productivity (van Lieshout *et al*, 2023). In our experiments, however, triple transfection unexpectedly resulted in higher titers for the PHP.B vector compared to double transfection, potentially due to suboptimal plasmid quality in the latter. Consequently, all subsequent PHP.B and PHP.eB vectors were produced via triple transfection, while AAV6 production employed the double transfection method due to the availability of only a corresponding dual-plasmid system.

For the viral harvesting step, two lysis methods, freeze/thaw and sonication, were compared. Sonication yielded slightly higher titers and was therefore adopted for the optimized protocol due to its simplicity and lower risk of damaging viral particles.

Purification posed more challenges than other production steps. Two methods were tested: iodixanol gradient ultracentrifugation (a standard technique, performed by Niklas Keppeler) and affinity chromatography using the AAVX Poros column (Florea *et al*, 2022). The iodixanol gradient approach resulted in substantial loss of viral particles, whereas the affinity chromatography method proved more efficient,

particularly in minimizing viral loss. However, purification outcomes varied depending on the serotype. The three tested vectors (AAV6, PHP.B, and PHP.eB) showed different binding efficiencies to the column, suggesting serotype-specific differences in affinity. Despite the advantages of the affinity chromatography approach, neither method yielded titers sufficient for use in downstream applications such as in vitro transduction experiments. As a result, unpurified vectors were used for these experiments.

While a limitation of small-scale AAV production is the relatively low yield of viral particles, in all cases sufficient quantities were generated for the intended applications, such as organ of Corti transduction assays. However, for future applications involving in vivo gene therapy, it may become necessary to scale up production or outsource vector manufacturing to specialized facilities or companies to obtain higher titers and fully purified vectors.

7.3 AAV in vitro transduction on organ of Corti cultures

AAVs have emerged as essential tools in inner ear gene therapy, offering a promising strategy for the treatment of genetic hearing loss and other auditory disorders. Their capacity to efficiently transduce cochlear and vestibular cells, while ensuring long-term gene expression, makes them ideal vectors for therapeutic gene delivery. Recent advancements in AAV engineering have led to the development of novel serotypes with enhanced tropism for specific inner ear cell types, thereby improving therapeutic outcomes. However, the increasing number of available serotypes has made it more challenging to identify the most suitable candidates for in vivo studies.

To address this challenge, we established a novel in vitro transduction platform designed to serve as a pre-screening tool for evaluating AAV serotype efficiency in the

organ of Corti. Initially, three AAV serotypes encoding GFP as a reporter were produced and tested: AAV6 (previously used as control in in vivo *Otof* gene therapy; (Al-Moyed *et al*, 2019)), and the two AAV9-derived serotypes PHP.B and PHP.eB. PHP.B has demonstrated efficient transduction of both IHCs and OHCs with robust GFP expression (Lee *et al*, 2020), whereas PHP.eB is recognized for its high efficiency at low doses, making it one of the most potent vectors for cochlear gene delivery (Hu *et al*, 2019).

Consistent with these prior reports, PHP.eB-GFP exhibited the highest transduction efficiency in IHCs and OHCs within both the apical and midbasal turns of the organ of Corti. Notably, PHP.eB transduction was restricted to sensory cells, which are primary targets in many gene therapy strategies, such as *OTOF* gene therapy. PHP.B also achieved high transduction rates, albeit lower than PHP.eB, and displayed a broader distribution beyond the sensory cells. In contrast, AAV6-GFP demonstrated the lowest transduction efficiency, with widespread but weak signal throughout the tissue. Interestingly, previous attempts to transduce hair cells in vitro using AAV6 had failed, indicating that our newly developed method represents a significant improvement and may be suitable for serotype screening prior to in vivo applications.

The differential tropism of AAV serotypes is governed by multiple mechanisms, including interactions between the viral capsid and host cell receptors, as well as intracellular processing following entry. Each serotype engages distinct primary receptors, such as heparan sulfate proteoglycan (AAV2), sialic acid (AAV5/6), or galactose (AAV9), along with co-receptors like integrins or fibroblast growth factor receptor 1 to facilitate viral entry (Castle *et al*, 2016; O'Carroll *et al*, 2021). PHP.B and PHP.eB are particularly effective at targeting IHCs and OHCs due to engineered capsid modifications that enhance cellular entry. In the case of PHP.eB, a seven-amino acid insertion in the AAV9 capsid promotes binding to LY6A, a receptor expressed in

endothelial and neuronal tissues (Chatterjee *et al*, 2022; Palfi *et al*, 2022). Additionally, weakened interaction with the canonical AAVR receptor shifts tropism toward LY6A-mediated pathways, thereby enhancing both efficiency and specificity in cochlear sensory cells (Fortuna *et al*, 2025).

These initial in vitro experiments confirm the utility of this screening approach for evaluating AAV serotypes prior to conducting in vivo studies. The method offers several advantages: it reduces the number of animals required, is less time-intensive than in vivo studies, and is relatively straightforward to perform.

Following the successful proof-of-concept, additional engineered serotypes were generously provided by the group of Prof. Dr. Stylianos Michalakis (LMU, Munich). These included two AAV1-derived vectors (AAV1 GL and AAV1 GLR), two AAV2-derived vectors (AAV2 PT and AAV2 RTAR), and one AAV9-derived vector (AAV9 RTAR), all originally developed to enhance retinal transduction.

Among the AAV1 variants, AAV1 GLR demonstrated relatively low transduction rates in both IHCs and OHCs, whereas AAV1 GL showed improved efficiency, particularly in the midbasal region of the organ of Corti. Both variants feature a twelve-amino acid insertion within the HSPG-binding motif (Pavlou *et al*, 2021; Romanovsky *et al*, 2025). Wild-type AAV1 is known to have good tropism for hair cells (60-94% of IHCs) (Tan *et al*, 2019; Wang *et al*, 2022; Zhang *et al*, 2023), and these insertions could further enhance its tropism in the cochlea. Importantly, because AAV1 tropism is not dependent on sulfate binding, it may achieve broader tissue penetration, which could explain the broader distribution observed for these variants (Kim *et al*, 2019). It must be noted, that the wild-type version of AAV1 is for example used in a current Chinese bilateral *OTOF* clinical study (Wang *et al*, 2024a). The AAV9 GLR variant showed reduced efficiency compared to PHP.eB and lacked sensory cell specificity, limiting its potential for targeted inner ear therapy. In contrast, both AAV2-derived variants (AAV2

PT and AAV2 RTAR) resulted in GFP expression specifically within IHCs and OHCs. Among all tested serotypes, AAV2 PT demonstrated the highest overall transduction efficiency, approaching ~100% in both apical and midbasal turns, and exhibited restricted transduction to sensory cells. This suggests that the PT insertion enhances both specificity and efficiency. The use of heparan sulfate as a potential receptor for AAV2 may contribute to this targeted distribution (Kim *et al*, 2019). Additionally, the previously reported decrease in AAV2 tropism from base to apex (Shu *et al*, 2016) was also observed in AAV2 RTAR, further supporting biological relevance.

Based on these findings, AAV2 PT appears to be the most promising candidate for future in vivo gene therapy applications targeting IHCs and OHCs. Another highly promising vector candidate evaluated both in vitro and in vivo in murine models by Landegger *et al*, (2017) and used in the *OTOF* clinical trial of Akouos/Elli Lilly (Vishnu, 2024) is the synthetic serotype Anc80L65. This capsid was designed in silico and demonstrated robust transduction efficiency of IHCs and OHCs, achieving 60–100% transduction in both the apical and basal regions of the organ of Corti in vitro (Landegger *et al*, 2017). Unlike AAV2 PT, Anc80L65 exhibited broader tropism, efficiently transducing multiple cochlear cell types beyond IHCs and OHCs. Consistent with the in vitro findings, in vivo experiments in mice revealed similarly high transduction efficiencies, with nearly 100% of IHCs and approximately 90% of OHCs being transduced. These results suggest that, at least for serotypes with high in vitro transduction efficiency, similar performance may be achievable in vivo. An advantage of in silico-engineered capsids such as Anc80L65 and AAV2 PT is that they are antigenically distinct from circulating AAVs. This fact may provide a potential benefit in terms of pre-existing immunity, which could limit the efficacy of wild-type AAV serotypes (Landegger *et al*, 2017). Nevertheless, it needs to be mentioned, that there can also be cross-reactivity of antibody response. If antibodies that bind to a certain

serotype (e.g. AAV7, AAV8 or AAV9) already exist, there are also antibodies that bind to AAV2 (Calcedo & Wilson, 2013).

To evaluate whether our in vitro method could also accommodate dual-AAV strategies, necessary for large transgenes such as *OTOF*, we tested the three previously produced serotypes (AAV6, PHP.B, and PHP.eB) in a dual-AAV setup. Each pair of AAVs carried either the N- or C-terminal fragment of the *Otof* sequence. In contrast to Al-Moyed et al. (2019), we used a protein-level recombination approach employing inteins, which are known to yield higher protein expression levels (Tornabene *et al*, 2019; Ferla *et al*, 2025; Tang *et al*, 2023). Two distinct splitting positions within the *Otof* sequence were tested, both containing the critical serine residue required for successful splicing by the GP41-1 split intein. This intein relies on specific extein residues (Y–1, S+2, S+3) and uniquely uses serine, rather than cysteine, at the +1 catalytic site, broadening its compatibility with various protein contexts (Beyer *et al*, 2020; Yao *et al*, 2020).

Version 1 (split at position 783) included the additional serine at the +2 position, while Version 2 (split at position 917) did not. Interestingly, neither version resulted in successful recombination when packaged in AAV6, consistent with the poor transduction efficiency observed for AAV6-GFP. In contrast, both PHP.B and PHP.eB enabled robust dual-AAV transduction in IHCs and OHCs, but only with Version 1. This supports the notion that the serine at the +2 position is critical for effective GP41-1-mediated recombination. In addition, other studies have shown, that loop structures are more suitable for intein insertion (Apgar *et al*, 2012; Sun *et al*, 2004). While the version 1 cutting site is positioned at a loop structure of otoferlins C2-FerA domain, the version 2 cutting site is positioned at the β-sheet. This could be an additional feature explaining why version 1 was more successful compared to version 2. As such, Version 1 and either the PHP.B or PHP.eB serotype should be prioritized for future in

vivo studies. The split intein method was already tested in mice by Tang *et al*, (2023), however with the Rma intein which has its origin in *Rhadothermus marinus* DnaB (Liu & Hu, 1997). Also, in this study, the chosen cutting site was positioned on a loop structure (S1114). The two *Otof* and intein sequences were packaged in the PHP.eB vector, which also revealed promising results in our in vitro study. One month after round window injection in P0-P2 *Otof* $^{-/-}$ mice, ABR measurements were performed which revealed a significant hearing rescue (responses to click and tone-burst stimuli) compared to untreated mice meaning that indeed inteins can be an alternative recombination option in dual-AAV gene therapy approaches in the inner ear (Tang *et al*, 2023). Interestingly, the co-transduction rate in IHCs was ~70% with PHP.eB, while in our in vitro experiments (with PHP.B and PHP.eB) it was ~100%. This could indicate, that different from single AAV transduction as shown by Landegger *et al*, (2017), dual-AAV transduction may differ between in vitro and in vivo experiments. It further must be mentioned that Tang *et al*, (2023) used a different split intein, which may also influence successful protein recombination. The artificially designed GP41-1 intein, used for the dual-AAV in vitro experiments was shown to have better constant rates especially compared to naturally occurring inteins like Npu DnaE (Carvajal-Vallejos *et al*, 2012), which may also be a reason for the better co-transduction efficiency. Nevertheless, these are only speculations, as the Rma was not tested in vitro. The advantage of the GP41-1 intein is that it is shorter (125 amino acids) compared to Rma (428 amino acids), used by Tang *et al*, (2023). As AAVs have only limited capacity a shorter intein with same or better efficiency would always be the preferred one. Taken together the GP41-1 intein is a very promising candidate for dual-AAV *Otof* gene therapy approaches that can be used for future in vivo studies.

7.4 Rab4b in the inner ear

RAB4B is a small GTPase belonging to the Ras superfamily and plays a critical role in the regulation of vesicular trafficking during endocytosis and exocytosis, particularly in the recycling of membranes and receptors. The protein localizes to early and recycling endosomes, where it coordinates cargo sorting and vesicle motility. Despite its well-characterized roles in general cellular processes, its function in the inner ear remains unknown. However, a dominantly inherited point mutation in the *RAB4B* gene was identified in several patients with progressive hearing loss, indicating the need to investigate its role in auditory function.

To address this, we performed RNA Scope and immunostaining analyses on cochlear sections and organ of Corti whole mounts to examine the expression of Rab4b RNA and protein. Both were detected in the stria vascularis, IHCs, OHCs, and SGNs of one-, six-, and twelve-month-old mice. Interestingly, Rab4b protein expression in IHCs and OHCs appeared stronger in six- and twelve-month-old mice compared to one-month-old mice. However, when immunostaining was conducted independently of RNA Scope, a similarly strong signal was also observed in IHCs and OHCs of one-month-old mice. Therefore, the initially observed difference is likely attributable to methodological variation rather than age-dependent biological changes.

Rab4b shares a high degree of sequence identity with Rab4a (~85% identical amino acid sequence), another member of the Rab family. As a result, there is a possibility that the Rab4b antibody may exhibit some cross-reactivity with Rab4a. Nevertheless, both Rab4b and Rab4a RNA and protein were found to colocalize, particularly in SGNs where expression levels were notably high. In general, the localization patterns of both proteins in the inner ear were nearly identical.

Given the critical roles of hair cells and SGNs in auditory processing, it is plausible that the *RAB4B* point mutation identified in patients contributes to their hearing impairment. Gene mutations that disrupt the function of proteins in SGNs, IHCs, or OHCs often result in a range of developmental and degenerative auditory deficits. For instance, *POU3F4* mutations impair SGN survival and synaptic regulation, leading to congenital deafness. Similarly, *VGLUT3* mutations disrupt glutamatergic signalling from IHCs, causing selective degeneration of type Ic SGNs (Zhang *et al*, 2022). Furthermore, as previously described, *OTOF* mutations impair Ca^{2+}-dependent glutamate release at IHC ribbon synapses, thereby disrupting signal transmission to SGNs (Strenzke *et al*, 2016).

Although we have now confirmed that Rab4b is expressed in important cochlear cell types involved in hearing, its precise function within these cells and the biological mechanisms affected by the T64M point mutation remain unclear. Interestingly, patients carrying this mutation have an auditory neuropathy, meaning that their OAEs are or were at the testing time point intact, although Rab4b was also found to be expressed in the OHCs. To further investigate the function of Rab4b and especially the mechanisms affected by the T64M mutation, a mouse line was generated carrying the T64M mutation. The F2 generation of heterozygous mice has already been born, and sequencing has confirmed the presence of the correct mutation. Future studies, including immunostainings, ABRs, DPOAEs, and additional analyses, are planned using heterozygous, homozygous T64M, and Rab4b knockout mice. These experiments will help elucidate the role of Rab4b in the inner ear and are essential for identifying potential therapeutic strategies for affected patients.

8. Conclusion and outlook

8.1 Characterization of the Otof-p. KL>M mouse line

In this study, we aimed to better understand the function of the otoferlin C2-FerA domain by generating a new mouse line carrying a mutation in this domain. By characterizing the Otof-p. KL>M mice and comparing them to wild-type mice, we found that the mutant mice exhibit age-related hearing loss and reduced ABR wave amplitudes at a young age. Furthermore, Otof-p. KL>M mice show reduced otoferlin levels, increased IHC loss, and reduced synapse numbers at older ages.

All of these observations could be the result of a misfolded C2-FerA domain, which could lead to protein degradation or disrupt the membrane or Ca^{2+} activity of the C2-FerA domain α-helices. In future studies it would be interesting prove that the α-helix is indeed shortened. Furthermore, performing dual-AAV gene therapy on those mice will give insights on how efficient this gene therapy approach is in *Otof* models with progressive hearing loss. Taken together, this study highlights the importance of otoferlin's C2-FerA domain in the hearing process.

8.2 AAV in vitro transduction in the organ of Corti

This study demonstrates the successful establishment of an in vitro AAV transduction model for the organ of Corti, which serves as a robust pre-screening platform for assessing AAV serotype tropism and transduction efficiency. Among all tested variants, AAV2 PT exhibited the highest specificity and efficiency in targeting IHCs and OHCs, making it the most promising candidate for future in vivo gene therapy approaches. Moreover, the dual-AAV experiments using intein-mediated protein recombination validated the feasibility of delivering large genes such as *Otof* in vitro.

The findings underscore the critical importance of capsid selection and recombination design in optimizing gene delivery strategies.

Looking ahead, it will be essential to compare the in vitro results with in vivo transduction data to determine the applicability of these vectors in live organisms, especially considering potential differences in transduction efficiency across the apical, middle, and basal regions of the cochlea. Furthermore, the injection method employed during in vivo delivery could significantly impact the distribution and efficiency of transduction within different parts of the cochlea. Therefore, continued investigation into the effects of injection techniques will be crucial for refining gene therapy approaches for the inner ear.

8.3 Rab4b expression in the inner ear

Our findings establish that Rab4b is expressed in multiple cochlear cell types essential for auditory processing, including IHCs, OHCs, SGNs, and cells of the stria vascularis. The identification of a dominantly inherited *RAB4B* point mutation in patients with progressive hearing loss, along with its confirmed expression in relevant auditory structures, strongly suggests a functional role in the inner ear. Although its precise molecular function remains to be determined, the development of a T64M mutant mouse model, alongside Rab4b knockout line, provides a robust platform for future studies. These investigations will be crucial for unravelling the underlying mechanisms of RAB4B, related hearing loss and for guiding the development of targeted therapeutic approaches.

8. References

Agbandje-McKenna M & Kleinschmidt J (2011) AAV capsid structure and cell interactions. *Methods Mol Biol* 807: 47–92

Akil O, Dyka F, Calvet C, Emptoz A, Lahlou G, Nouaille S, Boutet de Monvel J, Hardelin J-P, Hauswirth WW, Avan P, *et al* (2019) Dual AAV-mediated gene therapy restores hearing in a DFNB9 mouse model. *Proc Natl Acad Sci U S A* 116: 4496–4501

Allocca M, Doria M, Petrillo M, Colella P, Garcia-Hoyos M, Gibbs D, Kim SR, Maguire A, Rex TS, Vicino UD, *et al* (2008) Serotype-dependent packaging of large genes in adeno-associated viral vectors results in effective gene delivery in mice. *J Clin Invest* 118: 1955–1964

Al-Moyed H, Cepeda AP, Jung S, Moser T, Kügler S & Reisinger E (2019) A dual-AAV approach restores fast exocytosis and partially rescues auditory function in deaf otoferlin knock-out mice. *EMBO Mol Med* 11: e9396

Apgar J, Ross M, Zuo X, Dohle S, Sturtevant D, Shen B, Vega H de la, Lessard P, Lazar G & Raab RM (2012) A Predictive Model of Intein Insertion Site for Use in the Engineering of Molecular Switches. *PLOS ONE* 7: e37355

Baek M, DiMaio F, Anishchenko I, Dauparas J, Ovchinnikov S, Lee GR, Wang J, Cong Q, Kinch LN, Schaeffer RD, *et al* (2021) Accurate prediction of protein structures and interactions using a three-track neural network. *Science* 373: 871–876

References

Bartel MA, Weinstein JR & Schaffer DV (2012) Directed evolution of novel adeno-associated viruses for therapeutic gene delivery. *Gene Ther* 19: 694–700

Bartlett JS, Samulski RJ & McCown TJ (1998) Selective and rapid uptake of adeno-associated virus type 2 in brain. *Hum Gene Ther* 9: 1181–1186

Beyer HM, Mikula KM, Li M, Wlodawer A & Iwaï H (2020) The crystal structure of the naturally split gp41-1 intein guides the engineering of orthogonal split inteins from cis-splicing inteins. *FEBS J* 287: 1886–1898

Bulcha JT, Wang Y, Ma H, Tai PWL & Gao G (2021) Viral vector platforms within the gene therapy landscape. *Sig Transduct Target Ther* 6: 1–24

Calcedo R & Wilson JM (2013) Humoral Immune Response to AAV. *Front Immunol* 4

Carvajal-Vallejos P, Pallissé R, Mootz HD & Schmidt SR (2012) Unprecedented rates and efficiencies revealed for new natural split inteins from metagenomic sources. *J Biol Chem* 287: 28686–28696

Castle MJ, Turunen HT, Vandenberghe LH & Wolfe JH (2016) Controlling AAV Tropism in the Nervous System with Natural and Engineered Capsids. *Methods Mol Biol* 1382: 133–149

Cepeda AP, Al-Moyed H, Lenz C, Urlaub H & Reisinger E (2019) PKCα-dependent interaction of otoferlin and calbindin: evidence for regulation of endocytosis in inner hair cells. 779520 doi:10.1101/779520 [PREPRINT]

References

Chakrabarti R, Michanski S & Wichmann C (2018) Vesicle sub-pool organization at inner hair cell ribbon synapses. *EMBO Rep* 19: e44937

Chatterjee D, Marmion DJ, McBride JL, Manfredsson FP, Butler D, Messer A & Kordower JH (2022) Enhanced CNS transduction from AAV.PHP.eB infusion into the cisterna magna of older adult rats compared to AAV9. *Gene Ther* 29: 390–397

Chen B-J, Qian X, Yang X, Jiang T, Wang Y, Lyu J, Chi F, Chen P & Ren D (2021) Rab11a Regulates the Development of Cilia and Establishment of Planar Cell Polarity in Mammalian Vestibular Hair Cells. *Front Mol Neurosci* 14: 762916

Chiu Y-H, Wu C-C, Lu Y-C, Chen P-J, Lee W-Y, Liu AY-Z & Hsu C-J (2010) Mutations in the OTOF Gene in Taiwanese Patients with Auditory Neuropathy. *Audiology and Neurotology* 15: 364–374

Choi J-H, Yu N-K, Baek G-C, Bakes J, Seo D, Nam HJ, Baek SH, Lim C-S, Lee Y-S & Kaang B-K (2014) Optimization of AAV expression cassettes to improve packaging capacity and transgene expression in neurons. *Mol Brain* 7: 17

Corvino V, Apisa P, Malesci R, Laria C, Auletta G & Franze A X-Linked Sensorineural Hearing Loss: A Literature Review. *Current Genomics* 19: 327–338

Delprato A, Merithew E & Lambright DG (2004) Structure, exchange determinants, and family-wide rab specificity of the tandem helical bundle and Vps9 domains of Rabex-5. *Cell* 118: 607–617

References

Denard J, Rouillon J, Leger T, Garcia C, Lambert MP, Griffith G, Jenny C, Camadro J-M, Garcia L & Svinartchouk F (2018) AAV-8 and AAV-9 Vectors Cooperate with Serum Proteins Differently Than AAV-1 and AAV-6. *Mol Ther Methods Clin Dev* 10: 291–302

Denoyelle F, Weil D, Maw MA, Wilcox SA, Lench NJ, Allen-Powell DR, Osborn AH, Dahl HH, Middleton A, Houseman MJ, *et al* (1997) Prelingual deafness: high prevalence of a 30delG mutation in the connexin 26 gene. *Hum Mol Genet* 6: 2173–2177

Dominguez MJ, McCord JJ & Sutton RB (2022) Redefining the architecture of ferlin proteins: Insights into multi-domain protein structure and function. *PLoS One* 17: e0270188

Dong B, Nakai H & Xiao W (2010) Characterization of genome integrity for oversized recombinant AAV vector. *Mol Ther* 18: 87–92

Dong JY, Fan PD & Frizzell RA (1996) Quantitative analysis of the packaging capacity of recombinant adeno-associated virus. *Hum Gene Ther* 7: 2101–2112

Dong Y, Guo C-R, Chen D, Chen S-M, Peng Y, Song H & Shi J-R (2018) Association between age-related hearing loss and cognitive decline in C57BL/6J mice. *Molecular Medicine Reports* 18: 1726–1732

Duan D, Li Q, Kao AW, Yue Y, Pessin JE & Engelhardt JF (1999) Dynamin is required for recombinant adeno-associated virus type 2 infection. *J Virol* 73: 10371–10376

References

Duan D, Sharma P, Yang J, Yue Y, Dudus L, Zhang Y, Fisher KJ & Engelhardt JF (1998) Circular intermediates of recombinant adeno-associated virus have defined structural characteristics responsible for long-term episomal persistence in muscle tissue. *J Virol* 72: 8568–8577

Dulon D, de Monvel JB, Plion B, Mallet A, Petit C, Condamine S, Bouleau Y & Safieddine S (2024) A free intravesicular C-terminal of otoferlin is essential for synaptic vesicle docking and fusion at auditory inner hair cell ribbon synapses. *Prog Neurobiol* 240: 102658

Ferla R, Pugni E, Lupo M, Tiberi P, Fioretto F, Perota A, Duchi R, Lagutina I, Gesualdo C, Rossi S, *et al* (2025) Retinal gene therapy for Stargardt disease with dual AAV intein vectors is both safe and effective in large animal models. *Science Advances* 11: eadt9354

Ferrari FK, Samulski T, Shenk T & Samulski RJ (1996) Second-strand synthesis is a rate-limiting step for efficient transduction by recombinant adeno-associated virus vectors. *J Virol* 70: 3227–3234

Fields BN, Knipe DM & Howley PM (1996) Fields Virology Lippincott-Raven Publishers
Fischel-Ghodsian N (2003) Mitochondrial deafness. *Ear Hear* 24: 303–313

Fisher KJ, Gao GP, Weitzman MD, DeMatteo R, Burda JF & Wilson JM (1996) Transduction with recombinant adeno-associated virus for gene therapy is limited by leading-strand synthesis. *J Virol* 70: 520–532

References

Florea M, Nicolaou F, Pacouret S, Zinn EM, Sanmiguel J, Andres-Mateos E, Unzu C, Wagers AJ & Vandenberghe LH (2022) High-efficiency purification of divergent AAV serotypes using AAVX affinity chromatography. *Mol Ther Methods Clin Dev* 28: 146–159

Fortuna MG, Nyberg L, Taskin N, Weed N, Hunker A, Gudsnuk K, Berg M, Levi B, Lein E & Ting JT (2025) AAV serotype PHP.eB achieves superior neuronal transduction efficiency compared to AAV9 in pigtail macaques following intracerebroventricular administration. 2025.02.04.636515 doi:10.1101/2025.02.04.636515 [PREPRINT]

Gessler DJ, Li D, Xu H, Su Q, Sanmiguel J, Tuncer S, Moore C, King J, Matalon R & Gao G (2017) Redirecting *N*-acetylaspartate metabolism in the central nervous system normalizes myelination and rescues Canavan disease. *JCI Insight* 2

Ghosh A, Yue Y & Duan D (2011) Efficient Transgene Reconstitution with Hybrid Dual AAV Vectors Carrying the Minimized Bridging Sequences. *Hum Gene Ther* 22: 77–83

Gray SJ, Foti SB, Schwartz JW, Bachaboina L, Taylor-Blake B, Coleman J, Ehlers MD, Zylka MJ, McCown TJ & Samulski RJ (2011) Optimizing Promoters for Recombinant Adeno-Associated Virus-Mediated Gene Expression in the Peripheral and Central Nervous System Using Self-Complementary Vectors. *Hum Gene Ther* 22: 1143–1153

Grieger JC & Samulski RJ (2005) Packaging capacity of adeno-associated virus serotypes: impact of larger genomes on infectivity and postentry steps. *J Virol* 79: 9933–9944

References

Grimm D, Kay MA & Kleinschmidt JA (2003) Helper virus-free, optically controllable, and two-plasmid-based production of adeno-associated virus vectors of serotypes 1 to 6. *Molecular Therapy* 7: 839–850

Grimm D, Kern A, Rittner K & Kleinschmidt JA (1998) Novel tools for production and purification of recombinant adenoassociated virus vectors. *Hum Gene Ther* 9: 2745–2760

Gullapalli (2024) Sensorion completes first cohort enrolment in Phase I/II gene therapy trial. *Clinical Trials Arena*

Gurkan C, Lapp H, Alory C, Su AI, Hogenesch JB & Balch WE (2005) Large-Scale Profiling of Rab GTPase Trafficking Networks: The Membrome. *MBoC* 16: 3847–3864

Harsini FM, Bui AA, Rice AM, Chebrolu S, Fuson KL, Turtoi A, Bradberry M, Chapman ER & Sutton RB (2019) Structural Basis for the Distinct Membrane Binding Activity of the Homologous C2A Domains of Myoferlin and Dysferlin. *J Mol Biol* 431: 2112–2126

Harsini FM, Chebrolu S, Fuson KL, White MA, Rice AM & Sutton RB (2018) FerA is a Membrane-Associating Four-Helix Bundle Domain in the Ferlin Family of Membrane-Fusion Proteins. *Sci Rep* 8: 10949

Healthline (2025) Hearing Loss: Causes, Symptoms and Prevention. *Healthline*

References

Heidrych P, Zimmermann U, Bress A, Pusch CM, Ruth P, Pfister M, Knipper M & Blin N (2008) Rab8b GTPase, a protein transport regulator, is an interacting partner of otoferlin, defective in a human autosomal recessive deafness form. *Hum Mol Genet* 17: 3814–3821

Helfmann S, Neumann P, Tittmann K, Moser T, Ficner R & Reisinger E (2011) The crystal structure of the C_2A domain of otoferlin reveals an unconventional top loop region. *J Mol Biol* 406: 479–490

Howard DB & Harvey BK (2017) Assaying the Stability and Inactivation of AAV Serotype 1 Vectors. *Hum Gene Ther Methods* 28: 39–48

Hu X, Wang J, Yao X, Xiao Q, Xue Y, Wang S, Shi L, Shu Y, Li H & Yang H (2019) Screened AAV variants permit efficient transduction access to supporting cells and hair cells. *Cell Discov* 5: 1–4

Huang L-Y, Halder S & Agbandje-McKenna M (2014) Parvovirus Glycan Interactions. *Curr Opin Virol* 0: 108–118

Issa SS, Shaimardanova AA, Solovyeva VV & Rizvanov AA (2023) Various AAV Serotypes and Their Applications in Gene Therapy: An Overview. *Cells* 12: 785

Johnson KR, Tian C, Gagnon LH, Jiang H, Ding D & Salvi R (2017) Effects of Cdh23 single nucleotide substitutions on age-related hearing loss in C57BL/6 and 129S1/Sv mice and comparisons with congenic strains. *Sci Rep* 7: 44450

Jung S, Maritzen T, Wichmann C, Jing Z, Neef A, Revelo NH, Al-Moyed H, Meese S, Wojcik SM, Panou I, *et al* (2015) Disruption of adaptor protein 2μ (AP-2μ) in cochlear hair cells impairs vesicle reloading of synaptic release sites and hearing. *EMBO J* 34: 2686–2702

Kabahuma RI, Schubert W-D, Labuschagne C, Yan D, Blanton SH, Pepper MS & Liu XZ (2021) Spectrum of MYO7A Mutations in an Indigenous South African Population Further Elucidates the Nonsyndromic Autosomal Recessive Phenotype of DFNB2 to Include Both Homozygous and Compound Heterozygous Mutations. *Genes (Basel)* 12: 274

Kaddai V, Gonzalez T, Keslair F, Grémeaux T, Bonnafous S, Gugenheim J, Tran A, Gual P, Le Marchand-Brustel Y & Cormont M (2009) Rab4b Is a Small GTPase Involved in the Control of the Glucose Transporter GLUT4 Localization in Adipocyte. *PLoS One* 4: e5257

Kaludov N, Brown KE, Walters RW, Zabner J & Chiorini JA (2001) Adeno-associated virus serotype 4 (AAV4) and AAV5 both require sialic acid binding for hemagglutination and efficient transduction but differ in sialic acid linkage specificity. *J Virol* 75: 6884–6893

Kelich JM, Ma J, Dong B, Wang Q, Chin M, Magura CM, Xiao W & Yang W (2015) Super-resolution imaging of nuclear import of adeno-associated virus in live cells. *Mol Ther Methods Clin Dev* 2: 15047

References

Kelsell DP, Dunlop J, Stevens HP, Lench NJ, Liang JN, Parry G, Mueller RF & Leigh IM (1997) Connexin 26 mutations in hereditary non-syndromic sensorineural deafness. *Nature* 387: 80–83

Kim M-A, Ryu N, Kim H-M, Kim Y-R, Lee B, Kwon T-J, Bok J & Kim U-K (2019) Targeted Gene Delivery into the Mammalian Inner Ear Using Synthetic Serotypes of Adeno-Associated Virus Vectors. *Mol Ther Methods Clin Dev* 13: 197–204

Kimberling WJ, Weston MD, Möller C, van Aarem A, Cremers CWRJ, Sumegi J, Ing PS, Connolly C, Martini A, Milani M, *et al* (1995) Gene Mapping of Usher Syndrome Type IIa: Localization of the Gene to a 2.1-cM Segment on Chromosome 1q41. *Am J Hum Genet* 56: 216–223

Kimberling WJ, Weston MD, Möller C, Davenport SLH, Shugart YY, Priluck IA, Martini A, Milani M & Smith RJ (1990) Localization of Usher syndrome type II to chromosome 1q. *Genomics* 7: 245–249

Koeberl DD, Alexander IE, Halbert CL, Russell DW & Miller AD (1997) Persistent expression of human clotting factor IX from mouse liver after intravenous injection of adeno-associated virus vectors. *Proc Natl Acad Sci U S A* 94: 1426–1431

Krawczyk M, Leimgruber E, Seguín-Estévez Q, Dunand-Sauthier I, Barras E & Reith W (2007) Expression of RAB4B, a protein governing endocytic recycling, is co-regulated with MHC class II genes. *Nucleic Acids Res* 35: 595–605

Kroll J, Jaime Tobón LM, Vogl C, Neef J, Kondratiuk I, König M, Strenzke N, Wichmann C, Milosevic I & Moser T (2019) Endophilin-A regulates presynaptic Ca2+ influx and synaptic vesicle recycling in auditory hair cells. *EMBO J* 38: e100116

Kubisch C, Schroeder BC, Friedrich T, Lütjohann B, El-Amraoui A, Marlin S, Petit C & Jentsch TJ (1999) KCNQ4, a Novel Potassium Channel Expressed in Sensory Outer Hair Cells, Is Mutated in Dominant Deafness. *Cell* 96: 437–446

Lai Y, Yue Y & Duan D (2010) Evidence for the Failure of Adeno-associated Virus Serotype 5 to Package a Viral Genome ≥8.2 kb. *Molecular Therapy* 18: 75–79

Landegger LD, Pan B, Askew C, Wassmer SJ, Gluck SD, Galvin A, Taylor R, Forge A, Stankovic KM, Holt JR, *et al* (2017) A synthetic AAV vector enables safe and efficient gene transfer to the mammalian inner ear. *Nat Biotechnol* 35: 280–284

Leclère J-C & Dulon D (2023) Otoferlin as a multirole Ca2+ signaling protein: from inner ear synapses to cancer pathways. *Front Cell Neurosci* 17: 1197611

Lee J, Nist-Lund C, Solanes P, Goldberg H, Wu J, Pan B, Schneider BL & Holt JR (2020) Efficient viral transduction in mouse inner ear hair cells with utricle injection and AAV9-PHP.B. *Hear Res* 394: 107882

Lek A, Evesson FJ, Sutton RB, North KN & Cooper ST (2012) Ferlins: regulators of vesicle fusion for auditory neurotransmission, receptor trafficking and membrane repair. *Traffic* 13: 185–194

Li H, Li H-F, Felder RA, Periasamy A & Jose PA (2008) Rab4 and Rab11 coordinately regulate the recycling of angiotensin II type I receptor as demonstrated by fluorescence resonance energy transfer microscopy. *J Biomed Opt* 13: 031206

Li Y (2015) Split-inteins and their bioapplications. *Biotechnol Lett* 37: 2121–2137

van Lieshout LP, Rubin M, Costa-Grant K, Ota S, Golebiowski D, Panico T, Wiberg E, Szymczak K, Gilmore R, Stanvick M, *et al* (2023) A novel dual-plasmid platform provides scalable transfection yielding improved productivity and packaging across multiple AAV serotypes and genomes. *Mol Ther Methods Clin Dev* 29: 426–436

Liu X-Q & Hu Z (1997) A DnaB intein in Rhodothermus marinus: Indication of recent intein homing across remotely related organisms. *Proceedings of the National Academy of Sciences* 94: 7851–7856

Manchanda A, Bonventre JA, Bugel SM, Chatterjee P, Tanguay R & Johnson CP (2021) Truncation of the otoferlin transmembrane domain alters the development of hair cells and reduces membrane docking. *MBoC* 32: 1293–1305

Manno CS, Chew AJ, Hutchison S, Larson PJ, Herzog RW, Arruda VR, Tai SJ, Ragni MV, Thompson A, Ozelo M, *et al* (2003) AAV-mediated factor IX gene transfer to skeletal muscle in patients with severe hemophilia B. *Blood* 101: 2963–2972

Marchetta P, Eckert P, Lukowski R, Ruth P, Singer W, Rüttiger L & Knipper M (2022) Loss of central mineralocorticoid or glucocorticoid receptors impacts auditory nerve processing in the cochlea. *iScience* 25: 103981

Matsunaga T, Mutai H, Kunishima S, Namba K, Morimoto N, Shinjo Y, Arimoto Y, Kataoka Y, Shintani T, Morita N, *et al* (2012) A prevalent founder mutation and genotype–phenotype correlations of OTOF in Japanese patients with auditory neuropathy. *Clinical Genetics* 82: 425–432

McCarty DM, Fu H, Monahan PE, Toulson CE, Naik P & Samulski RJ (2003) Adeno-associated virus terminal repeat (TR) mutant generates self-complementary vectors to overcome the rate-limiting step to transduction in vivo. *Gene Ther* 10: 2112–2118

Meese S, Cepeda AP, Gahlen F, Adams CM, Ficner R, Ricci AJ, Heller S, Reisinger E & Herget M (2017) Activity-Dependent Phosphorylation by CaMKIIδ Alters the Ca2+ Affinity of the Multi-C2-Domain Protein Otoferlin. *Front Synaptic Neurosci* 9: 13

Michalski N, Goutman JD, Auclair SM, Boutet de Monvel J, Tertrais M, Emptoz A, Parrin A, Nouaille S, Guillon M, Sachse M, *et al* (2017) Otoferlin acts as a Ca2+ sensor for vesicle fusion and vesicle pool replenishment at auditory hair cell ribbon synapses. *Elife* 6: e31013

Migliosi V, Modamio-Høybjør S, Moreno-Pelayo MA, Rodríguez-Ballesteros M, Villamar M, Tellería D, Menéndez I, Moreno F & Del Castillo I (2002) Q829X, a novel mutation in the gene encoding otoferlin (OTOF), is frequently found in Spanish patients with prelingual non-syndromic hearing loss. *J Med Genet* 39: 502–506

Mills KV, Johnson MA & Perler FB (2014) Protein splicing: how inteins escape from precursor proteins. *J Biol Chem* 289: 14498–14505

References

Nakai H, Storm TA & Kay MA (2000) Recruitment of single-stranded recombinant adeno-associated virus vector genomes and intermolecular recombination are responsible for stable transduction of liver in vivo. *J Virol* 74: 9451–9463

Naso MF, Tomkowicz B, Perry WL & Strohl WR (2017) Adeno-Associated Virus (AAV) as a Vector for Gene Therapy. *BioDrugs* 31: 317–334

Nonnenmacher M & Weber T (2011) Adeno-associated virus 2 infection requires endocytosis through the CLIC/GEEC pathway. *Cell Host Microbe* 10: 563–576

Nonnenmacher M & Weber T (2012) Intracellular transport of recombinant adeno-associated virus vectors. *Gene Ther* 19: 649–658

Novikova O, Topilina N & Belfort M (2014) Enigmatic distribution, evolution, and function of inteins. *J Biol Chem* 289: 14490–14497

O'Carroll SJ, Cook WH & Young D (2021) AAV Targeting of Glial Cell Types in the Central and Peripheral Nervous System and Relevance to Human Gene Therapy. *Front Mol Neurosci* 13

Olusanya BO, Davis AC & Hoffman HJ (2019) Hearing loss grades and the International classification of functioning, disability and health. *Bull World Health Organ* 97: 725–728

Palfi A, Chadderton N, Millington-Ward S, Post I, Humphries P, Kenna PF & Farrar GJ (2022) AAV-PHP.eB transduces both the inner and outer retina with high efficacy in mice. *Mol Ther Methods Clin Dev* 25: 236–249

Pangrsic T, Lasarow L, Reuter K, Takago H, Schwander M, Riedel D, Frank T, Tarantino LM, Bailey JS, Strenzke N, *et al* (2010) Hearing requires otoferlin-dependent efficient replenishment of synaptic vesicles in hair cells. *Nat Neurosci* 13: 869–876

Pangršič T, Reisinger E & Moser T (2012) Otoferlin: a multi-C2 domain protein essential for hearing. *Trends Neurosci* 35: 671–680

Pavlou M, Schön C, Occelli LM, Rossi A, Meumann N, Boyd RF, Bartoe JT, Siedlecki J, Gerhardt MJ, Babutzka S, *et al* (2021) Novel AAV capsids for intravitreal gene therapy of photoreceptor disorders. *EMBO Mol Med* 13: e13392

Pereira-Leal JB & Seabra MC (2001) Evolution of the Rab family of small GTP-binding proteins. *J Mol Biol* 313: 889–901

Perrin L, Lacas-Gervais S, Gilleron J, Ceppo F, Prodon F, Benmerah A, Tanti J-F & Cormont M (2013) Rab4b controls an early endosome sorting event by interacting with the γ-subunit of the clathrin adaptor complex 1. *Journal of Cell Science* 126: 4950–4962

Pfeffer SR (2005) Structural clues to Rab GTPase functional diversity. *J Biol Chem* 280: 15485–15488

References

Pillay S, Meyer NL, Puschnik AS, Davulcu O, Diep J, Ishikawa Y, Jae LT, Wosen JE, Nagamine CM, Chapman MS, *et al* (2016) An essential receptor for adeno-associated virus infection. *Nature* 530: 108–112

Pillay S, Zou W, Cheng F, Puschnik AS, Meyer NL, Ganaie SS, Deng X, Wosen JE, Davulcu O, Yan Z, *et al* (2017) Adeno-associated Virus (AAV) Serotypes Have Distinctive Interactions with Domains of the Cellular AAV Receptor. *J Virol* 91: e00391-17

Rankovic V, Vogl C, Dörje NM, Bahader I, Duque-Afonso CJ, Thirumalai A, Weber T, Kusch K, Strenzke N & Moser T (2021) Overloaded Adeno-Associated Virus as a Novel Gene Therapeutic Tool for Otoferlin-Related Deafness. *Front Mol Neurosci* 13

Read AP & Newton VE (1997) Waardenburg syndrome. *J Med Genet* 34: 656–665

Regeneron (2025) Latest DB-OTO Results Demonstrate Clinically Meaningful Hearing Improvements in Nearly All Children with Profound Genetic Hearing Loss in CHORD Trial | Regeneron Pharmaceuticals Inc.

Reich SJ, Auricchio A, Hildinger M, Glover E, Maguire AM, Wilson JM & Bennett J (2003) Efficient trans-splicing in the retina expands the utility of adeno-associated virus as a vector for gene therapy. *Hum Gene Ther* 14: 37–44

Reisinger E, Bresee C, Neef J, Nair R, Reuter K, Bulankina A, Nouvian R, Koch M, Bückers J, Kastrup L, *et al* (2011) Probing the Functional Equivalence of Otoferlin and Synaptotagmin 1 in Exocytosis. *J Neurosci* 31: 4886–4895

Reisinger E & Trapani I (2024) Gene therapy proves successful in treating hereditary deafness. *The Lancet* 403: 2267–2269

Richter M, Iwata A, Nyhuis J, Nitta Y, Miller AD, Halbert CL & Allen MD (2000) Adeno-associated virus vector transduction of vascular smooth muscle cells in vivo. *Physiol Genomics* 2: 117–127

Romanovsky D, Scherk H, Föhr B, Babutzka S, Bogedein J, Lu Y, Reschigna A & Michalakis S (2025) Heparan sulfate proteoglycan affinity of adeno-associated virus vectors: Implications for retinal gene delivery. *Eur J Pharm Sci* 206: 107012

Roux I, Safieddine S, Nouvian R, Grati M, Simmler M-C, Bahloul A, Perfettini I, Le Gall M, Rostaing P, Hamard G, *et al* (2006) Otoferlin, defective in a human deafness form, is essential for exocytosis at the auditory ribbon synapse. *Cell* 127: 277–289

Schwander M, Sczaniecka A, Grillet N, Bailey JS, Avenarius M, Najmabadi H, Steffy BM, Federe GC, Lagler EA, Banan R, *et al* (2007) A Forward Genetics Screen in Mice Identifies Recessive Deafness Traits and Reveals That Pejvakin Is Essential for Outer Hair Cell Function. *J Neurosci* 27: 2163–2175

Schwartz SL, Cao C, Pylypenko O, Rak A & Wandinger-Ness A (2007) Rab GTPases at a glance. *J Cell Sci* 120: 3905–3910

Seabra MC (1996) Nucleotide dependence of Rab geranylgeranylation. Rab escort protein interacts preferentially with GDP-bound Rab. *J Biol Chem* 271: 14398–14404

Segelcke D, Fischer HK, Hütte M, Dennerlein S, Benseler F, Brose N, Pogatzki-Zahn EM & Schmidt M (2021) Tmem160 contributes to the establishment of discrete nerve injury-induced pain behaviors in male mice. *Cell Reports* 37: 110152

Shah NH, Eryilmaz E, Cowburn D & Muir TW (2013) Extein residues play an intimate role in the rate-limiting step of protein trans-splicing. *J Am Chem Soc* 135: 5839–5847

Shearer AE, Hildebrand MS, Odell AM & Smith RJ (1999) Genetic Hearing Loss Overview. In *GeneReviews*®, Adam MP Feldman J Mirzaa GM Pagon RA Wallace SE & Amemiya A (eds) Seattle (WA): University of Washington, Seattle

Shearer AE & Smith RJH (2012) Genetics: advances in genetic testing for deafness. *Curr Opin Pediatr* 24: 679–686

Shen F & Seabra MC (1996) Mechanism of Digeranylgeranylation of Rab Proteins: FORMATION OF A COMPLEX BETWEEN MONOGERANYLGERANYL-Rab AND Rab ESCORT PROTEIN (∗). *Journal of Biological Chemistry* 271: 3692–3698

Shu Y, Tao Y, Wang Z, Tang Y, Li H, Dai P, Gao G & Chen Z-Y (2016) Identification of Adeno-Associated Viral Vectors That Target Neonatal and Adult Mammalian Inner Ear Cell Subtypes. *Hum Gene Ther* 27: 687–699

Sloan-Heggen CM, Bierer AO, Shearer AE, Kolbe DL, Nishimura CJ, Frees KL, Ephraim SS, Shibata SB, Booth KT, Campbell CA, *et al* (2016) Comprehensive genetic testing in the clinical evaluation of 1119 patients with hearing loss. *Hum Genet* 135: 441–450

Smith RJH, Bale JF & White KR (2005) Sensorineural hearing loss in children. *Lancet* 365: 879–890

Smith RJH & Hildebrand M (2015) DFNA2 Nonsyndromic Hearing Loss.

Someya S, Xu J, Kondo K, Ding D, Salvi RJ, Yamasoba T, Rabinovitch PS, Weindruch R, Leeuwenburgh C, Tanokura M, *et al* (2009) Age-related hearing loss in C57BL/6J mice is mediated by Bak-dependent mitochondrial apoptosis. *Proceedings of the National Academy of Sciences* 106: 19432–19437

Song MH, Lee K-Y, Choi JY, Bok J & Kim U-K (2012) Nonsyndromic X-linked hearing loss. *Front Biosci (Elite Ed)* 4: 924–933

Sonntag F, Bleker S, Leuchs B, Fischer R & Kleinschmidt JA (2006) Adeno-associated virus type 2 capsids with externalized VP1/VP2 trafficking domains are generated prior to passage through the cytoplasm and are maintained until uncoating occurs in the nucleus. *J Virol* 80: 11040–11054

Sonntag F, Köther K, Schmidt K, Weghofer M, Raupp C, Nieto K, Kuck A, Gerlach B, Böttcher B, Müller OJ, *et al* (2011) The assembly-activating protein promotes capsid assembly of different adeno-associated virus serotypes. *J Virol* 85: 12686–12697

Sonntag F, Schmidt K & Kleinschmidt JA (2010) A viral assembly factor promotes AAV2 capsid formation in the nucleolus. *Proc Natl Acad Sci U S A* 107: 10220–10225

Stalmann U, Franke AJ, Al-Moyed H, Strenzke N & Reisinger E (2021) Otoferlin Is Required for Proper Synapse Maturation and for Maintenance of Inner and Outer Hair Cells in Mouse Models for DFNB9. *Front Cell Neurosci* 15: 677543

Stenmark H (2009) Rab GTPases as coordinators of vesicle traffic. *Nat Rev Mol Cell Biol* 10: 513–525

Strenzke N, Chakrabarti R, Al-Moyed H, Müller A, Hoch G, Pangrsic T, Yamanbaeva G, Lenz C, Pan K-T, Auge E, *et al* (2016) Hair cell synaptic dysfunction, auditory fatigue and thermal sensitivity in otoferlin Ile515Thr mutants. *EMBO J* 35: 2519–2535

Sun W, Yang J & Liu X-Q (2004) Synthetic two-piece and three-piece split inteins for protein trans-splicing. *J Biol Chem* 279: 35281–35286

Takago H, Oshima-Takago T & Moser T (2018) Disruption of Otoferlin Alters the Mode of Exocytosis at the Mouse Inner Hair Cell Ribbon Synapse. *Front Mol Neurosci* 11: 492

Tan F, Chu C, Qi J, Li W, You D, Li K, Chen X, Zhao W, Cheng C, Liu X, *et al* (2019) AAV-ie enables safe and efficient gene transfer to inner ear cells. *Nat Commun* 10: 3733

Tang H, Wang H, Wang S, Hu SW, Lv J, Xun M, Gao K, Wang F, Chen Y, Wang D, *et al* (2023) Hearing of Otof-deficient mice restored by trans-splicing of N- and C-terminal otoferlin. *Hum Genet* 142: 289–304

Tang Q, Keeler AM, Zhang S, Su Q, Lyu Z, Cheng Y, Gao G & Flotte TR (2020) Two-Plasmid Packaging System for Recombinant Adeno-Associated Virus. *Biores Open Access* 9: 219–228

Tertrais M, Bouleau Y, Emptoz A, Belleudy S, Sutton RB, Petit C, Safieddine S & Dulon D (2019) Viral Transfer of Mini-Otoferlins Partially Restores the Fast Component of Exocytosis and Uncovers Ultrafast Endocytosis in Auditory Hair Cells of Otoferlin Knock-Out Mice. *J Neurosci* 39: 3394–3411

Tornabene P, Trapani I, Minopoli R, Centrulo M, Lupo M, de Simone S, Tiberi P, Dell'Aquila F, Marrocco E, Iodice C, *et al* (2019) Intein-mediated protein trans-splicing expands adeno-associated virus transfer capacity in the retina. *Sci Transl Med* 11: eaav4523

Trainor PA, Dixon J & Dixon MJ (2009) Treacher Collins syndrome: etiology, pathogenesis and prevention. *Eur J Hum Genet* 17: 275–283

Trapani I (2019) Adeno-Associated Viral Vectors as a Tool for Large Gene Delivery to the Retina. *Genes (Basel)* 10: 287

Trapani I, Colella P, Sommella A, Iodice C, Cesi G, de Simone S, Marrocco E, Rossi S, Giunti M, Palfi A, *et al* (2014) Effective delivery of large genes to the retina by dual AAV vectors. *EMBO Molecular Medicine* 6: 194–211

References

Tsuzuki N, Namba K, Saegusa C, Mutai H, Nishiyama T, Oishi N, Matsunaga T, Fujioka M & Ozawa H (2023) Apoptosis of type I spiral ganglion neuron cells in *Otof*-mutant mice. *Neuroscience Letters* 803: 137178

Ullrich O, Stenmark H, Alexandrov K, Huber LA, Kaibuchi K, Sasaki T, Takai Y & Zerial M (1993) Rab GDP dissociation inhibitor as a general regulator for the membrane association of rab proteins. *Journal of Biological Chemistry* 268: 18143–18150

Varga R, Avenarius MR, Kelley PM, Keats BJ, Berlin CI, Hood LJ, Morlet TG, Brashears SM, Starr A, Cohn ES, *et al* (2006) OTOF mutations revealed by genetic analysis of hearing loss families including a potential temperature sensitive auditory neuropathy allele. *Journal of Medical Genetics* 43: 576–581

Varga R, Kelley PM, Keats BJ, Starr A, Leal SM, Cohn E & Kimberling WJ (2003) Non-syndromic recessive auditory neuropathy is the result of mutations in the otoferlin (OTOF) gene. *Journal of Medical Genetics* 40: 45–50

Vishnu P (2024) Akouos reports positive data from gene therapy trial for hearing loss. *Clinical Trials Arena*

Vogl C, Panou I, Yamanbaeva G, Wichmann C, Mangosing SJ, Vilardi F, Indzhykulian AA, Pangršič T, Santarelli R, Rodriguez-Ballesteros M, *et al* (2016) Tryptophan-rich basic protein (WRB) mediates insertion of the tail-anchored protein otoferlin and is required for hair cell exocytosis and hearing. *The EMBO Journal* 35: 2536–2552

Vona B, Rad A & Reisinger E (2020) The Many Faces of DFNB9: Relating OTOF Variants to Hearing Impairment. *Genes (Basel)* 11: 1411

Wandinger-Ness A & Zerial M (2014) Rab Proteins and the Compartmentalization of the Endosomal System. *Cold Spring Harb Perspect Biol* 6: a022616

Wang D, Tai PWL & Gao G (2019) Adeno-associated virus vector as a platform for gene therapy delivery. *Nat Rev Drug Discov* 18: 358–378

Wang H, Chen Y, Lv J, Cheng X, Cao Q, Wang D, Zhang L, Zhu B, Shen M, Xu C, *et al* (2024a) Bilateral gene therapy in children with autosomal recessive deafness 9: single-arm trial results. *Nat Med* 30: 1898–1904

Wang J, Zhao L, Gu X, Xue Y, Wang S, Xiao R, Vandenberghe LH, Peng KA, Shu Y & Li H (2022) Efficient Delivery of Adeno-Associated Virus into Inner Ear In Vivo Through Trans-Stapes Route in Adult Guinea Pig. *Human Gene Therapy* 33: 719–728

Wang J-H, Gessler DJ, Zhan W, Gallagher TL & Gao G (2024b) Adeno-associated virus as a delivery vector for gene therapy of human diseases. *Signal Transduct Target Ther* 9: 78

Wang Y, Ling C, Song L, Wang L, Aslanidi GV, Tan M, Ling C & Srivastava A (2012) Limitations of Encapsidation of Recombinant Self-Complementary Adeno-Associated Viral Genomes in Different Serotype Capsids and Their Quantitation. *Human Gene Therapy Methods* 23: 225–233

References

Wang Z, Ma H-I, Li J, Sun L, Zhang J & Xiao X (2003) Rapid and highly efficient transduction by double-stranded adeno-associated virus vectors in vitro and in vivo. *Gene Ther* 10: 2105–2111

Ward ES, Martinez C, Vaccaro C, Zhou J, Tang Q & Ober RJ (2005) From Sorting Endosomes to Exocytosis: Association of Rab4 and Rab11 GTPases with the Fc Receptor, FcRn, during Recycling. *MBoC* 16: 2028–2038

WHO (2021) World report on hearing.

WHO (2025) Deafness and hearing loss.

Wilson B, Flett C, Gemperle J, Lawless C, Hartshorn M, Hinde E, Harrison T, Chastney M, Taylor S, Allen J, *et al* (2023) Proximity labelling identifies pro-migratory endocytic recycling cargo and machinery of the Rab4 and Rab11 families. *J Cell Sci* 136: jcs260468

Wu J, Zhao W, Zhong L, Han Z, Li B, Ma W, Weigel-Kelley KA, Warrington KH & Srivastava A (2007) Self-complementary recombinant adeno-associated viral vectors: packaging capacity and the role of rep proteins in vector purity. *Hum Gene Ther* 18: 171–182

Wu Z, Asokan A & Samulski RJ (2006) Adeno-associated Virus Serotypes: Vector Toolkit for Human Gene Therapy. *Molecular Therapy* 14: 316–327

References

Xiao P-J & Samulski RJ (2012) Cytoplasmic Trafficking, Endosomal Escape, and Perinuclear Accumulation of Adeno-Associated Virus Type 2 Particles Are Facilitated by Microtubule Network. *J Virol* 86: 10462–10473

Xiao W, Warrington KH, Hearing P, Hughes J & Muzyczka N (2002) Adenovirus-Facilitated Nuclear Translocation of Adeno-Associated Virus Type 2. *J Virol* 76: 11505–11517

Yang H, Wang H & Jaenisch R (2014) Generating genetically modified mice using CRISPR/Cas-mediated genome engineering. *Nat Protoc* 9: 1956–1968

Yao Z, Aboualizadeh F, Kroll J, Akula I, Snider J, Lyakisheva A, Tang P, Kotlyar M, Jurisica I, Boxem M, *et al* (2020) Split Intein-Mediated Protein Ligation for detecting protein-protein interactions and their inhibition. *Nat Commun* 11: 2440

Yasunaga S, Grati M, Chardenoux S, Smith TN, Friedman TB, Lalwani AK, Wilcox ER & Petit C (2000) OTOF encodes multiple long and short isoforms: genetic evidence that the long ones underlie recessive deafness DFNB9. *Am J Hum Genet* 67: 591–600

Yasunaga S, Grati M, Cohen-Salmon M, El-Amraoui A, Mustapha M, Salem N, El-Zir E, Loiselet J & Petit C (1999) A mutation in OTOF, encoding otoferlin, a FER-1-like protein, causes DFNB9, a nonsyndromic form of deafness. *Nat Genet* 21: 363–369

Yildirim-Baylan M, Bademci G, Duman D, Ozturkmen-Akay H, Tokgoz-Yilmaz S & Tekin M (2014) Evidence for genotype–phenotype correlation for *OTOF* mutations. *International Journal of Pediatric Otorhinolaryngology* 78: 950–953

References

Yin N, Zhao J, Zhang P, Yu B, Chai R & Li G-L (2023) Functional and developmental changes in the inner hair cell ribbon synapses caused by Myosin VI knockout and deafness-inducing point mutation. *Cell Death Discov* 9: 177

Zerial M & McBride H (2001) Rab proteins as membrane organizers. *Nat Rev Mol Cell Biol* 2: 107–117

Zhang L, Chen S & Sun Y (2022) Mechanism and Prevention of Spiral Ganglion Neuron Degeneration in the Cochlea. *Front Cell Neurosci* 15: 814891

Zhang L, Wang H, Xun M, Tang H, Wang J, Lv J, Zhu B, Chen Y, Wang D, Hu S, *et al* (2023) Preclinical evaluation of the efficacy and safety of AAV1-hOTOF in mice and nonhuman primates. *Mol Ther Methods Clin Dev* 31: 101154

Zhang Q, Lan L, Shi W, Yu L, Xie L, Xiong F, Zhao C, Li N, Yin Z, Zong L, *et al* (2016) Temperature sensitive auditory neuropathy. *Hearing Research* 335: 53–63

Zhong L, Zhou X, Li Y, Qing K, Xiao X, Samulski RJ & Srivastava A (2008) Single-polarity recombinant adeno-associated virus 2 vector-mediated transgene expression in vitro and in vivo: mechanism of transduction. *Mol Ther* 16: 290–295

Zhou X, Zeng X, Fan Z, Li C, McCown T, Samulski RJ & Xiao X (2008) Adeno-associated virus of a single-polarity DNA genome is capable of transduction in vivo. *Mol Ther* 16: 494–499

9. Supplement

Table 28 - Restriction enzymes used for cloning.

Enzyme	Material Number
BamHI	FD0054, Thermo Fisher, Waltham, United States
BspTI	FD0834, Thermo Fisher, Waltham, United States
Bsu15I	FD0144, Thermo Fisher, Waltham, United States
EcoRI	FD0274, Thermo Fisher, Waltham, United States
Eco32I	FD0303, Thermo Fisher, Waltham, United States
HindIII	FD0505, Thermo Fisher, Waltham, United States
KflI	FD2164, Thermo Fisher, Waltham, United States
KpnI	FD0524, Thermo Fisher, Waltham, United States
MluI	FD0564, Thermo Fisher, Waltham, United States
NheI	FD0974, Thermo Fisher, Waltham, United States
NotI	FD0593, Thermo Fisher, Waltham, United States
PaeI	FD0604, Thermo Fisher, Waltham, United States
SalI	FD0644, Thermo Fisher, Waltham, United States
SmiI	FD1244, Thermo Fisher, Waltham, United States
XbaI	FD0684, Thermo Fisher, Waltham, United States
XhoI	FD0694, Thermo Fisher, Waltham, United States

Table 29 - Cloning primer.

ID	Name	Sequence 5'-3'
P2	hindIII_BFP_rev	CGCAAGCTTATTCAGCTTGTGCCCCAGTTTGCT
P3	NotI_CMV_Promotor_for	CGCGCGGCCGCATAGTAATCAATTACGGGGTCATTAGTTCA
P5	PaeI_alphaWPRE_for	CGCGCATGCAATCAACCTCTGGATTACAAAATTTGTG
P6	alphaWPRE_+9bp_gamma_rev	GCAAGAACTAACCAGGATTTATACAAGGAGGAG

P7	gammaWPRE_+AGTTC_+9bp_alpha_for	ATCCTGGTTAGTTCTTGCCACGGCGGAACTCA
P8	KpnI_XhoI_gammaWPRE_rev	CGCGGTACCCTCGAGACACCACGGAATTGTCAGTG
P9	XhoI_bGH_for	CACCTCGAGGCTGATCAGCCTCGACTGT
P10	KpnI_bGH_rev	CGCGGTACCCTGCTATTGTCTTCCCAATCCTC
P12	5'OTOF_V1_+9bp_N-Intein	GTCAAGGCAGCGGCCCTGGTCCTTGTC
P13	N-Intein_+9bp_5'OTOF_V1_for	CAGGGCCGCTGCCTTGACCTGAAAACCCA
P15	5'OTOF_V2_+9bp_N-Intein	GTCAAGGCAGAGGCCCAGCCACAGGTAGA
P16	N-Intein_+9bp_5_OTOF_V2_for	CTGGGCCTCTGCCTTGACCTGAAAACCCA
P19	BamHI_miniWPRE_for	CGCGGATCCAATCAACCTCTGGATTACAAAATTTGTG
P20	NotI_miniWPRE_rev	AATGCGGCCGCACACCACGGAATTGTCAGTGC
P21	MluI_CMV_Promotor_for	CGCACGCGTATAGTAATCAATTACGGGGTCATTAGTTC

P22	AccIII_EcoRI_CMV_Promotor_rev	AATTCCGGAGAATTCGGTGGCGCTAGCGGATCT
P23	EcoRI_C_Intein_for	CGCGAATTCATGATGCTCAAGAAGATCCTGAAGA
P24	C-Intein_+9bp_3_OTOF_V1_rev	GCGGGACGAATTGTGGGTCAGTATGTCGTTG
P25	3'OTOF_V1_+9bp_C-Intein_for	ACCCACAATTCGTCCCGCACCAGGCT
P26	KfII_3'OTOF_rev	CGCGGGTCCCTCCAGATATTGTAGCCATGTATGGAA
P27	C-Intein_+9bp_3_OTOF_V2_rev	CTGCTTGCTATTGTGGGTCAGTATGTCGTTG
P28	3'OTOF_V2_+9bp_C-Intein_for	ACCCACAATAGCAAGCAGCGAAAGGACTT
P29	NotI_3'Vector_Backbone_for	AATGCGGCCGCGCTGATCAGCCTCGACTGT
P30	MluI_3'Vector_Backbone_rev	GAGAACGCGTCCCCTAGTGATGGAGTTGGC
P31	3_OTOF_Sequencing1	CATTCCTTTCCGCCCATC
P32	3_OTOF_Sequencing2	AACACCACAGGGGAGGTTG

P33	3_OTOF_Sequencing3	CCCCATGGAGTCCATGTTG
P35	5_OTOF_Sequencing1	GGGGCACAAGCTGAATAAG
P36	5_OTOF_Sequencing2	TGAACATGGACCCTGTGG
P37	5_OTOF_Sequencing3	CATGTTGGGACTAGCTGTG
P38	AAV_Backbone_Sequencing1	TTCGCCCTTTGACGTTGG
P39	AAV_Backbone_Sequencing2_for	CGCCGCATACACTATTCTC
P40	AAV_Backbone_Sequencing3	GCAGAGCGCAGATACCAAA
P41	BFP_Sequencing	CCAGGGTTTTCCCAGTCAC
P43	Mini_WPRE_Sequencing	CTTTCTGCAGAAGCTACGC
P48	NotI_MluI_BFP_for	ATTTGCGGCCGCATTTACGCGTGCCACCATGGTGTCTAAGGG
P49	MluI_CMV_Promotor_rev	CGCACGCGTGATCTGACGGTTCACTAAACCAGCT
P50	BspTI_alphaWPRE_for_new	CGCGCCTTAAGGGGACCCAATCAACCTCTGGATTACAAAATTTGTG

P52	KflI_N-Intein_rev_new	CGATCGGGTCCCTCACTCTTTCACGTACAGACACATTCCTTC
P53	EcoRI_eGFP_for	CGCGAATTCGCCACCATGGTGAGCAAG
P54	KpnI_eGFP_rev	CGCGGTACCTCACTTGTACAGCTCGTCCATGC
P60	IsoformC_Sequencing1_for	TGTCGTAACAACTCCGCC
P67	SalI_5'OTOF_for	CGCGTCGACCCCTATGTGCAAGTCTTCTTTGC
P75	Bsu15I_PHP_B_rev	CGCATCGATTTACAGATTACGAGTCAGGTATCTGGTG
P76	SmiI_PHP_B_Cap_for	CGCATTTAAATATGGCTGCCGATGGTTATCTTCC
P77	PHPB_Sequencing1	GGTGCCAGACGCTTGCAC
P84	NheI_BFP_for	ATACGGCTAGCATGGTGTCTAAGGGCGAAGAGC
P85	KpnI_N-Intein_rev	CGCGGTACCTCACTCTTTCACGTACAGACACATTC

Table 30 - Sequencing barcodes used for cloning.

Plasmid	Barcode
pXS1	CVL831, CVL832, CVL833
pXS2	CVL834
pXS3	CVL837
pXS4	CVL851
pXS5	DFV723
pXS5.1	DFV726, DFV727
pXS6	DFV745, DFV746, DFV747
pXS6.1	EBZ622, EBZ623, EBZ624, EBZ625
pXS7	CVL836
pXS8	CVL838
pXS9	CVL844, CVL845, CVL846, CVL847 CVL853
pXS9.1	CVL848, CVL849, CVL850
pXS10	DFV728, DFV729
pXS10.1	DFV735, DFV736
pDGM-PHP.B	DFV740, DFV741

Table 31 - AAV production plasmids.

Plasmid Name	Concentration	Material Number
iCapminPHP.B	1750 ng/µL	103002, Addgene, Watertown, United States
pAdDeltaF6	417 ng/µL	112867, Addgene, Watertown, United States
pDGM6	1014.1 ng/µL	110660, Addgene, Watertown, United States
pUCiCapminPHP.eB	2550 ng/µL	103005, Addgene, Watertown, United States
pXS10	248.35 ng/µL	self-produced
pXS10.1	535.1 ng/µL	self-produced
pXS11	1104.4 ng/µL	self-produced
pXS6	733.25 ng/µL	self-produced
pXS6.1	73 ng/µL	self-produced

Table 32 - Titer of self-produced AAVs.

AAV	Titer (vg/mL)	Medium
PHP.B-GFP	$4.1x10^{12}$	PBS
PHP.eB-GFP	$1.5x10^{12}$	PBS
AAV6-GFP	$2x10^{11}$	PBS
AAV6-pXS6	$8.83x10^{11}$	F12 in vitro culture medium
AAV6-pXS10	$2.85x10^{11}$	F12 in vitro culture medium
AAV6-pXS6.1	$7.51x10^{12}$	F12 in vitro culture medium
AAV6-pXS10.1	$5.64x10^{12}$	F12 in vitro culture medium
PHPeB-pXS6	$8.66x10^{12}$	F12 in vitro culture medium
PHPeB-pXS10	$7.39x10^{12}$	F12 in vitro culture medium
PHPeB-pXS6.1	$2.46x10^{12}$	F12 in vitro culture medium
PHPeB-pXS10.1	$3.85x10^{12}$	F12 in vitro culture medium
PHP.B-pXS6	$3.63x10^{11}$	F12 in vitro culture medium
PHP.B-pXS10	$2.09x10^{12}$	F12 in vitro culture medium
PHP.B-pXS6.1	$1.21x10^{12}$	F12 in vitro culture medium
PHP.B-pXS10.1	$2.24x10^{12}$	F12 in vitro culture medium

Table 33 - Sequencing barcodes of Rab4b F1-generation animals.

Animal Number	Barcode
00	EBZ642, EBZ643
01	EBZ644, EBZ645
02	EBZ646, EBZ647
03	EBZ648, EBZ649
90	EBZ658, EBZ663
91	EBZ659, EBZ664
92	EBZ660, EBZ665
93	EBZ661, EBZ666
94	EBZ662, EBZ667

Table 34 - Sequencing barcodes of Rab4b F2-generation animals.

Animal Number	Barcode
68	JQY954, JQY953
70	JQY952, JQY957
74	JQY956, JQY955
75	JQY960, JQY959
76	JQY958, JQY963
77	JQY962, JQY961
78	JQY966, JQY965
79	JQY964, JQY969
80	JQY968, JQY967
82	JQY972, JQY971

Table 35 - 11.1x buffer ingredients.

Reagent	Stock conc	1 Vol / µl	2 Vol / µl	Conc. in final reaction in PCR tube
Tris-HCl pH 8,8	2M	167	334	45mM
Ammonium sulphate	1M	83	166	11mM
$MgCl_2$ (Sigma Cat No. M 1028-10x1mL)	1M	33,5	67	4,5mM
EDTA pH 8,0 (Life Technologies Cat No. 15575-020)	10mM	3,6	7,2	6,7mM
ß-mercaptoethenol	100%	3,4	6,8	4,4mM
dATP	100mM	75	150	1mM
dCTP	100mM	75	150	1mM
dGTP	100mM	75	150	1mM
dTTP (dNTP Set 4x100µmol, Bioline Cat No. BIO-39049)	100mM	75	150	1mM
BSA (Life Technologies Cat No. AM 2616)	50mg/mL	17	34	113µg/mL
H_2O		68	136	
Total		676	1352	

Table 36 - sgRNA and donor oligo information.

Order Number	21138052	21138052
Reference	239932588	239932589
Manufacturing ID	658853681	658854562
Product	Alt-R™ HDR Donor Oligo, 2 nmol	Alt-R™ CRISPR-Cas9 sgRNA, 2 nmol
Purification	Standard Desalting	Standard Desalting
Sequence Name	CD.HC9.JPPF3399+	Mm.HC9.CDPS8441.AA
Unit Size	0.015	0.15
Bases	82	100
Sequence	/Alt-R-HDR1/T*G*G GAA CCC AGG CTA CCT ACC GAA ACC GCT CCT GGC CAG CCA TGT CCC AAA TCT GTA GTT TCA CAG TCT TCC CCC CAA CG*T* T/Alt-R-HDR2/	mC*mU*mA* rCrArG rArUrU rUrGrG rGrArC rArCrU rGrCrG rUrUrU rUrArG rArGrC rUrArG rArArA rUrArG rCrArA rGrUrU rArArA rArUrA rArGrG rCrUrA rGrUrC rCrGrU rUrArU rCrArA rCrUrU rGrArA rArArA rGrUrG rGrCrA rCrCrG rArGrU rCrGrG rUrGrC mU*mU*mU* rU
Anhydrous Molecular Weight	25707	32369.8
nmoles/OD	1.33457894	0.97876089
ug/OD	34.3080048	31.6822893
Extinction Coefficient	749300	1021700
GC Content	56.097561	41
Tm (50mM NaCl) C	74.4095685	65.2915783
Modifications and Services	Phosphorothioate Bond Alt-R-HDR2 Alt-R-HDR1 Standard Desalting	Phosphorothioate Bond Standard Desalting
nmoles	2nmol	2nmol